Spark Ignition of Turbulent Non-premixed Flames

Samer Fikry Abdel Fattah Sayed Ahmed

Fitzwilliam College

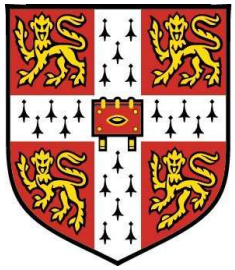

A dissertation submitted for the degree of

Doctor of Philosophy

Department of Engineering

University of Cambridge

2006

Declaration

The work described herein was undertaken in the Engineering Department within the Hopkinson Laboratory at the University of Cambridge between October 2003 and October 2006. This thesis is my own original work except where specifically indicated.

This dissertation contains approximately 40 000 words, 116 figures and two tables.

.....

Samer Ahmed

Friday, 23^{rd} September 2006

I would like to dedicate this thesis

TO

My parents FIKRY and LIYLA

TO

My wife SHAIMAA and my children MOHANED and YASMIN

and TO

My sisters HEBA and RANA

Acknowledgements

Firstly, I would like to express my thanks to my supervisor **Dr. Epaminondas Mastorakos**. I am extremely grateful for his support, invaluable guidance and for his continuing help even before I came to Cambridge. I also wish to thank him for providing a wonderful work atmosphere and good lab. facilities. I would also like to thank my advisor **Prof. Nick Collings** for his valuable suggestions and help.

I am very grateful to my MSc supervisor **Prof. Mohsen Radwan** for his great help to support me getting the BP Cambridge Scholarship for Egypt.

I would like to thank my friend Dr. Rama Balachandran for his great help and his valuable advices about the laser diagnostic techniques.

I am indebted to my colleagues from the Hopkinson Laboratory, namely Chang-Wook, Giorgio, Teresa, Haakon, Moncef, Ed, Andy, Ik Soo, Antonios, Martha, Jason, Christos, Nilanjan, Karthik, Terese, Andrew, Rob, Pedro, Claire, Kamal. Their help proved invaluable on many an occasion and the numerous tea breaks and discussions ensured that I kept my sanity and enjoyed my time in the Hopkinson Laboratory.

I am also in debt to the gentlemen of the workshop who were able to transform my drawings into physical constructs. I would like to thank

Michael, Peter, Robert, Roy, John and Trevor for their assistance in fabricating the apparatus. I acknowledge Dr. D. Dukic for designing and constructing the ignition unit.

I would like to express my thankfulness to the British Petroleum (BP) company in Egypt for the fellowship to study PhD in Cambridge. My project was also funded by Rolls-Royce plc., and the Department of Trade and Industry (DTI), UK, so thanks very much for them.

Finally, my sincere thanks go to my wife **Shaimaa** who offered her invaluable support to help me during this long education journey.

Abstract

This thesis investigates the spark ignition of various turbulent non-premixed flames namely, jet, counter-flow and bluff-body flames. This detailed fundamental study of spark ignition aims to provide useful information for solving the high-altitude relight problem in the aviation gas turbine.

A specially designed ignition unit has been built. Different spark parameters and flow conditions have been examined to study their effects on the ignition probability defined as successful flame establishment. The ignition probability results have been correlated with the measured or estimated flow velocity and mixture fraction. The whole ignition and flame propagation events have been visualized by a high-speed camera and OH-PLIF.

In the jet flames, it was found that after an initially spherical shape, the flame took a cylindrical shape with a propagating edge upstream. The probability of successful ignition P_{ign} increases with high spark energy, thin electrode diameter and wide gap, but decreases with increasing dilution of the jet with air. The flame kernel growth rate is high when the ignition probability is high for all parameters, except for jet velocity. Increasing the jet velocity decreases the ignition probability at all locations. The estimated net propagation speed relative to the incoming flow was about 3 to 6 laminar burning velocities of a stoichiometric mixture S_L.

In the counter-flow flames, it was found that the flame spread as an edge flame with a large scatter in its radial position. P_{ign} decreased with bulk velocity, which suggests that the local strain rate can be detrimental to ignition so that, even with the strongest spark tested, ignition could not be achieved at a bulk velocity about 90% of the extinction velocity. P_{ign} was greater than zero even in regions well into the fuel and air streams where the mixture fraction fluctuations were virtually zero, giving zero probability of finding flammable mixture at the spark location. The estimated edge flame speed relative to the radial flow is higher than S_L for the premixed flame and is less than S_L for the non-premixed flames.

In the bluff-body flames, three different shapes of flames were observed depending on the air and fuel velocities. The stability limits are much wider than the ignitability limits; however, they become closer if the swirl is used. How the flame propagates after the spark depends more on the ignition location than on the flow conditions. Three kinds of failed ignition as well as successful ignition have been visualized with OH-PLIF and OH*. A discrepancy between the ignition probability contours and the measured mixture fraction has been noticed and the mixing field is very sensitive to the air and fuel velocities. The present data provides a useful validation set for unsteady turbulent combustion models, for example those based on LES.

Contents

List of Figures

List of Tables

Nomenclature

AC	alternating current (mA)
A/F	air to fuel ratio
BR	blockage ratio
CDR	confinement diameter ratio
CRZ	central recirculation zone
Da	Damköhler number
DC	direct current (mA)
D, d	diameter (mm)
d_q	quenching distance (mm)
E	activation energy (kJ/kg)
E_{min}	minimum ignition energy (mJ)
F	flammability factor
fps	frame per second
H	counter-flow jet separation (mm)
$ICCD$	intensified charge coupled device
LDV	laser doppler velocimeter
L_h	lift-off height (mm)
L_{turb}	integral length scale (mm)
l/min	liter per minute
MFC	mass flow controllers
OH^*	OH chemiluminescence
P	pressure (bar)
P_{ign}	ignition probability
PIV	particle image velocimeter
$PLIF$	planar laser induced florescence
PMT	Photomultiplier Tubes
R	radius (mm)
r	radial position (mm)
Re	Reynolds number

$r.m.s$	root mean square
S	strain rate (s^{-1})
S_L	laminar flame speed (m/s)
SRZ	side recirculation zone
S_T	turbulent flame speed (m/s)
T^*	flame front temperature (K)
T_o	surrounding temperature (K)
U	axial velocity (m/s)
u'	axial velocity fluctuations (m/s)
V	radial velocity (m/s)
v'	radial velocity fluctuations (m/s)
X	air volume fraction in the fuel stream $(\%)$
Y	mass fraction
Z	element mass fraction
z	axial position (mm)

Greek Symbols

χ	scalar dissipation rate (s^{-1})
η_K	Kolmogorov length scale (mm)
ν	dynamic viscosity $(kg/(m.s))$
ρ	density (kg/m^3)
ϕ	equivalence ratio
τ_K	Kolmogorov time scale (μs)
θ	bluff-body cone angle
ξ	mixture fraction

Subscripts

$acet$	acetone
b	bulk or bluff-body
$edge$	edge flame
ext	extinction
f	fuel
j	jet
o	outer
st	stoichiometric

Chapter 1

Introduction

The capability to relight at high-altitude imposes an important limitation on the design of a gas turbine combustor. With the modern trends of aircraft gas turbine to use lean mixture and to reduce the emission levels, the solution to the high-altitude relight problem becomes a high priority for the aircraft gas turbine combustor. Currently, quite old empirical correlations are being used for design and the computational models used for predictions are not validated as extensively as desired. There is hence a need for well-characterized, focused experiments on how turbulent non-premixed flames can be ignited. Knowledge of the phenomena involved can assist with the design of gas turbine combustor. Therefore, this work aims to investigate experimentally the problem of high-altitude relight in a gas turbine combustor by trying to understand the characteristics of forced (spark) ignition in different turbulent non-premixed flow configurations namely; jet, counter-flow and bluff-body flames.

In this chapter, the ignition is defined from a fundamental point of view. The practical importance of ignition is also mentioned with an example of a real gas turbine ignition loop. Then, different kinds of ignition sources are presented and discussed in terms of their advantages and disadvantages. The different

types of turbulent combustion are defined with a particular attention on non-premixed turbulent combustion characteristics. Finally, the chapter ends with the objectives and outline of this thesis.

1.1 Importance of Ignition

Ignition can be defined as the initiation of rapid exothermic reactions or the appearance of a flame in a combustible mixture. Ignition may be caused with the help of an external stimulus such as an electric spark, or without any external source such as auto-ignition in a compression ignition engine. However, we are going to concentrate on the ignition with external source because this is the main concern of this work. The external source that provides localized heating in a combustible mixture may be an electric spark or another kind of heat source such as a laser or plasma jet (Aggarwal, 1998). Ignition is a crucial event in the operation of many systems such as gas turbines, spark ignition engines, industrial furnaces and boilers. The ignition in jet engine combustors is an important phenomenon due to the desirability of fast ignition and its relation to the issue of flame stabilization. Similar considerations apply to spark ignition engines, where fast well-controlled ignition is important to engine efficiency and emissions.

Of prime important to the gas turbine is the need for easy and reliable light-up during ground starting while the engine is being cranked up to its self-sustaining speed. With the aircraft gas turbine, an additional requirement is for rapid relighting of the chamber after a flameout in flight. Under adverse climatic conditions, or on takeoff from a wet runway, where there is a risk of ingestion of excessive amount of water or ice, the ignition system must also be capable of continuous operation in order to ensure immediate relighting of the engine in the event of flame extinction. The ignition of a combustible mixture may be accom-

plished by various means, but in the gas turbine it is usually effected by means of an electric spark. Large amounts of energy are needed to ignite the heterogeneous and highly turbulent mixtures flowing at velocities of the order of 25 m/s (Lefebvre, 1998). The heterogeneous mixture is a mixture of fuel and oxidizer that exist in different physical states, i.e. gas-liquid, while the homogeneous mixture is the one which both fuel and oxidizer in the same physical states.

The ignition performance of an aircraft engine, for instance, is usually expressed in terms of the range of flight conditions over which combustion can be re-established after a flameout at altitude. To determine the relighting capabilities of an engine, it is customary to carry out a series of combustor rig tests in which the inlet parameters are varied to produce a range of flight conditions. For constant combustor inlet pressure, temperature, and air mass flow, ignition is attempted at various values of fuel/air ratio. Successful ignition is indicated by continued burning after the ignition source has been switched off. Such definition is considered in the present work for the successful ignition event as well. The procedure is repeated for a range of mass flows until a complete ignition loop can be drawn. A typical loop for an aircraft combustion chamber is shown in Fig. 1.1. It can be noted that the ignitability limit is lower than the stability limit, which indicates that there are some flow conditions that are suitable to stabilize the flame, but these conditions are not suitable for the ignition and flame propagation.

1.2 Sources of Ignition

Although the spark ignition is the only source of ignition used in this work, other means of ignition are available for certain special applications. These other sources of ignition are briefly discussed in this section.

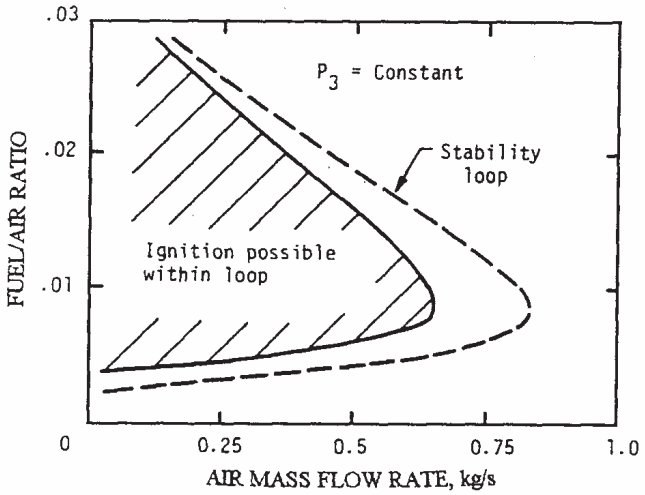

Figure 1.1: Typical gas turbine combustor ignition loop (Lefebvre, 1998).

Spark ignition

For gas turbines, the most satisfactory and convenient mode of ignition is some form of electrical discharge, such as a spark or arc discharge (Lefebvre, 1998). A distinguishing feature of spark ignition is the transient deposition of ignition energy in a short duration (tens to hundreds of microseconds), and in a concentrated region (characteristic size: millimeter and smaller) of a combustible mixture. The basic idea then is to examine whether or not this energy deposition leads to a state of ignition and appearance of a flame, identify this state of ignition and determine how long it takes to attain this state. In addition, complete control can be exercised over the frequency, duration, and amount of energy in each discharge. The parameters affecting the spark ignition will be highlighted in more detail in Section 3.1.2.

Laser ignition

The development of lasers as laboratory tools occurred sufficiently recently that the first open-literature publications in this area were not until the later 1960s. The research done by Bourne (2001) concluded that laser ignition was possible in many explosives of varying sensitivity. This phenomenon has obvious potential for the ignition of combustible mixtures and appears to have a number of advantages over conventional methods of ignition. It allows the ignition site to be accurately positioned at some points, and also avoids the various heat losses that are incurred when the igniter is located at the liner wall. At the present time, much interest is being shown in this novel form of ignition, but more research and development will need to be done before it can be regarded as a serious contender to the existing high-energy spark system.

Plasma jet

This method has been studied by Orrin et al. (1981). The plasma jet used in their experiments differ from a normal igniter in that the electrical discharge occurs in a small cavity that is supplied with a suitable plasma medium via a small capillary as shown in Fig. 1.2. The very high pressures and temperatures generated by the discharge cause the plasma to be ejected as a supersonic jet through an orifice located at the downstream end of the cavity. By varying the feed to the cavity, the energy input, and the size of the discharge orifice, it is possible to vary the temperature of the plasma jet and its velocity (and hence its penetration distance). The gases tested include nitrogen and hydrogen and their effectiveness as an ignition source is attributed to their high content of radicals (Orrin et al., 1981).

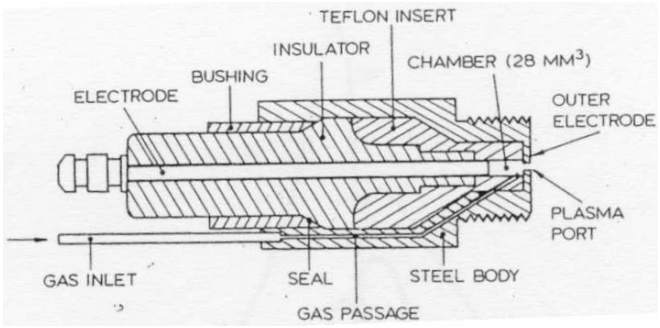

Figure 1.2: Plasma jet igniter (Orrin et al., 1981).

Torch igniter

The torch igniter incorporates a spark plug and an auxiliary fuel jet in a common housing. The juxtaposition of these two components is such that ignition of the fuel by the spark produces a "torch" of burning products that ignite the main fuel. The performance of the torch igniter is fairly insensitive to its location (Lefebvre, 1998). Usually in the gas turbine combustor, it is fitted into the annulus formed between the liner and the air casing near the upstream end of the chamber. The main problem with torch igniters is that of fuel cracking and gumming (Lefebvre, 1998). Inlet air temperature, fuel volatility, and fuel/air ratio are the most important parameters affecting this type of ignition.

Glow plug

The function of a glow plug is to provide rapid re-ignition of the flame should extinction occur as a result of the sudden ingestion of water or ice, or through temporary fuel starvation. The typical plug would be in the form of a hollow cylinder, 25 mm in length and 15 mm in external diameter. Nitride-bonded silicon carbide is the common material for the plug providing service lives exceeding 4000 hours have been realized in the military aircraft (Anon, 1961). According to Rolls

Royce, successful relights were achieved for periods of up to 12 seconds after the engine shut down. However, the main drawback of the glow plug is the risk of a plug or part of it becoming detached and damaging the turbine blades. This is why they have found so few applications. However, they appear to merit consideration for helicopter engines for which they seem almost ideally suited (Lefebvre, 1998).

Hot-Surface ignition

This type of ignition is not normally regarded as a practical proposition in gas turbines due to the very high rates of heat transfer that would be needed to evaporate the fuel and raise the vapor-air temperature to the point of ignition in the very short time that the mixture is in contact with the hot surface. This, of course, is why the spark ignition is so successful: a spark provides an almost instantaneous (< 150 μs) transfer of heat to the fresh mixture. However, hot-surface igniter is used in some applications such as the PT6 engine (Anon, 1961).

Chemical ignition

There are a number of chemicals, such as pyrophoric fuels, which ignite spontaneously on contact with air and produce a high rate of heat release. However, practical means of storage and injection must be found before they can be used in civil aircraft. They are obviously very dangerous in the event of a crash, and this would appear to restrict their use to military aircraft (Lefebvre, 1998).

Gas addition

The effect of gas addition on ignition limits has been studied before using a combustor supplied with Kerosine fuel (Lefebvre, 1998). In some experiments

the gaseous fuel was injected into the air upstream of the combustor; in others it was injected through the spark plug itself. The results show that ignition limits can be extended to lower levels of pressure by local injection of gaseous fuel into the spark kernel.

Oxygen injection

The beneficial effect of oxygen addition to almost all aspects of combustion performance is well known. In the context of ignition, increasing the oxygen content of a propane-air mixture, for example, from the normal value of 21% to 50% reduced the ignition energy requirement by a factor of 40 (Chin, 1982). This beneficial effect is found to also apply to the ignition of fuel sprays in gas turbine combustors, where ignition at low pressures is greatly facilitated by the injection of oxygen into the primary zone. As oxygen is normally carried on aircraft for other purposes, it would appear to be an attractive means of raising altitude relighting limits in circumstances where more conventional methods have proved inadequate (Chin, 1982).

From the previous review, it can be observed that the spark ignition is still the most common way used to produce ignition in the practical systems. In addition, the spark has well defined characteristics, which they can be controlled easily. Finally, it is easy to build a spark ignition system in the laboratory. Therefore, the present research used this method in the experimental investigations about the ignition in non-premixed flames.

1.3 Turbulent Combustion

In recent years, nothing seems to have inspired researchers in the combustion community so much as unresolved problems in turbulent combustion. Turbu-

lence itself is far from being fully understood. In technical processes, combustion nearly always takes place within a turbulent rather than a laminar flow field. The reason for this is twofold. First, turbulence increases the mixing processes and thereby enhances combustion. Second, combustion releases heat and thereby generates flow instability by buoyancy and gas expansion, which then enhances the transition to turbulence (Peters, 2000). Combustion requires that fuel and oxidizer be mixed at the molecular level. This depends on the turbulent mixing process. The general view is that once a range of different size eddies has developed, strain and shear at the interface between the eddies enhance the mixing. During the eddy break-up process and the formation of smaller eddies, strain and shear will increase and thereby steepen the concentration gradients at the interface between reactants, which in turn enhances their molecular inter-diffusion. Molecular mixing of fuel and oxidizer, as a prerequisite of combustion, therefore takes place at the interface between small eddies. Technical processes in turbulent combustion can be divided in terms of mixing into: premixed, non-premixed, or partially premixed turbulent combustion.

1.3.1 Premixed turbulent combustion

Premixed combustion requires that fuel and oxidizer be completely mixed before combustion is allowed to take place. Once fuel and oxidize have homogeneously been mixed and a heat source is supplied it becomes possible for a flame front to propagate through the mixture. This happens if the fuel-to-air ratio lies between the flammability limits. For example, flammable mixtures range from approximately $\phi = 0.5$ to 1.5 for methane, where ϕ is the fuel-air equivalence ratio. Examples of practical applications are spark-ignition engines, stationary lean-burn gas turbine, and household burners. In the present work, a limited number of experiments have been done on premixed combustion with either counter-flow

flames or bluff-body flames.

1.3.2 Non-premixed turbulent combustion

In many combustion applications fuel and oxidizer enter separately into the combustion chamber where they mix and burn during continuous inter-diffusion. Non-premixed combustion is sometimes called diffusive combustion or combustion in diffusion flames since diffusion is the rate-controlling process. The time needed for convection and diffusion, both being responsible for turbulent mixing, is typically much larger than the time needed for combustion reactions to occur. This type of combustion is employed in the majority of practical combustion systems, principally because of the ease with such flames can be controlled (Weinberg, 1975). Applications of non-premixed combustion include furnaces, diesel engines, and aircraft gas turbine engines.

A very important quantity for the description of non-premixed combustion is the mixture fraction ξ (sometimes also denoted by f or Z) which plays a role in determining the flame surface and is a key parameter in determining the flammable region in the cold flow. Bilger defined the mixture faction ξ of a hydrocarbon fuel C_mH_n as (Bilger, 1988) :

$$\xi = \frac{Z_C/(mW_C) + Z_H/(nW_H) + 2(Y_{O_2,2} - Z_O)/(\upsilon_{O_2}W_{O_2})}{Z_{C,1}/(mW_C) + Z_{H,1}/(nW_H) + 2Y_{O_2}/(\upsilon_{O_2}W_{O_2})} \tag{1.1}$$

where, Z_C, Z_H and Z_O denote the element mass fraction of C, H and O and W_C, W_H and W_{O_2} their molecular weight respectively. $Y_{O_2,2}$ is the mass fraction of oxygen in the oxidizer stream. υ_{O_2} is the stoichiometric coefficient of oxygen, ξ = 1 in the fuel stream, and ξ = 0 in the oxidizer stream. For a stoichiometric mixture, the stoichiometric mixture fraction ξ_{st} :

$$\xi_{st} = \frac{1}{(A/F)_{st} + 1} \tag{1.2}$$

where $(A/F)_{st}$ is the stoichiometric air/fuel ratio. For pure fuels mixed with air, the stoichiometric mixture fraction is, for instance, 0.0284 for H_2, 0.055 for CH_4, 0.0635 for C_2H_4, 0.0601 for C_3H_8, and 0.072 for C_2H_2. Most of the experiments in this work have been run on non-premixed combustion with gaseous fuel and in particular methane CH_4 and the concept of mixture fraction is crucial for interpreting the data.

1.3.3 Partially premixed turbulent combustion

If the fuel and oxidizer enter separately, but partially mix by turbulence, combustion takes place in a stratified medium, once the mixture is ignited. Such a mode of combustion has traditionally been called partially premixed combustion. Turbulent flame propagation in a stratified mixture occurs, for instance, in aircraft gas turbine during ignition. Another example is partially premixed flame propagation in direct injection gasoline engines, where a spray of liquid gasoline is injected directly into the cylinder rather than into the intake manifold. The most important manifestation of partially premixed combustion is lift-off and stabilization at the lift-off height in turbulent jet diffusion flames. In the present work, lifted-jet flame has been taken into consideration. However, the expression "partially premixed" has not been used in the present work. Instead, "dilution" was used to describe the situation of small amount of air mixed with the fuel upstream of the burner exit with the flame still having a non-premixed characteristics.

1.4 Scope of the Thesis

1.4.1 Objectives

The spark ignition of turbulent non-premixed flames has not been studied as extensively as the spark ignition of turbulent premixed flames. Detailed literature reviews will be included in the following chapters. In addition, the practical importance of this kind of ignition described earlier is another motivation for the present research. Therefore the specific objectives of this work are:

- To visualize the ignition process from the moment of spark to the stabilization of the flame by using high-speed imaging.

- To study different structures of the flame front during propagation after the ignition by using laser diagnostic techniques such as the OH-PLIF (Planar Laser Induced Florescence) imaging.

- To measure the mixture fraction distributions, which is useful to understand and correlate the probability of ignition.

- To measure the probability of successful ignition in different locations in the flow field and to investigate the influence of different flow conditions and different spark parameters on the ignition probability. This forms the main target of this work.

- Finally, to measure the turbulent flame propagation speed in some flow configurations and to try to estimate the relative flame propagation in respect to the flow velocity.

1.4.2 Outline of the thesis

The outline of this thesis is as follows. In Chapter 2, a full description of the experimental methods used is given, including the burner designs and configurations, and the instrumentation used for measurements. These include velocity

measurement techniques, laser diagnostics such as acetone-PLIF and OH-PLIF, high-speed imaging and chemiluminescence measurement techniques. Experimental errors are discussed. In Chapter 3, a literature review about the turbulent jet flame is provided followed by the experimental results about the spark ignition of turbulent jets. These results include flow measurements, visualization of ignition and flame propagation, effect of ignition location on the lift-off height, ignition probability, flame propagation speed, calibration of OH*/CH* ratio with mixture fraction. In Chapter 4, the literature review and then the experimental results covering similar areas like the jet results with detailed mixture fraction measurements are presented for the spark ignition of turbulent counter-flow flames. In Chapter 5, the literature review and the experimental results of the spark ignition of turbulent bluff-body flames are presented together with velocity and mixture fraction measurements. Each of the previous chapters ends with conclusions from the results in the particular chapter. Moreover, in Chapter 6, general conclusions and suggestions for future research in this field are provided. There are three appendixes about the ignition unit used in the work, the image processing techniques, and the recent publications of this work. The thesis ends with a list of references used.

Chapter 2

Experimental Methods

This chapter presents the experimental apparatus used in the present work. In addition, a full description of the ignition unit is provided in Section 2.2. The flow measurements techniques are presented next. Planer Laser Induced Fluoresence (PLIF) imaging (acetone PLIF and OH PLIF) is described and explained in terms of the set up and accuracy. Furthermore, the high speed imaging technique is described followed by a clarification of the chemiluminescence measurements. The chapter ends with a presentation of the method used in measuring the ignition probability and the error analysis associated with these measurements.

2.1 Burners

In the present work, three burners were used in three different sets of experiments. They are the turbulent jet, counter-flow and bluff-body burners. The turbulent jet burner was designed and built during this work. The turbulent counter-flow burner was originally designed and built by Mastorakos (1993). However, some modifications have been done in the present work such as introducing spark ignition arrangements to the burner as clarified in Section 2.1.2. The bluff-body

burner was originally designed and built by Balachandran (2005). However, this design was for premixed bluff-body flame investigations. In the present work, a non-premixed bluff-body was designed and built and this new bluff-body replaced the previous one. However, both bluff-bodies have the same outside dimensions in order to keep the flow pattern the same. These burners are described fully in the next sections. A review of previous work in these geometries is postponed to Chapters 3, 4 and 5 for the jet, counter-flow and bluff-body respectively.

2.1.1 Turbulent jet

Figure 2.1 shows a schematic diagram of the test rig designed for the turbulent jet. It consists of a $d_j = 5 \pm 0.05$ mm internal diameter stainless steel tube. The tube has a length to diameter ratio of 128 (tube length = 640 mm) to assure a fully developed turbulent pipe flow at the jet exit (Granger, 1985). The fuel was delivered from the jet exit as a turbulent jet with different exit velocities covering the range from $U_j = 6.31$ m/s to 28.4 m/s, measured by dividing the volume flow rate by the exit area of the pipe, (with $\pm$ 5.5% maximum error). This range corresponds to jet Reynolds number (Re_j) from 2000 to 9000 respectively. The fuel used was mainly pure methane (99.96% purity), which was supplied from a standard pressurized cylinder fitted with a regulator that supplied the gas at constant pressure. Sometimes, the fuel was premixed with air to alter the stoichiometric mixture fraction and to reduce the amount of unburnt fuel, with air volume fraction in the fuel stream X ranges between 10 and 40%, or diluted with nitrogen with similar volumetric percentages.

The fuel tube is surrounded by a concentric 200 mm co-flow tube. Low-speed air ($\sim$ 0.1 m/s with $\pm$ 2.5% maximum error) passes through a cone, with appropriate dimensions to avoid separation (Lefebvre, 1998), and a wire mesh with 0.25 mm hole diameter to the co-flow exit. This co-flow air was meant to

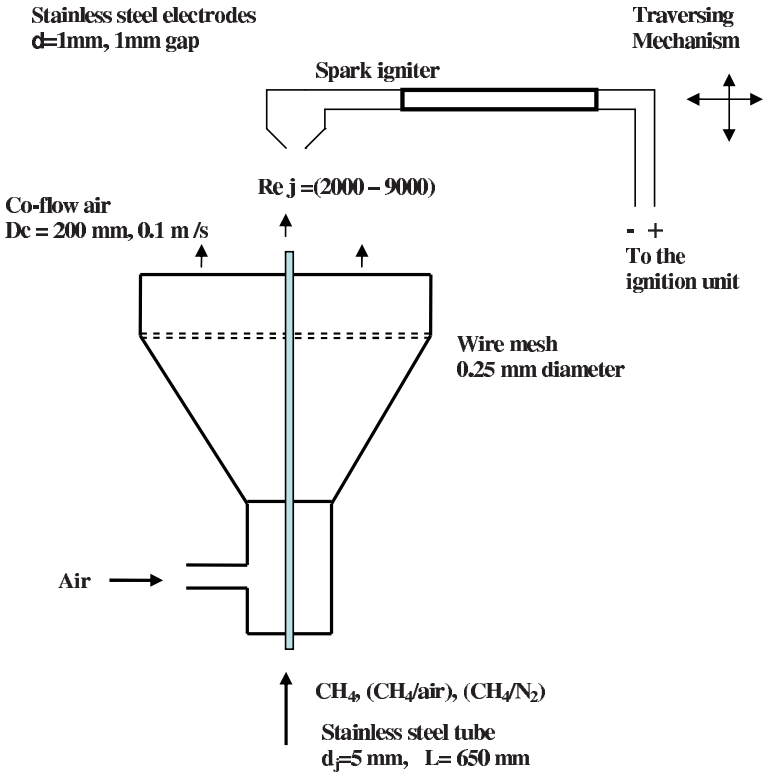

Figure 2.1: Schematic diagram of the turbulent jet burner with the spark electrodes.

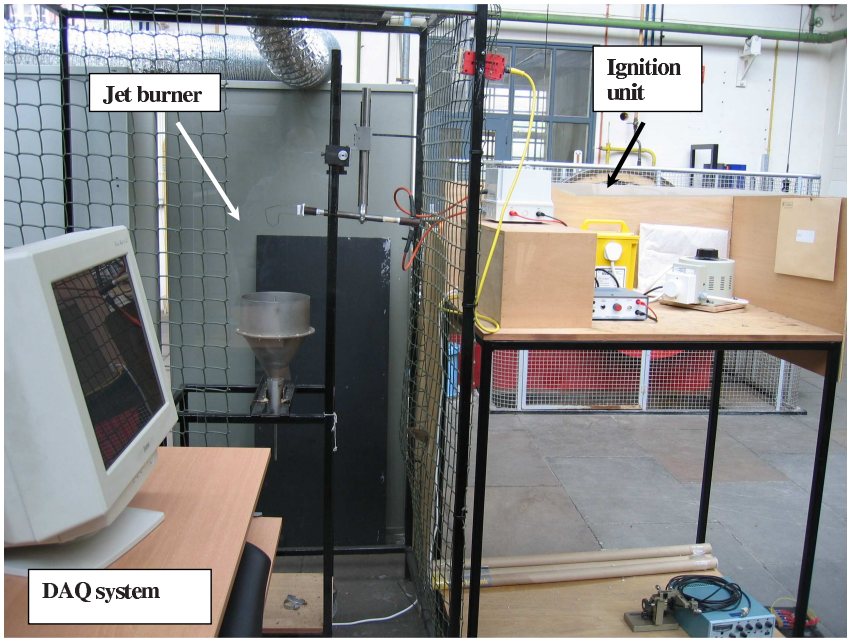

Figure 2.2: Photograph of the jet test rig.

eliminate the disturbances from room air currents. The outer wall of the fuel tube, with a lip thickness of 0.3 mm, was tapered at a half cone angle of 2° with respect to the burner exit. This is because the lip thickness of the fuel tube has a considerable effect of flame stabilization, as the flame stability is controlled by the flame-base holding in the thick-walled fuel tube wake (Takahashi and Schmoll, 1990). Figure 2.2 shows a photograph of the jet rig with the ignition unit and the data acquisition system (DAQ). A description of the ignition unit and electrodes configuration is given in Section 2.2.

2.1.2 Counter-flow

Figure 2.3 shows a schematic diagram of the geometric arrangements of the counter-flow burner. It consists of two opposed straight stainless steel tubes, each of inside diameter $D = 25 \pm 0.1$ mm and 40 diameters long, separated by a

vertical distance $H = 1D = 2R$, where R is the radius of the tube. To promote turbulence, perforated plates with holes of 3 mm diameter giving 40% solidity were fixed within each of the tubes by the spring-action of four legs. These perforated plates have been placed at a distance, H_P, equals 60 mm upstream of the tube exits. Outer straight tubes of $D_o = 50 \pm 0.1$ mm diameter and 300 mm long were also fitted to, and made concentric with, the inner tubes by adjusting three screws arranged at 120° angular separation between each two of them. Both assemblies were clamped to a frame and vertical alignment of the two assemblies was performed by adjusting the screws until the two opposing inner tubes were facing each other to within 0.1 mm as measured by a caliper, Fig. 2.4. With this alignment, the flames were horizontal, i.e. normal to the burner axis.

The upper tube carries air supplied by the laboratory compressor at 10 bar and reduced by a commercial pressure regulator to the atmospheric pressure. The lower tube carries methane, pure or premixed with air. The degree of premixing is described by X, which ranges from 0 to 80%. Despite this high premixedness, the flame has a non-premixed character because the mixture is beyond the rich flammability limit. The flow in the annular space between the outer and the inner tubes was nitrogen and its purpose was to shield the inner reactant jets from entraining air. The nitrogen co-flow is also essential to limit the stagnation region between the two jets; failure to achieve this resulted in flames being attached on the fuel-nozzle rim. The nitrogen was supplied from a standard pressurized cylinder with a pressure of 200 bar then through a gas regulator which supplied the gas at constant pressure. The bulk velocity of the upper jet is U_b covering the range from 1 to 4 m/s (with $\pm$ 4% maximum error) measured by dividing the flow rate by the exit area of the jet. To achieve a symmetric flow, the momentum flow rates of the two jets were kept equal. The co-flow velocity was kept constant at 0.6 m/s.

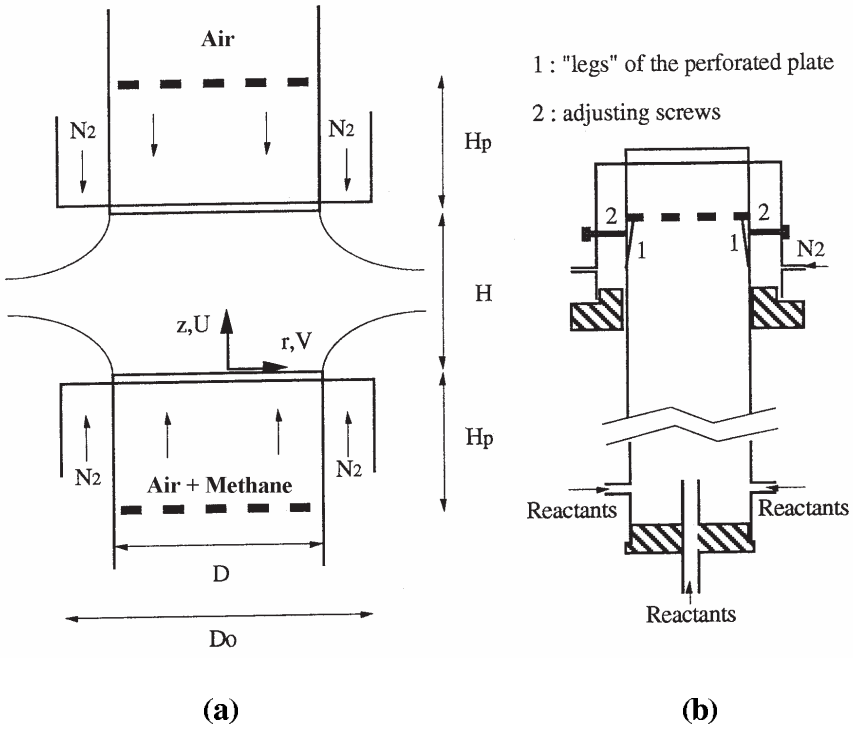

Figure 2.3: (a) Schematic diagram of the counter-flow burner. (b) More details of the rear part showing the way the reactants are fed. This burner was originally designed by Mastorakos (1993).

Figure 2.4: Photograph of the counter-flow test rig with spark electrodes.

2.1.3 Bluff-body

Figure 2.5 and 2.6 show the schematic and photograph of the non-premixed bluff-body burner. It is consists of two concentric circular ducts of length 400 mm. The inner diameter of the outer duct D_s is 35±0.1 mm. The inner duct is a 6 mm internal diameter tube and its end at the burner exit has a conical bluff-body of diameter $D_b = 25 \pm 0.05$ mm, giving a blockage ratio $BR = D_b^2/D_s^2 = 50\%$. The flame area was enclosed using a 80 mm long fused silica quartz cylinder of inner diameter 70 mm, which provided optical access for the imaging and also avoided air entrainment from the surrounding. In some experiments, a 60° swirl vane was introduced to the flow and located at 50 mm upstream of the bluff-body surface, Fig. 2.7. The swiller has a 35 mm outer diameter and 14.6 mm hight and it was fitted as shown in Fig. 2.5.

The annulus between the outer and inner ducts serves as the passage for the air, which flows through a 200 mm long plenum of inner diameter 100 mm. The plenum has a divergent and convergent cross-sections at the inlet and the exit

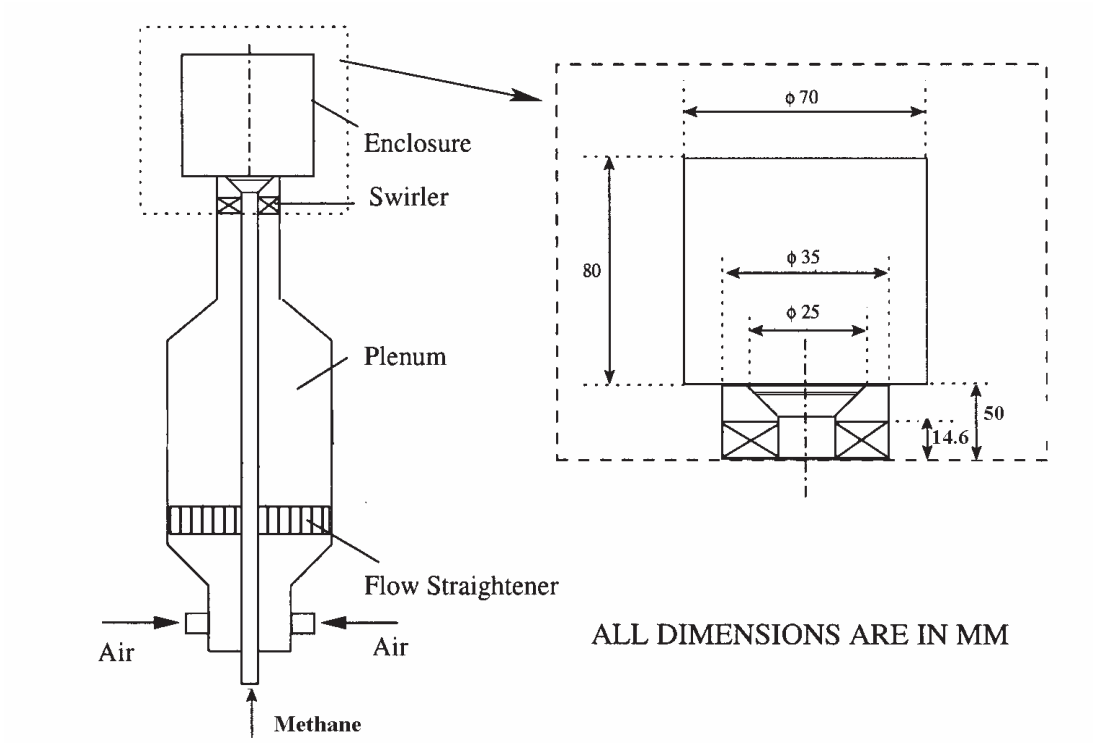

Figure 2.5: Schematic diagram of the bluff-body burner. This burner was originally designed by Balachandran (2005).

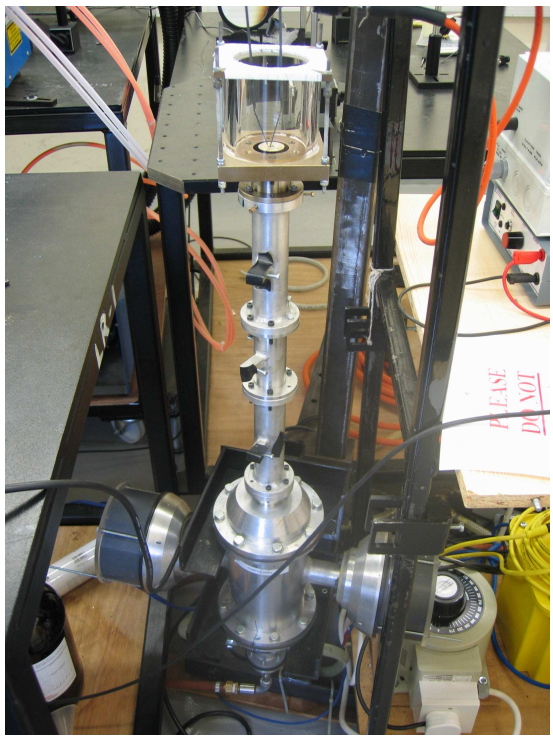

Figure 2.6: Photograph of the bluff-body test rig with spark electrodes.

Figure 2.7: Photograph of the 60° swirl vane.

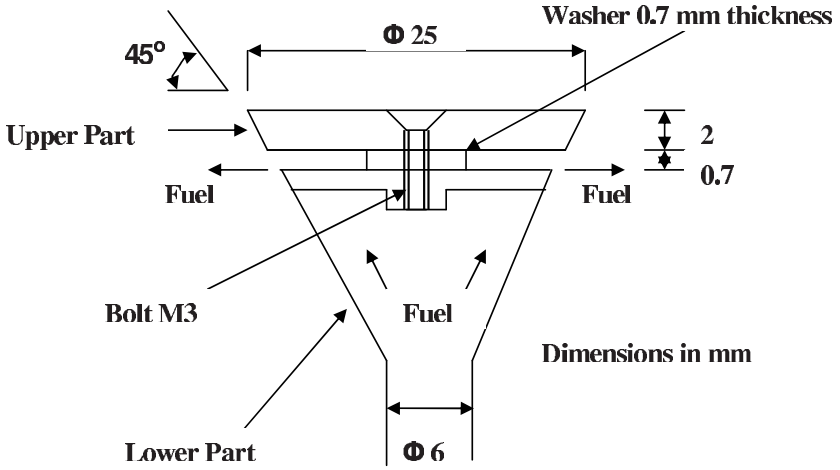

Figure 2.8: Schematic diagram of the non-premixed bluff-body design.

respectively, which helps to avoid the flow separation during the expansion and contraction. The air flow was streamlined inside the plenum chamber by flow straighteners. The fuel, pure methane, passed through the inner tube all the way along the burner without mixing with the air until it reached the bluff-body. The bluff-body has a certain design, which was developed in the present work, to allow the fuel to be injected radially through a 0.7±0.01 mm circular gap to the main air flow just 2±0.1 mm before the exit of the burner, Fig. 2.8. The aim of this design was to achieve a non-premixed flame with radial fuel injection to avoid penetration of the recirculation zone. More comments on this will be given in Chapter 5. The air velocity at the exit was mainly at $U_{air} = 10$ m/s and at limited experiments $U_{air} = 15$ m/s. The fuel velocity at the exit area of the bluff-body gap was ranging from $U_f = 4$ to 8 m/s. Both air and fuel flow rates were controlled by mass flow controllers, Section 2.3.1. In the case of premixed flames, the air and methane were mixed together 2 m upstream of the burner exit and the mixture passed through the annulus between the outer and inner ducts. No flow passed through the bluff-body tube in this case.

2.2 Ignition Unit

An inductive ignition system was specially designed (Dukic, 2003) to produce repeatable sparks whose energy and duration could be varied independently. Figure 2.9 and 2.10 show a block diagram and a photograph of the ignition unit components. It consists of a SCKN auto-transformer to transfer AC to DC current. The voltage of the DC current coming from the transformer can be controlled by a Clairtronic variac, which varies the output voltage from 0 to 270 volt. This output voltage goes to the ignition coil as an input voltage. The ratio between the number of turns of the secondary coil to those of the primary one in the ignition coil is 100. This means that the spark voltage can be up to 27 kV. The ignition coil is attached to the control unit, Fig. 2.10. This unit controls the spark duration and controls the external and internal spark trigger. More technical details and safety instructions about the ignition unit are given in Appendix A.

The main features of the unit are: breakdown voltage (fully variable) 0 to 27 kV; maximum spark current 450 mA; available spark electrical energy 0 to 300 mJ; spark duration (fully variable) 300 to 600 μs. Figure 2.11 shows the current waveforms of five different sparks with similar specifications measured by a two-channel digital oscilloscope (Tektronics TDS 3012) with 1 MHz sampling rate. By integrating the product of the voltage and the current over the time, a value of the electric energy can be obtained. It is evident that the sparks produced by the ignition unit are very similar. Quantitatively, the maximum deviation in the calculated spark energy from traces such as those in Fig. 2.11 was 0.8%, which demonstrates the high repeatability of the ignition system. It should be mentioned that the repeatability of the spark does not depend on the flow conditions.

The spark was created in the jet and counter-flow experiments between two

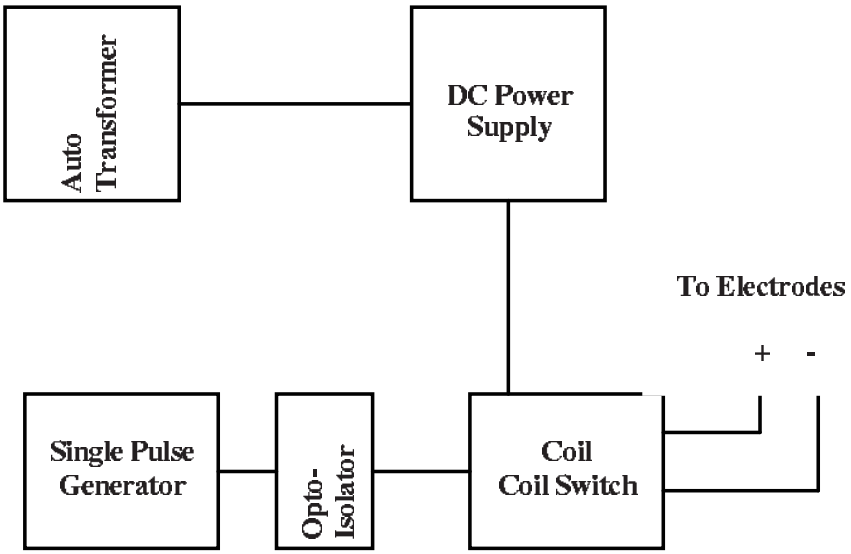

Figure 2.9: Block diagram of the ignition unit components.

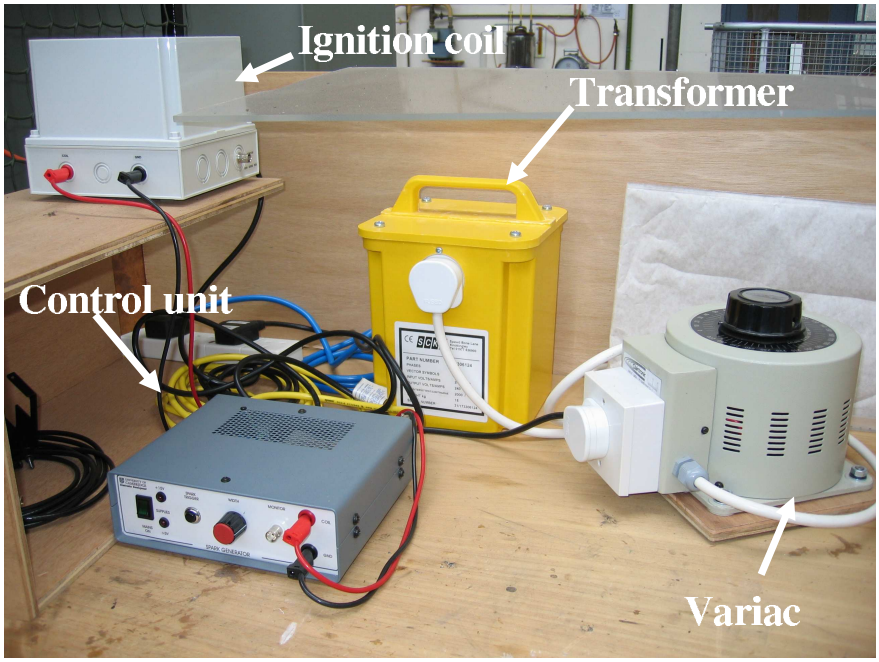

Figure 2.10: photograph of the ignition unit.

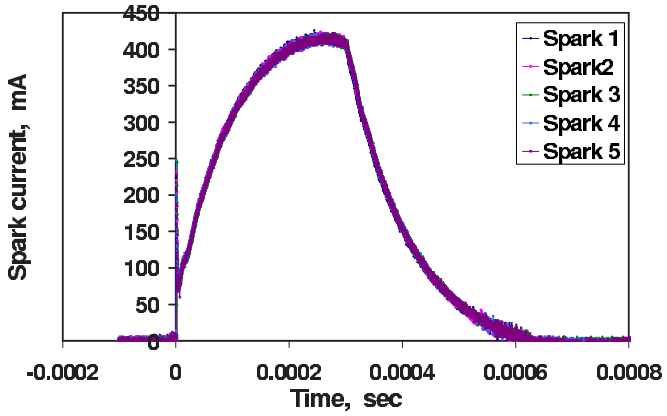

Figure 2.11: Oscillogram of typical current pulse waveforms in the spark gap. Five realizations of the spark with the same settings are superimposed.

stainless steel electrodes. However, in the bluff-body experiments two tungsten electrodes were used in order to sustain the higher flame temperatures. The electrodes were placed as shown in Figs. 2.1, 2.4 and 2.6 for the jet, counter-flow and bluff-body burners respectively, to ensure minimum disturbance to the flow (Smith et al., 1986). Three electrode diameters have been used in the present work, 1, 0.7 and 0.5 mm, and three spark gap widths, 1, 2 and 3 mm. Details of such dimensions are mentioned in the following chapters for each type of the three experiments. The electrodes had pointed edges to reduce the heat loss from the spark. Therefore, the estimated energy transfer efficiency from the spark to the mixture for the igniter configuration used in this work is about 30% (Teets and Sell, 1988). This energy is much higher than the minimum ignition energy (6.41 mJ) required to ignite methane-air mixtures within the flammability limits under atmospheric conditions (Lewis and Elbe, 1987). The two electrodes were attached to a two-dimensional traversing mechanism by a ceramic tube, which allowed the igniter to be traversed axially and radially to cover the whole flow field with 0.1 mm resolution.

2.3 Flow Measurements

2.3.1 Flow-rate measurements

The measurement of the flow rate in the present work was different for each set of experiments. In the jet flames, the volume flow rates of methane, nitrogen and air were measured by using rotameters calibrated by the manufacturers, with measuring ranges of 2-36 l/min, 2-25 l/min, and 20-200 l/min respectively, with a minimum resolution of the full scale 2 l/min, 1 l/min and 5 l/min respectively. The pressure difference between the burner exit and the measuring point was detected by using a pressure gauge fitted immediately downstream of the rotameter to correct for any pressure above the calibration pressure and hence assure the accuracy of the measurements.

In the case of the counter-flow flames, all the flow rates were metered by calibrated rotameters and were arranged such that each of the jets could be fed as follows: 0-100 l/min of air; 0-100 l/min of nitrogen; 2-36 l/min of methane. The minimum resolution of the full scale were 5 l/min, 5 l/min and 2 l/min respectively. The estimated uncertainties in the measured flow rates is expected to be 5%, as suggested by the manufacturer.

For the bluff-body flame experiments, the mass flow rate of the air and methane were controlled and monitored with BRONKHORST HI-Tech mass flow controllers with measurements ranges of 12-600 l/min for air and 1.2-60 l/min for methane, with an accuracy of 0.5% of the full scale deflection.

2.3.2 Hot wire

Hot-wire anemometry was used to measure the flow velocity and turbulent fluctuations in a turbulent air jet having $U_j = 21$ m/s and air co-flow velocity of 0.1 m/s, in order to compare the characteristics of the present turbulent jet with

those of turbulent jets found in the literature. A single constant-temperature Dantec 55P16 platinum-plated tungsten hot wire (5 μm diameter and 1.25 mm length) was used with a DISA 55M01 standard bridge for these measurements. The hot wire was placed perpendicular to the flow direction. The measurements were taken with different sampling rates (10-30 kHz) depending on the location of the hot wire. The signal from the hot wire was amplified, digitized and saved using a DAQ system with analog to digital (A/D) converter. A National Instrument PCI 6034E DAQ card with 16 bits resolution and with an input voltage range of 10$\pm$0.05 volt was used for this purpose. 60,000 samples were recorded at each location. The maximum statistical uncertainty for the reported mean velocities is estimated as 2%.

2.3.3 Laser Doppler Velocimeter

For a very limited set of data in the jet flame experiments, the instantaneous axial velocity at approximately the moment of the spark and at approximately the spark location was measured with a Laser Doppler Velocimeter (LDV) system. The system consists of 35 mW (nominal) He-Ne laser with a wavelength of 632.8 nm and beam diameter of 1.2 mm produced by a lens with the focal length of 310 mm. The optical unit is DISA Model 55X7 fitted with a single Bragg cell to give an optical frequency shift of 40 MHz, while the receiving optics comprised a 150 mm focal-length lens, which focused the forward-scatter light from the seed onto a 350 μm pinhole in front of a photomultiplier Hamamatsu R1477.

The two laser beams were focused 1 mm below the spark gap to avoid reflections from the electrodes. The spark was located at 30 d_j downstream of the jet exit. Smoke was used as a seeder, which was produced from a commerical ProSound MFX-700 Fog machine using a water based, non-toxic fog liquid. Smoke was seeded in the co-flow only, but at the location of interest the velocity

measurements so performed were identical to when the smoke was seeded in the jet. To ensure uniform smoke seeding to the flow, the smoke generated by the fog machine was contained in a rectangular reservoir and the co-flow air passed through this reservoir before entering the burner. Data rates of about 3-4 kHz were achieved. By triggering the LDV system and the spark simultaneously from a signal generator, the axial velocity not more than 0.5 ms before the initiation of the spark could be determined. 80 such events were measured. The ignition status was recorded for each of these measurement in order to establish whether a correlation exists between the local, instantaneous velocity and the spark success.

2.4 PLIF Measurements

Laser diagnostics have been proven to be suited to acquiring chemical species data. Planar laser-Induced Fluorescence (PLIF) can be performed by spreading the laser beam into a sheet, yielding species concentration/number densities information from a 2-D planar image. The PLIF system requires either a charge coupled device (CCD) camera, an intensified CCD (ICCD) camera or some other detectors that provides two dimensional imaging. Laser-induced florescence is performed by first, bringing the species of interest to an excited electronic state by generally using lasers. In the present work, a tunable-dye laser pumped by an Nd:YAG laser was used. Figures 2.12 and 2.13 show a schematic and a photograph of the PLIF set up performed with the jet flames. The excited molecules then fluoresce, by emitting photons to attain lower energy states. The emitted photon can be at the same wavelength as the excited source. It is more convenient if its not, since detection can take place without interference from the laser source (Crosley, 1993).

The laser system used in the present work consists of one Nd:YAG Contin-

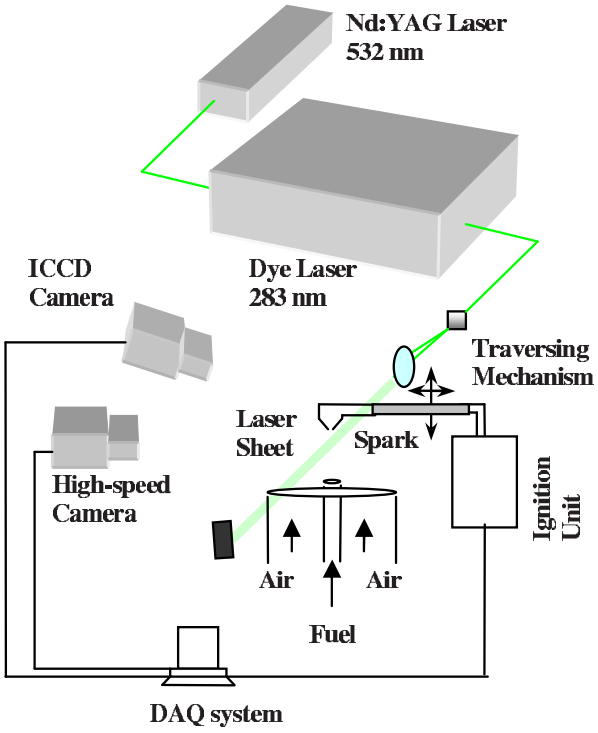

Figure 2.12: Schematic diagram of the PLIF measurements in the jet flame experiments.

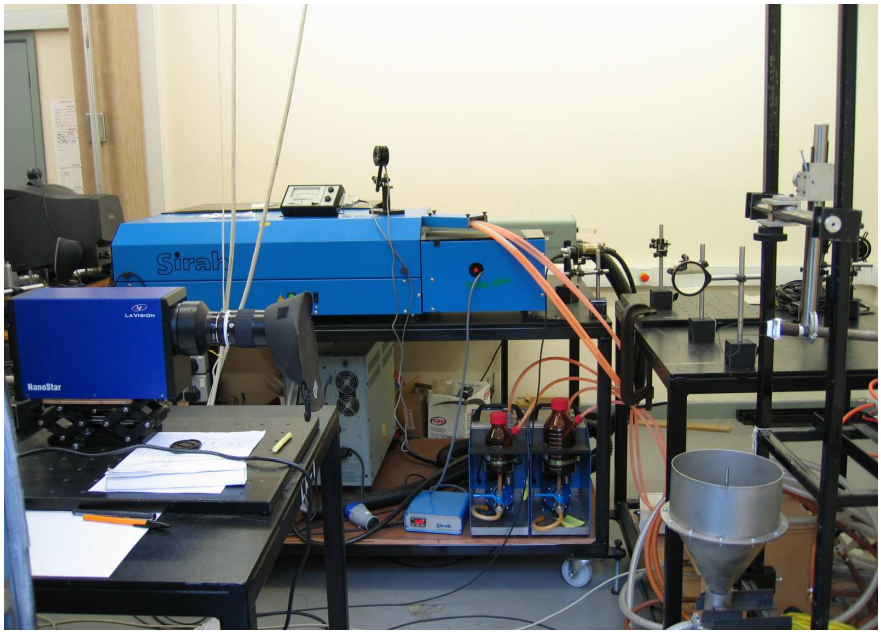

Figure 2.13: Photograph of the PLIF arrangements in the jet flame experiments.

uum Surelite laser, one Dye Sirah Cobra-Stretch laser and two high-resolution double-plused ICCD LaVision Nanostar cameras. The Nd:YAG laser produces 660 mJ/pluse at 1064 nm (infra-red) and is equipped with a second harmonic generation system to provide beam at 532 nm (green). The 532 nm beam pumps the dye laser. The ICCD camera used has a spectral response from 190-900 nm and its sensitivity is more than 80 counts/electon. The camera uses a 1280×1024 CCD array with pixel size equals to 6.7 mm and the minimum exposure time around 1.5 ns. Digitization is done with 12 bits intensity resolution. The two cameras were fitted with a Nikkor AF 50 mm focal length and f/1.4 maximum aperture lens, used at a measurement aperture of f/2.8.

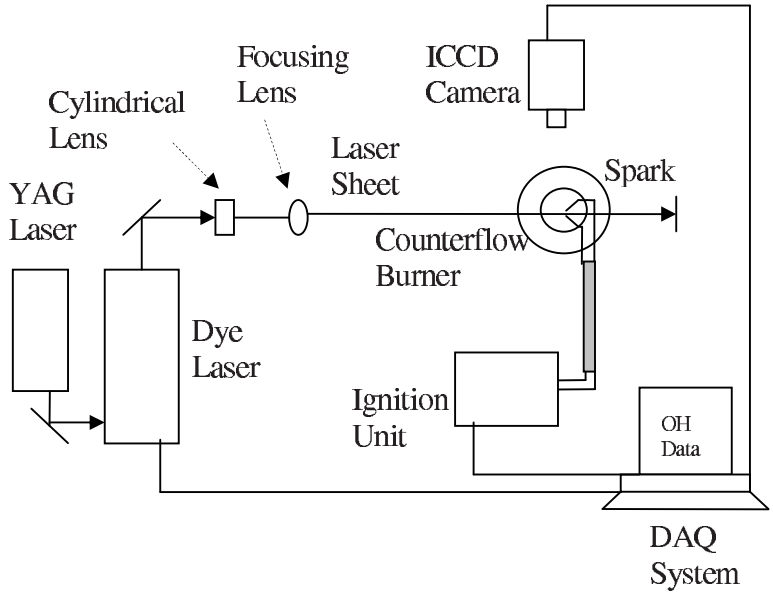

Figure 2.14: Schematic diagram of the PLIF measurements in the counter-flow flame experiments.

2.4.1 Acetone PLIF

Acetone PLIF was used to measure the mixture fraction distribution in the counter-flow field, Section 4.2.2, and in the bluff-body flow field, Section 5.2.4.2. More details about using the acetone as a tracer to measure the mixture fraction in the inert flow can be found in Section 5.1.3.1. In these two experiments, the acetone was seeded in the fuel stream, but carried by air, i.e. the fuel was replaced by air in the acetone PLIF experiments. This was done for safety reasons, but has implications for the reliability of the measurements, as we shall see. The seeder is an eight nozzle vessel working at atmospheric conditions, which produces a mixture of air and acetone vapor with approximately 10% by volume. This seeder was always placed in a warm water bath to keep the acetone temperature constant in order to have a uniform seeding all the time of the experiment.

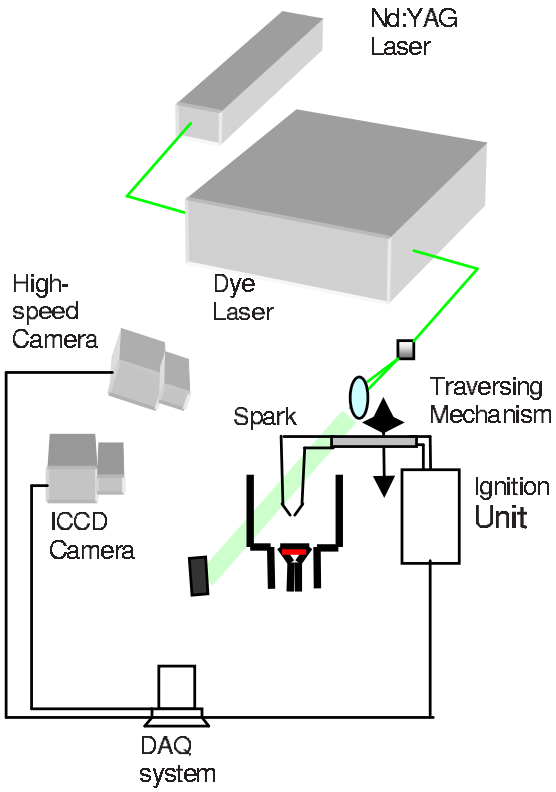

Figure 2.15: Schematic diagram of the PLIF measurements in the bluff-body flame experiments.

To excite the acetone, the laser beam was taken directly from the Nd:YAG laser equipped, in this case, with a fourth harmonic crystal to produce a laser beam with 266 nm at 10 Hz. In order to remove any residual second harmonic (532 nm) component from the laser beam, a Schott UG5 filter was placed before the measuring domain and a Schott WG305 cut-off filter was placed in front of the camera lens. At the exit of the Nd:YAG laser, the beam power was more than 80 mJ. A cylindrical lens of focal length 25 mm and a spherical lens of focal length 500 mm were used to form a thin laser sheet of about 50 mm width. The sheet $1/e^2$ waist thickness at the focusing point was measured by translating a razor blade with a micrometer (knife-edge technique (Hornak, 2002)) and found to be 0.1 ± 0.03 mm. The focusing point of this sheet was placed at the centerline of the burner under investigation. One of the two ICCD cameras was used to image the mixing field. The other one was used for the simultaneous beam profile recording and for the shot-to-shot laser power variation. This was done by splitting the laser sheet before reaching the burner into two parts. One passed through the burner axis and the other part passed through a Dye cell. About 1000 images were taken for each condition studied. Details about the image domain in each experiment, the accuracy of the image size and the flow conditions can be found in Section 4.2.2 and 5.2.4.2 for the counter-flow and bluff-body experiments respectively. A description of the image processing techniques used to correct the raw images from the acetone PLIF to be used for the mixture fraction calculations can be found in Appendix B.

2.4.2 OH PLIF

PLIF of OH was used in the present work to examine the flame front structure during the flame propagation after the spark. In addition, OH PLIF was also used to measure the flame front position and to estimate the flame propagation

speed in the counter-flow flames. To excite the OH radical, the output from a Nd:YAG laser was used to pump a Dye laser. Figures 2.14 and 2.15 show the OH PLIF arrangements for the counter-flow and the bluff-body flame experiments respectively. The frequency-doubled beam was tuned at 283 nm to excite the Q1(6) transition of the $A^1\sum$-$X^2\prod$ (1-0) band. A vertical laser sheet with thickness of about 0.1±0.03 mm at the focal plane was created by a combination of a 25 mm focal length cylindrical lens and a 500 mm focal length spherical lens and passed through the spark gap along the jet centerline. The OH fluorescence from the (0,0) and (1,1) bands near 310 nm was captured by a Nikkor 50 mm lens and an ICCD camera fitted with a combination of Scott glass UG11 and WG305 filters (Balachandran, 2005). The instantaneous images, about 100 images for each instant after the spark, were corrected for the background noise and beam profile variation. For some experiments, these images were converted into black and white images by a thresholding procedure and the coordinates of the flame edge were detected from these individual images (one image for each successful ignition event). The average flame edge position was hence quantified as a function of time from the spark.

2.5 High-Speed Imaging

The high-speed imaging was obtained in the present work by using a 512×512 pixel Phantom V4.2 digital high-speed camera. The camera can take images up to 100 kHz, with an on-chip shuttering capability of down to 10 μs. The camera CMOS sensor is only sensitive to visible and infra-red light in the range 350-1000 nm. Moreover, the high sensitivity of the CMOS sensor is assisted by a large 22 μm pixel size. The image size in this camera is linked to the framing rate and to the exposure time of each image, so for instance, 4,200 fps (frame per second)

is linked with maximum image size 512×215 pixel with 238 μs exposure time. However, for 20,000 fps, the maximum image size is 150×150 pixel with 38 μs exposure time. The camera has also an advantage of taking digital photos with controlled and long exposure time up to 2.2 ms.

In the present work, the camera was used in a number of ways. In the jet experiments, it was used to measure the lift-off height of the flame by taking ten images of the flame for each case with 2.2 ms exposure time. These images were analyzed by a Matlab code to calculate the lift-off height at each condition, Section 3.2.4. In addition, the camera was used to measure the flame front position with the time after the ignition in order to measure the flame propagation speed, Section 3.2.7. Ten movies were recorded at 4,200 fps for the whole propagation event, each movie has about 2000 frames. These images were analyzed by another Matlab code to detect the most downstream position of the flame front at each frame. The average results from the ten movies were used to calculate the flame propagation speed. Finally, the camera was also used to measure the flame kernel growth by taking ten movies for each case of interest at 20,000 fps. A Matlab code was used to calculate the average diameter of the flame kernel for each frame and plot the results against time, Section 3.2.6.

In the counter-flow and bluff-body flame experiments, the camera was just used to visualize different successful and failed ignition events, Section 4.2.3.1 and 5.2.5.1 respectively. Many movies were recorded for such purposes at 8100 fps and an exposure time of 113 μs with a maximum image size of 215×215 pixel.

2.6 Chemiluminescence Measurements

Chemiluminescence is radiation emitted from electronically excited molecules, while returning to a lower energy state. The wavelength of this radiation is char-

acteristic of the particular molecule and the particular transition the molecule undergoes. For simple diatomic molecules, the spectrum exhibits one major peak and relatively few, weak secondary peaks. For complicated molecules, the radiation spectrum is broader. OH* and CH* are examples of molecules exhibiting a simple spectrum with major peaks at 308 and 431 nm respectively (Haber, 2000). The reason for which chemiluminescence from flames is interesting is that the concentrations of excited molecules seen in flames exceed the equilibrium concentrations expected at the same temperature without chemical reaction by several orders of magnitude. It can be deduced from this fact that excited molecules are not only produced by thermal excitation, but also are produced as the products of reactions (Haber, 2000).

The chemiluminescence measurements in the present work were done by using Hamamatsu R3788 side-on Photomultiplier Tubes (PMT), which consist of collection optics with focal length of 500 mm that transport the signal to the PMT through appropriate filters. These filters were interference filters of 10 nm bandwidth centered at 307 nm and 435 nm for the measurements of OH* and CH* respectively. The PMT signals were recorded simultaneously with the two-channel digital oscilloscope with 1 MHz sampling rate. An attempt was made to use the chemiluminescence measurements in the jet experiments to calibrate the mixture fraction with the average OH*/CH* ratio. The PMTs were focused on the spark area and the signal from the two PMTs were recorded for each mixture strength, Section 3.2.8. In the bluff-body experiments, the OH* was recorded alone with the same technique for different successful and failed ignition events, Section 5.2.6, in order to visualize the development of these signals with the time from the moment of the spark to the stabilization of the flame.

2.7 Ignition Probability

For the determination of the ignition probability, the whole process was controlled by a DAQ system with the LabView program. The computer was programmed to switch on a solenoid valve in the fuel gas supply, wait for 5 seconds for the flow to become fully established and then send a signal to the ignition unit to generate a single spark. If ignition happened and the flame was established, an R-type thermocouple (Pt/PtRh(13%)) located 1.2 m above the jet exit detected the rise in temperature and sent a signal to the computer to stop the fuel supply immediately. After 10 seconds to allow the combustion products to disperse and to reduce the amount of unburned fuel in the exhaust, the fuel supply valve would be reopened and the sequence repeated. If no ignition happened, the ignition unit would then generate another spark after 3 seconds. The whole process continued until the required number of sparks have been generated. The same number of sparks has been applied at all locations of interest in the flow field. It should be noted that in the counter-flow and bluff-body flame experiments, the detection of the flailed and successful ignition was observed manually. This is because in these two cases the flame domain is compact and there was a type of failed ignition where the whole flame was established for few milliseconds and then extinguished. Such type of failed ignition was not observed in the jet flame.

For each set of N trials, the observations consisted of the number of successful ignitions J. From these figures, the probability of ignition P_I, is J/N. The standard deviation of the statistical uncertainty associated with these probabilities is given by $[P_I(1 - P_I)/N]^{1/2}$ (Smith et al., 1986). In the present experiments, $N = 50$, which implies an uncertainty of 7.5% at 50% ignition probability.

Chapter 3

Jet Flames

This chapter investigates the ignition characteristics of turbulent jet flames. Most of the flames studied here are lifted flames. The chapter starts with a literature review about the factors affecting the spark ignition, the flow field structure and the flame behavior after the ignition. Then, the results are presented and discussed. The chapter ends with the conclusions.

3.1 Literature Review

3.1.1 Introduction

In many applications, such as gas turbines, fuel enters into the combustion chamber as a turbulent jet. In this review, an understanding of the basic properties of turbulent free jets and turbulent jet diffusion flames are provided. These properties will help understanding of the ignition behavior of this kind of turbulent flow and how the flame front propagates after the ignition to stabilize the flame. Particular attention is given here to the factors affecting the spark ignition in turbulent flows in order to help interpreting the ignition probability results in turbulent jets. After the ignition, the flame stabilizes as an attached or lifted

flame depending on the initial jet velocity. A brief description about the characteristics of the lifted jet flame is highlighted at the end of this review with some explanations of the stabilization mechanisms.

3.1.2 Factors affecting spark ignition

A certain minimum energy is always required to ignite a flammable mixture. However, there are a number of physical and electrical variables affecting the ignition and combustion of fuel-air mixtures. Therefore, it is possible to pass small electric sparks through an explosive gas without producing ignition. When spark energy is increased, a threshold energy is eventually obtained at which the spark becomes incendiary in the sense that a combustion wave propagates from the spark through the volume of gas. A successful ignition event generally begins with an "ignition kernel", a localized region of high reactivity and heat release, followed by the establishment of a flame. This depends upon a number of parameters, such as the structure of the local flow field, the mixture composition, and the mode of depositing ignition energy. These parameters have been fully investigated in flowing flammable mixtures by Swett (1957), Ballal and Lefebvre (1975a), Ballal and Lefebvre (1976), Rao and Lefebvre (1976), Ballal and Lefebvre (1977), Ballal and Lefebvre (1978), Ballal and Lefebvre (1979) and Ballal and Lefebvre (1980) and inside a combustion vessel by Lewis et al. (1954), Bradley et al. (1982), Lewis and Elbe (1987), Bradley and Lung (1987), Kaminski et al. (2000b), Dreizler et al. (2000), and Dreizler et al. (2002). These parameters are going to be divided into two groups; one group is related to the spark ignition system which includes: spark energy, spark duration, spark rate, electrode diameter and electrode gap width, and the other group is related to the flow field which includes: mixture strength, flow velocity, flow pressure, turbulence scale and turbulence intensity. It should be mentioned that most of the previous parameters have been examined

in the past for premixed fuel-air mixtures, but will be examined in the present work in terms of their effects on the success of ignition of non-premixed flames.

Spark energy

Generally, it was found that the minimum energy required to ignite the flowing mixture depends upon a number of parameters (Lefebvre, 1998). We are going to discuss the effect of each of these parameters individually to find the optimum value for each parameter which corresponds to the minimum ignition energy of the flow. However, in general, increasing the spark energy increases the ability of igniting the flowing mixture. This is due to the increase in the amount of heat that is transfered from the spark to the mixture.

Spark duration

Spark duration is one of the important parameters that affects the spark energy and, as a result, affects the ignition of the flow. When the spark discharge is rapid, the energy losses are very high; on the other hand, if the spark duration is too long, the energy is dispersed over a large volume of the flowing mixture, and the gas temperature is too low to cause ignition. Ballal and Lefebvre (1975a) studied the effect of spark duration on the minimum ignition energy in flowing propane air mixture. They found that the optimum spark duration decreased with increase in velocity, due to "stretching" of the spark which increase its electrical resistance, but it was unaffected by the turbulence. Bradley and Lung (1987) used electric sparks with 200, 400 and 600 μs duration to investigate the effect of the spark duration on the flame kernel development in turbulent gaseous mixture inside a combustion vessel. They found that at high gas velocity the thermal spreading and the kernel spreading speed were greatest with the shortest duration spark of 200 μs. In addition, they concluded that the spark duration should be less than

the ignition delay and there is an advantage in short duration sparks. 200 μs was the same spark duration, which was used by Dreizler et al. (2000) as an optimum spark duration for ignition in a combustion vessel.

Spark rate (frequency)

The increase in spark rate is likely to be far more effective for ignition than an increase in spark energy, especially for problems like start-up and relight of the aircraft gas turbine (Lefebvre, 1998). Foster (1951) examined the influence of spark frequency on altitude ignition performance in J-33 combustion chamber, and demonstrated a slight improvement in relighting capability as the sparking rate was increased from 2 to 150 per second. Presumably, the effect of sparking rate can only be really significant if it is sufficiently high for sparks to be generated in gas which has already been heated as a result of previous sparks (Foster, 1951). Experience has shown that a spark frequency of between one and two per second, depending on the application, generally entails the minimum expenditure of power and gives the most compact ignition unit (Lefebvre, 1998). In the present work, the effect of the spark frequency on ignition has been investigated in Chapter 4.

Electrode diameter and gap width

The size and shape of the spark electrodes can critically affect both quenching distance and ignition energy through their influence on the heat loss from the incipient spark kernel to the electrodes. Ballal and Lefebvre (1975a) studied the effect of electrode diameter on the minimum ignition energy E_{min} and the quenching distance d_q of flowing propane air mixture. They found that both E_{min} and d_q increase with electrode diameter due to a higher heat loss caused by the larger area of exposed metal surface. The more rapid increase of ignition energy with electrode diameter observed with richer mixtures is attributed to

a higher heat loss of active radicals to the electrodes. They concluded that electrodes terminating in a sharp point would be expected to give minimum heat loss. However, pointed electrodes tend to suffer from rapid wear and an inconsistent energy release. It is important to mention that they used electrodes tapered from 3 mm diameter base down to 1 mm diameter, and then continued as a parallel shank for further 6 mm length before terminating in a flat tip, in all their experiments. It should be mentioned that the effect of the electrodes material on E_{min} is very small and can be neglected. Therefore, the effect of the electrodes material on the ignition probability has not been considered in the present work.

It has been recognized for many years that the spark electrodes can have a powerful quenching effect on the spark kernel. As the gap width is increased, the quenching effect is diminished, but if the gap becomes too wide, then energy is wasted in creating a larger spark kernel than is needed to achieve ignition. Thus, for every combustible mixture there is an optimum spark gap width corresponding to E_{min}. Roberts and Eichenberger (1999) used electrodes with 1 mm diameter and 2 mm gap width in studying the ignition of turbulent methane-air mixture to reduce thermal losses and disruptions to the flow.

Mixture strength

As might be expected from simple considerations of all aspects of the ignition process, optimum conditions for ignition are when the mixture strength is roughly stoichiometric, i.e., when flame speed and flame temperature are highest. This theory has been confirmed by Ballal and Lefebvre (1976) and Ballal and Lefebvre (1978), and by Danis et al. (1988) in their studies about the effect of mixture strength on the minimum ignition energy of pre-vaporized n-heptane and methanol.

Flow velocity

One beneficial effect of an increase in velocity stems from convecting of the spark in a downstream direction, which reduces the loss of heated and active species from the spark to the electrodes. However, offsetting these advantages is the convective heat loss suffered by the spark kernel during the initial phase of its development. This loss of heat, which increases almost linearly with velocity, impairs ignition performance unless it is compensated for by an increase in spark energy. Another effect of an increase in velocity is that it gives the spark kernel less time in which to propagate before being swept downstream (Lefebvre, 1998). Swett (1957) observed an increase in ignition energy with increasing the flow velocity of propane-air mixture.

Flow pressure

All the existing experimental data obtained from stagnant mixtures, idealized flowing systems, and practical combustors, highlight the fact that an increase in pressure reduces the minimum ignition energy. For heterogeneous fuel-air mixtures, the effect of pressure on E_{min} may be appreciably less, depending on the extent to which fuel evaporation rates are limiting to the onset of ignition. In case the ignition process is fully controlled by chemical reaction rates, $E_{min} \propto P^{-2}$. If evaporation rates control the ignition process, then $E_{min} \propto P^{-0.5}$. Thus the pressure exponent is always between -0.5 and -2. Also, the gas heat capacity increases with pressure while the gas thermal conductivity is roughly independent of the pressure. This leads to a reduction in the heat losses and, as a result, a reduction in E_{min} (Teets and Sell, 1988). Most of the published data on practical combustors were obtained by Foster (1951). Although the results are few and show appreciable scatter, they all follow the same trend as noted above in regard to the adverse effect of a reduction in pressure on ignition performance.

It should be noted that the effect of pressure on ignition has not been studied in the present work.

Turbulence scale and turbulence intensity

Turbulence increases burning velocity and this tends to reduce up to a certain limit E_{min}. However, it also increases the rate of heat loss from the spark kernel to the surrounding fresh mixture, thereby increasing E_{min}. The experimental data by Ballal and Lefebvre (1977) show that the net effect of an increase in turbulence intensity is to increase E_{min}. They also noted that under conditions of low turbulence, E_{min} either decreased slightly with increase in scale or remained sensibly independent of scale, whereas at high turbulence levels there was a clear tendency towards higher values of E_{min} with increase in scale. Bradley and Lung (1987) also reported that in the earlier stages the main effect of turbulence was to convect the spark kernel bodily rather than to spread it.

3.1.3 Conserved scalars in turbulent jets

The structure of non-premixed turbulent jets has been studied experimentally by Wygnaski and Fiedler (1969), Birch et al. (1978a), Birch et al. (1978b), Yip and Long (1986), Masri et al. (1988b), Starner et al. (1992), Richards and Pitts (1993), Bilger et al. (1996) and Kelman and Masri (1997), and theoretically by Peters (1986), Masri et al. (1988a), Masri et al. (1988c) and Alvani and Fairweather (2002) among many others. In non-premixed reacting flows, it is common to describe the mixing process in terms of a conserved scalar, i.e., a quantity unaffected by the reaction. Many quantities may serve as a basis for, or are in themselves, conserved scalars. Any one chemical element or inert species mass fraction, total enthalpy (in adiabatic flows) or linear combinations of these quantities may serve (Starner et al., 1992). Combinations of reactive scalars can also,

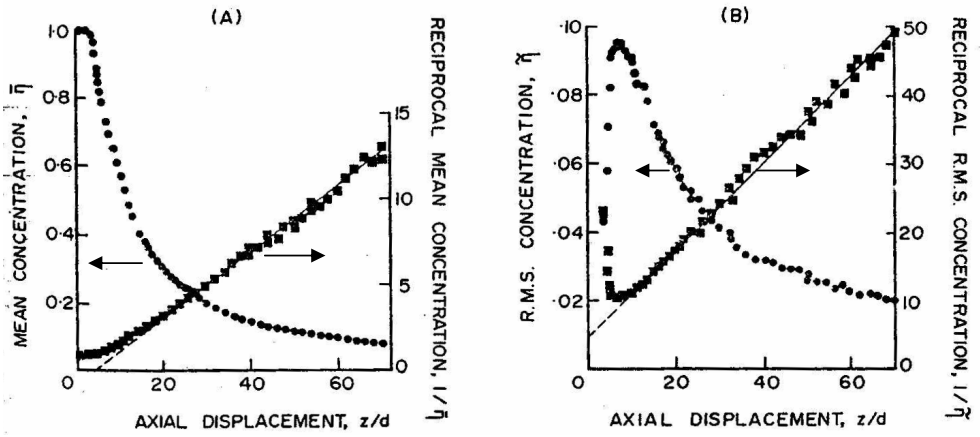

Figure 3.1: (a) Mean concentration decay along the jet centerline, (b) r.m.s concentration decay along the jet centerline (Birch et al., 1978a).

with certain restrictions, be used to from a suitable conserved scalar. The choice is highly problem independent and simplifications are usually possible for particular flow situations. In diffusion flames, the term mixture fraction ξ, which has been defined in Eq. 1.1, is an important conserved scalar, and it is often used.

Birch et al. (1978a) have measured the turbulent concentration parameters using Raman spectrometer of a turbulent free jet of natural gas having a Reynolds number of 16,000. Autocorrelation and probability analysis have been applied to investigate the concentration field of the jet. Figure 3.1 shows the results of mean and r.m.s. concentration along the jet axis; the asymptotic value of volume fraction fluctuation intensity was found to be 30%. The probability density function was found to be approximately gaussian on the center line but highly non-gaussian in the off-axis intermittent region.

Richards and Pitts (1993) have studied the self-preservation behavior of turbulent free jets. They found that the final asymptotic state of all momentum-dominated axisymmetric jets depends only on the rate of momentum addition.

Regardless of the initial conditions, axisymmetric turbulent free jets decay at the same rate K_c, spread at the same half-angle θ_c, and both the mean and r.m.s mass fraction values collapse in a form consistent with full self-preservation. Also, they have demonstrated that if a systematic experimental program is undertaken in which care is taken to ensure that the flows are uncontaminated by buoyancy and co-flow effects, then the far-field behavior of variable-density jets is essentially indistinguishable from a constant-density jet. Moreover, they have correlated the mean mixture fraction for all axisymmetric free turbulent jets as following:

$$\overline{\xi}(z,\eta) = \frac{9.52 r_{\varepsilon}}{z - z_{0Y}} \exp(-59\eta^2) \tag{3.1}$$

In Eq. 3.1, $\overline{\xi}(z,\eta)$ is the mean mixture fraction at the axial location z and non-dimensional radial coordinate η, $\eta = r/(z - z_{0Y})$, z_{0Y} is the virtual origin taken as $7.2r_0$ for nozzles with fully-developed turbulent pipe flow (Richards and Pitts (1993) and Mi et al. (2001)), and $r_{\varepsilon} = r_0(\rho_0/\rho)^{1/2}$. ρ_0 and ρ are the density of the methane jet and ambient air respectively. This expression is supported by the excellent agreement with the previous experimental data of the constant-density experiment by Dowling and Dimotakis (1990). However, Richards and Pitts (1993) reported that the dependence of z_{0Y} on such system parameters as Re requires additional investigation because they noticed that with increasing Re, there is a downstream shift of $\overline{\xi}$. Furthermore , the r.m.s fluctuations of the mixture fraction (ξ') have been correlated with the following:

$$\xi'(z,\eta) = \frac{9.52 r_{\varepsilon}}{z - z_{0Y}} [0.23 + 0.35\eta + 9.09\eta^2 - 116.48\eta^3 + 240.81\eta^4] \tag{3.2}$$

This expression provides a good agreement with Dowling and Dimotakis (1990) as well. Therefor, it has been concluded that Eq. 3.1 and 3.2 can be used to estimate the mean and r.m.s. of the mixture fraction for any turbulent jet. Therefore, they can be used in the present investigation if the turbulent jets used in the present

work have the same characteristics of the turbulent jet of Richards and Pitts (1993).

3.1.4 Ignition probability

The ignition probability is defined as the ratio of the number of successful ignition events divided by the total number of breakdown sparks. Bear in mind that the definition of successful ignition in the present work is the one that results in a continuing stable flame for quite a long time (few seconds after the spark). Ignition probability is the most important parameter for the high altitude relight of the aircraft gas turbine combustor. Determining the igniter locations that give high probability of successful ignition at different flow conditions is essential for increasing the relighting capabilities of the engine.

The ignition probability for turbulent non-premixed flow, such as a turbulent jet, depends upon a number of parameters, some of them related to the flow, and the others related to the igniter. When the fuel jet emerges into quiescent air, the jet expands and entrains air. The entrained air mixes with the fuel to create combustible mixtures with different mixture fractions across the flow field. Since the dominance of any particular process including mixing at a particular distance depends upon flow parameters such as the jet diameter, the jet co-flow, the air entrainment, etc., the location of the optimum mixture fraction for successful ignition will change when the flow conditions changes. Thus, efficient ignition of a variable jet flow requires the ignition location to be changeable. In addition, the mixture fraction fluctuations in the same flow conditions causes randomness in the ignitability of this non-premixed flow.

Very few studies have investigated the ignition probability of turbulent reacting flows, some of them have examined the ignition probability of turbulent jets (Birch et al., 1981) and (Smith et al., 1986), and the ignition probability of

flowing mixtures (Kono et al., 1984) by using electric spark ignition. Others have investigated the ignition probability of laminar jets using laser ignition (Phuoc et al., 2002). Smith et al. (1986) have studied the ignition probability along the axis of turbulent free jets of natural gas, propane and a simulated town gas by using an electric spark igniter, with spark energy of 100 mJ, and spark duration of 20 ms at a repetition rate of 2 Hz. The electrodes were mounted vertically from a horizontal arm, they were 320 mm in length and separated by 50 mm, with the lower ends curved towards each other to give a spark gap of 3 mm. Their flow system consisted of a turbulent round free jet of flammable gas issuing vertically from a 6.35 or a 12.7 mm diameter cylindrical pipe, with jet velocities of 50 m/s and 20 m/s respectively. They defined the successful ignition as the breakdown followed by a flame kernel giving either light-back or blow-out, while they defined the light-back as the breakdown followed by a flame kernel resulting in complete light-up of the jet. They reported that localized ignitions can take place over the approximate range $z/d_j = 15$ to 180, but over the range $z/d_j = 75$ to 105 any flame kernel resulted in either light-up of the jet or flame propagation downstream and extinction, where z is the axial location along the jet axis and d_j is the jet diameter. However, at any axial displacement less that $z/d_j = 75$, the formation of any flame kernel always lights-back and establishes a stable flame, Fig. 3.2. In addition, they found that there is a good agreement between the observed ignition probability and the estimated flammability factor F, where

$$F = \int_{\xi_{lean}}^{\xi_{rich}} P(\psi) d\psi \tag{3.3}$$

where ξ_{rich} and ξ_{lean} are the rich and lean flammability limits respectively, and $P(\psi)$ is the pdf of the mixture fraction. It should be noted that the flammability factor F, which is presented by Eq. 3.3 is the cumulative probability of a potentially flammable mixture occurring at a given point in a turbulent free jet. This factor may be defined as the area under the probability density function of the

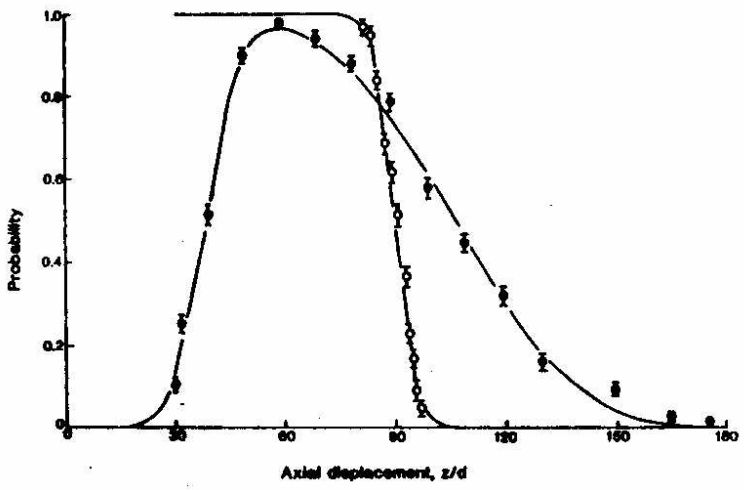

Figure 3.2: Ignition (solid circle) and light-back probabilities on the axis of a natural gas jet (d_j = 12.7 mm, U_j = 20 m/s, Re_j = 17400) (Smith et al., 1986).

volume fraction concentration of fuel gas between the static flammability limits ξ_{rich} and ξ_{lean}.

All the previous work that has been done by Smith et al. (1986) to examine the ignition probability in turbulent free jets concentrated only on the jet axis without examining the whole flammable area of the jet. Moreover, they have not investigated the effect of changing the spark parameters and the flow conditions on the ignition probability. For example, the spark duration they used (20 ms) is longer than the convection time of the largest eddy $L_{turb}/\bar{U}$ (L_{turb} is the integral length scale), which is about 7 ms at $z/d_j = 30$. As a result, the spark in their work samples many mixture fraction values that may affect the interpretation of the ignition probability results in terms of a frozen value of mixture fraction at the moment of the spark. All these points are covered in the present work.

In order to understand the effects of spark and flow parameters on the probability of successful ignition, the early stage of flame kernel growth should be

investigated as well. The flame kernel growth has been measured following the spark inside a combustion bomb (Lim et al., 1987) and in a flowing homogeneous mixture (Maly, 1981). The efficiency of the electrode to convert the electrical energy to thermal energy (Teets and Sell, 1988), the amount of energy that should be delivered to the spark gap (Cho et al., 1992), the heat transfer from the spark kernel to the electrodes (Ko and Anderson (1989) and Pischinger and Heywood (1990)), and the amount of heat losses from the flame kernel to the flowing gases are the most important parameters affecting the early stage of kernel growth and therefore affecting the ignition itself. It was found that if the flame kernel survives the first few milliseconds after the spark, the ignition is likely to be successful (Eichenberger and Roberts, 1999). Another possible reason that affects the early stage of ignition is related to the strain rate. If the local strain rate exceeds a critical value, the premixed flame front can be quenched and results in failure of ignition (Kaminski et al., 2000a), a conclusion also reached by numerical simulations of forced ignition in laminar counterflow non-premixed flames (Richardson and Mastorakos, 2007).

3.1.5 Turbulent flame propagation

Turbulent flame propagation following localized ignition is one of the most important parameters to achieve relight of the gas turbine combustor. To have high relighting capacities of an engine, it is important to get continued burning after the ignition source has been switched off. This can be achieved by getting a successful ignition followed by flame propagation and a stable flame in the combustor. Therefore, it is important to investigate the flame propagation behavior after ignition, and the effects of different flow conditions on this behavior. Since the turbulent flame propagation is a quite huge topic, this section reviews only the basic points that have been used in the present work.

3.1.5.1 Premixed flame propagation

Unlike a laminar premixed flame, which has a propagation velocity that depends uniquely on the thermal and chemical properties of the mixture, a premixed turbulent flame has a propagation velocity that depends on the character of the flow, as well as on the mixture properties. For an observer traveling with the flame, we can define a turbulent flame speed, S_T, as the velocity at which unburned mixture enters the flame zone in a direction normal to the flame (Turns, 2000). A combustion wave propagates by thermal and molecular diffusion and the observed distortions of combustion wave in turbulent flow are of a scale that is rather large in comparison to the width of the wave, showing that the random eddies responsible for the effect are large compared to the wave width. Eddies that are small in comparison cannot wrinkle the wave surface in such a gross manner. However, as has been originally pointed out by Damköhler, the small eddies increase the transfer rates of heat and mass within the wave so that the burning velocity should increase above the rate of laminar flow (Lewis and Elbe, 1987).

A number of studies have attempted to measure the turbulent flame propagation speed in a combustion bomb by Maly and Vogel (1978), Abdel-Gayed et al. (1984a), Abdel-Gayed et al. (1984b), Soete (1984), Bradley et al. (1994) and Bradley et al. (2003), but few studies measured this speed in turbulent flow (Ballal and Lefebvre (1975b) and Sinibaldi et al. (2003)). Bradley et al. (2003) have measured the turbulent flame propagation in a fan-stirred combustion bomb. They used central spark ignition to create mean spherical flame propagation and the propagation speed was measured from Mie scattering of tobacco smoke in a thin planar laser sheet. High speed schlieren images were captured simultaneously. They defined the turbulent burning velocity depending upon the chosen associated flame radius. In a given thermal explosion, the burning velocity in-

creased with time and radius, as a consequence of the continual broadening of the effective spectrum of turbulence to which the flame was subjected. In addition, they found that the Markstein number, M_a, which expresses the influence of strain rate on the laminar mass burning velocity, is a more general expression of the relevant phenomena than the Lewis number because it indicates the propensity of the flame to become unstable. A decrease in the Markstein number of the mixture was found to increase the turbulent burning velocity.

Ballal and Lefebvre (1975b) have examined the influence of turbulent intensity, scale and vorticity on burning velocity and flame structure for flowing premixed propane-air mixture supplies at atmospheric pressure. Turbulent burning velocities were derived as the product of the inlet velocity and the sine of the angle between the flow direction and the surface of the flame. They found that, at low turbulence level and low velocity, $u' < 2S_L$ where S_L is the laminar burning velocity of the mixture, the burning velocity is increased due to the effect of turbulence in wrinkling the flame and thereby extending its surface. At the region of strong turbulence, $u' > 2S_L$, it is postulated that the eddies entering the reaction zone are too small to produce any appreciable flame wrinkling. Between the two extremes of low and high turbulence, $u' = 2S_L$, there is a broad transition region in which the proportions of small and large eddies are both sufficiently high to materially affect the structure of the flame and hence also the burning velocity. They also reported that turbulent burning velocity reaches a maximum when the rate of production of vorticity is equal to about half the rate of viscous dissipation.

3.1.5.2 Triple flame propagation

The flame propagation speed has been measured in *laminar* non-premixed jets by Ko and Chang (1999), Lee et al. (2003) and Qin et al. (2004), and it was found

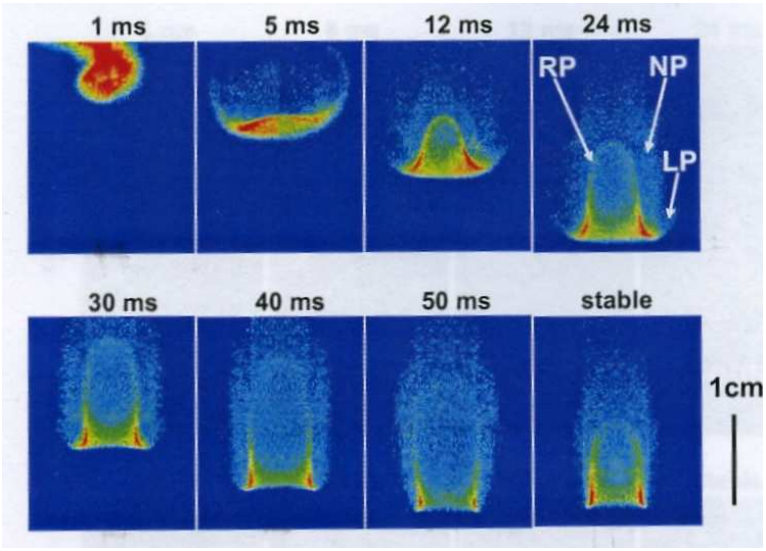

Figure 3.3: High-speed video images showing the temporal evolution of ignition and flame propagation in a laminar methane jet Qin et al. (2004).

that the flame is a triple flame propagating along the stoichiometric mixture fraction contour, Fig. 3.3. Consistent with previous theoretical and numerical predictions (Ruetsch et al., 1995), the flame propagation speed was between 0.7 to 0.9 m/s in methane jets, i.e. higher than the stoichiometric laminar burning velocity of 0.4 m/s (Ko and Chang, 1999). Similar ignition fronts in *turbulent* jet flames have not been examined in detail yet, but such measurements can assist model validation and are important from a combustor ignition point of view. The absence of such data partly motivated the present work.

3.1.6 Lifted turbulent jet flames

At a sufficiently low exit velocity U_j, a turbulent jet non-premixed flame is attached to the jet exit. By increasing the jet velocity, the diffusion flame sheet will be stretched and finally disrupted. As a consequence the flame lifts off and

stabilizes itself further downstream within the jet. The velocity at which this occurs is called the lift-off velocity and the distance between the burner rim and the base of the lifted flame is called the lift-off height. The lift-off height increases with increasing the jet exit velocities, but cannot exceed a critical value at which the flame completely blows out. If one reduces the exit velocity of a lifted flame again, there is a critical velocity at which the flame will reattach to the burner (Peters, 2000). This velocity is different from the lifted-velocity and hence there is a hysteresis phenomenon between lift-off and reattached. Since the explanations of the stabilization mechanism of the lifted turbulent jet diffusion flames have been quite controversial, different explanation theories will be presented in this section.

A lot of investigations have been done to study the characteristics and the structure of the lifted turbulent diffusion flames, and to understand the stabilization mechanism of this flame at different conditions. The first analysis of this mechanism was presented by Wol et al. (1949). They proposed that a diffusion flame will lift when the mean velocity gradient at the burner rim exceeds a certain critical value and that it will stabilize itself at the position where the burning velocity is equal to the mean flow velocity. Vanquickenborn and Van-Tiggelen (1966) gave another explanation based on a large number of measurements of lift-off heights in turbulent jets of methane, that fuel and air are fully premixed at the base of lifted diffusion flame and stabilization occurs at the position where the mean flow velocity at the contour of mean stoichiometric mixture is equal to the burning velocity of stoichiometric premixed turbulent flame. Along the same line, Eickhoff et al. (1984) reported on time-averaged temperature, concentration, and velocity measurements at positions just upstream and downstream of the stabilization region of lifted flame. They found that upstream of the stabilization region, there is a substantial amount of air entrainment, which generates premixed

conditions at the flame base. They concluded that stabilization is governed by premixed turbulent flame propagation. They also found this to be supported by a more intense burnout at the flame base than at any position in an attached diffusion flame. In contrast, Peters and Williams (1983) proposed that diffusion flamelet extinction is responsible for flame stabilization. They argued that there is insufficient residence time below the flame base to achieve spatial and temporal uniformity of the mixture.

Generally, many references support the idea that the lifted diffusion flame local extinction and the subsequent lift-off of diffusion flames happen because of the fact that in turbulent shear layers large coherent structures are formed that lead to instantaneous peaks of the scalar dissipation rate, and they argued that local extinction is likely to occur during these events.

A number of studies observed a hysteresis behavior in the flame lift-off and reattachment characteristics. One of these studies (Zsak et al., 1984) attributed this behavior to the decrease of the height of the onset of turbulence, which implies that the transition to turbulence is a prerequisite for the stabilization of a lifted flame in the downstream region. However, Gollahalli et al. (1986) based on schlieren photographs and measurements at locations near the fuel exit, argued that the local flame velocity is a function of the fuel concentration in the jet fluid and the rate of its diffusion into the ambient fluid. The local flow velocity depends upon the shape of the velocity profile at the nozzle exit and the rate of momentum diffusion. At the base of an attached flame over a nozzle which produces a top-hat profile, this balance point lies outside the narrow shear layer. At the base of the lifted flame; however, the entrainment caused by organized structures shifts the O_2 concentration profile inwards and moves the flammable zone towards the jet. Furthermore, the wide shear layer results in a higher flow velocity at that location than that at the corresponding location in the attached

flame. Hence to achieve the reattachment, the jet exit velocity has to be reduced below the value at which the flame lifted off originally. As a result, they conclude that the flame lift-off is controlled by the laminar flow and molecular processes, but the reattachment is governed by the dynamics of the organized structure.

Miake-Lye and Hammer (1988) have studied the effect of premixing air with methane on the lift-off height of lifted turbulent jet flames. They found that as the fuel mass fraction in the jet fluid Z_f is decreased, the lift-off height increases. They explained this behavior by deriving an equation for the lift-off height in terms of the laminar flame speed and the thermal diffusivity. Equation 3.4 presents that the lift-off height of the turbulent jet flames depends upon the large-scale strain profile of the flame. The corresponding physical picture is that the flame must propagate from one structure to its upstream neighbor, which will be possible until the strain between these two structures exceeds a critical value. Thus, at the lifted flame height, strain rate must fluctuate near but below its critical value, but further, the concentration field must be such that there are regions where combustion can proceed up to this critical strain rate. The result is that:

$$L_h = 14 \frac{k Y_{st}}{S_L^2 Z_f} U_j \tag{3.4}$$

where, L_h is the lift-off height, k is the thermal diffusivity and Y_{st} is the elemental mass fraction of pure fuel in air at stoichiometric conditions.

3.1.7 Summary

From the previous review, the following points can be summarized: (1) spark parameters (energy, duration, electrode diameter and gap width) and flow characteristics (velocity, turbulence, etc) affect the ignition in general and they should be examined for turbulent non-premixed ignition in the present work; (2) All turbulent free jets, regardless of the initial conditions, have self-preserving behavior

in terms of the flow characteristics and mixing distributions; (3) Limited experiments have been done to measure the ignition probability in turbulent jets and more detailed and accurate studies are needed in order to understand the parameters affecting the ignition probability in such flow; and (4) The flame propagation speed has been studied in turbulent premixed flames and laminar jets; however, in turbulent jets, flame propagation speed has not been measured yet.

3.2 Results and Discussion

3.2.1 Introduction

In this section, the results are presented and discussed. The measurements of the velocity field is discussed first followed by a description of the mixture fraction distribution and the turbulent timescales in the flow. Visualization of the flame kernel evolution and the subsequent flame propagation are then presented, while details on the ignition probability are subsequently given. Finally, flame propagation data are discussed. It is important to mention that, in the following results, the flow conditions are reported by the jet velocity U_j and air dilution X, while the spark is characterized by its duration, energy, gap width and electrode diameter. For most experiments, $X = 30\%$ (i.e. 70% CH_4, 30% air by volume) and $U_j = 12.5$ m/s. Despite this premixedness, the flame has a non-premixed character because additional air is needed for combustion. Based on lean and rich equivalence ratios of methane of 0.5 and 1.5 respectively, the flammability limits of this air-diluted fuel in air are $\xi_{lean} = 0.05032$ (lean) and $\xi_{rich} = 0.1582$ (rich) and the stoichiometric mixture fraction is $\xi_{st} = 0.0976$.

3.2.2 Flow characteristics

3.2.2.1 Mean and r.m.s. velocities

The velocity in the jet was measured with a hot wire, Section 2.3.2, to ensure that the jet is axisymmetric and that the characteristics of the jet are similar to those of a standard turbulent round jet. This allows the use of well-established correlations in order to estimate the mixture fraction distribution in the present jet. Both the mean velocity and the mean mixture fraction distributions will be used later qualitatively and in some cases quantitatively.

An air jet with a velocity $U_j = 21$ m/s (i.e. Re_j=6800) was used for the hot wire measurement to avoid any errors due to the variation in density and thermal conductivity with fuel jets. Figure 3.4 shows the radial distribution of the mean axial velocity at $z/d_j = 10$ to 50, which covers the area of interest concerning the ignition of the jet. The velocity at each radial location (U) is normalized by the centerline velocity at that axial location (U_m) after subtracting the co-flow velocity (U_c) from both. The radial distance from the jet axis (r) has been divided by the axial distance from the nozzle (z). The present results show good agreement with those reported by Wygnaski and Fiedler (1969). Figure 3.4 also shows that the jet reaches self-similarity after $z/d_j > 30$, consistent with Townsend (1976) and Pope (2000). Generally, the results show that the velocity profile of the present jet is similar to our expectations from an axisymmetric turbulent free jet. Therefore, an estimation of the mean axial velocity $\overline{U}$ that will be used later for the flame propagation speed calculation will be done using the empirical fit from Tieszen et al. (1996):

$$\frac{\overline{U}}{U_0} = 11.8(\frac{\rho_0}{\rho})^{1/2}(\frac{r_0}{z}) \exp\left[-93.7(\frac{r}{z})^2\right] \tag{3.5}$$

In Eq. 3.5, $\overline{U}$ is the mean axial velocity, r the radial location, U_0 is the jet-exit velocity, r_0 is the jet-exit radius, and ρ_0 and ρ are the density of the diluted methane

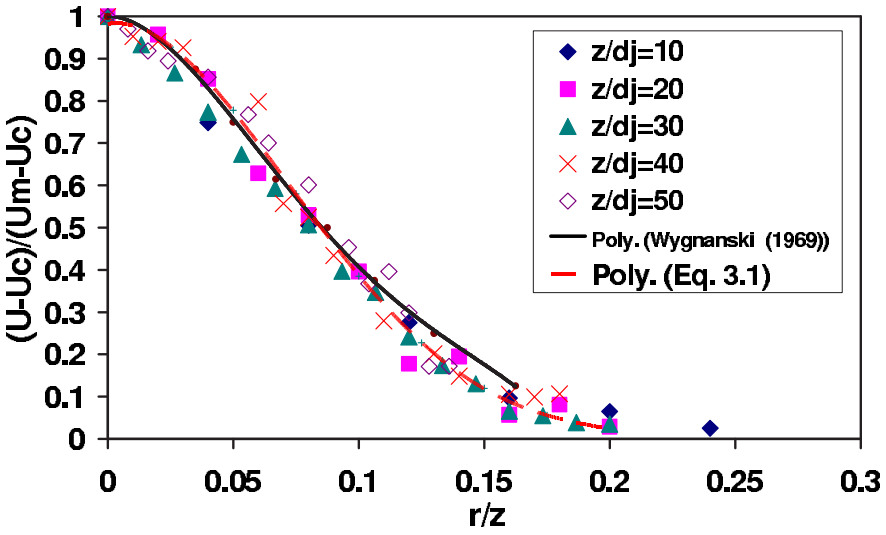

Figure 3.4: Mean axial velocity radial distribution. Air jet, $U_j = 21$ m/s.

jet and ambient air respectively. This equation shows an excellent agreement with the present hot-wire velocity measurements, Fig. 3.4.

The r.m.s. values of the longitudinal turbulent intensity fluctuations were also obtained. The radial distribution of the turbulent intensities, at the same locations in which the velocity was measured, is shown in Fig. 3.5 and a comparison with the data of Wygnaski and Fiedler (1969) is made. The radial distribution of the r.m.s. velocity is in good agreement with previous work. At $z/d_j = 50$, our data are very close to Wygnaski and Fiedler (1969) (taken from at $z/d_j = 60$ where the jet reaches the self-preserving region), but the r.m.s. at $z/d_j = 20$ is about 20% smaller than that of Wygnaski and Fiedler (1969) at the same downstream location at the core of the jet, with better agreement after a radius corresponding to the jet's half-width. In general, our velocity measurements are within the scatter of data from various investigators of this flow.

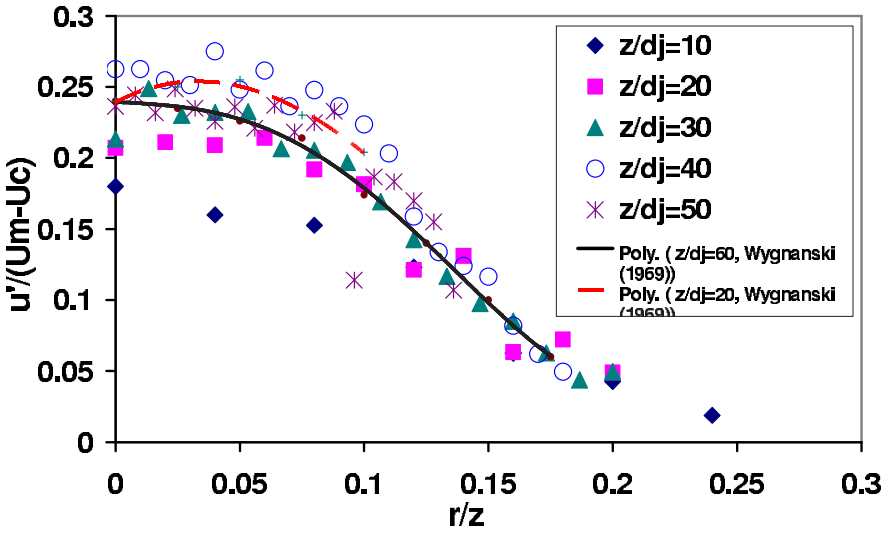

Figure 3.5: Axial velocity fluctuations radial distribution. Air jet, $U_j = 21$ m/s.

3.2.2.2 Mixture fraction distribution

Since the velocity profile and the turbulent intensity fluctuation have shown good agreement with those of a standard turbulent jet, the mixture fraction distribution in our jets should be similar to that measured previously for this flow. In particular, the well-known result that altering the jet velocity does not alter the mixture fraction distribution in the free turbulent jet is important for some of the interpretations of the ignition probability data that follows later in Section 3.2.5.

An estimation of the mean mixture fraction distribution can be done using the correlation of Richards and Pitts (1993), Eq. 3.1, supported by various constant- and variable-density experiments (Dowling and Dimotakis, 1990). It should be mentioned that the effect of the co-flow air on the mixture fraction distribution is neglected here due to the very low co-flow velocity and the fact that we are interested in axial locations where the centreline velocity is still very high compared to the co-flow and the jet is momentum-dominated. Our jets have Reynolds

numbers between about 3000 and 5780. Round jets with Re_j down to about 2000 had a spreading rate only 10% different than jets at Re_j = 40,000, which was high enough for the jet to attain self-similar behavior according to Richards and Pitts (1993), Mi et al. (2001) and Yoda et al. (1994). Hence, based on these comments and on the good agreement of the present velocity measurements with those from jets at higher Reynolds numbers from which the self-similar Eq. 3.1 has been constructed, we expect that the mean mixture fraction in our jets can be described to within 10% by Eq. 3.1 and therefore we expect small changes in the mixture fraction distribution with U_j.

3.2.2.3 Timescales

To fully correlate the ignition success with the local mixture fraction, as done by Smith et al. (1986), the spark duration should be short relative to the flow scales. More specifically, in order for the spark to "freeze" the mixture fraction distribution, the convection time of the smallest eddy should be greater than the spark time. The former can be calculated as $\eta_K/\overline{U}$, where η_K is the Kolmogorov length scale that can be estimated as $\eta_K = L_{turb}(Re_t)^{-3/4}$, L_{turb} is the integral length scale and Re_t is the turbulent Reynolds number. $L_{turb}(z)$ can be estimated in a turbulent jet as (0.08 z), while $Re_t = u' L_{turb}/\nu$. ν is the dynamic viscosity of the jet. At U_j = 25.5 m/s, $L_{turb}/\overline{U}$ varies from about 1 ms at z/d_j = 20 to 6 ms at z/d_j = 50, while $\eta_K/\overline{U}$ varies from 5.5 μs to 34 μs respectively. Hence, the spark durations used in the present work are shorter than the convection time of the largest eddy, but they were not able to freeze the value of the mixture fraction at the moment of the spark. This was even more prominent in the data of Smith et al. (1986), where much longer sparks (20 ms) were used.

3.2.3 Visualization of ignition and flame propagation

3.2.3.1 Direct visualization

When a spark is applied in the jet, one out of three different events is observed. A spark without any flame front, a spark followed by flame propagating downstream that then blows off, or a spark followed by flame propagation both downstream and upstream resulting in either an attached flame or a lifted flame. Following the spark, three main stages for the ignition and the subsequent flame propagation have been observed and investigated in the present work. These stages are the following: (1) flame kernel growth; (2) downstream flame propagation and radial expansion; and finally (3) upstream flame propagation.

The first stage, kernel growth, covers the time from the moment of starting the spark to the time when the flame kernel starts propagating downstream. It takes about 1.4 ms on average. Figure 3.6 shows instantaneous high speed video camera images taken at 20,000 fps that show the early stage of the kernel growth and it is evident that the flame kernel keeps an almost spherical shape. Based on such images, the rate of growth of the kernel is discussed quantitatively in Section 3.2.6. Following this stage, the downstream edge of the flame kernel starts propagating downstream with the flow.

The second stage covers the period from the beginning of the flame kernel's downstream propagation to the moment when the flame front starts propagating upstream against the flow. Figure 3.7 shows high speed camera images for this stage. In this stage of flame propagation, the downstream edge of the flame front first propagates with the flow until it reaches a certain position. This position, 6 d_j with $U_j = 25.5$ and 3 d_j with $U_j = 12.5$ m/s, depends on the jet velocity and the ignition location. Then, the flame expands radially until it reaches a width of about 7 d_j at the z location shown. This stage takes about 17 ms and 10 ms with

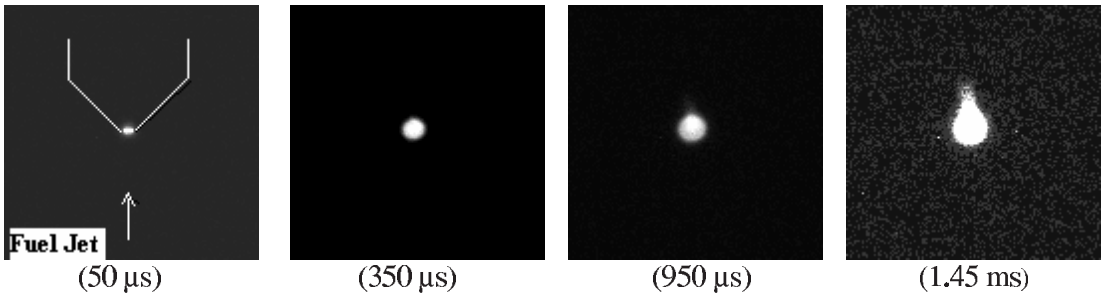

Figure 3.6: High speed camera images of flame kernel growth. $U_j = 25.5$ m/s, 20,000 fps. Spark at $r/d_j = 0$, $z/d_j = 30$. Spark: 100 mJ, 400 μs, 1 mm electrode, 1 mm gap width. Number below images shows the time after the spark starts.

the higher and lower jet velocity respectively. During this period, the upstream edge of the flame front stays at approximately the same axial location. Following the radial expansion, the flame front starts propagating upstream. It takes about 32 ms from the spark initiation for the flame front to pass the spark location again, with $U_j = 25.5$ m/s, as it now moves upstream. We should note that since these are line of sight images, it is not clear if actually there is a reaction zone at the centerline or only at some larger radial distance. The OH-PLIF images shown later clarify this point better.

The third stage includes the upstream flame propagation from the spark area until the flame stabilizes (as a lifted flame in the present case). Figure 3.8 shows high speed camera images for this stage of flame evolution. Based on similar images, more quantitative information on this stage will be given in Section 3.2.7. The average flame propagation speed upstream is an important quantity for the ignition of combustors and it would be interesting to see whether advanced turbulent combustion models can capture the present observations qualitatively and quantitatively.

The three stages above occur if the spark is applied along the jet centerline.

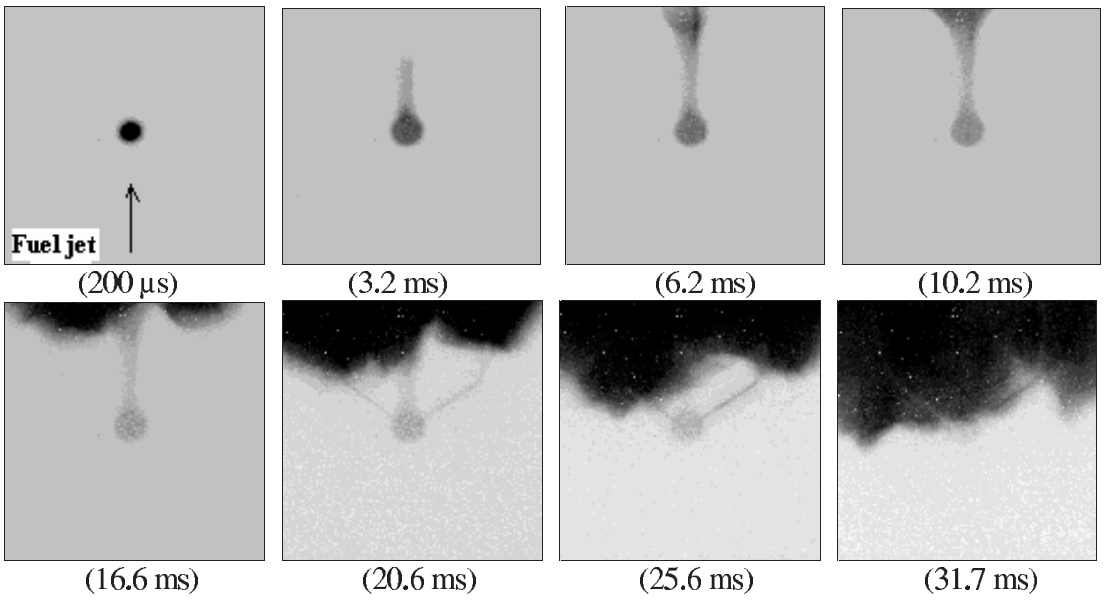

Figure 3.7: High speed camera images of the downstream flame propagation. Spark at $r/d_j = 0$, $z/d_j = 30$, spark and flow parameters are similar to Fig. 3.6. Number below images shows the time after the spark starts.

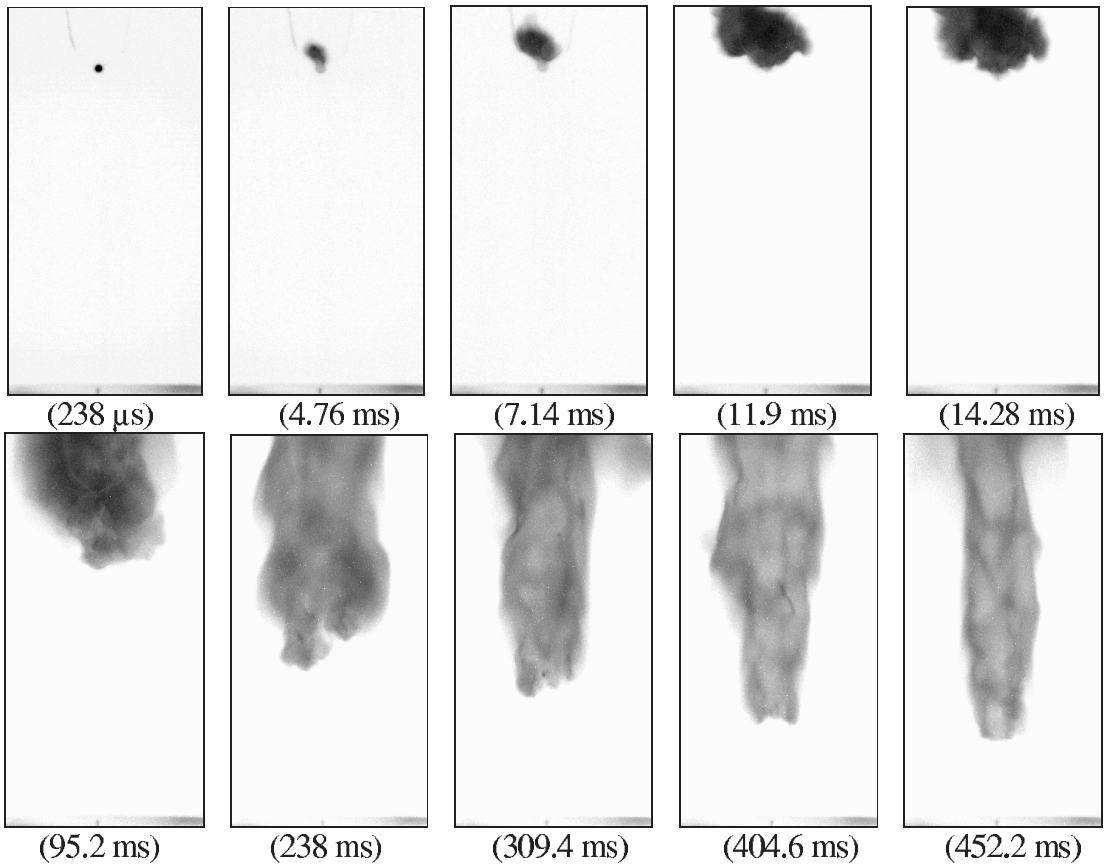

Figure 3.8: High speed camera images of ignition at $r/d_j = 0$, $z/d_j = 40$ followed by flame propagation upstream, spark and flow parameters are similar to Fig. 3.6, $U_j = 25.5$ m/s, 4200 fps. Number below images shows the time after the spark starts.

However, if the flame is ignited at an off-axis location, the flame behaves similarly to the previous case for the first and the third stages, but different in the second stage, Figure 3.9. Following the kernel growth stage, the downstream edge of the flame starts propagating downstream along an inclined path until the jet centerline. Then, the flame propagates upstream similar to the case where the flame was ignited along the axis. Finally, in another observation, the spark was applied at $z/d_j = 4$ and $r/d_j = 1$, i.e. below the expected lift-off height. This ignition event results in flame kernel followed by propagation only downstream with the flow and not in the upstream direction. Then the flame stabilizes as a lifted flame. Figure 3.10 shows some images of this ignition event captured by the high speed camera with 4200 fps.

3.2.3.2 OH-PLIF

In order to examine the flame front structure during propagation after ignition, PLIF of the OH radical, Section 2.4.2, was used at various instants covering the range of 5 to 100 ms following the spark. It can be observed from the OH-PLIF images shown in Fig. 3.11 that the flame following ignition initially has a sphere-like shape, more evident when the jet velocity is low. The flame then expands radially before it starts moving upstream. There seems to be a reaction zone at the centreline when the kernel is small, but this flame front disappears later and, at a certain location, the flame takes a hollow cylindrical shape with an edge flame front (see image at 100 ms at 12.5 m/s, Fig. 3.11). The central front disappears between 30 and 60 ms after ignition for both jet velocities and this happens between 35 and 32 d_j downstream of the jet exit. The $\overline{\xi} = \xi_{rich}$ contour crosses the centreline at about 30 d_j. Hence, the loss of the front normal to the axis may be attributed to quenching as the flame faces progressively richer mixture fractions and higher flow velocities along the jet centerline. Finally, Fig. 3.11 also

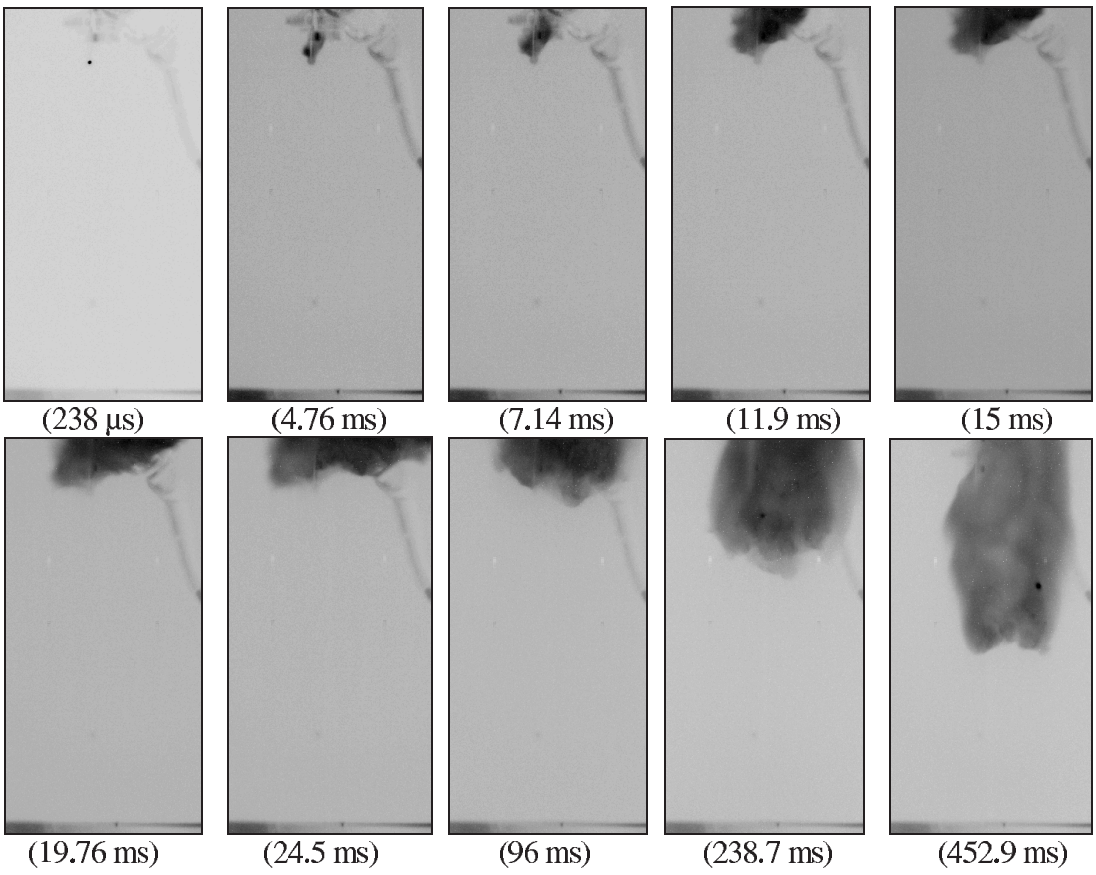

Figure 3.9: High speed camera images of ignition at $r/d_j = 4$, $z/d_j = 40$ followed by inclined downstream propagation, then flame propagation upstream, spark and flow parameters are similar to Fig. 3.6, $U_j = 25.5$ m/s, 4200 fps. Number below images shows the time after the spark starts.

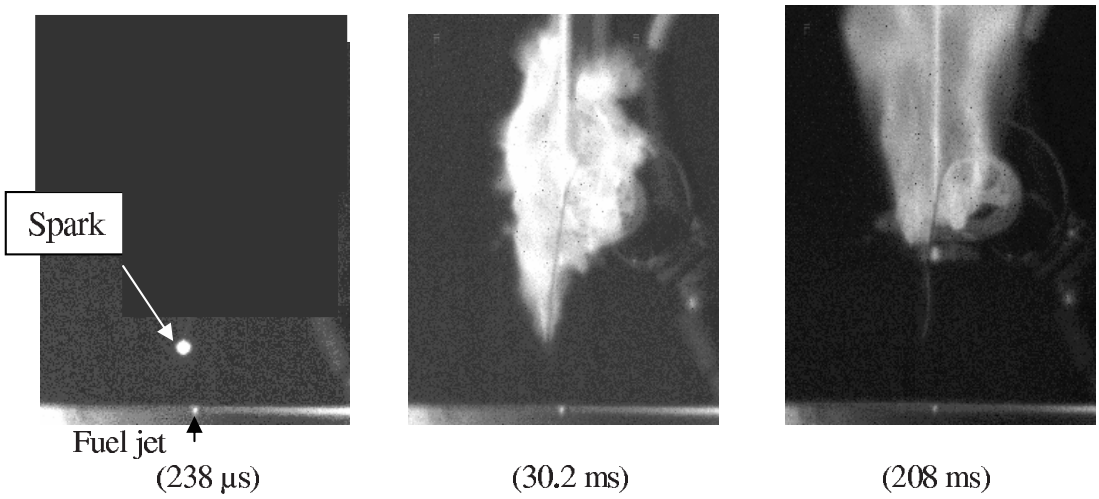

Figure 3.10: High speed camera images of ignition below the lift-off height of the diluted jet ($X = 30\%$), spark and flow parameters are similar to Fig. 3.6, $U_j =$ 25.5 m/s, 4200 fps. Number below images shows the time after the spark starts.

shows that with an increase in jet velocity, the flame front becomes very wrinkled as a result of the higher turbulence. The central region of the jet quickly becomes relatively free of OH radical, indicating absence of reaction there.

3.2.4 Effect of ignition location on the lift-off height

The lift-off height was measured by taking the average of ten images using the high speed camera for each condition. The exposure time of each of these images was set to be long enough (2.2 ms) to avoid the effect of the fluctuations in the lift-off height of the methane flame. The stable flame resulting from the ignition could be an attached or a lifted flame, depending upon the fuel jet velocity. Here, we investigate the effect of changing the ignition location on the lift-off height of the flame, since it is known that lifted flames show a hysteresis behavior according to Gollahalli et al. (1986) and Zsak et al. (1984) and it is not clear

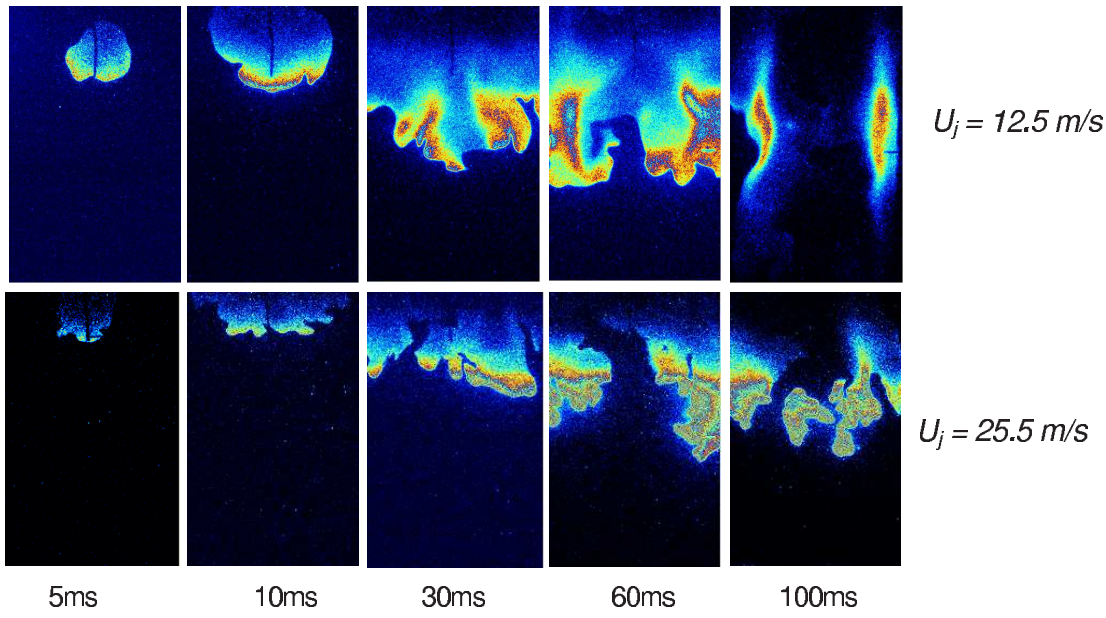

Figure 3.11: OH-PLIF images of the flame at different instants from the spark from different successful spark realizations. Ignition at $r/d_j = 0$, $z/d_j = 40$, spark parameters are similar to Fig. 3.6. The fuel jet is from below. The imaged region corresponds to $21d_j$ and $13d_j$ in the axial and radial directions respectively and the lower side of the images is at $z/d_j = 24$.

whether the flame that results from the spark ignition follows the liftoff height of the increasing velocity path or the decreasing velocity path. In the present work, the lift-off height, L_h, is defined as the distance between the burner rim and the most upstream position of the lifted flame base.

In the experiments discussed in this section, a methane jet was used with a range of velocities starting from $U_j = 6.3$ m/s ($Re_j = 2000$), which results in an attached flame. The flame detaches when the velocity exceeds about 13 m/s. The lift-off height increases as the jet velocity increases, Fig. 3.12. When the jet velocity decreases from this condition, the lift-off height decreases. However, it follows a different $L_h - U_j$ path from the one when the velocity increases. This behavior has been observed before, (Gollahalli et al. (1986) and Zsak et al. (1984)), and has been attributed to the change in composition structure below the flame base between increasing and decreasing velocity paths. This experiment was repeated with different air dilutions ($X = 10\%$ to 40%) and all of these flames show the same hysteresis behavior with the observation that the liftoff height increases with X at the same jet velocity, Fig. 3.12. Furthermore, with large dilution percentages ($> 20\%$ air by volume), the relation between lift-off height and velocity deviates from linearity. It is expected that this deviation is due to the overly simple chemical dilution criterion used in the strain-out condition, and it is not related to the fluid dynamical aspects. That is related to the fact that the reaction chemistry of methane differs substantially in case of dilution (Miake-Lye and Hammer, 1988). Any further increase in dilution percentage above 50% air by volume causes flame blow-out immediately.

For the diluted methane/nitrogen flame, the same behavior for the lift-off height with the velocity has been observed. Also, as we increase the dilution percentage of nitrogen, the lift-off height increases rapidly at all velocities, Fig. 3.13. This is because of the decrease in the laminar burning velocity due to the increase

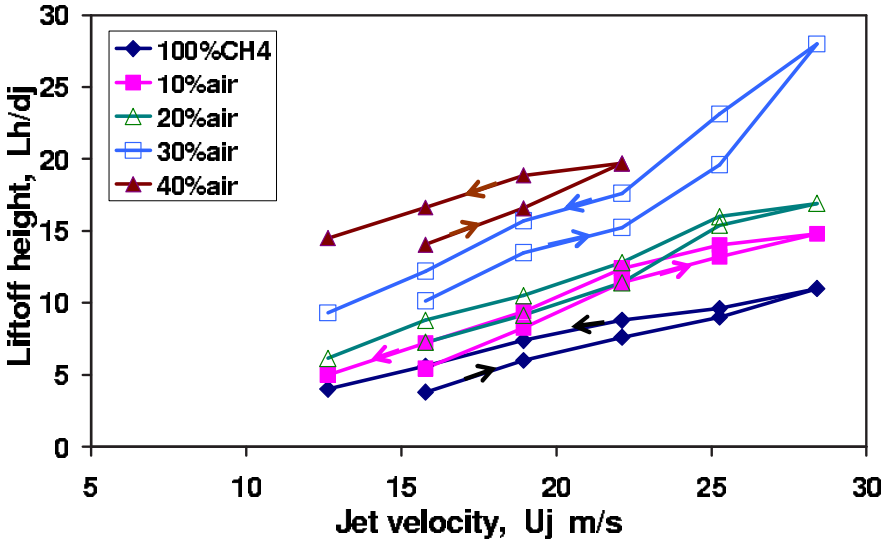

Figure 3.12: Lift-off hysteresis as a function of jet velocity for the indicated air dilution.

in the dilution percentage, which relates directly to the local burning velocity at the base (Takahashi et al., 1984). If the dilution percentage of nitrogen increases above 40% by volume, the flame will blow-out suddenly. It has been noticed that the color of the flame becomes lighter with the nitrogen dilution than that with the air dilution. Also, the color becomes lighter as we increase the nitrogen dilution percentage. The increase in nitrogen dilution percentage causes reduction in the soot formation and this affects the flame color. Comparing with the air premixing, the lift-off height of the diluted methane/nitrogen flame is higher than that of the premixed methane/air flame at the same dilution percentages and the same jet velocities. The present measurements of the lift-off heights are in excellent agreement with Miake-Lye and Hammer (1988).

The effect of changing the ignition location on the lift-off height was studied by applying a spark with the same characteristics at six axial locations downstream, from $z/d_j = 25$ to 50, and two radial locations, $r/d_j = 0$ and 4. Three different

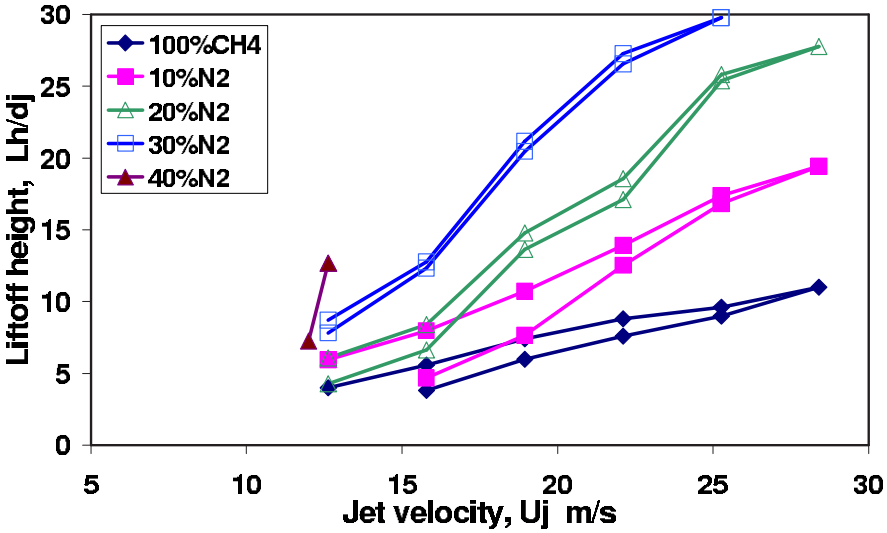

Figure 3.13: Lift-off hysteresis as a function of jet velocity for the indicated N_2 dilution.

jet velocities were examined (12.5, 19 and 28.5 m/s). The $U_j = 12.5$ m/s flame is attached when this condition is approached from an attached, ignited flame at a lower velocity, but lifted when approached from ignition at this velocity. The higher velocities always resulted in lifted flames. Figure 3.14 shows the results of this experiment with the pure methane jets. The results show that the lift-off height of the ignited flame is always the same, no matter where the ignition happens even if the ignition is below the expected lift-off height of the flame (e.g. Fig. 3.10). Similar results have been observed with methane jets premixed with air ($X = 20\%$) and diluted with nitrogen, Fig. 3.15 and Fig. 3.16 respectively. The flame after the ignition always stabilized at a lift-off height almost equal to the value of L_h in the decreasing velocity path in the hysteresis curves shown in Fig. 3.12. The present data imply that modelling efforts of lifted flames should pay attention to the way the steady-state solution is reached.

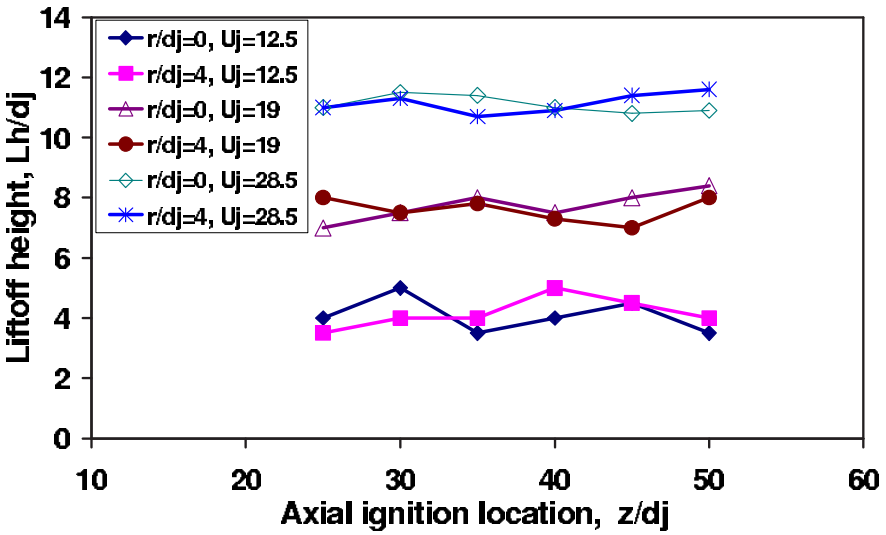

Figure 3.14: Effect of ignition location on the lift-off height of the pure methane jet at the indicated velocity.

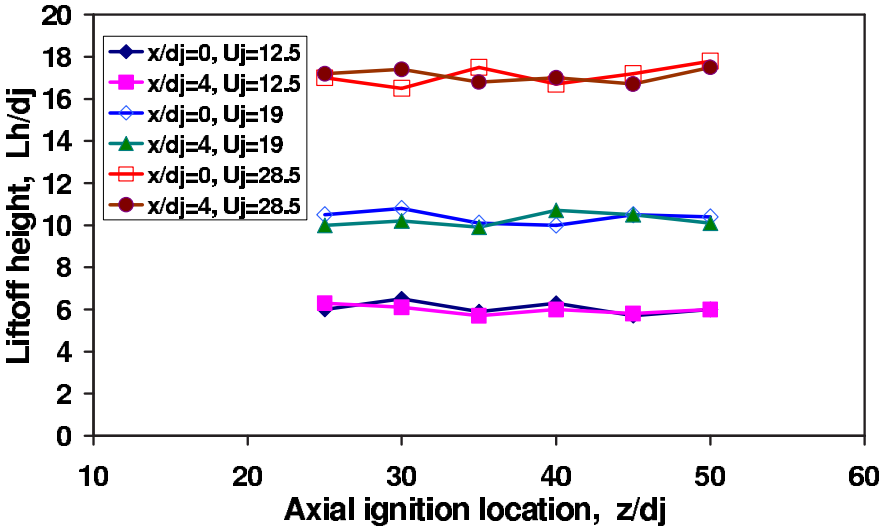

Figure 3.15: Effect of ignition location on the lift-off height of the methane jet diluted with air at the indicated velocity, X=20%.

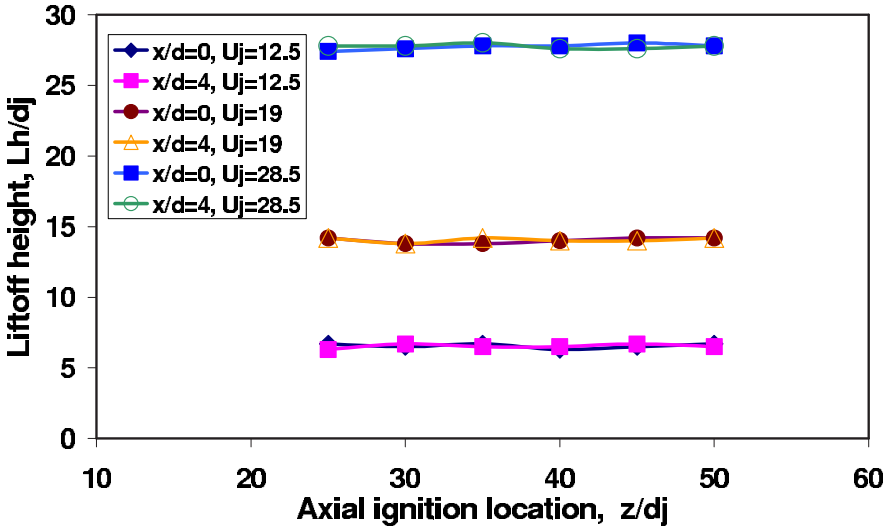

Figure 3.16: Effect of ignition location on the lift-off height of the methane jet diluted with N_2 (20% by volume) at the indicated velocity.

3.2.5 Ignition probability

The successful ignition, in the present work, is defined as a flame kernel formation, as a result of a spark, followed by flame propagation upstream to result in a stable flame (for our velocities, a lifted flame). This definition is called sometimes a "light-back" (Smith et al., 1986). Both flow and igniter characteristics affect the ignition of the jet. The effects of these parameters are investigated separately in the next sections.

3.2.5.1 Effect of jet velocity

Three different jet velocities were examined, U_j = 9.5, 12.5 and 25.5 m/s which are equivalent to Re_j = 2170, 2878 and 5780 respectively. The spark igniter used to examine the ignition probability of these jets has the same characteristics. Figure 3.17 shows two-dimensional contours of the probability of successful ignition of these jets. The contours have been assembled from a matrix of 42x12

points across and along the jet respectively. Iso-lines of $\overline{\xi} = \xi_{rich}$, ξ_{lean} and ξ_{st} calculated from Eq. 3.1 are also shown for comparison. Based on the agreement of our velocity measurements with the expected velocity distribution from self-preserving jets (Section 3.2.2.1) and on the finding that small differences in the spreading rate of jets are expected with Re_j (Yoda et al., 1994), we expect that the mean mixture fraction distributions for the jet velocities of the spark-ignition experiments are approximately the same.

The following observations can be made. First, the radial extent of the ignitable region is wider than the nominally flammable region (in the mean). However, it follows the radial extend of the calculated flammability factor contour (F calculated from Eq. 3.3) shown in Fig. 3.18, in complete agreement with the main qualitative findings of Birch et al. (1981) and Smith et al. (1986), and attributed to finite mixture fraction fluctuations. Second, the axial locations with $P_{ign} > 0$ lie upstream of the rich limit contour, again attributed to the f fluctuations which are about 24% of the mean along the jet centerline (Richards and Pitts, 1993). Third, P_{ign} drops to zero at about $z/d_j = 50$, well upstream of the $\overline{\xi} = \xi_{lean}$ contour with $F > 80\%$, Fig. 3.18. This is because ignition at these locations does not result in light-back, but simply in a kernel that is eventually blown off. Possibly this is due to the low flame speeds of the lean mixtures at these locations that do not allow upstream flame propagation. Finally, the highest ignition probabilities are observed at axial locations between the rich limit and the stoichiometric contour. In general, these findings are consistent with the limited light-back data of Smith et al. (1986).

Figure 3.17 also shows that the area that gives high probability of ignition shrinks as the velocity increases. Along the jet centerline, this area is between $z/d_j = 18$ to 43, $z/d_j = 32$ to 42 and $z/d_j = 35$ to 43 for $U_j = 9.5$, 12.5 and 25.5 m/s respectively. Radially, the area is reduced from $r/d_j = \pm 5$ at U_j

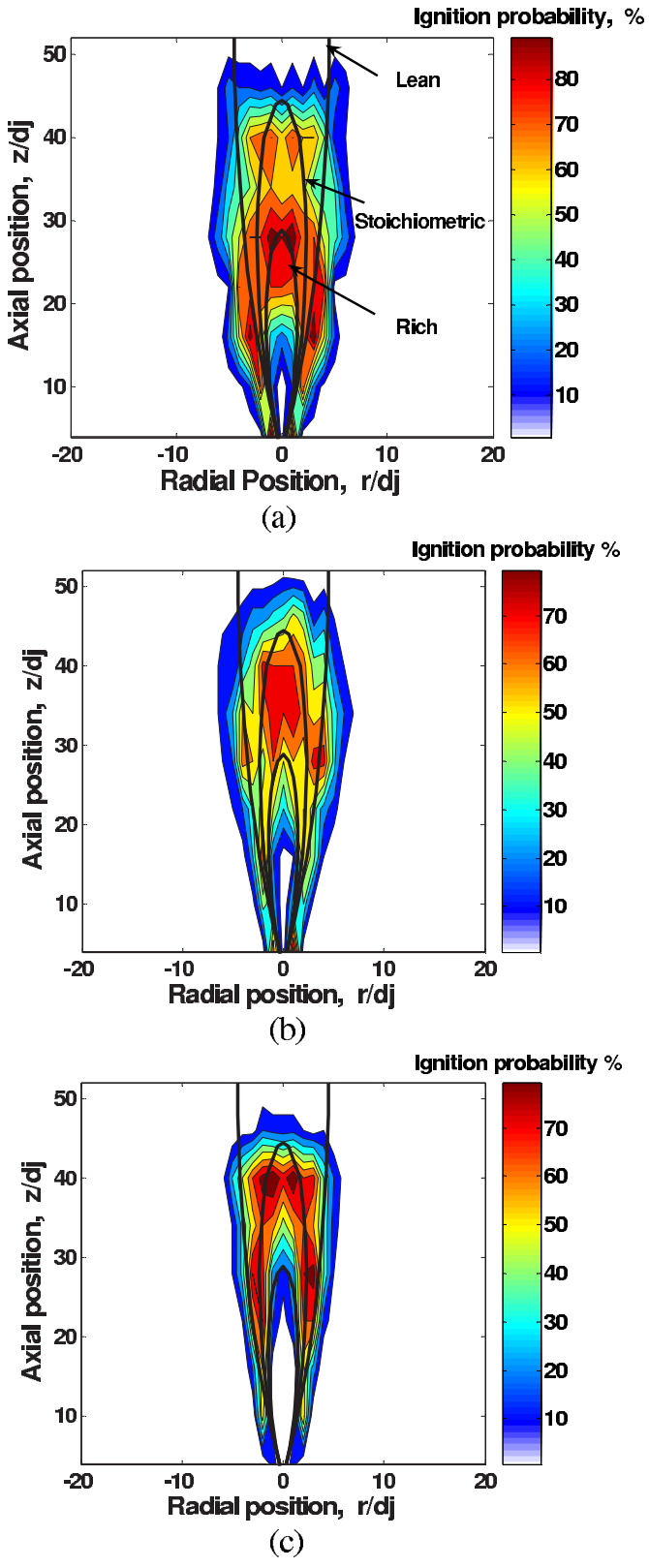

Figure 3.17: Ignition probability contours. Spark parameters are similar to Fig. 3.6, $X = 30\%$. (a) $U_j = 9.5$, (b) $U_j = 12.5$ and (c) $U_j = 25.5$ m/s.

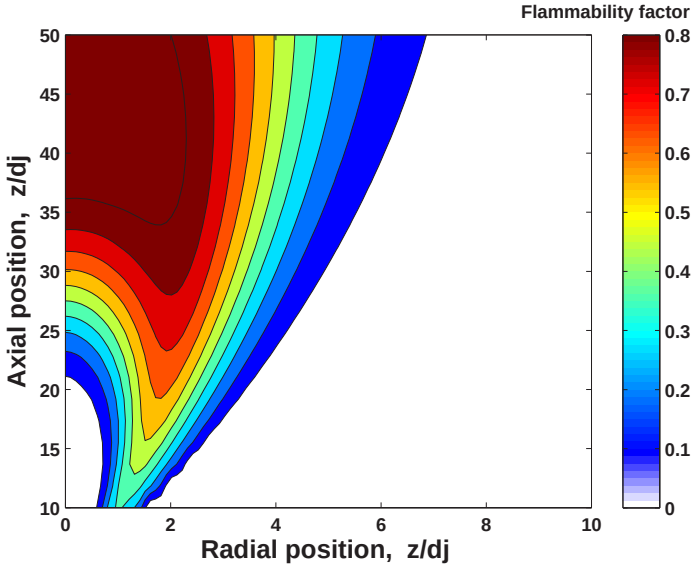

Figure 3.18: Flammability factor (F) contour of $X = 30\%$, calculated from Eq. 3.3.

$= 9.5$ m/s, to $r/d_j = \pm 4$ and $r/d_j = \pm 3$ at $U_j = 12.5$ and $U_j = 25.5$ m/s respectively. As the jet velocity increases, the highest ignition probability region shifts downstream, along the jet axis, until it coincides approximately with the stoichiometric mixture fraction at $U_j = 25.5$ m/s and ignition can hardly be achieved upstream of the rich flammability limit. The probability of getting a spark kernel followed by propagation downstream resulting in extinction increases as the velocity increases, especially above $z/d_j = 50$. Generally, it is clear that as the velocity increases, it is hard to achieve a successful ignition and to establish a stable flame. This behavior was also observed by Smith et al. (1986) for a pure natural gas jet at higher Re_j than the ones used here.

The effect of increasing the jet velocity at a constant spark energy on the probability of successful ignition can be partly attributed to the convective heat loss suffered by the spark kernel during the initial phase of its development when

it is still "anchored" to the electrodes. This loss of heat, which increases with velocity, impairs ignition performance unless it is compensated for by an increase in spark energy. Another effect of an increase in velocity is that it gives the spark kernel less time in which to propagate before being swept downstream (Lefebvre (1998) and Swett (1957)). These effects become stronger as the igniter moves upstream. This may explain why the ignition can not be achieved earlier than $z/d_j = 35$ along the jet centerline at $U_j = 25.5$ m/s. However, the effect of increasing velocity on the successful ignition is very small at the downstream edge of the flammable region with $P_{ign} \longrightarrow 0$ at approximately the same z/d_j for all U_j tested. Fluid dynamical effects can be also taken into consideration, as the increase in turbulent strain rate may lead to quenching, which causes lower ignition probability.

To emphasize the effect of velocity on ignition further, the instantaneous axial velocity was measured with LDV 1 mm below the spark gap and the ignition behavior was simultaneously observed. The seeding rate in the jet was high enough to give a velocity measurement within 0.5 ms before the initiation of the spark. Fig. 3.19 shows that the ignition is likely to be successful when the local velocity is low. The average local velocity for the successful ignition events shown in Fig. 3.19 is about 4.2 m/s, while that for the failed ones is 5.5 m/s. Hence, it seems that the instantaneous velocity value at the spark plays an important role in determining the success of the ignition. More extensive measurements, possibly with PIV so that the strain rate is also available before the spark, would be very useful in highlighting in more detail the effect of turbulence on spark ignition.

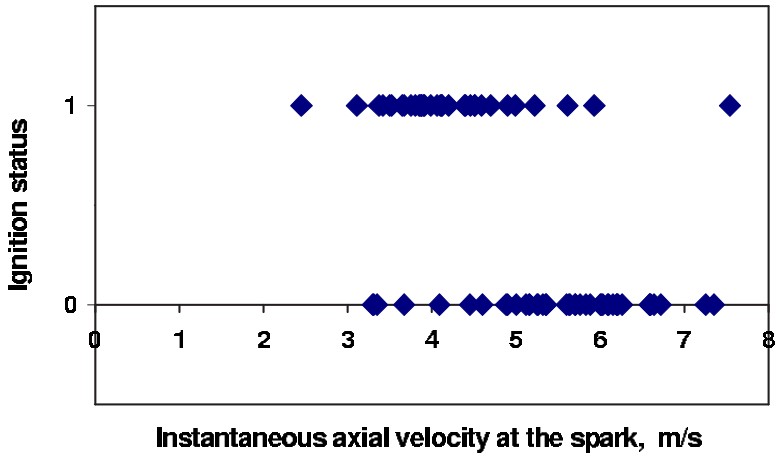

Figure 3.19: Success (1) or not (0) of ignition versus the instantaneous axial velocity at approximately the moment of spark initiation 1 mm upstream of the spark, at $z/d_j = 30$ along the jet axis for $U_j = 25.5$ m/s, $X = 30\%$. Spark parameters are similar to Fig. 3.6.

3.2.5.2 Effect of air dilution of the fuel jet

The ignition probability was examined for various degrees of air-dilutions (or premixing) of the fuel jet. The air volume fraction in the fuel stream X was increased from 10% to 40%. For X higher than about 50%, it was very hard to achieve ignition and, if it happened, the ignited flame was highly unstable and extinguished immediately. Figure 3.20 shows the effect of X on the ignition probability along the jet centerline. Figure 3.20 also includes a comparison between the present results and the ignition probability (light-back) of a pure natural gas jet taken from Smith et al. (1986). The spark igniter characteristics were kept the same, and $U_j = 12.5$ m/s for all dilution conditions.

The longest axial distance of the spark that leads to successful ignition decreases by about 15 d_j for X=10% compared to that of Smith et al. (1986).

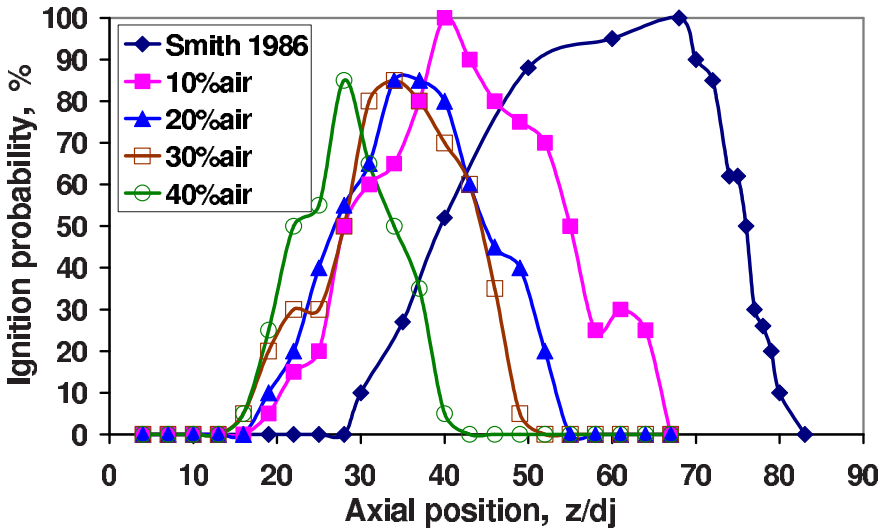

Figure 3.20: Ignition probability versus axial location of the spark. Spark parameters are similar to Fig. 3.6, $U_j = 12.5$ m/s, for the indicated dilution.

The maximum probability of successful ignition does not exceed 85% for any X higher than 10%. By adding air to the fuel, the mass fraction of the fuel in the jet fluid decreases. This results in an upstream shift of the flammable region and a reduction in its length, Fig. 3.21. It is clear that for all X, $P_{ign} \longrightarrow 0$ before the contour $\overline{\xi} = \xi_{lean}$, but also that P_{ign} is finite upstream of $\overline{\xi} = \xi_{rich}$ contours, consistent with the data of Fig. 3.17. The lower probability at higher X could be due to the fact that when the flammable region shifts upstream, the flame kernel is more likely to experience higher strain rates and it is hence more likely to quench. The same reason can be also applied to explain the trend between the ignition probability and the calculated F along the jet axis shown in Figs. 3.22 and 3.23 for the conditions of $X = 10$, 20% and $X = 30$, 40% respectively.

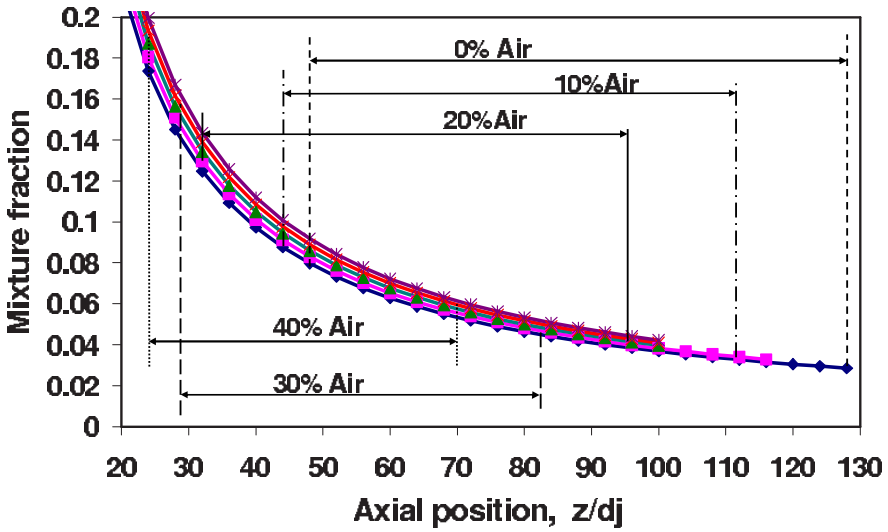

Figure 3.21: Effect of air dilution on the calculated axial position of mean flammability limits of the turbulent methane jet. Mixture fraction ξ is calculated using Eq. 3.1. Dashed lines indicate the locations where $\overline{\xi} = \xi_{rich}$ and ξ_{lean} for each dilution.

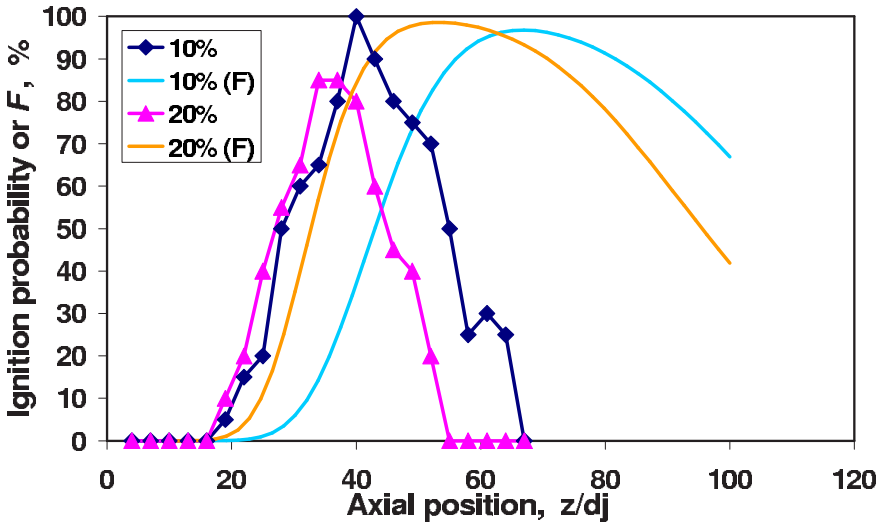

Figure 3.22: Ignition probability compared with the calculated flammability factor F of $X = 10\%$ and $X = 20\%$, $U_j = 12.5$ m/s.

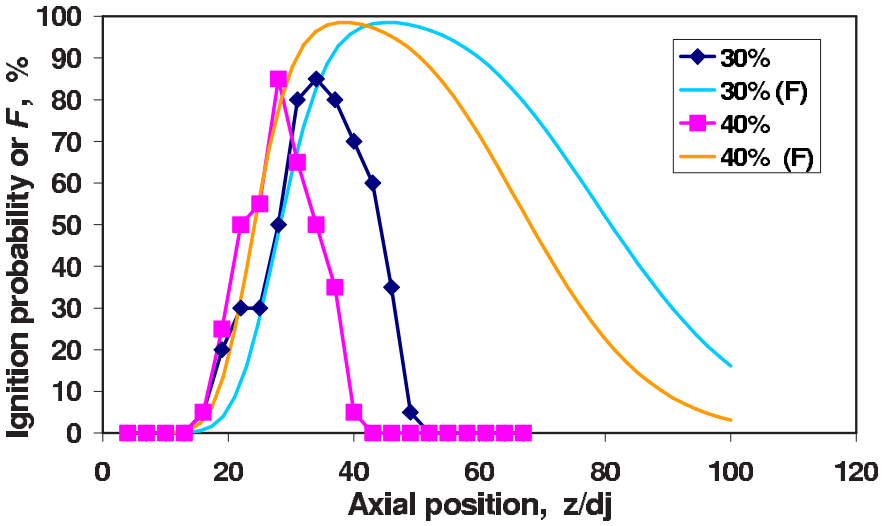

Figure 3.23: Ignition probability compared with the calculated flammability factor F of $X = 30\%$ and $X = 40\%$, $U_j = 12.5$ m/s.

3.2.5.3 Effect of spark parameters

Spark duration

The ignition probability was examined by sparks with different durations (400 μs, 500 μs and 600 μs) applied to a 30% air diluted jet with $U_j = 12.5$ m/s. The other spark parameters were kept constant at: 100 mJ, 1 mm electrode diameter, 1 mm gap. Figure 3.24a and b show the effect of changing the spark duration on the ignition probability along the jet centerline and radially at $z/d_j = 40$ respectively. It can be observed that the shortest duration gives high probability of ignition along the jet centerline, especially around the stoichiometric mixture fraction ($z/d_j = 28$ to 44). However, the longest one is more effective if we move away from the centerline.

With an increase in flow velocity, the spark duration should be short to achieve ignition due to the stretching of the spark. This stretch increases the spark

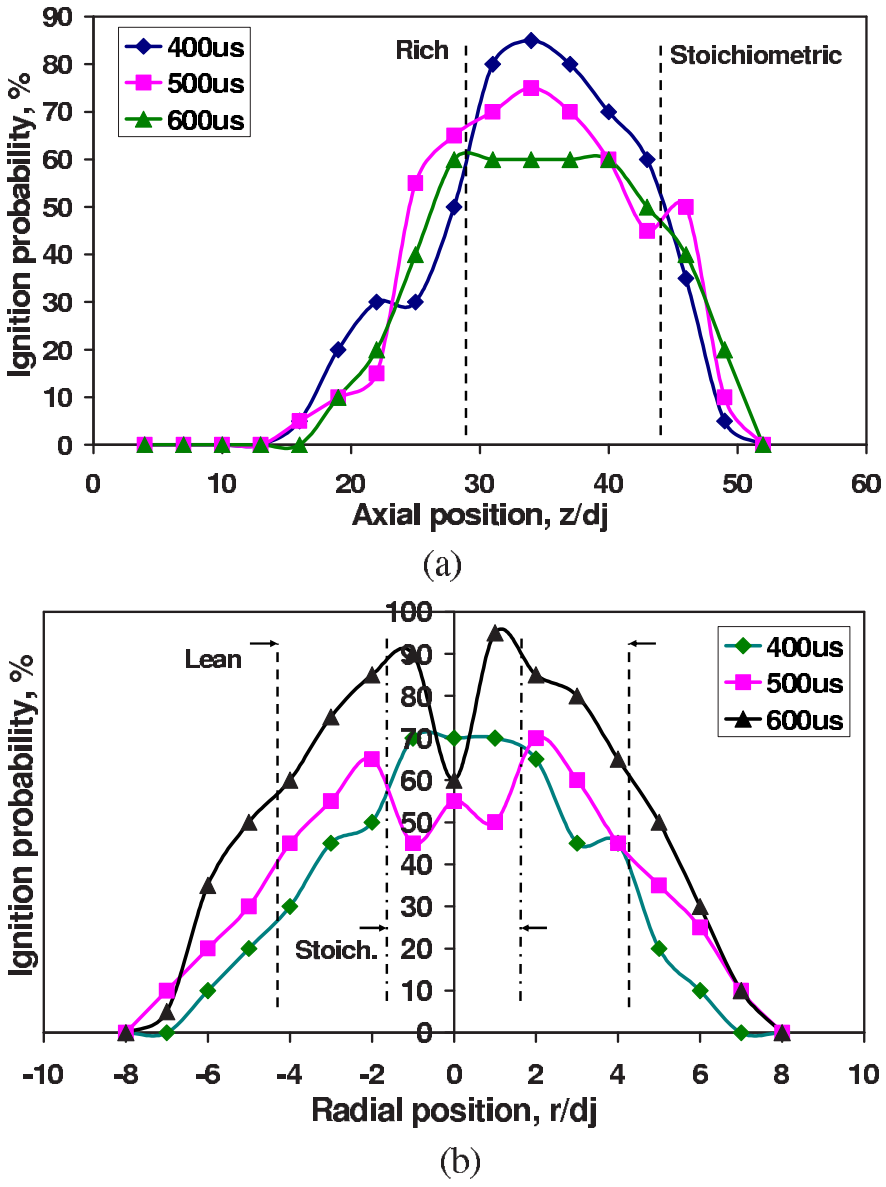

Figure 3.24: Effect of spark duration on ignition probability. (a) Along the jet centerline, (b) radially at $z/d_j = 40$. Spark: 100 mJ, 1 mm electrode, 1 mm gap. $U_j = 12.5$ m/s, $X = 30\%$. Dashed lines indicate the location where $\overline{\xi} = \xi_{st}$ and ξ_{lean}, $\overline{\xi}$ calculated from Eq. 3.1.

electrical resistance and reduces the breakdown voltage which results in reducing the overall energy transferred to the mixture and reduces the ignition probability (Ballal and Lefebvre, 1975a). However, high flow velocity reduces the energy losses to the electrodes by moving the plasma and the heated gas away from them, so by shortening the duration, both the breakdown voltage and the arc phase energy increase and this increases the mixture temperature and causes ignition. That is why short duration is more effective along the jet centerline where the flow velocity is high. On the other hand, at lower flow velocity locations, heat transfer from the flame kernel to the electrodes, as well as loss of active species to the electrodes is high due to the large contact area between the flame kernel and the electrodes (Pischinger and Heywood, 1990) and (Verhoeven, 1995). In this case, long duration is preferable to increase the overall energy transfer from the spark to the mixture. In addition, by increasing the spark duration, the probability of flammable material passing through the spark gap increases because in the present experiments the spark duration is longer than $\eta_K/\overline{U}$ (but shorter than $L_{turb}/\overline{U}$), and it is plausible that this increases the chance of ignition.

Spark energy

Although a few millijoules could be enough to ignite a flowing methane-air under atmospheric conditions (Ballal and Lefebvre, 1978), much higher spark energy should be applied between solid electrodes to achieve that ignition. That is because only a small fraction of the electrical energy is actually delivered to the gas (Teets and Sell, 1988), since a lot of the energy is lost to heating the electrodes. In this experiment, the spark energies were chosen to be much higher than the minimum ignition energy (6.41 mJ) (Lewis and Elbe, 1987) required to ignite methane-air mixtures within the flammability limits. The spark duration was kept constant at 500 μs in order to reach the maximum spark energy produced

from the ignition unit (300 mJ). Figure 3.25 shows that along the jet centerline, there is little improvement in the ignition probability as the spark energy increases, while radially about 30% improvement in the ignition probability can be observed, especially in the lean mixture fraction region ($r/d_j > \pm\ 2$). These results can be attributed to the excessive heat loss from the flame kernel due to the high gas velocity. In the low velocity regions, high spark energy means high temperature of the mixture, which causes high probability of ignition. Surprisingly, if we compare the results of spark energy with those of spark duration, we will find that the highest ignition probability that can be achieved by short duration (400 μs) and low energy (100 mJ) along the jet centerline is similar to that with higher energy (300 mJ) and longer duration (500 μs). Radially, the highest probability with long duration (600 μs) and low energy (100 mJ) is similar to that with higher energy (300 mJ) and lower duration (500 μs). This suggests that by controlling the spark duration, the same ignition probability may be achieved as by controlling the energy.

Electrode diameter

The effect of the electrode was studied in the present work by choosing three different electrodes with 1, 0.7, 0.5 mm diameter respectively. All these electrodes have sharp points to reduce the heat loss from the spark to the electrodes. Figure 3.26 show the ignition probability with these electrode diameters. It can be observed that the ignition probability increases with decreasing the electrode diameter. Along the jet centerline, the ignition probability reaches 100% with 0.5mm diameter around the stoichiometric mixture fraction, about 15% more than that with 1 mm diameter. This difference in the ignition probability increases when the spark moves radially, especially at lean mixture fraction. This difference reaches 40% between 0.5 and 1 mm electrode diameter at some locations.

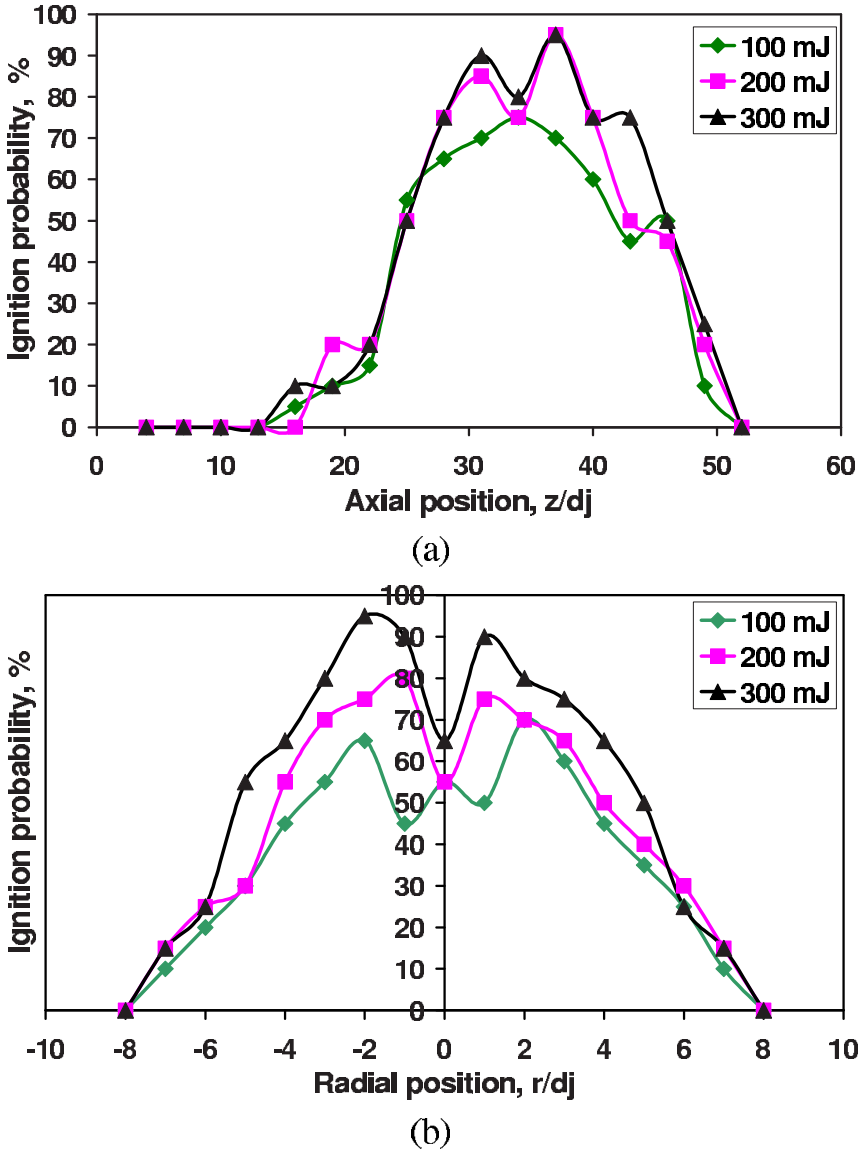

Figure 3.25: Effect of spark energy on ignition probability. (a) Along the jet center line, (b) radially at $z/d_j = 40$. Spark: 500 μs, 1 mm electrode, 1 mm gap. $U_j = 12.5$ m/s, $X = 30\%$.

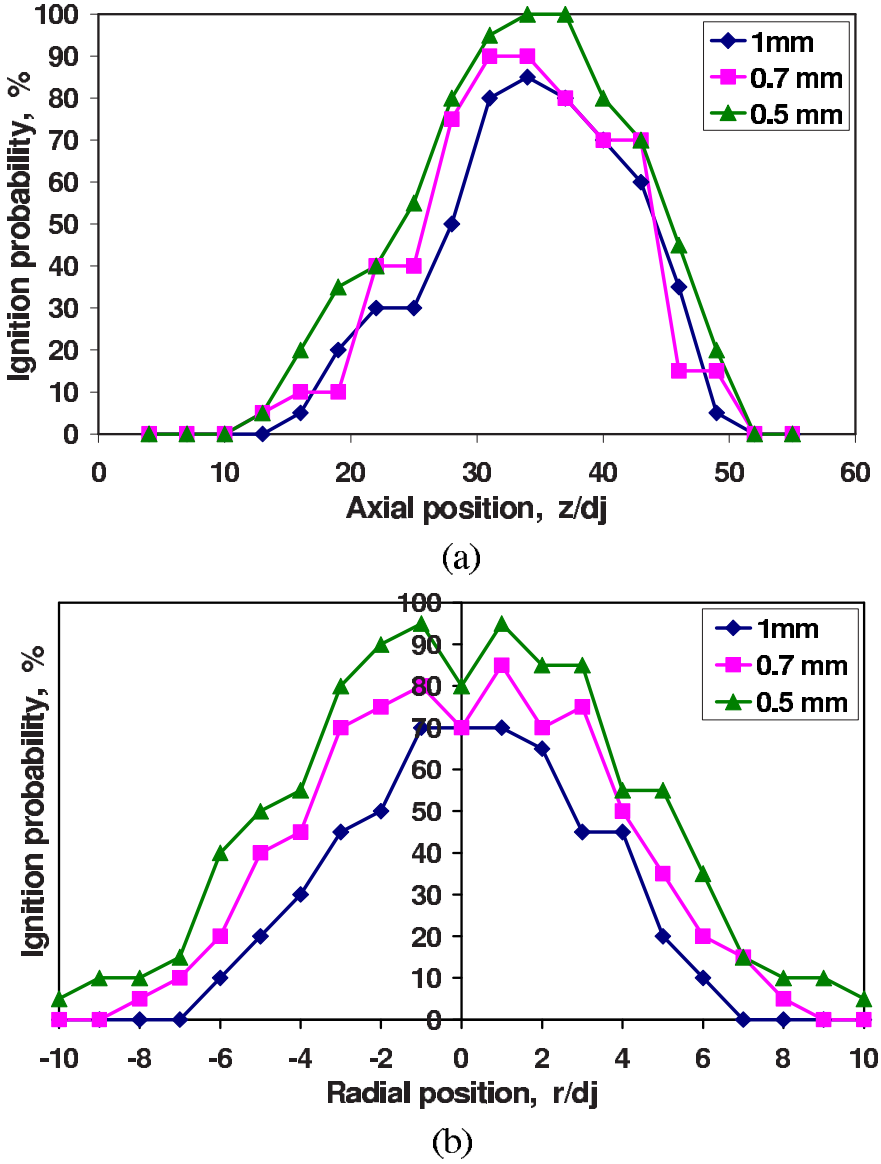

Figure 3.26: Effect of the electrode diameter on the ignition probability. (a) Along the jet center line, (b) radially at $z/d_j = 40$. Spark: 100 mJ, 500 μs, 1 mm gap. $U_j = 12.5$ m/s, $X = 30\%$.

The great improvement in the ignition probability of the turbulent jet with the smallest diameter can be attributed to the following reasons. First, the larger the electrode diameter, the higher the loss of heat and active radicals from the flame kernel to the electrodes, which affects the growth of the flame kernel in its early stage and leads to the extinction of the flame front (Ko and Anderson, 1989). Secondly, large electrode diameter may lead to strong vortex formation in the wake of the electrodes, which may kill the flame kernel in its early stage of growth. However, thin electrodes tend to suffer from rapid wear and an inconsistent energy release (Lefebvre, 1998). The effect of the electrode material has not been tested in the present work, as the electrode material has no or minor effect on the ignition (Ballal and Lefebvre, 1975a).

Spark gap width

The effect spark gap width on the ignition probability was studied by using 1 mm diameter electrode. Three gap widths were examined: 1, 2, 3 mm. These gaps were chosen to be less, equal and more than the quenching distance of stoichiometric methane-air mixture in atmospheric conditions which is about 2 mm (Lewis and Elbe, 1987). However, many parameters affect this distance, such as velocity and mixture strength. Figure 3.27 shows the effect of gap width on the ignition probability. The results show that 2 mm and 3 mm gap widths give much higher ignition probability than 1 mm gap. There is no much difference between the ignition probability of 2 and 3 mm gap, except in some regions below and above the stoichiometric mixture fraction along the jet centerline.

The results emphasize the fact that if the gap width is less than the quenching distance (2 mm for the stoichiometric methane-air mixture (Lewis and Elbe, 1987)), which is believed to be the case of 1 mm gap, the effect of the heat loss from the spark kernel to the electrode is maximize. In addition, the efficiency of

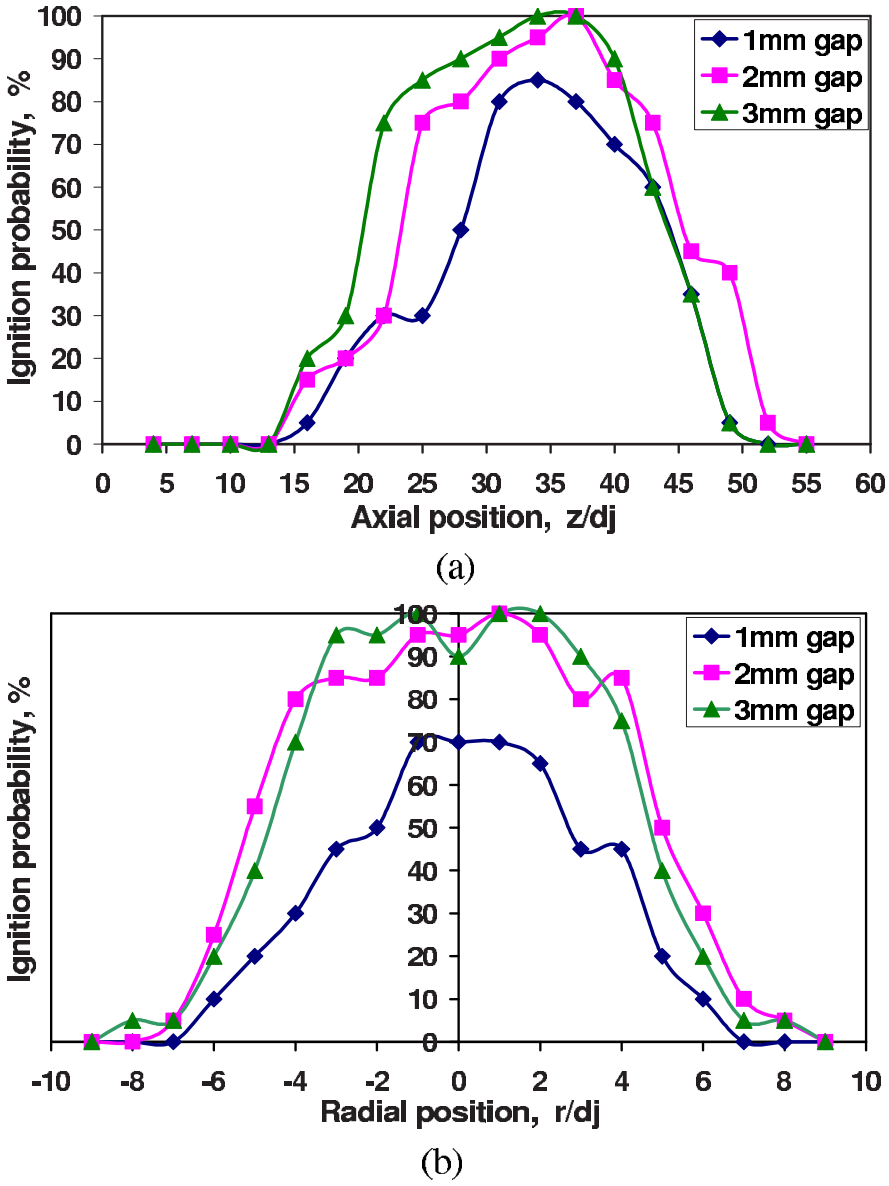

Figure 3.27: Effect of the electrode gap width on the ignition probability. (a) Along the jet center line, (b) radially at $z/d_j = 40$. Spark: 100 mJ, 500 μs, 1 mm electrode. $U_j = 12.5$ m/s, $X = 30\%$.

the electrodes to transfer the electric energy to thermal energy reduces with the small gap (Teets and Sell, 1988). With 2 and 3 mm gap, the effect of the heat loss is weak because the fraction of plasma surface area exposed to the electrodes material is small. However, as we can observe from Fig. 3.27, if the gap is too wide like the case of 3 mm, the energy is wasted in creating a larger spark kernel than is needed to achieve ignition. This may explain why 2 mm gap gives higher probability some times. The only region where 3 mm gap gives higher probability than 2 mm gap is between 15 and 30 jet diameters downstream of the jet exit. As the spark moves closer to the nozzle, the strain rates induced by the flow distortion behind the electrode are higher, which implies that, in conjunction with the higher heat losses of the small gap spark, the flame kernels from the 2 mm gap tend to be more prove to extinction.

3.2.6 Flame kernel growth

The early flame kernel growth is investigated here to explore any possible connection with the ignition probability and to put more emphasis on the explanations that have been proposed earlier. For the experiments in this section, the spark was applied at $z/d_j = 30$. As mentioned in Section 2.5, ten movies similar to Fig. 3.6 are averaged and the mean kernel diameter is here reported as a function of time. Figure 3.28 shows that as the jet velocity increases, the flame kernel grows more rapidly. This can be related to the fact that high flow velocity reduces the energy losses to the electrodes by moving the plasma away from them. However, soon after that, the flame kernel itself suffers excessive heat loss, which reduces the burning velocity. This behavior can also explain why the probability of getting propagation downstream followed by extinction increases with an increase in jet velocity. This, in turn, reduces the ignition probability, Fig. 3.17, as we have seen earlier.

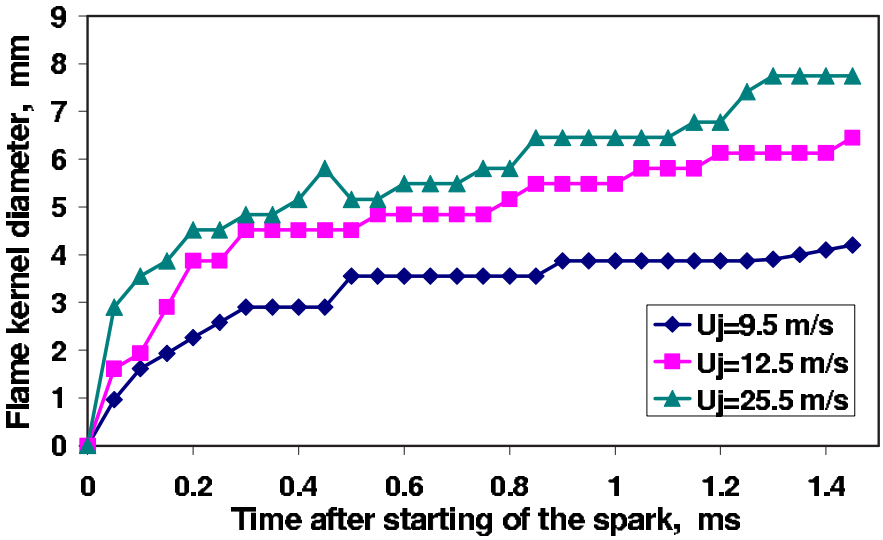

Figure 3.28: Effect of jet velocity on flame kernel growth. Spark: 100 mJ, 400 μs, 1 mm electrode, 1 mm gap, located at $r/d_j = 0$, $z/d_j = 30$. For all $X = 30\%$.

Figure 3.29 shows the effect of spark duration on the flame kernel growth. The step-wise nature of the curves is due to the relatively coarse resolution of the images (0.32 mm per pixel). It can be observed that the highest rate of kernel growth in the first 1 ms is with 500 μs duration. However, after that the growth rate of the 400 μs spark starts increasing rapidly, and it is almost equal to that of 500 μs at 1.4 ms after the spark. This result matches with the result of the ignition probability, Fig. 3.24, at $z/d_j = 30$. As mentioned in Section 3.2.5.3, the effect of spark duration on the ignition probability depends upon the location of the spark relative to the flow field. The present measurements of the rate of kernel growth seem to confirm this conjecture, as the highest rate at $z/d_j = 30$ are with 400 μs and 500 μs duration and the lowest rate is with 600 μs. The results shown in Fig. 3.24 indicate that the highest ignition probability, at $z/d_j = 30$, can be achieved with 400 μs duration and the lowest ignition probability is with 600 μs. As a result, it can be concluded that the spark duration that

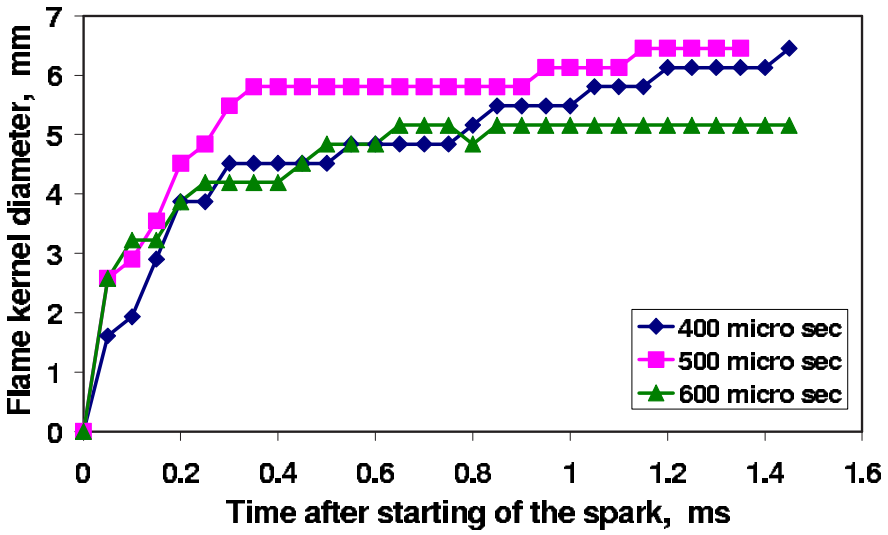

Figure 3.29: Effect of spark duration on flame kernel growth. $U_j = 12.5$ m/s, Spark: 100 mJ, 1 mm electrode, 1 mm gap, located at $r/d_j = 0$, $z/d_j = 30$. For all $X = 30\%$.

gives high ignition probability is the shortest duration if the spark is located at a high velocity field. On the other hand, long duration is more effective to achieve ignition if the spark is applied at a low velocity field.

The rate of flame kernel growth increases with increasing spark energy especially with 300 mJ which gives the highest growth rate, Fig. 3.30. This is considered a well-known result especially in premixed flames (Cho et al., 1992). However, the rate of that increase in kernel growth in the turbulent jet depends upon a number of parameters. For instance, the mixture fraction at the spark location, flame stretch, heat loss, the thermo-chemical state of the gas within the flame kernel and turbulence are perhaps the most important of these parameters. All of these parameters, except turbulence, affect flame growth by directly affecting the laminar flame speed. As the spark energy increases, the temperature of the flame kernel increases, which results in increased laminar flame speed (Cho

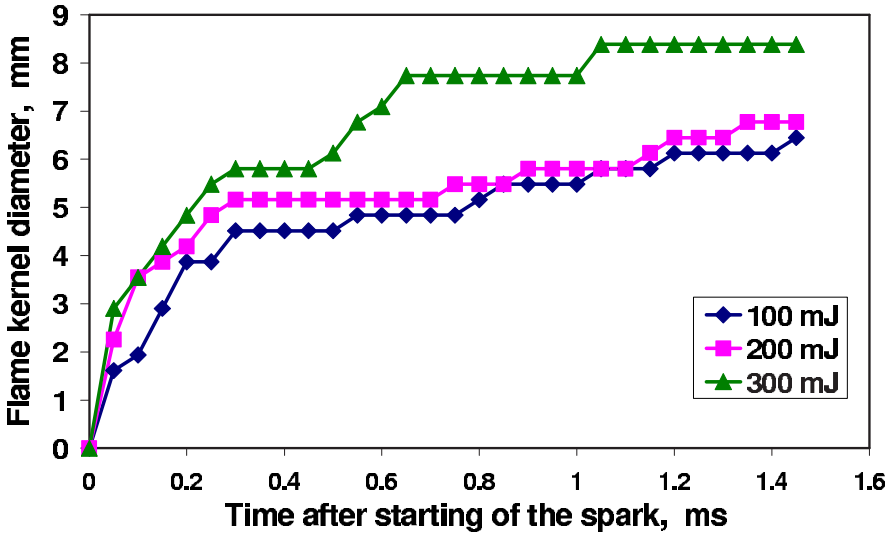

Figure 3.30: Effect of the spark energy on the flame kernel growth. $U_j = 12.5$ m/s, Spark: 500 μs, 1 mm electrode, 1 mm gap, located at $r/d_j = 0$, $z/d_j = 30$. For all $X = 30\%$.

et al., 1992). Therefore, the amount of spark energy affects both the initial size of the flame kernel and its subsequent growth. This is consistent with the results shown in Fig. 3.25, which indicates that the ignition probability increases as the spark energy increases.

The effect of electrode diameter on the rate of the flame kernel growth is shown in Fig. 3.31. The flame kernel grows rapidly with thin electrodes. After 1.2 ms, we can observe that the rate of growth with the 0.5 mm electrodes increases significantly. That is because of the small surface area of the electrodes in which the kernel surface is exposed to, which means low rate of heat transfer, compared to the case of 1 mm diameter electrodes in which the rate of growth is much slower. Again, these results are consistent with the ignition probability results, Fig. 3.26, which emphases more the connection between the growth rate and the ignition probability. The heat loss from the flame kernel affects the flame growth

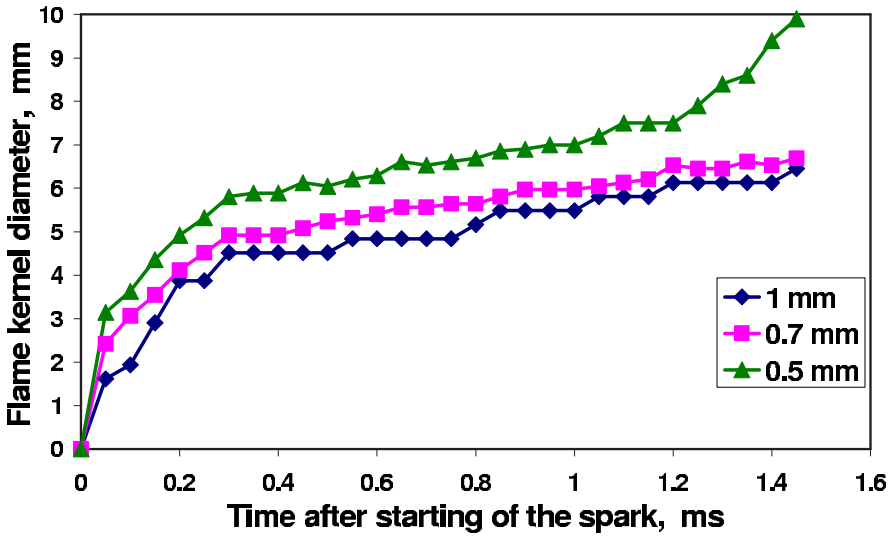

Figure 3.31: Effect of the electrode diameter on the flame kernel growth. U_j = 12.5 m/s, Spark: 100 mJ, 400 μs, 1 mm gap, located at $r/d_j = 0$, $z/d_j = 30$. For all $X = 30\%$.

through two mechanisms: (1) it decreases the kernel temperature, leading to relative contraction of the kernel due to its lower density, and (2) it takes heat out of the flame front, and thereby decreases the burning velocity (Pischinger and Heywood, 1990). It should be mentioned that in the case of 300 mJ spark energy and 0.5 mm electrode diameter, the flame kernel diameter reaches 8.7 and 9.8 mm diameter as spheres, respectively. These diameters are slightly larger than the diameter of the kernel sphere measured inside a combustion bomb with atmospheric propane-air mixtures which is 7 mm diameter at most (Kono et al., 1988), before the flame becomes fully turbulent.

Figure 3.32 shows the relation between the spark gap width and the rate of flame kernel growth. The rate of growth increases with the increase in gap width. However, the kernel diameter of 2 mm and 3 mm gap reaches the same value after 0.6 ms from the moment of the spark. This confirms the results of the ignition

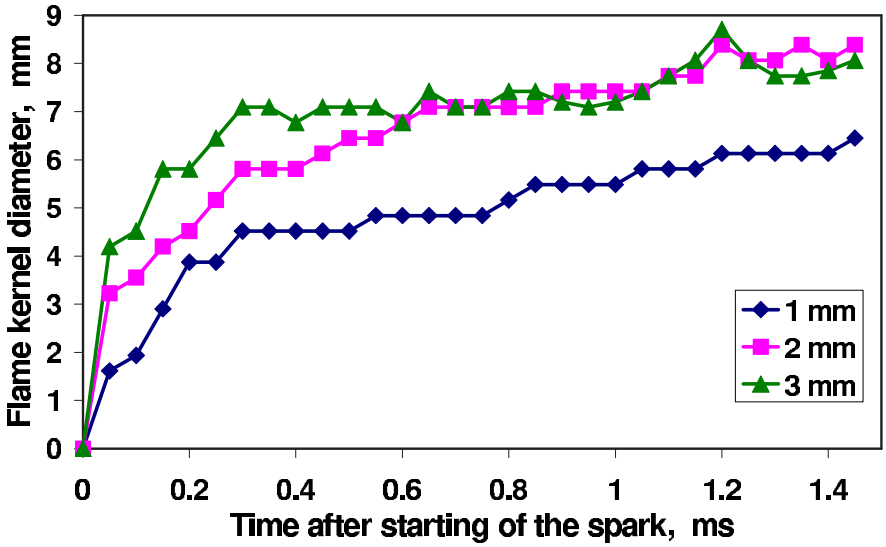

Figure 3.32: Effect of the spark gap width on the flame kernel growth. $U_j = 12.5$ m/s, Spark: 100 mJ, 400 μs, 1 mm electrode, located at $r/d_j = 0$, $z/d_j = 30$. For all $X = 30\%$.

probability which indicate that the highest ignition probability can be achieved with either 2 mm or 3 mm diameter, Fig. 3.27, as the quenching effect reduces with 2 mm gap or more.

The above results show that the spark parameters giving high kernel growth rate are those that also give high ignition probability. The only difference is when the jet velocity increases. In this case, a high velocity implies a high growth rate and a reduced ignition probability.

3.2.7 Flame propagation speed

The average flame position at various instants following successful ignition has been measured by using the high speed camera with 4200 fps and exposure time 238 μs, which is short enough to effectively freeze the relatively slow flame motion at this stage of flame expansion, Section 2.5. The data are important for

quantifying how quickly a turbulent non-premixed edge flame expands and are also aimed for model validation, especially as modern LES methods produce unsteady features of combustion that are not often compared with unsteady flame evolutions from experiment. The spark was applied at $r/d_j = 0$ for two velocities and axial locations. The time evolution of the flame from the moment of spark until the flame stabilized at the lift-off height was measured by the high speed digital camera. Ten movies were captured for each case and the average of the most upstream flame axial position inferred from these movies was plotted against time. At the same time from the spark, these ten different realizations of flame position did not vary by more than 9%, i.e. about a local jet half-width. Figure 3.33 shows the average flame position with time and it is clear that the flame in the high velocity jet needs a longer time to propagate upstream to the stabilization height. The flame needs about 650 ms for $U_j = 25.5$ m/s and 400 ms for $U_j = 12.5$ m/s to reach its lift-off height when the ignition happens at $z/d_j = 40$, while it needs 400 and 300 ms, respectively, to reach the same liftoff height with ignition at $z/d_j = 30$. These timescales correspond to about 10 to 20 flow-through times of the fluid at the centreline (estimated from $\int_0^z dz/\overline{U}$, $\overline{U}$ calculated from Eq. 3.5).

Figure 3.34 shows the time evolution of the downstream and the upstream edges of the flame front for both jet velocities at the higher ignition location ($z/d_j = 40$). This early stage of flame propagation has been visualized in Fig. 3.7. For $U_j = 25.5$ m/s, the downstream edge of the flame front propagates about 6 diameters downstream of the ignition location, and it reaches the peak point after 17 ms from the ignition. Then the flame front starts propagating upstream. However, for $U_j = 12.5$ m/s, the front reaches its peak, 3 diameters downstream of the ignition location, after about 10 ms, and then propagates upstream.

The average flame front position during propagation measured by the fast

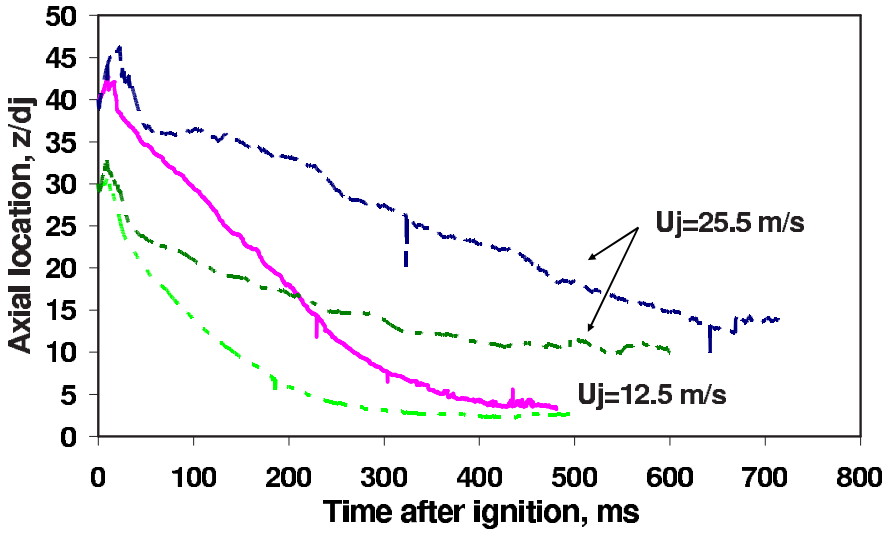

Figure 3.33: Flame position versus time for the indicated U_j and $X = 30\%$. Ignition at $z/d_j = 40$ and 30 along the jet axis. Spark parameters are similar to Fig. 3.6

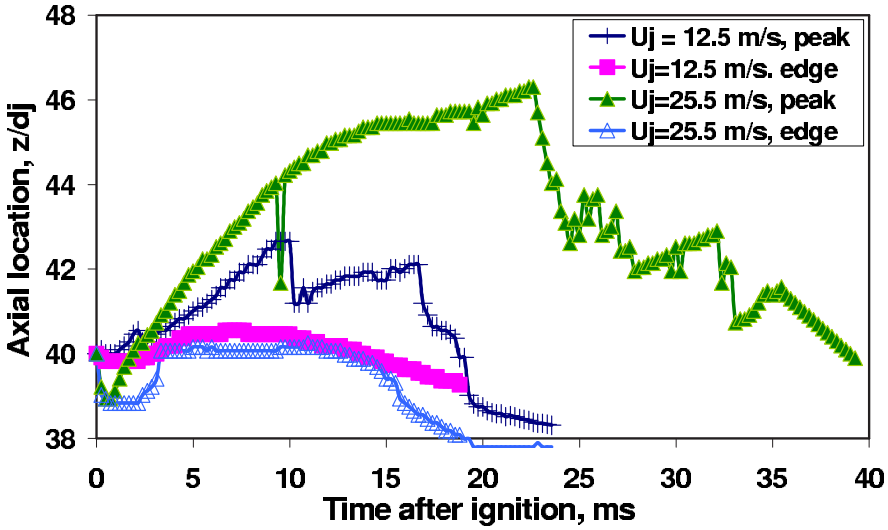

Figure 3.34: Early stage of flame propagation, $X = 30\%$. Ignition at $z/d_j = 40$ along the jet axis. Spark parameters are similar to Fig. 3.6

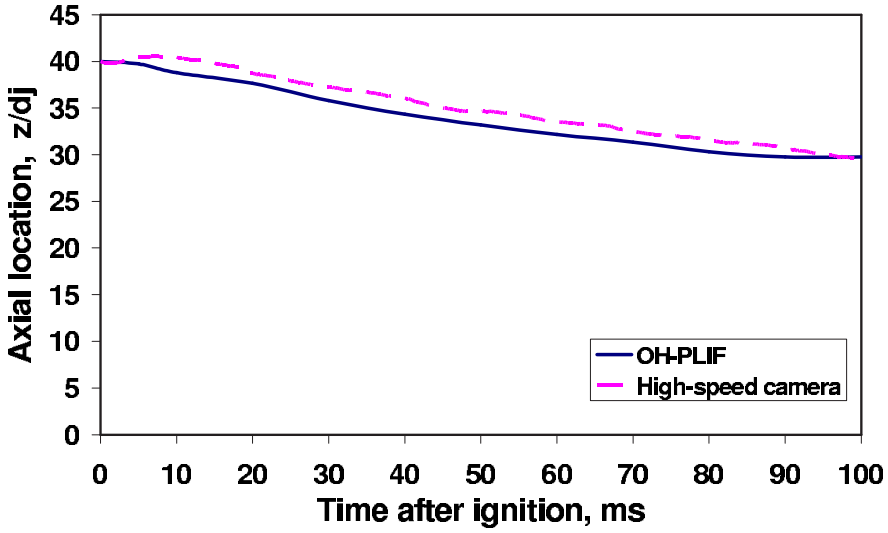

Figure 3.35: Comparison between the average upstream flame front position measured by the fast camera and that measured by using the OH-PLIF images. U_j = 25.5 m/s, X = 30%. Ignition at $z/d_j = 40$ along the jet axis. Spark parameters are similar to Fig. 3.6

camera has been compared to the average edge flame position detected from averaging 100 OH-PLIF images such as those in Fig. 3.11 at the same time instant from the spark. This is shown in Fig. 3.35. It can be observed that the actual flame front position from the OH-PLIF images is very close to that of the line-of-sight imaging measured by the fast camera. This gives credence to using line-of-sight imaging techniques to measure the flame propagation speed in this flame configuration.

The net flame propagation speed with respect to the laboratory coordinates was calculated by differentiating a fifth-order polynomial fit to the curves shown in Fig. 3.33. The results show that, Fig. 3.36, the net flame speed varies significantly with z, as expected by examining the slope of the curves in Fig. 3.33, and that it decreases from about 0.65 to 0.25 m/s as the jet velocity increases from U_j =12.5

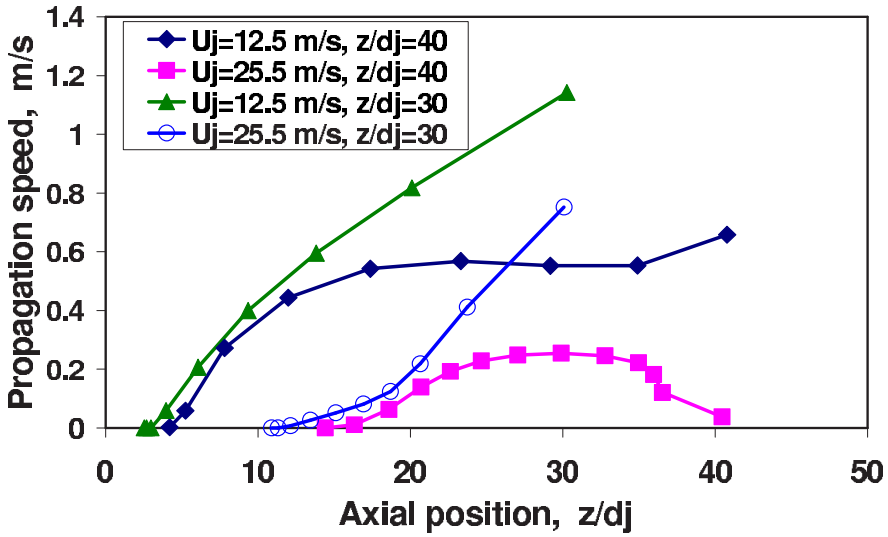

Figure 3.36: Net measured flame propagation speed versus axial position calculated from Fig. 3.33

to 25.5 m/s, if the ignition at z/dj = 40, respectively. On the other hand, it decreases from 1.15 to 0.75 m/s, if the ignition happens at z/dj = 30, respectively. Finally, to calculate the propagation speed relative to the flow, an estimation of the mean flow velocity was performed using Eq. 3.5 at a radius corresponding to the stoichiometric mixture fraction contour estimated by Eq. 3.1, following Terry and Lyons (2005) where an identical procedure was used to discuss the flow speed at the base of stabilized lifted flames. The relative propagation speed was calculated by adding the net propagation speed to the average flow velocity. These results are shown in Fig. 3.37. The relative propagation speed seems to decrease as the flame moves upstream and it increases from 1.5 to 2.5 m/s as the jet velocity increases from U_j = 12.5 to 25.5 m/s, if ignition happens at z/d_j = 40. On the other hand, it increases from 2 to 2.5 m/s, if ignition happens at z/d_j = 30.

The net flame propagation speed reduces with an increase in the jet velocity,

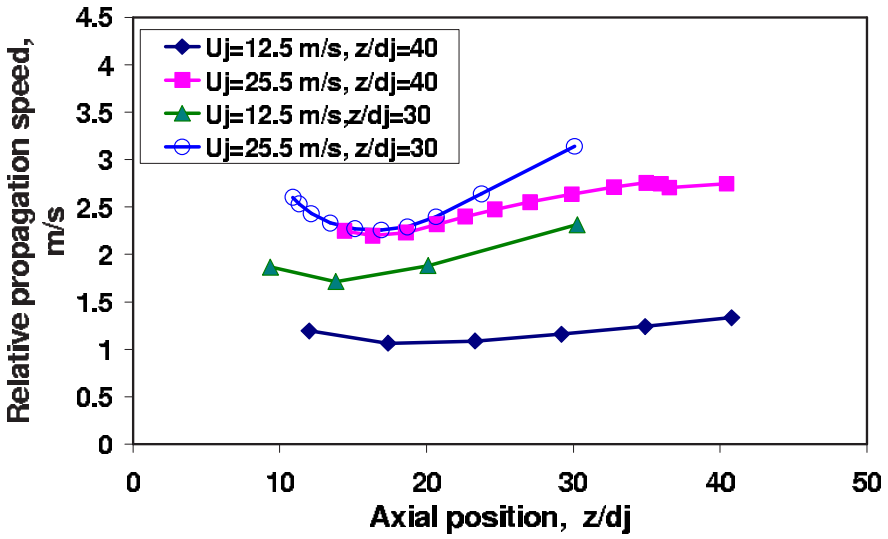

Figure 3.37: Relative flame propagation speed with respect to the flow versus axial position.

as expected, while the relative speed increases with an increase in jet velocity. Both these findings have also been observed in the propagation of laminar jet flames (Ko and Chang, 1999). The relative propagation speed here is between 3 to 6 times the stoichiometric laminar burning velocity of methane ($S_L = 0.4$ m/s), while in the laminar jet flame propagation, an edge flame propagation can reach 2.5 S_L (Qin et al., 2004). Generally, the flame starts propagating fast, but its speed decreases as the flame moves closer to the jet exit. Close to the nozzle, the mixture fraction gradient and the edge flame curvature increase, which results in a reduction in the propagation speed, since the flame front edge loses heat not only by preheating the unburned mixture upstream, but also to both sides in the radial direction according to Ko and Chang (1999), Ruetsch et al. (1995), Muller et al. (1994) and Buckmaster and Matalon (1988). The observed trend that the relative speed increases with U_j (Fig. 3.37) is inconsistent with this explanation. The reason for this is not clear at this stage, but may be related to the uncertainty

in the mean fluid speed to estimate the data in Fig. 3.37 and to curvature effects in the azimuthal direction that may cause locally flame"tongues" to accelerate.

It should be cautioned that the relative propagation speeds presented here are crude estimates with significant room for error due to the curve-fitting involved, the estimate of flame position by estimating the radial location of $\overline{\xi} = \xi_{st}$ (Eq. 3.1), and the estimate of flow velocity at the flame position (Eq. 3.5). Modelling efforts should more properly use the direct measurement of flame location, i.e. Fig. 3.33.

3.2.8 Calibration of OH*/CH* ratio with mixture fraction

In order to correlate the ignition probability results with instantaneous mixture fraction at the moment of the spark, an attempt to calibrate the mixture fraction value with the spark-emission measurements has been done following some recent publications (Aleiferis et al. (2004) and Hardalupas and Orain (2004)). The OH* and CH* have been measured simultaneously at the moment of the spark by using two PMT with OH and CH filters, Section 2.6. The spark gap of 2 mm was placed 5 mm above the jet nozzle, which carries premixed flow of methane and air with different equivalence ratios. About 50 simultaneous measurements for both emissions have been taken for every equivalence ratio covering the range between $\phi = 0.17$ and 3.77, which equals to $\xi = 0.01$ and 0.26. Figure 3.38 shows raw signals for the OH* and CH* at the spark with $\phi = 0.9$. The signals were filtered first before averaging them by using a least-square smoothing filter. In addition, the effect of changing the flow velocity on the signal was examined by changing the jet velocity from $U_j = 0$ to 22 m/s with air only. Figure 3.39 shows that the change in air velocity does not have too much effect on the average OH*/CH* ratio.

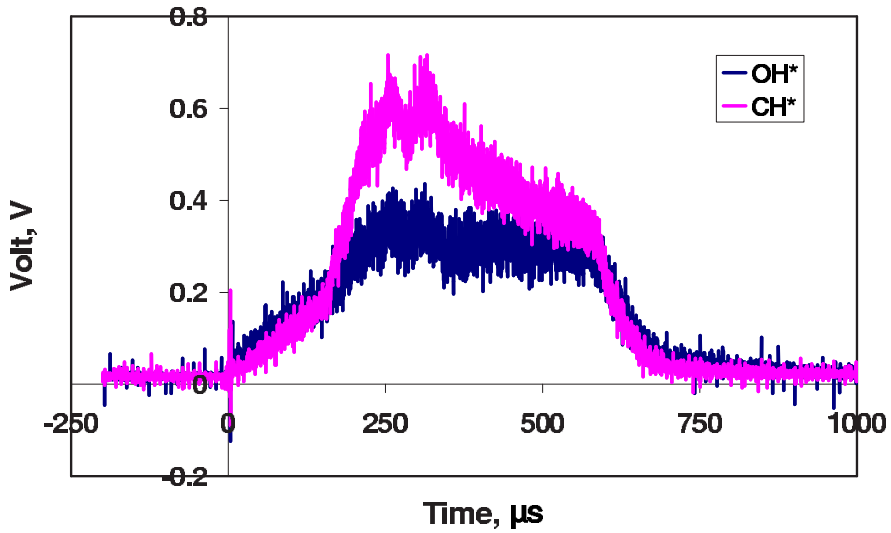

Figure 3.38: Raw signals of OH* and CH* at the moment of spark of a mixture with $\phi = 0.9$, $U_j = 12.5$ m/s. Spark: 300 mJ, 600 μs, 1 mm electrode and 2 mm gap.

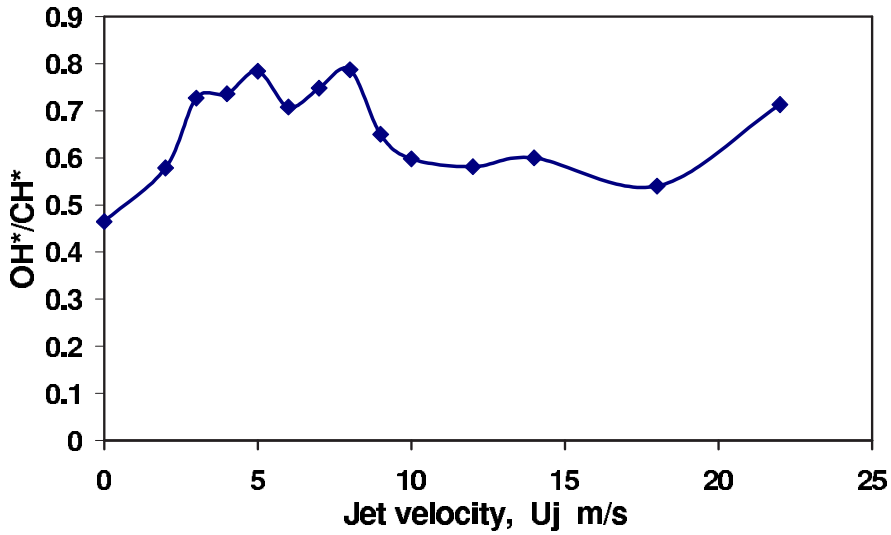

Figure 3.39: Effect of changing the flow velocity on the average OH*/CH* signal at the moment of spark of air jet, $\phi = 0.9$. Spark parameters are similar to Fig. 3.38.

Figure 3.40 shows two calibrations of the OH*/CH* ratio with the mixture fraction. It can be observed that for the region between $\xi = 0.07$ and 0.26 the calibration is monotonic. However, if the whole range of ξ is included, the calibration becomes non-monotonic, as the ratio of OH*/CH* increases with ξ up to 0.07, but it decreases with any further increase in ξ. In fact, these results have not been observed before because the range of calibration of Aleiferis et al. (2004) was relatively narrow between $\phi = 0.7$ and 1.3, which is monotonic. However, in the present work the whole range of calibration is needed in order to correlate the successful and failed ignition events with the instantaneous mixture fraction value. Therefore, the experiments were stopped at this point. However, according to Fansler et al. (2002), this calibration can be monotonic with the whole range of ϕ if CN* was calibrated with ϕ rather than OH* or CH*. Unfortunately, due to the lack of time and equipment, this calibration has not been done. However, it can be considered in future research.

3.3 Conclusions

Spark ignition and subsequent flame propagation in non-premixed turbulent jets at various velocities and air premixedness have been investigated experimentally. The following conclusions can be made:

- The ignitable region of the jet, defined as the locus of points where a spark can result in a full flame establishment, was wider than the estimated region between the mean mixture fraction contours corresponding to the lean and rich flammability limits in the radial direction and lies upstream of the rich limit contour in the axial direction.

- The ignition probability decreased sharply to zero downstream of the mean stoichiometric contour. The region of high probability of successful ignition was

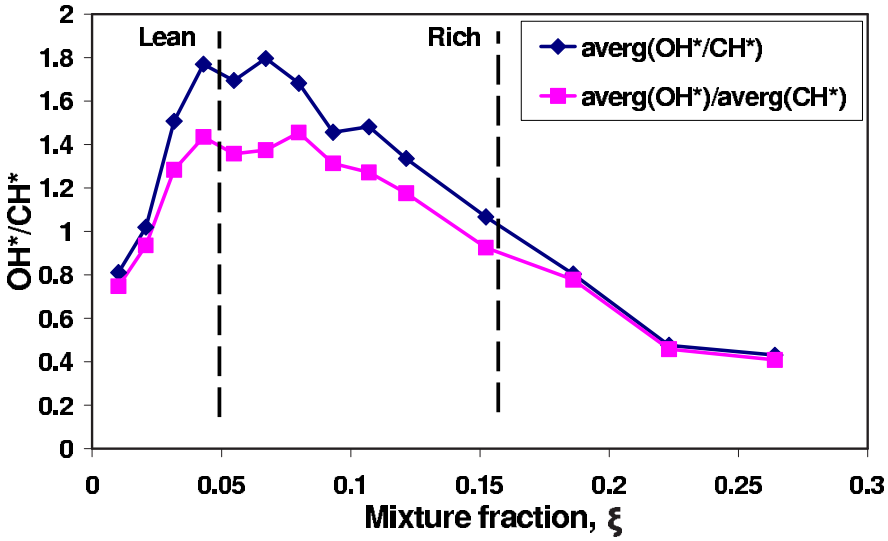

Figure 3.40: Calibration of OH*/CH* ratio with the mixture fraction by two different ways. Dashed lines indicate ξ_{rich} and ξ_{lean} of the jet with $X = 30\%$. Spark parameters are similar to Fig. 3.38

smaller with an increase in jet velocity.

- Simultaneous measurements of local velocity at approximately the spark location and of ignition success showed that failed sparks were statistically associated with high local velocities.

- The ignition probability decreased with increasing air volume fraction in the fuel stream.

- The ignition probability improved with an increase in spark energy. Short spark duration is more effective along the jet centerline, while long duration gives the highest probability in off-axis locations.

- The effects of the other spark parameters (electrode diameter and spark gap) on ignition of the present non-premixed flame are in full agreement with the trends from ignition of premixed mixtures. The ignition probability increases with thinner electrodes and with wider gaps.

- The early flame kernel growth rate has been measured with different flow and spark parameters. The results show that higher growth rate correlated with higher ignition probability for all parameters studied, except for jet velocity. For high jet velocities, the initial kernel may grow quickly, but the ignition probability clearly decreases.

- The flame front following the ignition has a spherical shape initially, but quickly became an edge flame with a front that propagated upstream until it the flame stabilized at a certain lift-off height.

- The lift-off height after the ignition was always equal to the lift-off height of the decreasing velocity branch of the height-velocity hysteresis loop of jet lifted flames.

- The average edge flame front location has been measured as a function of time from the spark using line-of-sight images and OH-PLIF and both techniques gave very similar results. From these measurements, a net propagation speed was calculated and then, using estimates of the mean flow velocity at the stoichiometric contour, a mean flame speed relative to the flow was estimated to lie between 3 to 6 times the laminar burning velocity, increasing with an increase in jet velocity.

- The calibration of OH*/CH* ratio with the mixture fraction at the moment of the spark is non-monotonic over the whole range of interest of the mixture fraction and the calibration of CN* with the mixture fraction is recommended for the future research.

- The data provide a useful validation set for unsteady turbulent combustion models.

Chapter 4

Counter-flow Flames

This chapter presents the experimental investigation of spark ignition of turbulent counter-flow flames. Most of the experiments have been carried out on non-premixed flames, while a few experiments on premixed flames have also been performed. The chapter starts with a literature review about the flow structure and the extinction characteristics of non-premixed counter-flow flames. The review includes also the edge-flame propagation behavior in this flow configuration. In Section 4.2, the results of these experiments, which include mixture fraction data, visualization and measurements of flame structure and spreading and ignition probability, are presented and discussed. The chapter ends with conclusions.

4.1 Literature Review

4.1.1 Introduction

The counter-flow configuration is an engineering field that pertains to the research, development and design of many practical systems demanding a dynamic mixing of two or several jet flows. Among these systems, the system may be a side dump combustor of a vertical short takeoff and landing aircraft and the

environment control system of a civilian aircraft (Stan and Johnson, 2001). In the counter-flow, sometimes called opposed-jet, a fuel or a mixture jet impinges on a counter-flowing oxidizer or a mixture stream. The reactants mix in a thin layer close to the stagnation plane and burn. The reaction can be regarded as a combination of four nonlinear, coupled, spatially and temporally distribution processes: convection, stretching, diffusion and pressure interaction (Geyer et al., 2005). The opposed-jet geometry is compact, has well-controlled boundaries, and is rotationally symmetric. Overall, it is a simple, but district configuration that allows efficient testing of important flow parameters like strain rate, for instance, in terms of its effect on ignition.

No experimental data are available on the effect of strain on the success of ignition in non-premixed flames, which may possibly reduce the ignition probability. A numerical analysis of laminar counterflow non-premixed flames with one-step chemistry showed that the location of the spark relative to the mixing layer is important and that there exists a critical Damköhler number above which, even if the stoichiometric mixture is sparked, no flame results (Rashkovsky, 1999). These findings have been reproduced with simulations with detailed chemistry and it was found that the highest strain rate for ignition could be lower than the extinction strain rate (Richardson and Mastorakos, 2007). More experiments on spark ignition of turbulent non-premixed counter-flow flames would help our understanding of the effect of such fluid mechanics parameters on the success of ignition.

4.1.2 Flow field

The flow field of the turbulent counter-flow configuration was subjected to many investigations to measure the velocity, turbulence intensity and strain rate in the inert flow. In addition, the mixture fraction distribution, in case of non-

premixed counter-flow, was also studied. Some of these investigations were done experimentally by Cho et al. (1988), Kostiuk et al. (1989), Rolon et al. (1991), Kostiuk et al. (1993b), Mastorakos (1993), Sardi et al. (1998), Seiser et al. (2000), Kitajima et al. (2000) and Lindstedt et al. (2005), and also theoretically by Smooke et al. (1986), Bray et al. (1991) and Tanoff et al. (1996).

Mastorakos (1993) measured the mean and r.m.s. of the axial and radial velocity in addition to the mixture fraction in the inert flow of turbulent non-premixed counter-flow burner with methane as a fuel and nitrogen co-flow. This burner has exactly the same dimensions and flow conditions like those of the burner used in the present work. He found that the turbulent fluctuations, u' , and the integral lengthscale, L_{turb}, at the exit of the nozzles are uniform across the pipe and approximately $u'/U_b = 10\%$ and 3 mm respectively. For the jet spacing of 25 mm ($H = 2R$), the axial velocity profile across the jet exits is not distorted by the opposing flow and hence remains approximately top-hat. In addition, the bulk velocity gradient (bulk strain rate S_b) is not far from the value estimated by the potential flow model, i.e. $2U_b/H$. At the stagnation region, u'/U_b increases to about 40% and the radial fluctuations v'/U_b to about 20%, while a measurement of the two-point correlation of the temperature (i.e. with combustion) in the radial direction at the stagnation plane gave a radial lengthscale of about 7 mm due to the elongation of the eddies by the mean strain. For $r < 10$ mm, the scalar distributions are indistinguishable from those at the centreline, which suggests that dilution by the co-flow is not evident up to this radius (Mastorakos, 1993).

Kostiuk et al. (1993b) reported that LDV measurements show that small differences in the momenta of the two jets caused the mean location of the stagnation plane to differ from the mid-point between the nozzles by up to $0.15D$. Korusoy and Whitelaw (2001) showed that the velocity profile at the nozzle exit with smaller nozzle separations became increasingly non-uniform as the separation was

reduced below $0.4D$, with a minimum at the axis and peaks at the nozzle rim. They found that the static pressure between the nozzles and the radial velocity at the stagnation plane beyond the nozzle rim was shown to increase with reduction in nozzle separation. The peak in exit velocity produced a non-uniform distribution of strain rate at the stagnation plane with a dark ring signifying local extinction of a methane flame at the location of the peak stain rate.

Lindstedt et al. (2005) used the Particle Image Velocimetry (PIV) technique to measure the velocity and strain rate in an isothermal turbulent counter-flow. They concluded that for small separation (H $< 0.5D$) the axial and radial strain rates cannot be represented in terms of the bulk velocity, that the highest strain rates exist away from the stagnation plane and the instantaneous values can be very large. Figure 4.1 shows the effect of decreasing jet separation on the mean radial strain rate. It should be noted that the nozzle separation in the present work is $1D$, which indicates that the strain rate is uniform along the stagnation plane.

Sardi et al. (1998) measured the mixture fraction distribution in turbulent non-premixed inert counter-flow. They showed that the distribution of the mean mixture fraction and its fluctuations, and hence the mean thickness of the mixing layer between the fuel and air streams, were independent of the bulk velocity. The probability distribution of the mixture fraction fluctuations was bimodal at the stagnation plane, consistent with the fact that the residence time, $t_{res} = 1/S_b$, in the mixing layer was short in comparison to the eddy turn-over time, $t_{ov} = L_{turb}/u'$ (Sardi et al., 1998). In addition, they observed at the boundaries of the mixing layer simultaneous occurrence of the largest values of scalar dissipation and the largest values of the mixture fraction fluctuations. However, at the stagnation plane, the largest values of scalar dissipation were associated with small values of the mixture fraction fluctuations.

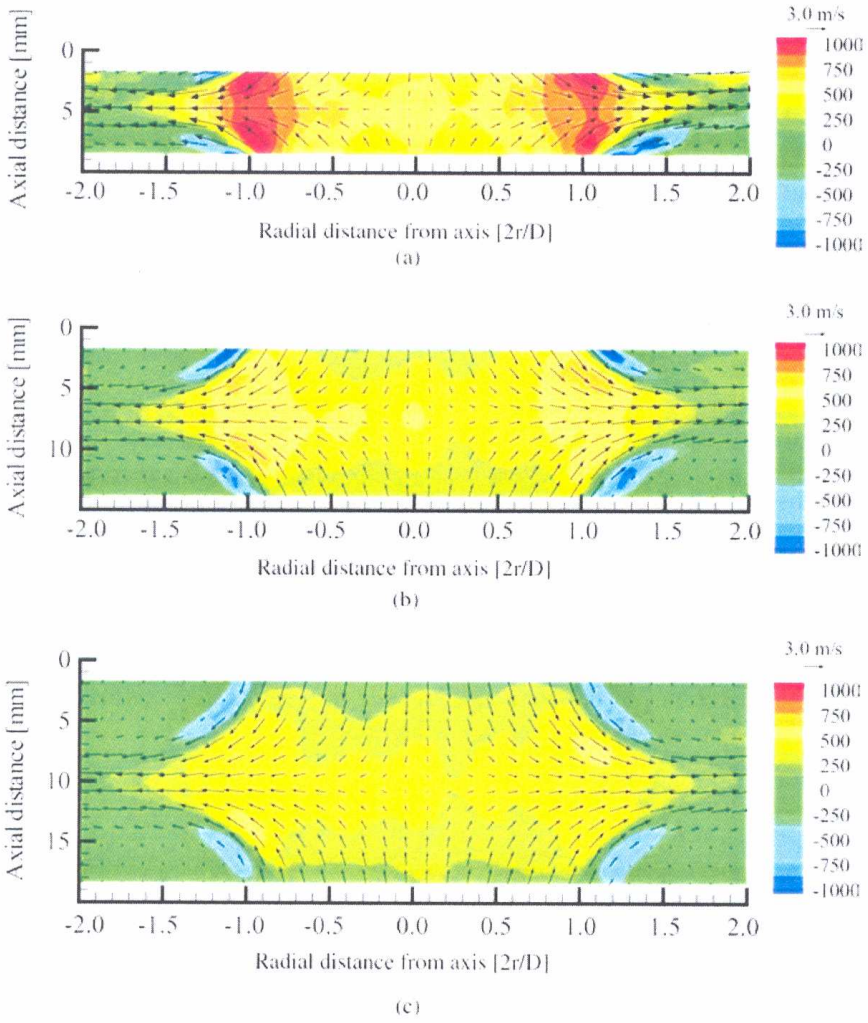

Figure 4.1: Contours of mean radial strain rate with velocity vectors with a bulk velocity of $U_b = 3$ m/s and increasing nozzle separation. $H/D =$ (a) 0.4, (b) 0.6 and (c) 0.8. Reproduced from Lindstedt et al. (2005).

4.1.3 Extinction limits

Extinction of turbulent non-premixed flames is particulary important and is directly related to control of the non-premixed combustion in a practical combustor. The extinction of turbulent counter-flow flames has been studied in only in a few cases. The experimental studies were done by Mastorakos et al. (1992a), Kostiuk et al. (1993a), Tsuji et al. (1994), Kitajima et al. (1996), Kitajima et al. (2004) and Seiser and Seshardi (2005), and the theoretical ones by Mastorakos et al. (1992b) and Kim and Mastorakos (2006). In addition, Chelliah et al. (1990) and Puri and Seshadri (1986) studied the extinction of laminar counter-flow flames.

Mastorakos et al. (1992a) reported that the velocity at the extinction increases with nozzle separation and with initial air premixedness in the fuel stream. They observed that the velocity at extinction increases by a factor of 1.8 with the increase of X (air volume fraction in the fuel stream) from zero to 0.8. In addition, it was noted that the higher strain rates due to higher turbulence lead to flame extinction. Therefore, both the bulk flow stretch rate exerted by the mean flow and turbulent stretch rate exerted by small eddies of Kolmogorov scale lead to extinction of turbulent counterflow diffusion flames. Moreover, small-scale eddies of Kolmogorov scale are much more effective than large-scale eddies in the local extinction, and the chemical reaction that occurs in molecular scale is not affected by the small eddies of the Kolmogorov scale (Tsuji et al., 1994). Mastorakos et al. (1992a) mentioned also that the appropriate quantity to describe diffusion flame extinction is the scalar dissipation rate, rather than strain rate. It was found that extinction occurred at a critical value of the scalar dissipation rate at stoichiometric mixture fraction that increased with partially premixing.

Kitajima et al. (1996) mentioned that the extinction limits of methane-air turbulent non-premixed flames are influenced mainly by the turbulence of the air stream rather than that of the fuel stream. This behavior of the extinction can

be explained in relation to flame location, as the stoichiometric mixture fraction is 0.055 and hence the flame is in the air side of the stagnation plane. Thus, it is natural that the extinction limits are affected mainly by the air stream. In addition, Kitajima et al. (1996) observed that the flame stretch caused by the curvature of flamelet plays a more important role on the flame extinction than that caused by small-scale turbulence. The order of the stretch rate caused by the curvature of flamelet was estimated as:

$$K_t = \frac{2V_{fl}}{R_{fl}} \tag{4.1}$$

Here,V_{fl} is the flow velocity at the boundary of the flamelet and R_{fl} is the radius of curvature of the flamelet. Kitajima et al. (2004) found that extinction is more sensitive to change in the mass fraction of oxygen in the oxidizer stream rather than that of the fuel in the fuel stream because of the stoichiometric fuel-to-mass ratio of the CH_4-O_2 reaction system.

In their modelling work, Mastorakos et al. (1992b) reported that extinction occurs at a critical value of the mean scalar dissipation rate for the whole spectrum of partial premixing up to the rich flammability limit for premixed flame propagation and this critical value increases from about 2 to 17 s^{-1} from the pure diffusion to flame partially premixed with air 80% by volume. It is clear from the previous review that these parameters, which can cause extinction, can affect the success of ignition, as the flame kernel after ignition will not be able to propagate and stabilize. Therefore, the present work investigates the successful ignition in a high-staining flow close to the extinction strain rate.

4.1.4 Edge flame propagation

Flame propagation is very important part in order for the ignition to be successful. In a high-strained non-premixed flow, the flame propagates as an edge flame.

The behavior and speed of this propagation are currently of increasing interest. The laminar edge flame has been observed experimentally by Law et al. (1986), Vedrarajan and Buckmaster (1998), Shay and Ronney (1998), Liu and Ronney (1999), Santoro and Liñán (2000), Takagi et al. (2002), Amantini et al. (2005), Carnell-Jr and Renfro (2005) and Seiser et al. (2005), and studied theoretically by Buckmaster (1996), Vedarajan et al. (1998), Favier and Vervich (2001) and Frouzakis et al. (2002).

The first definition of the edge flame was mentioned by Buckmaster and his collaborators. Vedrarajan and Buckmaster (1998) said that an edge flame is the propagating structure in the neighborhood of a flame-sheet edge and its local structure is neither a diffusion flame nor a premixed flame, but is hybrid in nature. This edge will move as a reactive-diffusive wave with a well-defined speed that is controlled by the Damköhler number Da (i.e., proportional to the rate of strain). Buckmaster (1996) predicted that the ratio of Da at the flame edge to the extinction Da for a uniformly strained flame is given by $\beta(1-\varepsilon)/e^2$, where $e = 2.718$, $\varepsilon = T_0/T^*$, T_0 is the ambient temperature and T^* is the flame front temperature, and $\beta = E/RT^*$ is the nondimensional activation energy, E is the activation energy and R is the gas constant. Thus, the ratio of the maximum possible strain rate of the edge flame, S_{edge}, to the extinction strain rate of the non-premixed flame, S_{ext}, is

$$\frac{S_{edge}}{S_{ext}} = \frac{e^2}{\beta(1-\varepsilon)} \tag{4.2}$$

Since practical values of β and ε are typically 10-20 and 0.15-0.2, respectively, S_{edge}/S_{ext} is typically only slightly less than unity and thus edge flames are expected to be only moderately weaker than uniformly strained flames. One physical explanation of this prediction is that the additional heat losses that occur from the flame edge to the unburned gases in the direction parallel to the flame sheet causes this ratio to be less than one (Buckmaster, 1996).

Shay and Ronney (1998) examined the previous prediction experimentally in laminar non-premixed flames in nonuniformly strained flows. It was found that the strain rate at the flame edge is lower for nonuniformly strained flame than the extinction strain rate of uniformly strained flame having the same reactants. The ratio between them varies experimentally from about 0.65 to 1. Moreover, Liu and Ronney (1999) showed that the previous prediction applies for the premixed flames as well. They found experimentally that the ratio between the two strain rates is 0.93 for single premixed counter-flow flames and 0.49 for twin premixed flames.

Santoro and Liñán (2000) reported that HCHO-PLIF images of the edge flames showed tribrachial structure for standing triple flames at large Da and simple edge flames at moderate Da. They also observed that the dependence of the nondimensional edge flame velocity on the Da is monotonically increasing and reaches a value of approximate 2.6. This value should be of the same order as the square root of the density ratio between the unburned mixture and burned gas.

Amantini et al. (2005) studied the behavior of an edge flame undergoing a transition from extinction mode to traveling propagation mode. Under conditions of local extinction, the displacement velocity is of order of laminar flame speed. Farther away from the stagnation point, the tangential velocity increases dramatically and overwhelms the front propagation velocity, sweeping it along. Eventually, as the scalar dissipation rate decreases in the direction tangential to the mixing layer, the Da increases and the extinction edge turns into a propagation edge flame. Amantini et al. (2005) also mentioned that no evidence of a negative propagation velocity was found and the propagation velocity of the edge flame is of order of the stoichiometric laminar flame speed.

In the present work, some attention has been given to the edge flame struc-

ture following the spark during propagation in turbulent opposed-jet flames in terms of visualizing the flame front at different time delays from the spark. In addition, the measurements of the radial and axial scatter of the edge flame front position during propagation were performed in addition to a rough estimation of the propagation speed. Finally, the ratio of the maximum strain rate that the ignition can be successful to the extinction strain rate has been measured and compared to Buckmaster's prediction (Buckmaster, 1996).

4.1.5 Summary

From the previous review, the following points can be summarized: (1) Since the present burner has exactly the same dimensions and flow conditions like those of Mastorakos (1993), his velocity and turbulence measurements can help in interpreting the present results. (2) The nozzle separation in the present work was $H = 1D$. Hence, it can be expected that the distribution of the strain rate is uniform along the stagnation plane. (3) For $r < 10$ mm, the mixture fraction distributions are indistinguishable from those at the centreline. (4) The partial premixed flames have high resistance to extinction. (5) The maximum strain rate that the edge flame can sustain is lower than the extinction strain rate of the stable flame and (6) at high scalar dissipation rate, the triple flame becomes an edge flame.

4.2 Results and Discussion

4.2.1 Introduction

In this section the results are presented and discussed. Mixture fraction measurements are shown first with a comparison between the pdf of the measured mixture

fraction and the β-function presumed shape. Visualization of ignition events with high-speed camera for both premixed and non-premixed flames is then presented. OH-PLIF images show the structure of the flame front of both types during the propagation and the analysis of such images has been used to measure the radial and axial scatter of the flame front position during propagation. The flame propagation speed was roughly estimated. The ignition probability results and discussion are presented for different cases of premixed and non-premixed flames. Finally, the chapter ends with a comparison between the maximum strain rate at ignition and the extinction strain rate.

4.2.2 Mixing field

The mixture fraction has been measured by Planar Laser Induced Fluorescence (PLIF) of acetone seeded in the fuel stream. An area of 25×75 mm was imaged with a projected pixel resolution of about 55 μm. Instantaneous $2D$ contours of the mixture fraction, ξ, were obtained by normalizing the individual PLIF images using the signal at the fuel-stream exit (i.e. the lower burner in Fig. 4.2). The scalar dissipation rate, χ, ($\chi = 2D_{mol}(\nabla\xi)^2$) was also evaluated in the two imaged dimensions. The diffusivity of acetone in air was taken as D_{mol}=1.04×10^5 m^2/s. About 1000 instantaneous images were processed individually and then averaged to obtain the mean, $\bar{\xi}$, and the r.m.s., σ, of the mixture fraction and the mean scalar dissipation, $\bar{\chi}$. The probability density function of ξ was also determined and compared with the β-function presumed shape.

The mixing in the turbulent counterflow has been measured previously with point and line techniques (Mastorakos (1993) and Geyer et al. (2005)) and two-dimensional data are reported here that supplement and confirm previous findings. Figure 4.2 shows a raw PLIF image and the corresponding instantaneous mixture fraction contour. It is evident that mixing occurs across a thin interface

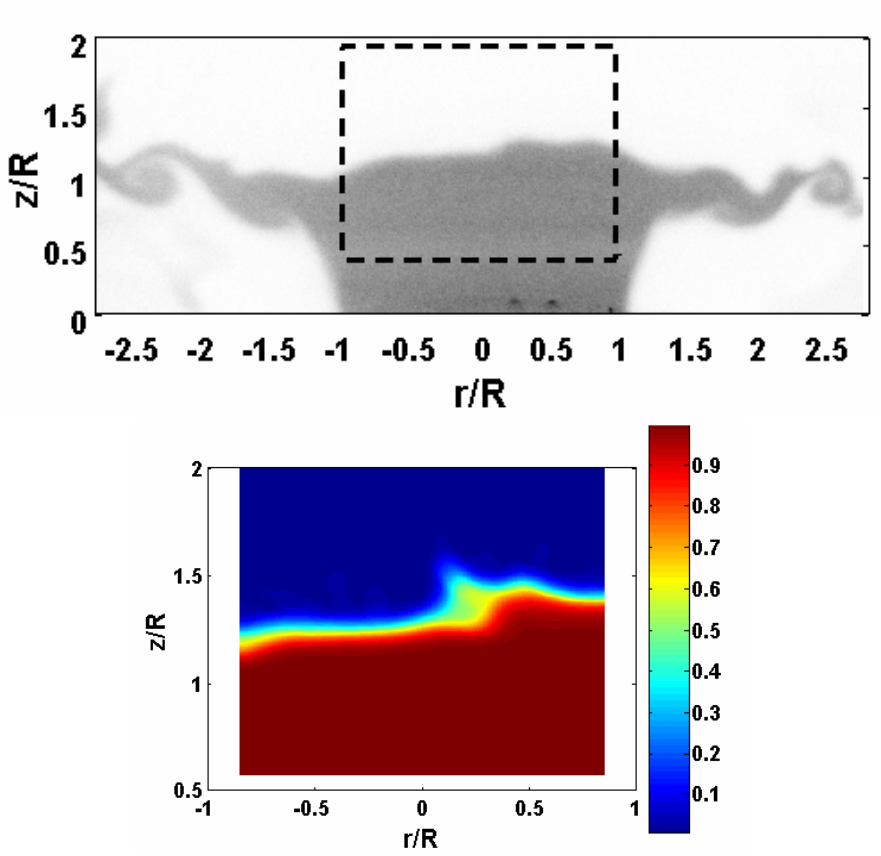

Figure 4.2: Typical raw instantaneous acetone PLIF image showing the region of interest and the corresponding mixture fraction image $U_b = 2$ m/s.

between the upper and lower streams that is about 1 mm thick, which seems to undulate due to the turbulence. It is also evident that mixing occurs between the jet and the co-flow, but these locations are not of interest here because we concentrate on the region up to about a pipe radius. Due to the "flapping" of the fuel-air interface, the mean mixture fraction decreases from unity to zero over a wide region with thickness about 10 mm (Fig. 4.3). The r.m.s. of the mixture fraction peaks at around 0.4 at the center of the layer, decreasing on either side of the stagnation plane.

Figure 4.3b shows typical PDFs of the mixture fraction, $P(\xi)$. It is evident that $P(\xi)$ is bimodal, with peaks at 0 and 1 and with small contributions from intermediate values, consistent with the view that mixing in this flow is understood by the random axial motion of a thin interface (Geyer et al., 2005). The shape of the PDF is captured very well with the β-function presumed shape. This suggests that the mean and r.m.s. data of Fig. 4.3a can lead to a calculation of the flammability factor from Eq. 3.3 using a presumed shape, without resorting to the more noisy measured PDF. Finally, the mean, variance, and $P(\xi)$ have been found to depend only on axial distance, at least for $r < R$, and they do not depend on the jet velocity, consistent with previous work (Mastorakos, 1993). Hence, the flammability factor F depends only on z and not on U_b.

4.2.3 Visualization of ignition and flame propagation

4.2.3.1 Direct visualization

When a spark is applied, either a successful ignition or failed ignition can be observed. The successful ignition results in a stable flame. However, the failed ignition in this flow can be in three forms: a spark without flame kernel initiation, a spark followed by flame propagation downstream and extinction, or a spark followed by flame propagation and a stable flame for few milliseconds then blows

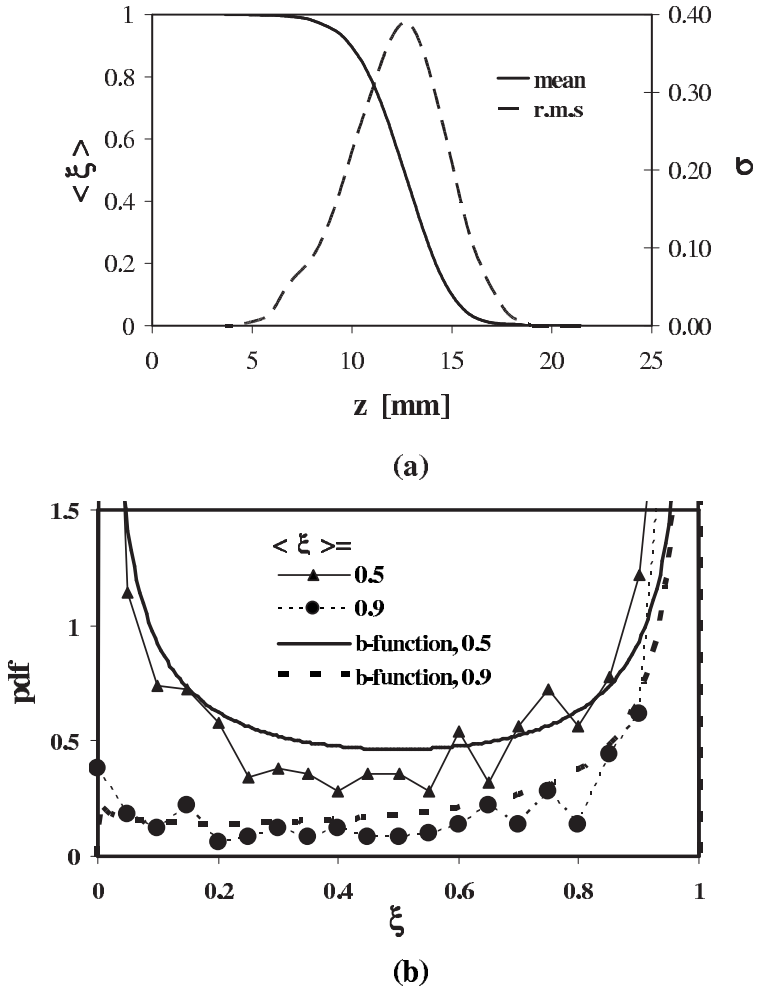

Figure 4.3: (a) Mean and r.m.s. of the mixture fraction along the centreline. (b) The pdfs of the mixture fraction at $\langle\xi\rangle = 0.5$ and 0.9 and comparison with the β-function model. $U_b = 2$ m/s.

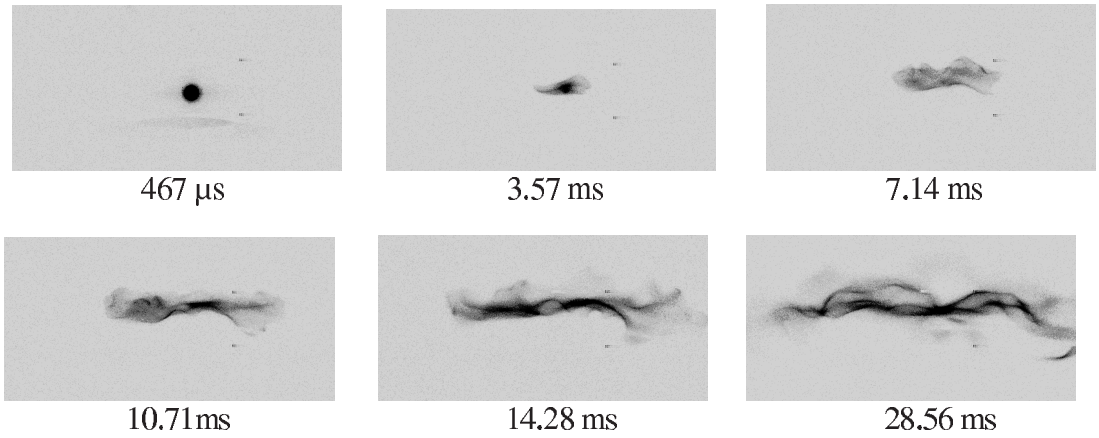

Figure 4.4: Instantaneous high-speed camera images of the non-premixed flame during propagation at different times after the ignition with 8100 fps and exposure time 113 μs. Spark applied at axis and halfway between the jet nozzles (center of the image). Fuel from below, air from above. U_b = 2 m/s, X = 80%. The images shown correspond to a region about 50×25 mm.

off. It should be mentioned that the last type of failed ignition has not been noted in the spark ignition of turbulent jets (Section 3.2.3.1), but has been noted rarely in the bluff-body flames (Section 5.2.5.1). Such events have not been considered as a successful ignition in determining the ignition probability.

A spherical kernel of about 3 mm diameter is visible when the spark ends. This kernel diameter seems to vary little with location of the spark and with flow speed. In successful ignitions, this kernel decays quickly to form a flame sheet that expands in the radial direction to fill the whole stagnation region. Figure 4.4 shows instantaneous high-speed camera images of a successful ignition event with the spark at the axis and halfway between the jets, i.e. presumably at the stagnation point (in the mean). It should be noted that the spark used in this ignition event is a single spark.

Figure 4.5 shows instantaneous high-speed camera images of the second type

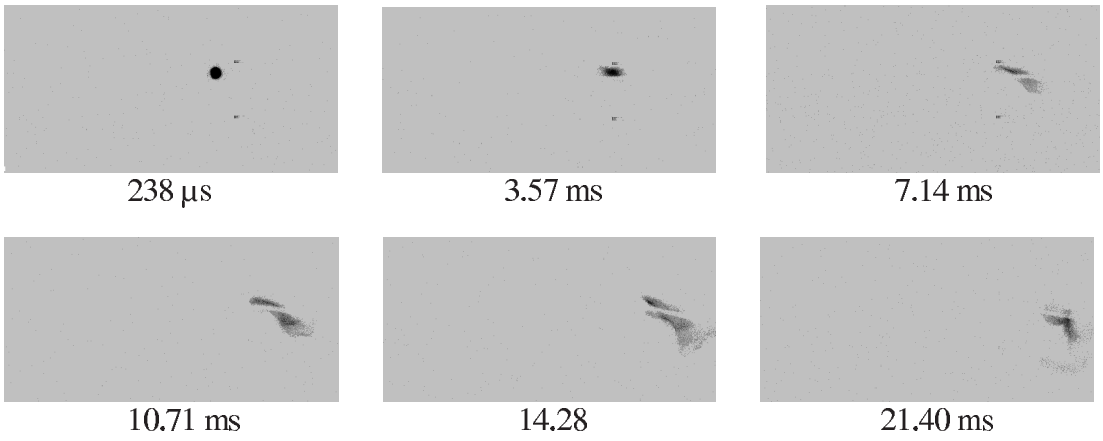

Figure 4.5: Instantaneous high-speed camera images of the second type of failed ignition. Spark applied at $r = 9$, $z = 12.5$ mm. Flow conditions and image domain are identical to Fig. 4.4.

of failed ignition. The flame after ignition propagates downstream without propagating against the flow direction to stabilize the flame. The reason behind that could be related to the high radial velocity as the spark moves radially from the stagnation point. Therefore, the flame can not propagate against the flow as the flame speed is less than the local flow velocity.

The third type of failed ignition is visualized in Fig. 4.6. The flame after the spark propagates to fill the stagnation plane. However, after a few milliseconds the flame brush breaks from the middle and the whole flame blows-out of the image domain or quenches. It should be mentioned that this type of failed ignition is common when the flame is ignited at a velocity close to the extinction velocity. This can suggest that the reason behind this type of failed ignition could be that the propagation may not have resulted in a fully continous flame sheet and the holes left in the flame sheet can become extinction waves, as seen in laminar flames by Chelliah et al. (1990) and turbulent flames by Pantano (2004).

Figure 4.7 shows a successful ignition event of a premixed flame. In this case,

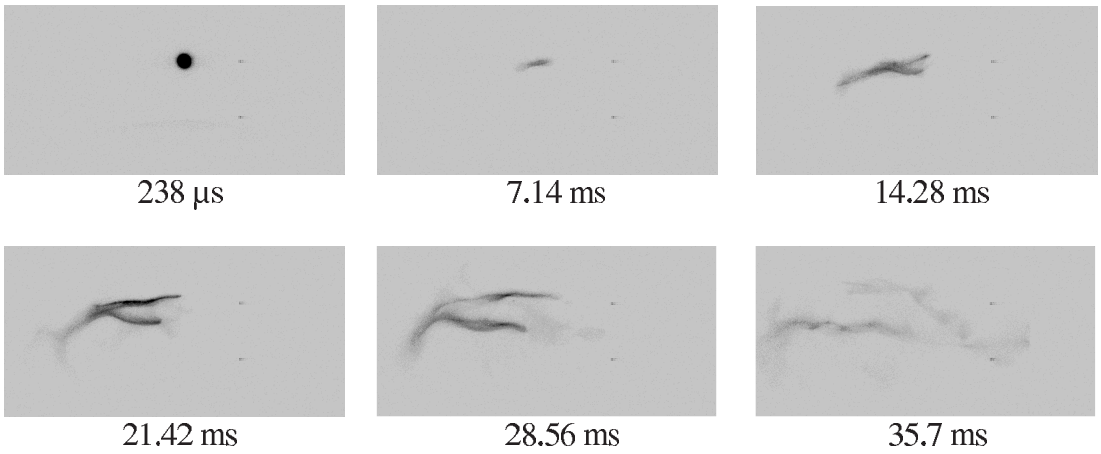

Figure 4.6: Instantaneous high-speed camera images of the third type of failed ignition. Spark applied at $r = 0$, $z = 16$ mm. Flow conditions and image domain are identical to Fig. 4.4.

the fuel-air mixture is the lower stream and the air is the upper stream is with an equivalence ratio of 0.8. In this ignition event, high frequency spark (50 Hz) produced form an AC-DC transformer is used and the spark is so far away from the stagnation plane that the probability of finding a flammable mixture there is zero. It can be observed that the flame is initiated away from the spark location and propagates to establish the whole flame. This is attributed to the fact that the flow can convect the heat of the spark towards the stagnation region, where the chances of finding flammable mixture are finite. Hence, a flame may be initiated by a non-local spark. A similar effect has been observed in non-premixed flame ignition.

4.2.3.2 OH-PLIF

PLIF of OH has been used to investigate the flame front structure after the ignition during propagation from the spark location until the stabilization of the

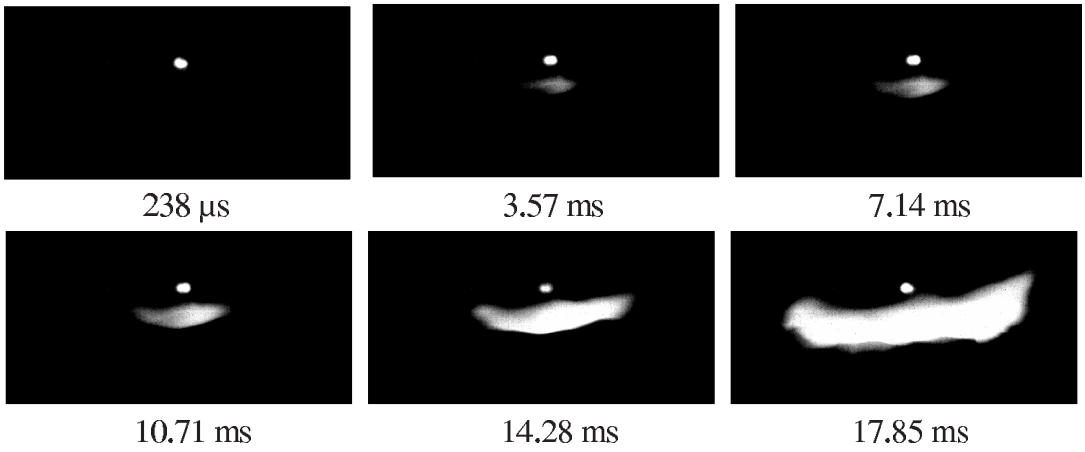

Figure 4.7: Instantaneous high-speed camera images at different instants following a 50 Hz spark in the air stream of an opposed-jet premixed flame with 4200 fps and exposure time 238 μs. Air from above, air-fuel mixture at ϕ =0.8 from below. The images correspond to a region about 150×70 mm.

flame. Figure 4.8 shows instantaneous OH-PLIF images of a non-premixed flame front with $U_b = 2$ m/s and $X = 80\%$. The images show that the flame propagates as a thin flame sheet, probably along the stoichiometric contour, and its leading edge is an edge flame. Figure 4.9 shows the OH intensity profile of the edge flame front, which indicates that there is only a single reaction zone at the flame front. No evidence of triple reaction zone was evident in the OH-PLIF images. A similar observation was found with the limited OH-PLIF images taken at the condition of $U_b = 2$ m/s and $X = 50\%$, Figs. 4.10 and 4.11. An estimation the scalar dissipation, χ, was performed by calculating the axial and radial gradients of the mixture fraction. For the conditions of the flames in Figs. 4.8 and 4.10, the instantaneous scalar dissipation at stoichiometry is between 1 and 10 s^{-1}. For high scalar dissipations, the lean and rich branches of a triple flame may merge. In addition, the local instantaneous stretch compresses the two branches of a

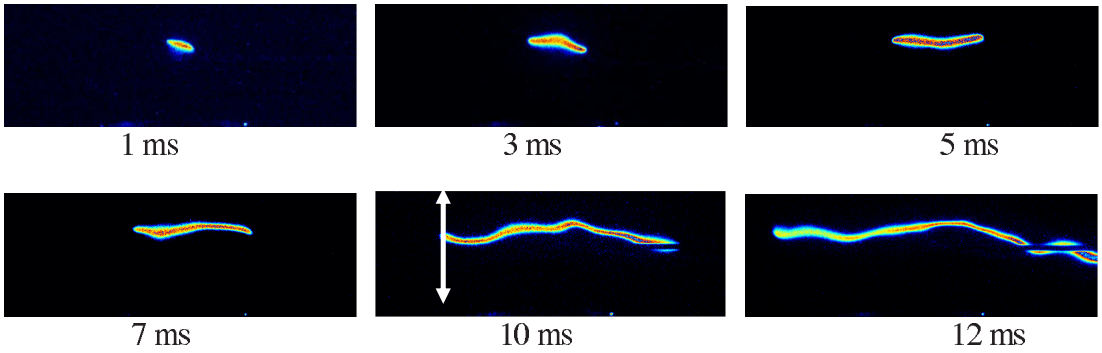

Figure 4.8: Instantaneous OH-PLIF images of the non-premixed flame during propagation at different times after ignition from different successful ignition events. Spark applied at $r = 0$, $z = 12.5$ mm (center of the image). Fuel from below, air from above. $U_b = 2$ m/s, $X = 80\%$. The images shown correspond to a region about 40×25 mm.

triple flame, and hence in the present turbulent flow an edge flame is reasonable (Santoro and Liñán (2000) and Buckmaster (1996)).

Figure 4.12 shows average OH-PLIF distributions of the non-premixed flame propagation. These images have been calculated from about 100 successful ignition events similar to Fig. 4.8. These images show that the flame, on average, propagates approximately within the mixing layer, but the axial thickness of the brush is much larger than the instantaneous thickness of the flame due to the flapping of the stoichiometric mixture fraction iso-surface.

Figure 4.13 shows instantaneous OH-PLIF images of a premixed flame during propagation after ignition. It can be observed that the flame is thicker than the non-premixed flame. This is due to the fact that the premixed flame is located farther away from the stagnation plane than the non-premixed flame. The flame front structure is also an edge flame in this case as well. Figure 4.14 shows average OH-PLIF images of a premixed flame during propagation. It can be noted that

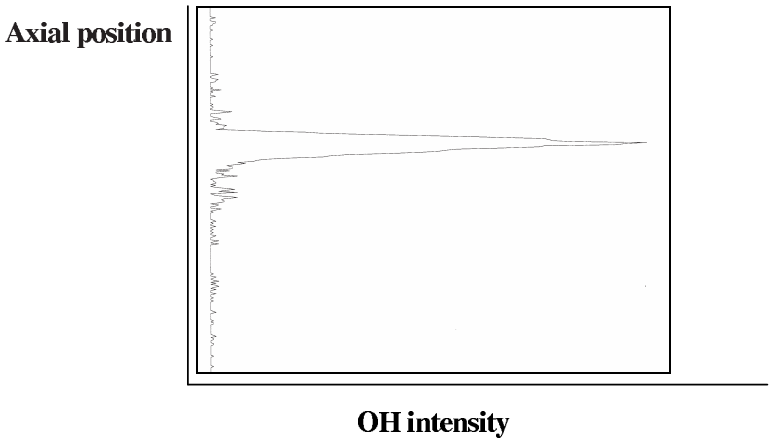

Figure 4.9: OH intensity profile of the edge flame front along the white line shown in Fig. 4.8.

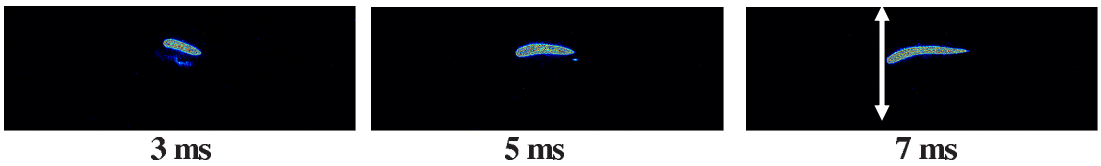

Figure 4.10: Instantaneous OH-PLIF images of the non-premixed flame during propagation at different times after ignition from different successful ignition events. Spark applied at $r = 0$, $z = 12.5$ mm (center of the image). Fuel from below, air from above. $U_b = 2$ m/s, $X = 50\%$. The images shown correspond to a region about 40×25 mm.

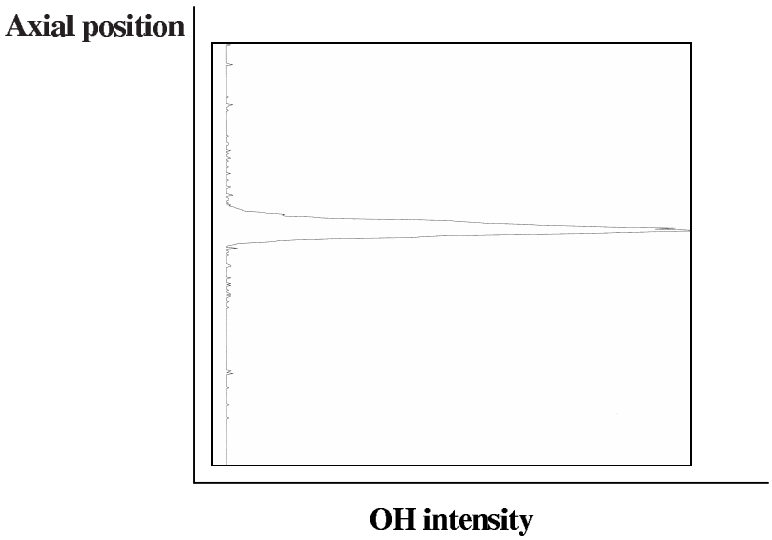

Figure 4.11: OH intensity profile of the edge flame front along the white line shown in Fig. 4.10.

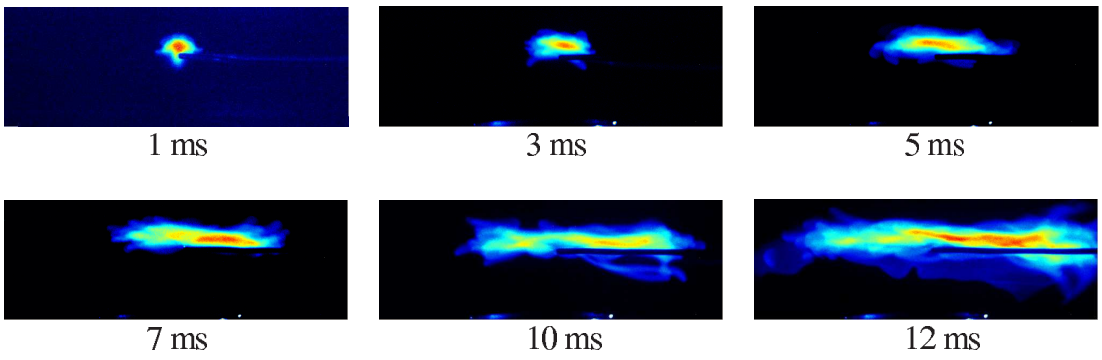

Figure 4.12: Average OH-PLIF images of the non-premixed flame during propagation at different times after the ignition. Flow conditions and spark parameters are identical to Fig. 4.8.

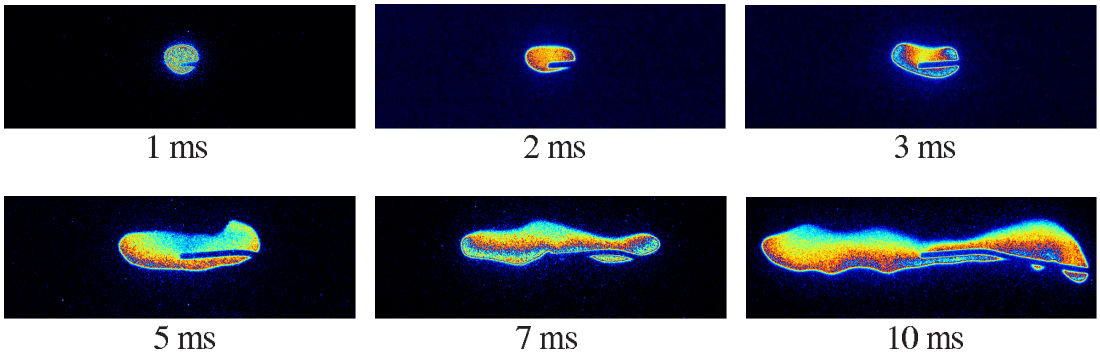

Figure 4.13: Instantaneous OH-PLIF images of the premixed flame during propagation at different times after the ignition from different successful ignition events. Spark applied at $r = 0$, $z = 12.5$ mm (center of the image). Fuel from below, air from above. $U_b = 2$ m/s, $\phi = 0.8$. The images shown correspond to a region about 40×25 mm.

the average images have almost the same thickness like the instantaneous images shown in Fig. 4.13. This is because the location of the premixed flame is away from the stagnation plane towards the air-fuel jet and hence the region between the flame and the stagnation plane contains hot products and hence OH. In contrast, the non-premixed flame had a stoichiometric mixture fraction of 0.452, which lies approximately at the stagnation (symmetry) plane (Fig. 4.3).

4.2.4 Ignition probability

The ignition probability was measured in this flow configuration by applying 50 sparks at each location of interest, and the number of successful events that result in a stable flame was divided by 50 to calculate the ignition probability. At most of the conditions studied in this section, the spark has energy of 100 mJ and duration of 400 μs, which is shorter than the estimated Kolmogorov timescale at the stagnation plane ($\tau_k = 1.25$ ms). This indicates that the spark freezes

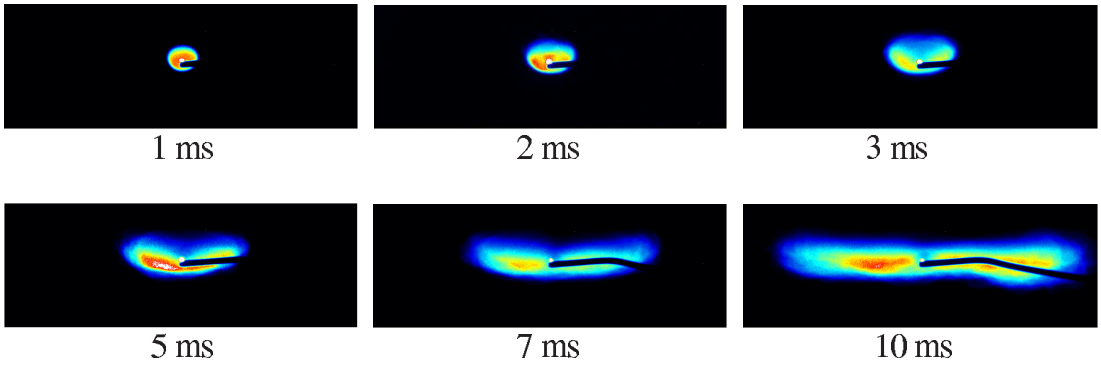

Figure 4.14: Average OH-PLIF images of the premixed flame during propagation at different times after the ignition. Flow conditions and spark parameters are identical to Fig. 4.13.

the mixture fraction value at the moment of ignition. The spark was created between two stainless steel electrodes having 0.7 mm diameter each with sharp ends and the spark gap was 2 mm. Each of the ignition probability contours measured here was assembled from a matrix of 25×25 points across and along the burner, respectively. The effects of the bulk velocity, air volume fraction in the fuel stream and high frequency spark on the ignition probability are discussed in this section. Table 4.1 shows the flow conditions examined.

4.2.4.1 Non-premixed flames

Figure 4.15 shows contours of ignition probability, P_{ign}, covering the whole region between the jets. The following points can be made: (i) the ignition probability decreases as the velocity increases; (ii) P_{ign} becomes zero at $r > 10$ mm; (iii) the ignition probability can be zero at the centreline (Fig. 4.15d) at axial locations where off-axis positions ignite; (iv) finite probability is found far from the stagnation region along the centreline; (v) the shape of the contour is different than the shape of the flammability factor contour, which is uniform in the radial direction

Table 4.1: The flow conditions and their flammability limits used in the ignition probability results.

Flame	U_b m/s	X %	ξ_{lean}	ξ_{st}	ξ_{rich}	Remarks
$NC1$	1.5	80	0.233	0.452	0.732	effect of U_b
$NC2$	2	80	0.233	0.452	0.732	effect of U_b
$NC3$	1.5	50	0.080	0.154	0.250	effect of X
$NC4$	2	50	0.080	0.154	0.250	effect of X
$NC5$	1	0	0.028	0.055	0.089	effect of X
$PC1$	1.5	ϕ=0.8	-	-	-	effect of premixing
$PC2$	2	ϕ=0.8	-	-	-	effect of premixing

because $P(\xi)$ is uniform in r. Lines corresponding to ξ_{lean} and ξ_{rich} have also been included in Fig. 4.15 to demonstrate, consistent with Birch et al. (1981) and Smith et al. (1986), that the fluctuations of mixture fraction widen the flammable region. These findings are explained and discussed further below by comparison with the calculated flammability factor from Eq. 3.3 and a β-function PDF using the measured $\bar{\xi}$ and σ.

Firstly, P_{ign} becomes zero in radial locations where $F \neq 0$, while still $r < R$ and hence no dilution has occurred. This is partly because the radial velocity increases linearly with radius and hence, after a certain radius, the edge flame speed is not greater than the local flow velocity to allow the flame to spread. At $r > R$, the turbulence intensity increases (Mastorakos (1993) and Geyer et al. (2005)), dilution with the co-flow nitrogen is inevitable, and hence the chances of flame kernel growth decrease.

Secondly, ignition can occur with sparks even at locations where $F = 0$. This is shown in more detail in Fig. 4.16, where it is evident that the distribution of P_{ign}

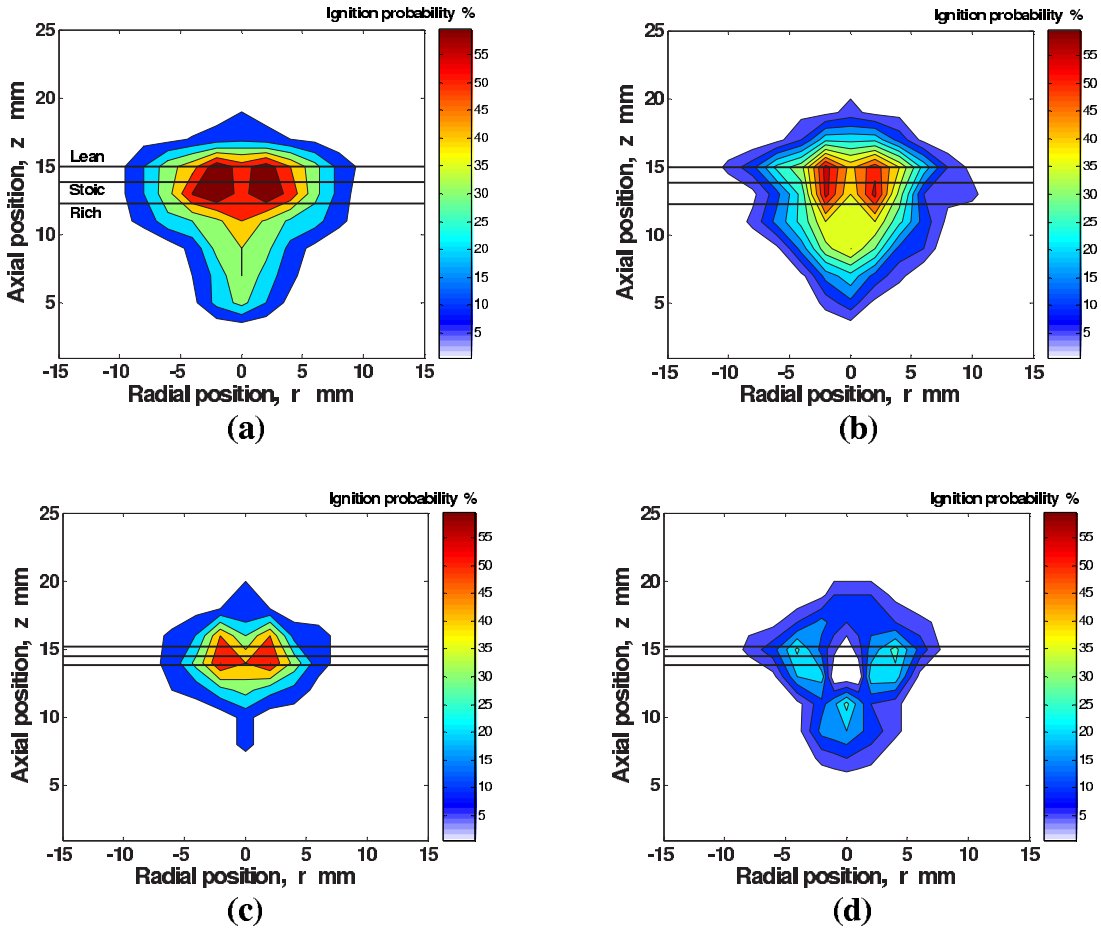

Figure 4.15: Ignition probability contour for non-premixed flames with (a) U_b = 1.5 m/s, X = 80% ($NC1$); (b) U_b = 2 m/s, X = 80% ($NC2$); (c) U_b = 1.5 m/s, X = 50% ($NC3$); (d) U_b = 2 m/s, X=50% ($NC4$). Spark: 100 mJ, 400 μs, 0.7 mm electrode, 2 mm gap.

is wider than that of F. Figure 4.17 confirms this for all mixtures tested and also shows that often P_{ign} is higher than F. Both trends can be explained partly by the fact that the initial spark kernel is not a point, but about 3 mm in diameter, which hence increases the chances that hot fluid touches flammable mixture fractions, and partly by considering non-local effects for example the convection of heat or radicals visualization in Fig. 4.7. Figure 4.16 includes measurements of ignition probability with different sparks. It can be noted that increasing the spark energy from 100 mJ to 300 mJ does not improve the ignition probability, except in the region where $\bar{\xi} = \xi_{st}$ where P_{ign} improves slightly. When depositing multiple sparks by sparking at a frequency of 3 Hz for 3 seconds (i.e. 9 sparks, each lasting 400 μs with 100 mJ) P_{ign} peaks at 100%. An improvement in ignition capability with multiple sparks has also been observed before in homogeneous mixtures (Kono et al., 1984). With this sparking sequence, the P_{ign} profile is very wide and reaches axial locations where $\bar{\xi} = 0$ or 1 (from Fig. 4.3). With a 1 Hz sequence of stronger sparks so as to deliver the same total energy (i.e. 3 sparks of 300 mJ each), this cumulative effect is smaller (Fig. 4.16). These effects cannot be explained by the finite spark size, but are consistent with the explanation that the heat from the spark, even if it is away from the mixing layer, is convected to the flammable region. We conclude that a discrepancy can emerge between P_{ign} and F due to convection effects.

Thirdly, an increase in U_b does not alter the mixing field, but it consistently decreases P_{ign}, consistent with the measurements in the turbulent jet flame presented in Section 3.2.5. This implies that high velocities are detrimental to ignition despite the presence of flammable mixtures. The flame with $X = 50\%$ extinguishes at a lower velocity (2.2 m/s) than the flame with $X = 80\%$ (2.7 m/s), and so at $U_b = 2$ m/s, the $X = 50\%$ flame is closer to extinction than the 80% flame. This explains why P_{ign} for $X = 50\%$ is generally lower than for

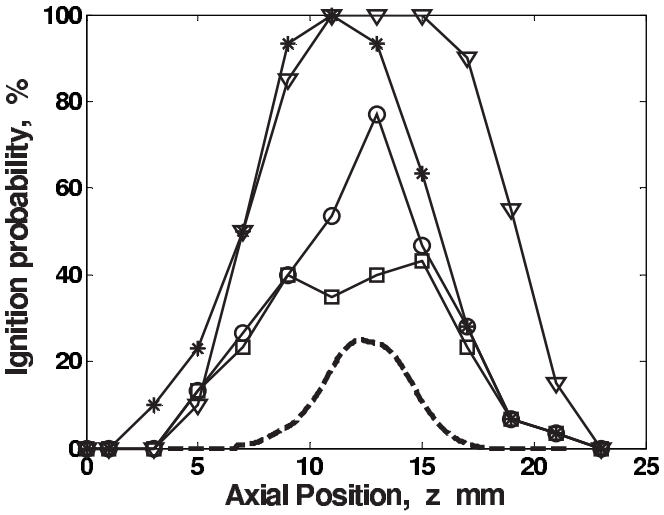

Figure 4.16: Axial distribution of P_{ign} for different sparks and the flammability factor profile for U_b = 2 m/s, X = 80%. Square: single spark- 100 mJ, circle: single spark- 300 mJ, triangle: 3 Hz spark- 100 mJ, star: 1 Hz spark- 300 mJ, dashed line: flammability factor F (Eq. 3.3).

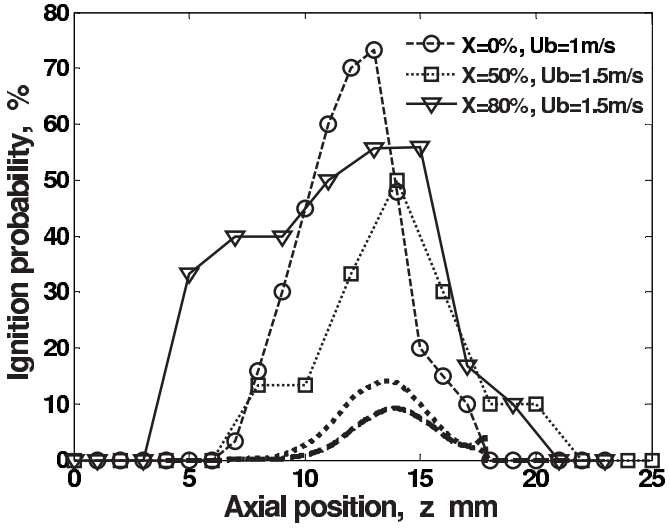

Figure 4.17: Measured P_{ign} and calculated flammability factor along the centerline. Dashed line: F for $X = 50\%$, long-dashed line: F for X=0%. Spark parameters are identical to Fig. 4.15.

80% and why the flame at $X = 0\%$ (Fig. 4.17), which was measured at a low U_b (1 m/s) quite far from extinction (1.7 m/s), shows a high P_{ign}. A severely reduced ignition probability results when trying to ignite at conditions close to the extinction limit, e.g. Fig. 4.15d.

Finally, we see that ignition at the centreline may never be successful (Fig. 4.15d), despite the finite flammability factor there and the fact that off-axis locations have finite P_{ign}. All the contours in Fig. 4.15 show that P_{ign} peaks off-axis (i.e. about $r = 4$ mm). This observation can be related to the increase in radial velocity as we move slightly away from the axis and is consistent with measurements of minimum ignition energy as a function of flow velocity in uniform mixtures that showed an initial advantageous effect of velocity (Kono et al., 1984). The explanation offered was that a small flow velocity causes a reduction in the heat loss from the flame kernel to the electrodes relative to the completely stagnant

mixture because the presence of flow distorts the spark and hence the kernel has a better chance to survive (Kono et al., 1984). However, with a further increase in velocity, the kernel itself suffers an excessive heat loss and so it is more likely to be quenched, which is another reason why the present data show a consistent and monotonic reduction in P_{ign} after $r > 4$ mm. The fact that P_{ign} can reach zero at the centreline in Fig. 4.15d is probably due to the fact that the flow is close to extinction and emphasizes further the discrepancy between the ignition probability and the flammability factor F when local flow effects are important.

4.2.4.2 Premixed flames

Figure 4.18 shows contours of ignition probability, P_{ign}, for premixed flames for the same equivalence ratio but two values of the bulk velocity (flame $PC1$ and $PC2$). Despite the fact that both contours have the same equivalence ratio spatial distribution, the ignition region clearly shrinks with the increase in velocity. Ignition is not possible for any radial location larger than $r = 15$ mm at $U_b = 2$ m/s, while ignition with about 20% probability can be observed up to $r = 18$ mm at $U_b = 1.5$ m/s. This is possibly due to the fact that the flow velocity there is high and hence the flame cannot expand against the radially-flowing fluid and also due to the dilution with the opposing air. However, ignition is always possible well into the fuel-air stream (i.e. at low z and r). Figure 4.18 also shows that above $z = 17$ mm in the axial direction there is no ignition and that P_{ign} decreases from 100% to zero across a region of thickness around 6 mm in the low velocity case and 10 mm in the high velocity case. Overall, there is a significant reduction in the ignition probability values between the two cases. Since the equivalence ratio field and its fluctuations are not expected to be different with an increase in velocity, the change in ignition probability suggests that the flow plays a role. In particular, we attribute the reduction in ignition probability to the detrimental

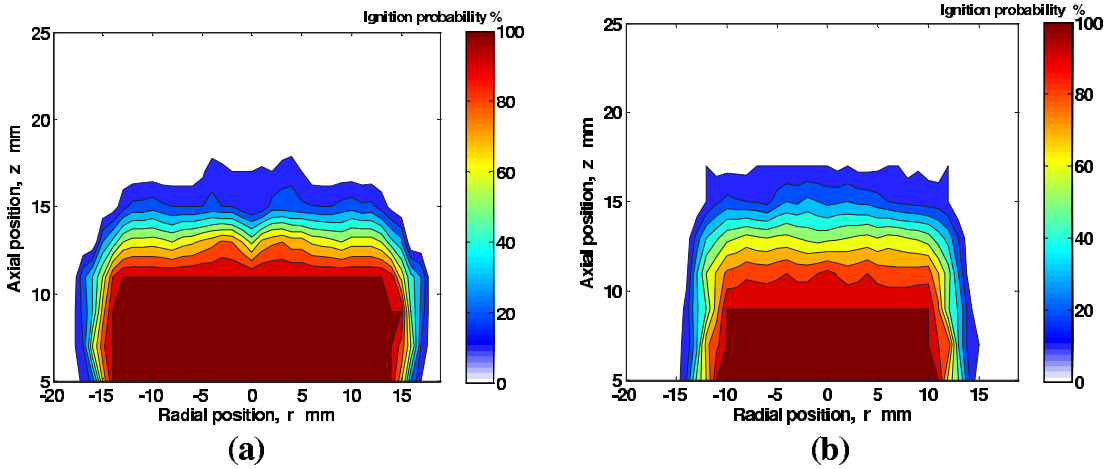

Figure 4.18: Ignition probability contour for premixed flames with (a) $U_b = 1.5$ m/s, $\phi = 0.8$; (b) $U_b = 2$ m/s, $\phi = 0.8$. Spark parameters are similar to Fig. 4.15.

effect of local high turbulence on the success of ignition regardless of the existence of flammable mixture at the location of the spark. Similar behavior has been observed before with the ignition of turbulent jets, Section 3.2.5.

4.2.4.3 Ignitability limits

In another experiment, the maximum velocity that the flame can be ignited has been measured for the premixed and non-premixed conditions and compared to the extinction velocity of the same flame. For all flames, with the strongest spark scenario studied here (9 sparks in total at 3 Hz), which can give $P_{ign} = 1$ at the stagnation plane at low velocities, it is not possible to ignite the flame if the bulk velocity exceeds 90% of the extinction velocity. Figure 4.19 shows that both velocities increase with X, peak at the stoichiometric mixture, and decrease towards very lean premixed flames. The fact that the maximum velocity for ignition is smaller than the extinction velocity is in full agreement with the theoretical study of Buckmaster (1996), which predicts that the maximum strain

rate that a steady laminar flame edge can sustain is less than the extinction strain rate of the corresponding premixed or non-premixed flame. For methane, $E = 160$ kcal/mol and $T^* = 2226$ K (Turns, 2000), thus according to Eq. 4.2 the predicted ratio $S_{edge}/S_{ext} \approx 0.82$. This was related to the fact that the edge flame during propagation is subjected to a higher heat flux away from the reaction zone in the radial direction ahead of the flame front, which results in excessive reduction in the flame front temperature and then flame extinction, Section 4.1.4. The data suggests that, even if the operating conditions are those of stable combustion, ignition of the flame may not be possible. Laminar flame calculations (Richardson and Mastorakos, 2007) showed that ignition may not be feasible even at a strain rate as low as 50% of the extinction value, which is consistent with the present observation and also with typical gas turbine ignition data (Lefebvre, 1998) that show an ignition loop narrower than an extinction loop.

4.2.5 Edge flame spreading

Figure 4.20 shows a scatter plot of the edge flame position at different time delays from the spark, compiled from about 100 OH-PLIF images of successful ignition events similar to those shown in Fig. 4.8. It is evident that the flame front is located within an axial region about 10 mm thick, which is almost equal to the mixing layer. The axial fluctuation of the flame front is probably related to the flapping of the instantaneous stoichiometric iso-surface across the mixing layer. The radial fluctuations of the flame edge position are much larger due to the action of the mean extensional strain and the radial turbulence.

Figure 4.21 shows the mean radial edge flame position during propagation at different time delays from the spark for non-premixed flames with $U_b = 2$ and 1.5 m/s, and a premixed flame with $U_b = 2$ m/s. It can be observed that the

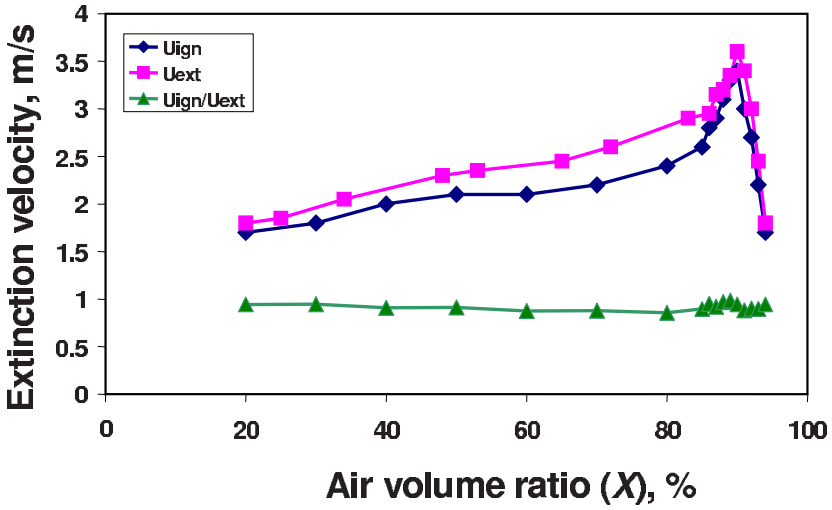

Figure 4.19: The extinction velocity, the maximum possible velocity for ignition, and their ratio as a function of air volume ratio of the fuel stream. The flame is deemed premixed for $X > 85\%$. The peak extinction velocity corresponds to a stoichiometric mixture in the lower jet.

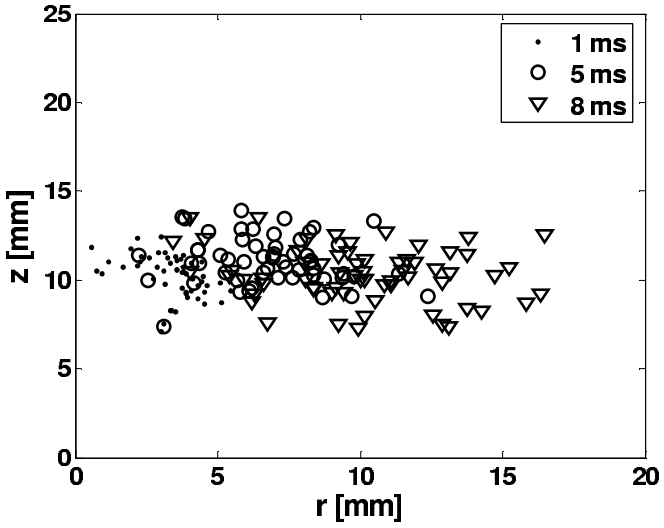

Figure 4.20: Scatter plot of edge flame position. $U_b = 2$ m/s, $X = 80\%$.

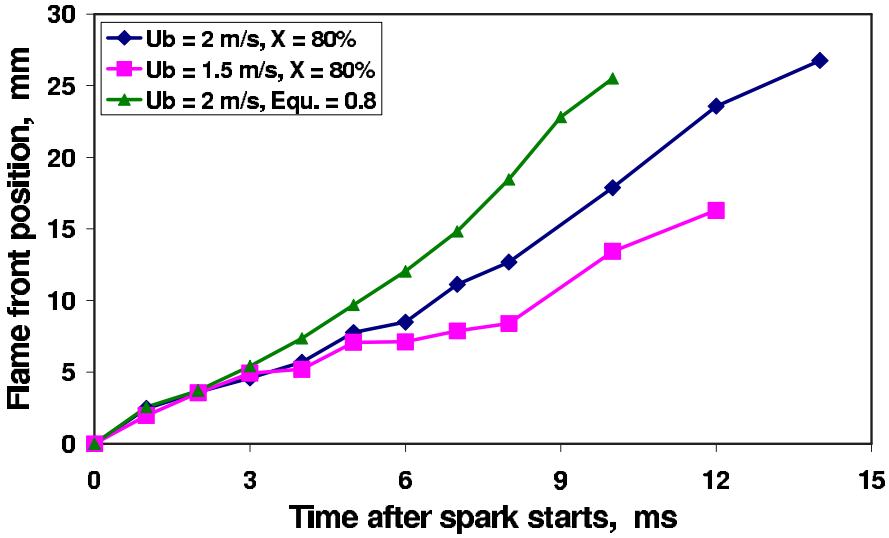

Figure 4.21: Mean of the edge flame radial position versus time.

premixed flame propagates faster than the non-premixed flame with the same U_b. Moreover, the non-premixed flame with U_b = 2 m/s is faster than that with U_b 1.5 m/s. Figure 4.22 shows the r.m.s of the radial edge flame position for the previous three cases. The three graphs of the r.m.s values are quite close to each other, which indicates that the radial turbulence is the main factor responsible for the radial fluctuation of the position of the edge flame. This radial turbulence is the same regardless the flow is non-premixed or premixed.

Differentiating the data in Fig. 4.21 and using the data up to r = 15 mm, the average edge propagation speed is about 2.4 m/s for the premixed flame at U_b = 2 m/s, while it is about 1.7 m/s for U_b = 2 m/s and about 1.4 m/s for U_b = 1.5 m/s in the non-premixed flame. In these experiments, the flame is ignited on the centreline and hence the radial velocity assists flame spreading. The mean radial velocity is estimated as $V = 2U_b r/H$ (Mastorakos, 1993) and this has been subtracted from the measured average edge flame propagation speed as a function of radius, estimated from Fig. 4.21 by calculating the derivative. The result is

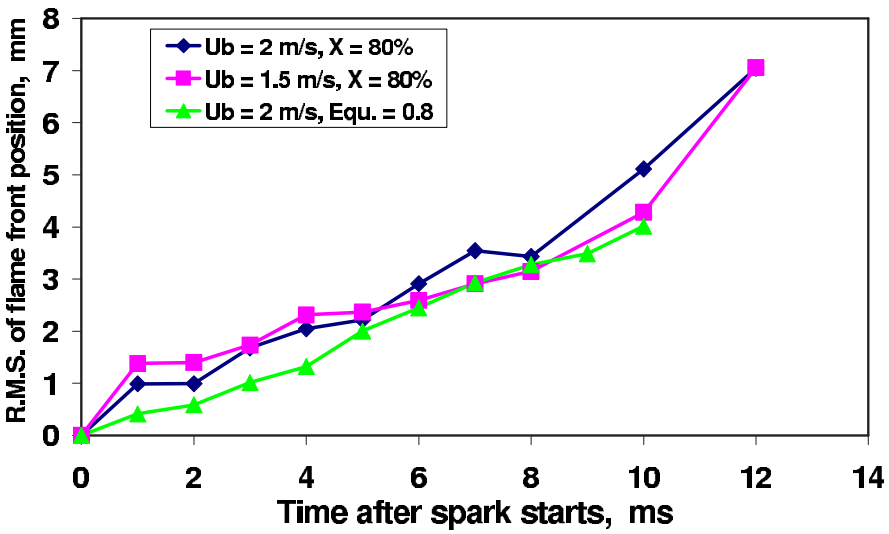

Figure 4.22: R.M.S. of the edge flame radial position versus time.

an estimate of the relative edge flame propagation speed (i.e. speed relative to the flow) and this is shown in Fig. 4.23. It is evident that after about 5 mm from the centreline, the net speed is approximately constant at about 0.6 m/s for the premixed flame and about 0.3 m/s for the non-premixed flame. The latter is slightly lower than the laminar burning velocity, S_L, of a stoichiometric methane air premixed flame (0.4m/s), while the former is about twice the S_L of a mixture of $\phi = 0.8$. The previous values are close to the laminar non-premixed edge flame speed, which is about one S_L (Santoro and Liñán, 2000). More detailed measurements would of course necessitate a detailed measurement of the flow velocity ahead of the flame.

4.3 Conclusions

The success of igniting planar non-premixed and premixed turbulent counterflow flames of methane with a spark has been quantified by measuring the ignition

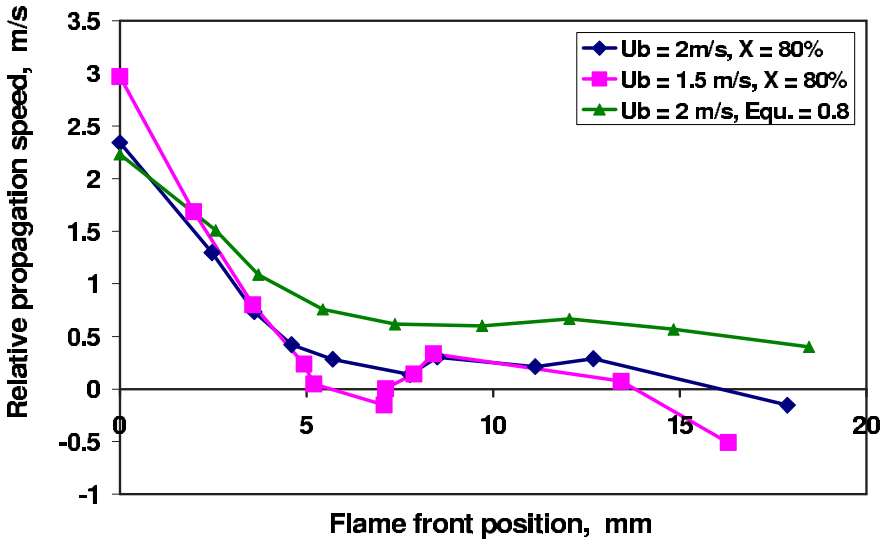

Figure 4.23: Estimated relative flame propagation speed versus radial flame front position from spark.

probability for various bulk strain rates and fuel premixing with air. PLIF of OH and of acetone have also been used to visualize the flame following ignition and to measure the mixture fraction. The main findings are given below:

- The ignition probability consistently decreased with increasing bulk velocity.

- The ignition probability was greater than zero along the centreline even at distances from the stagnation plane where the probability of finding flammable material was zero. This is attributed to the mean convection that carries the gases heated by the spark towards the flammable air-fuel region and to the finite size of the spark.

- The probability of ignition became zero at large radii, possibly because the flame kernel at large radii experiences large adverse radial velocities and hence cannot expand.

- A severely reduced ignition probability results when trying to ignite at conditions close to the extinction limit. Moreover, for all flames, it is not possible to

ignite the flame if the bulk velocity exceeds 90% of the extinction velocity.

- The flame expands as an edge flame, with no evidence of triple flame structure, probably due to the large scalar dissipation rates experienced in this turbulent counterflow.

- The edge flame speed relative to the laboratory coordinates increases with U_b, while the estimated edge flame speed relative to the radial flow is higher than S_L for the premixed flame and is less than S_L for most of the radial travel of the non-premixed flame as it expands to fill the stagnation plane.

- The data indicates that the local strain rate is detrimental to ignition and implies the existence of non-local effects that can help ignition of the flammable mixture. The measurements can be used for validating advanced models of unsteady combustion, for example those based on LES.

Chapter 5

Bluff-Body Flames

This chapter presents the experimental investigation of spark ignition of turbulent bluff-body flames. Most of the experiments have been carried out on non-premixed bluff-body flames without swirl. A few experiments on the non-premixed bluff-body with swirl and on premixed bluff-body flames have also been performed. The chapter starts with a literature review about the aerodynamics and stability of bluff-body flames, and then in Section 5.2, the results of these experiments are presented and discussed. The chapter ends with conclusions.

5.1 Literature Review

5.1.1 Introduction

Bluff-body flame holders are widely used to stabilize flames in flowing combustible mixtures and their many practical applications include ramjet and turbojet afterburner systems. The practical importance of bluff-body stabilizers has given rise to a large number of theoretical and experimental studies. Much of our present understanding of the flame stabilization process is due to the pioneering studies carried out in the 1950s by Longwell et al. (1953), Zukowski and Marble

(1955), Zubay (1950) and Spalding (1953). A bluff-body flame is stabilized by the recirculation zone formed in the wake of the bluff-body. This zone serves a triple purpose: (i) it produces a region of low velocity, (ii) it provides long residence time for the flame to propagate into the incoming fresh mixture, and (iii) it serves as a source of continuous ignition for the incoming fuel-air mixture. Thus, a steady flame is stabilized (Pan et al. (1992a) and Pan et al. (1992b)).

Many different geometric shapes of bluff-bodies, such as a cylinder, cone, disk, vee-gutter, or sphere, can be used as flame stabilizers. The geometry of the bluff-body affects the recirculation zone. The apex angle of the bluff-body causes parallel streamlines of the incoming flow to curve and increase the width of the recirculation zone. This aerodynamic effect, in addition to the type of fuel, whether the flow is premixed or non-premixed and the flow confinement (pressure-gradient effect) are responsible for the flame stability. Thus, a complex aerodynamics-chemistry-pressure gradient interaction is present in reactive recirculatory flow. This fact, together with its existence in many practical combustor configurations, especially the gas turbine combustor, makes any investigation of this type of flow field of considerable practical significance.

Despite the fact that bluff-bodies are extensively used in practical systems, there is still lack of understanding of exactly how ignition of this type of flame occurs and how the flame kernel is initiated and propagates to form the stable flame. The majority of the previous investigations concentrated on improving the stability characteristics, especially for premixed flames, and only few studies examined the general ignition characteristics of the real combustors, Section 5.1.5. However, aviation gas turbine manufacturers are interested to improve the relight capability of their combustor at high altitude by improving the efficiency of the ignition system of the engine and by investigating the igniter location in respect to the mixing field so that to achieve high ignition probability. Therefore, the

present work focuses more on the spark ignition characteristics of the bluff-body non-premixed flames in order to provide a greater understanding of the ignition in this flow.

5.1.2 Aerodynamics of Bluff-Body Burners

The aerodynamic characteristics of the wake behind the bluff-body were subjected to numerous investigations both experimentally and theoretically by Correa and Pope (1992) and Ma and Harn (1994). Most of the experimental investigations used disk, as by Huang and Lin (1994) and Durao and Whitelaw (1978), cone as by Taylor and Whitelaw (1984), Brum and Samuelsen (1987) and Esquiva-Dano et al. (2001), or cylindrical bluff-bodies as by Roquemore et al. (1986), Namazian et al. (1992), Schefer et al. (1994), Schefer et al. (1996) and Al-Abdeli and Masri (2003). The cone bluff-body is the main interest of this review as it is the one used in the present work, Section 2.1.3. In principle, the wake behind a cone bluff-body is divided into three zones: the recirculation zone with length between 1-2 bluff-body diameters, followed by the transition zone with nearly similar length, and then the established flow zone (Beer and Chigier, 1972). This review covers the structure of the recirculation zone and the effect of different parameters, such as the blockage ratio (BR), the cone angle (apex angle (θ)), the confinement of the flow, and the incoming velocity and turbulence intensity on the recirculation zone characteristics.

5.1.2.1 Flow field visualization

In his study, Balachandran (2005) used smoke with a laser sheet to visualize the structure of the recirculation zones of a confined 45° cone bluff-body with exactly the same dimensions as the bluff-body used in this work. The images were used to draw a schematic diagram of the flow field structure shown in Fig. 5.1. The

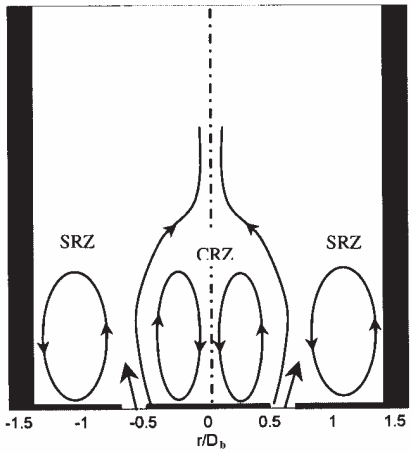

Figure 5.1: Schematic of the flow field in a bluff-body combustor. (Balachandran, 2005)

recirculation zone formed in that visualization consisted of a central recirculation zone (CRZ) formed in the wake of the bluff-body and a so called side recirculation zone (SRZ) formed by the rearward-facing step (dump plane). With 10 m/s exit velocity, the width and the height of the recirculation zone were about 1 and 1.5 bluff-body diameters respectively. When swirl vanes with angles 45° and 60° were introduced to the flow, the size of the CRZ increased, while the size of SRZs decreased and the length of the SRZ was around 1.5 and 1 bluff-body diameter for the two swirl vanes respectively (Balachandran, 2005). This observation agrees with Gupta et al. (1984) who pointed to that when the swirl is introduced in a bluff-body flow, both CRZ and SRZ are affected by the swirl more than by the bluff-body.

5.1.2.2 Effect of the blockage ratio

The blockage ratio of the bluff-body (BR) is defined as D_b^2/D_s^2 where D_b is the bluff-body diameter and D_s is the diameter of the surrounding flow defined in

Fig. 5.1. Pan et al. (1992a) investigated the effect of BR of a confined cone bluff-body on the structure of the recirculation zone. They divided the recirculation zone into three regions. Region (1) covers the axial distance between the base of the bluff-body and the location of maximum recirculation zone width, region (2) covers the axial distance downstream up to the stagnation point, and region (3) is downstream of the stagnation point. It was found that increasing BR causes a decrease in the pressure gradient in the first region, a decrease in the recirculation zone length in the second, and an increase in the acceleration of the flow in the third. They concluded that increasing BR slightly decreases the recirculation zone length and produces a moderate increase in the shear stress and the turbulent kinetic energy in either the interior or at the periphery of the recirculation zone. A similar conclusion was provided by Durao and Whitelaw (1978) from experiments carried out on a disk bluff-body flow.

Taylor and Whitelaw (1984) observed that the effect of increasing BR on the recirculation zone in an open flow is opposite to that in a confined flow, as the length and the width of the recirculation zone tended to increase with the increase in BR. They related this difference to the confining wall, both preventing the generation of large streamline curvature towards the stagnation point and maintaining large axial velocities at all downstream stations. In addition, they investigated the influence of the bluff-body shape when a disk was replaced by a 45° cone, both with the same blockage ratio of 25%. This influence was summarized as follows: (a) the recirculation zone is shortened and narrowed by 10%; (b) the recirculation mass flow rate is decreased by 40%; (c) the largest value of turbulent kinetic energy is reduced by 40%. Finally, another interesting observation was that for a 25% blockage disk the maximum turbulent kinetic energy lied near the stagnation point, whereas for the 50% blockage disk it was far from the centerline, in the shear layer.

The effect of the blockage ratio on the mean velocity has been reported by Ma and Harn (1994) following a numerical study of a confined cone bluff body with axial fuel injection. They found that the greater the blockage ratio, the greater the decline in the velocity, and the stronger the circulation in the recirculation zone. It should be mentioned that the bluff-body used in the present work has $BR = 50\%$.

5.1.2.3 Effect of the cone angle

Ma and Harn (1994) observed the behavior of the recirculation zone by increasing the cone angle gradually. In case of a cylindrical bluff-body ($\theta = 0$), the recirculation zone is of moderate size and with limited turbulence. When the bluff body cone angle increases to 15°, the recirculation zone behind the bluff-body becomes larger and oval. When the angle increases continuously, the length of the recirculation zone shortens, but the width increases, and the curvature increases. The length of the recirculation zone is around 1.1-1.3 D_b, and the width around 1.1-1.2 D_b. In a more detailed experimental investigation, Pan et al. (1992a) reported that increasing the cone angle increases the deflection of the mean separation stream line from the trailing edge of the bluff-body. In the cold flow, this increases the aerodynamic blockage and hence the recirculation zone width. In region (1) of the confined combusting flow (see Section 5.1.2.2), the recirculation zone width increases due to the increased streamline curvature. In addition, in region (2), the recirculation zone is elongated because the wall confinement decreases the streamline curvature. The net effect of these two changes is to produce a slightly larger recirculation zone volume and to widen the flame stability limits. However, in confined flows, rigid walls accelerate the flow in the vicinity of the flame and this may adversely affect flame stabilization with further increases in cone angle.

In fact, the size of the recirculation zone is considered to be the most important factor in the non-premixed flame stability (Beer and Chigier, 1972). The proportion of the flow from the main stream that is recirculated within the recirculation zone can be considered as a measure of the strength of the recirculation zone. Reverse mass flow rates are determined at each axial station by:

$$\dot{M}_r = \int_0^{r_\circ} 2\Pi r \rho \bar{U} dr \tag{5.1}$$

where $r_\circ$ is the radial position of the zero velocity boundary ($\bar{U} = 0$). Relative reverse mass flow is increased by the blockage ratio and reduced by reducing the cone angle of the bluff-body (Beer and Chigier, 1972). In another quantification of the recirculation zone strength, Chen and Driscoll (1989) proposed that the strength of the recirculation zone is Γ, where

$$\Gamma = U_{rz} \cdot r_\circ \tag{5.2}$$

U_{rz} is the characteristic recirculation zone velocity and is precisely defined as the volumetric flow rate of gas that recirculates divided by the cross-sectional area through which all of the recirculating gas pass. The most direct way to increase the recirculation zone strength is to increase the axial flow velocity (Chen and Driscoll, 1989). Moreover, it was found that the bluff-body flows have the same U_{rz} as swirl flows that are operated at a swirl number of approximately 0.5.

5.1.2.4 Effect of the confinement

Confined bluff-body burners are widely used in industrial burners and gas turbine combustors. Despite this practical importance, only limited fundamental studies on the effect of the confinement on the bluff-body flames have been attempted (IFRF, 1989). This is probably due to the difficulty of applying laser-based diagnostics to confined flows. Typically the Confinement Diameter Ratio (CDR)

is the ratio of the bluff-body and the confinement diameters defined in Fig. 5.1. For most of the burners of 50 kW to 1 MW capacity, designed so that combustion within the confinement is attached to the burner, this ratio ranges from 0.61 to 0.9. In contrast to these tightly confined cases, burners above 1 MW are generally designed so that the flame extends into the furnace. These large confinement cases typically have a CDR of less than 0.5.

The influence of the confinement on the flow patterns depends completely on the CDR. Schefer et al. (1996) studied the effect of the confinement on a cylindrical bluff-body flow with CDR ranging from 50% to 90% by comparing the flow in each of these cases with the open flow with the same bluff-body. They reported that for CDR with 50% the confinement does not affect the recirculation zone length and it is similar to the open flow, but with the increase in CDR the flow patterns are altered. The recirculation zone length and the stagnation point location are related to the pressure gradient and the jet streamline curvature constraints imposed by the confinement. With unconfined flows, the externally imposed pressure is constant and the flow momentum is diffused into the ambient air. However, with confinement the flow momentum in not diffused and the flow is constrained to be parallel to the confinement wall. This causes the recirculation zone to increase in size when confinement is added. In the present work, the CDR is 35%, which suggests that the confinement does no have any effect on the recirculation zone structure.

5.1.2.5 Effect of the incoming velocity and turbulence

The wake behind the bluff-body becomes fully developed when the Reynolds number of the flow based on D_b is in order of 10^4 (Zukowski and Marble, 1955). In most of the previous experiments, it has been reported that the increase of the incoming velocity does not affect the recirculation zone, at least at the

higher Reynolds number, although slightly larger lengths were noted for the lowest Reynolds number according to Durao and Whitelaw (1978) and Pan et al. (1992a). Furthermore, the inlet velocity does not have a significant effect on the velocity fluctuations. However, as mentioned before, increasing the incoming velocity increases the recirculation zone strength.

The measured distribution of the turbulence characteristics show that a region of high turbulence intensity and shear exists within the recirculation zone. Regions of highest turbulence intensity coincide with the "eye" of the vortex where the static pressure is at a minimum. The turbulence decays rapidly to free jet properties within three bluff-body diameters (Beer and Chigier, 1972). The effect of increasing the approach turbulence intensity on the recirculation zone has been studied by Pan et al. (1992a). By putting a grid, they increased the turbulence intensity from 2% (no grid was used) to 22%. In Region (1), see section 5.1.2.2, the increase in turbulence shifts the location of maximum recirculation width upstream from 0.8 to 0.4 D_b. It is also shortens the length of Region (2) from 2 to 1.1 D_b. In Region (3), this increase accelerates the flow downstream of the recirculation zone.

5.1.3 Non-premixed flame characteristics

Non-premixed bluff-body stabilized burners represent an important class of practical burners. Through variation in design and operating conditions, these burners can produce flames of varying stability, efficiency, pollutant formation and heat transfer. Effective application of these burners require better understanding of how design and operating conditions influence the flame processes, particulary the process whereby the initial unmixed fuel and air are brought together on a molecular scale and react. This understanding can then be used to construct accurate flow and combustion models that can be ultimately used to help optimize

burner design. The majority of the previous investigations of the turbulent non-premixed bluff-body flames used axial fuel injection as Namazian et al. (1989), Meier et al. (2000), Prade and Lenze (1992), Kalt et al. (2002), Fallot et al. (1997) and Dally et al. (1998), and only very few investigations examined annular or radial fuel injection, for example Milosavljevic et al. (1990), Cheng et al. (1998) and Olivani et al. (2005). In some of these investigations, swirl flow was introduced to the bluff-body flow. In the text below, the mixing field and the stability characteristics of some non-premixed bluff-body burners are reviewed.

5.1.3.1 Mixing field

Different techniques have been used in the last decade to measure the mixture fraction distribution in the non-premixed bluff-body flow. Planar flow visualization using Mie scattering from seed particles added to the fuel stream (Namazian et al., 1989) and the single point Raman signal measurements (Kalt et al., 2002) are popular ways to measure the mixture fraction in both cold and reacting flow. Recently, the development of Tracer-LIF diagnostics gives a simple, safe, clean and reliable way to measure the fuel concentration in the isothermal (cold) flow (Schultz and Sick, 2005). When seeding acetone to the desired gas flow, the local LIF intensity gives direct information about the local concentration of the fuel. It should be noted that the last method is the one which has been used in the present work, Section 2.4.1.

Namazian et al. (1989) measured the mixture fraction of methane by using Mie scattering in non-premixed cylindrical bluff-body flow with axial fuel injection under the isothermal and reacting cases. It was shown that the instantaneous central fuel jet is asymmetric and time varying and that large-scale mixing structures engulf external fluid into the jet. The gradient at the boundaries of these structures are eight times higher than the mean gradient. The movement of these

sharp boundaries results in high r.m.s fluctuation levels in the methane concentration. The presence of high air-flow velocity causes the fuel jet to stagnate on the axis and spread radially, transporting fuel into the near burner zone by large-scale structures. The near burner zone can be considered as an organized recirculation flow only in a time-average sense. Instantaneously, the flow in this zone is very irregular.

Dally et al. (1998) investigated the mixing field in a burner similar to the previous one. Three mixing layers are identified in the recirculation zone: an outer layer between the outer vortex and the air flow, an intermediate layer between the outer vortex and the inner vortex, and an inner layer between the inner region and the fuel jet. The relative contribution of each layer to the overall mixing varies with the fuel and air velocity. The increase in the fuel-jet momentum flux decreases the strength of the mixture in the outer vortex and at a sufficiently high jet velocity, the stoichiometric mixture fraction contour shifts from the outer region to the inner region of the recirculation zone. Meier et al. (2000) measured the mixture fraction by using Raman scattering in an axial fuel injection bluff-body burner with swirl, known as the TECFLAM burner. Figure 5.2 shows the measured mixture fraction contour. It can be observed that the stoichiometric mixture fraction, line (0) in Fig. 5.2, surrounds the recirculation zone. However, inside the recirculation the mixture fraction is rich and becomes even richer close to the fuel injector.

To avoid the penetration of the recirculation zone by the fuel jet, Milosavljevic et al. (1990) used a radial fuel injection bluff-body burner with swirl. A nozzle with radial injection of the natural gas was used, with a radial velocity equal to 0.68 of the axial velocity. Unfortunately, no mixture fraction measurements have been reported in this study, but the stability and the symmetry of the flame improved significantly with the radial injection. The previous observation will

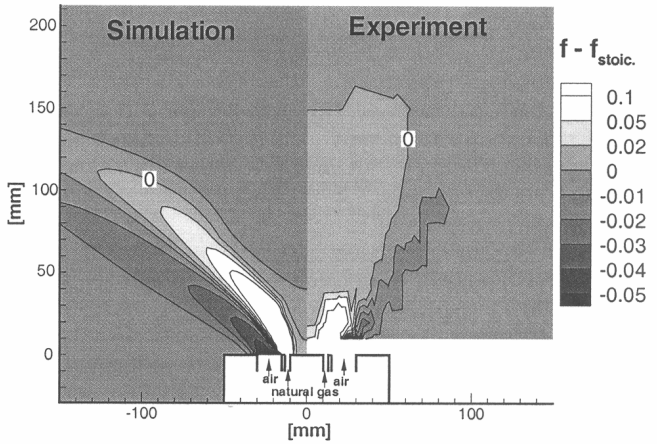

Figure 5.2: Two-dimensional distributions of Favre-averaged mean mixture fraction (Meier et al., 2000).

be discussed in the next section. A similar burner has been used in a recent study to investigate the thermal and aerodynamic field in the close vicinity of the burner throat (Olivani et al., 2005). Two fuel injection directions, axial and radial, leading to different mixing mechanisms, were investigated. The results indicated that although the global mixing process and the main flame structure are governed by the swirl motion imparted to the air stream, the two different fuel injection modes have a significant effect on mixture formation and flame stabilization in the primary mixing zone. In the case of axial injection, turbulent interaction between the central fuel jet and backflow generated by swirl can induce an intermittent fuel penetration in the recirculated hot products and formation of a central sooting luminous plume, a phenomenon totally absent in the case of radial injection. Again, detailed measurements of the mixture fraction have not been reported.

5.1.3.2 Flame stability

The bluff-body system generates a recirculation zone in which the fuel and air streams mix and react. This heat transfer permits a flame to be stabilized over wide ranges of approach-flow velocities and mixture ratios. In the outer regions of the wake with high-velocity gradients, flame stretch occurs. When the flame stretch factor (Karlovitz number) exceeds a critical value, the flame blows off (Gupta et al., 1984). In fact, the stability of the non-premixed bluff-body flame is controlled by the aerodynamics of the flow, which involves the bluff-body shape and the flow velocity, and by the fuel to air flow ratio. These parameters were subjected to extensive investigations both experimentally by Chen et al. (1990), Correa and Gulati (1992), Huang and Lin (1994), Chen et al. (1998), Masri et al. (2004) and Ata et al. (2005), and theoretically by Masri and Bilger (1984) and Masri et al. (2000).

The influence of the bluff-body geometry on the flame stability has been observed in many investigations. An improvement in flame stability can be achieved with increasing the bluff-body diameter (blockage ratio). This was related to the longer residence time of the reactants in the recirculation zone (Lefebvre, 1998). In addition, the shape of the bluff body plays an important role in flame stability. Esquiva-Dano et al. (2001) have observed that the cone bluff-body promotes flame stabilization over a wide range of velocities compared to the disk. That was related to the difference in flow divergence due to the conical bluff-body shape, which is associated to a change in the length and the width of the recirculation zone. This phenomenon is also related to different recirculating velocities, as the disk induces larger reverse values of the axial mean velocity, which results in an increase in the recirculating velocities and in the turbulent kinetic energies.

When axial fuel injection is used in the bluff-body non-premixed flames, the flame behavior is mainly controlled by the average velocity ratio between the air

and the fuel streams based on the flow rates. Chen et al. (1998) classified the stable flame in this case into three modes: recirculation zone flames, central jet dominated flames, and jet-like flames. A similar classification has been mentioned elsewhere by Huang and Lin (1994). When the fuel jet momentum is too weak to overcome that of the reverse air flow in the recirculation bubble, formation of a stable jet flame is impossible and all the fuel mass will be retained behind the bluff-body to form a recirculation zone flame. When the fuel jet has a much higher momentum than that of the recirculation air flows, the fuel (inner) vortex may no longer exist behind the bluff-body and part of the annular air flows can even be entrained downstream into the jet stream. In this case, the characteristics of the mean flow field behind the bluff-body is dominated by the air vortex, where insufficient fuel mass can be captured to reach the lean flammability limit. Finally, when the fuel jet and annular momentum are comparable, a central jet dominated flame can be developed. It should be mentioned that, at sufficiently high swirl, the flames were more stable than without swirl.

In comparison with the axial fuel injection, annular and radial fuel injection have been less studied in terms of flame stability. All the annular and radial fuel injection bluff-body flames found in the literature were accompanied by swirl flow and the stability of such flames has not been examined in the absence of swirl, as far as the author is aware. Milosavljevic et al. (1990) observed that the angled annular injection of the fuel results in the rich stability limit occurring at leaner equivalence ratios, as compared with axial fuel injection. For radial fuel injection, there is no lower limit of swirl number below which the flame cannot be stabilized due to the bluff-body effect. Moreover, the stability limits of the radial injector are the least affected by the change in the bulk air velocity of the three fuel nozzles that were tested. In other investigations, when the annular and radial fuel injection were used, enhancement in the mixing process leading to

higher flame temperature has been observed (Cheng et al. (1998), Olivani et al. (2005)).

An interesting observation mentioned by Prade and Lenze (1992) is that there is a good agrement between the location of the flame front and the limits of flammability in the isothermal flow of an axial fuel injection disk stabilized flame. Therefore, certain flame extinction limits can at least qualitatively be predicted, if the mixing field of the cold flow is known. This is important, because the isothermal flow field can be calculated satisfactory, even if the calculation started without measured values besides the total mass fluxes. In another interesting observation, a good improvement in the lean flame stability of bluff-body flames has been achieved by applying of DC electric field near the exit of the burner (Ata et al., 2005).

5.1.4 Summary

From the previous review, the following points can be summarized: (1) the bluff body used in the present work is 45° cone with $BR = 50\%$ in order to keep the flow structure similar to (Balachandran, 2005), (2) the width and the hight of the recirculation zone of the present flow field are expected to be about 1 and 1.5 D_b respectively, (3) in case of 60° swirl vane, which is the only kind of swirl vane used here, an increase of the size of the CRS can be expected, (4) the CDR is 35%, which indicates that the confinement does no have any effect on the recirculation zone structure and (5) with the radial fuel injection, a wide range of flame stability can be expected.

5.1.5 Ignition of Gas Turbine Combustors

Many of gas turbine ignition investigations (Jarymowycz and Mellor (1987), Naegeli and Dodge (1991)) were aimed to improve the ignition performance of

the existing designs of the gas turbine combustor by examining the ignitability of different flow conditions or different spark parameters. However, a fundamental and a detailed study of ignition in respect to the mixing flow field has not been done yet. The spark location, for instance, was determined in the gas turbine combustor based on the accessibility for fitting and replacement and not based on the mixing pattern. With the recent development in the gas turbine combustor, which aims to achieve high ignition performance at high altitude and to reduce emissions, the need for such fundamental study becomes even more important. Therefore, the work in this chapter focuses on studying in detail the ignitability of a flow close to what exists in the real combustor, with better controlled geometry and mixing patterns.

5.2 Results and Discussion

5.2.1 Introduction

Considering the fact that turbulent non-premixed bluff-body flames with radial fuel injection have not been studied extensively before, this section provides information on the appearance and the stability limits with and without swirl. The ignitability limits are also compared with the stability limits. Velocity (Dawson et al., 2007) and mixture fraction measurements in inert flow are presented to help interpreting the ignition probability results. The successful and failed ignition are also studied by recording the OH* emission of both types of ignitions.

5.2.2 Flame characterization

The air flow will be described by U_{air} and the velocity of the fluid coming out from the fuel nozzle by U_f. "Swirl" indicates the usage of the 60° swirl vane. For

all flames, 100% CH_4 was used (i.e. no dilution or premixing). For the acetone PLIF data, the fuel was replaced by air and in those cases, U_{acet} refers to the velocity of the air and 10% acetone vapor mixture coming out of the fuel slit. The spark parameters have not been changed in this chapter and they are: 200 mJ energy, 500 μs duration, 1 mm electrode and 2 mm spark gap.

5.2.3 Flame visualization and stability limits

Direct visualizations of the flame with and without swirl at the main flow condition investigated in this work (U_{air} = 10 m/s and U_f = 5 m/s) are shown in Fig. 5.3. The flame is attached to the bluff-body and expands to touch the enclosure at around 1.5 to 1 D_b, after which the flame occupies the whole enclosure. If swirl is introduced, the flame becomes shorter and expands in a much wider angle than the case without swirl to touch the enclosure at about 1 D_b or less. This flame shape can be understood from the mixing filed, Section 5.2.4.2, as the flame follows the stoichiometric mixture fraction iso-surface up to the limit that it touches the enclosure. However, after this location the flame has a premixed character as the mixing is quite fast in such flows (Cheng et al., 1998). With swirl, the mixing becomes even faster, which shortens the non-premixed region. In addition, the length of the recirculation zone becomes shorter with the swirl, which results in the shape of the flame shown in Fig. 5.3b.

The structure of this type of flame is visualized by the OH-PLIF images shown in Fig. 5.4 for the bluff-body flames and in Fig. 5.5 for the swirl bluff-body flames at the same flow conditions. Instantaneously, both flames are hollow at the center due to the rich mixture inside the recirculation zone, as we will see in Section 5.2.4.2. However, on average, OH radical appears in the center, but it becomes more intense at the sides of the recirculation zone where the mixture fraction iso-surface has the stoichiometric value. Moreover, comparison of Fig. 5.4a with

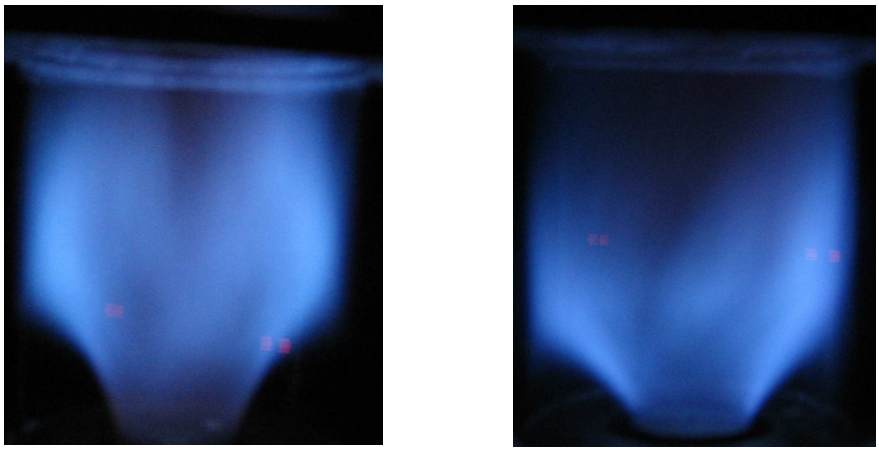

Figure 5.3: Photograph of a bluff-body flame (a) without swirl, (b) with 60° swirl. U_{air} = 10 m/s, U_f = 5 m/s giving a global $\phi = 0.55$.

Fig. 5.5a shows that the flame brush seems to be more irregular in the case of the swirl due to the higher turbulence.

The lean and rich stability limits of the bluff-body flames have been studied by increasing gradually the fuel flow rate at constant air flow rate, and repeating the same procedure for different air velocities. The air and fuel flow rates were controlled by using mass flow controllers, Section 2.3.1. It was found that three types of flames could be observed when the fuel velocity increased at the same air velocity, Fig. 5.6. The flame was attached above the lean stability limit, then with the increase in fuel velocity, the flame lifted-off and the lift-off height increased until it reached a maximum value (maximum lift-off height) in which any further increase in fuel velocity did not affect the lift-off hight, flame (c) in Fig. 5.6. The flame stayed at this maximum lift-off height until it reached the rich limit. The same flame behavior has been observed with all the air velocities studied in this experiment. The lean stability limit was measured first by igniting the flame

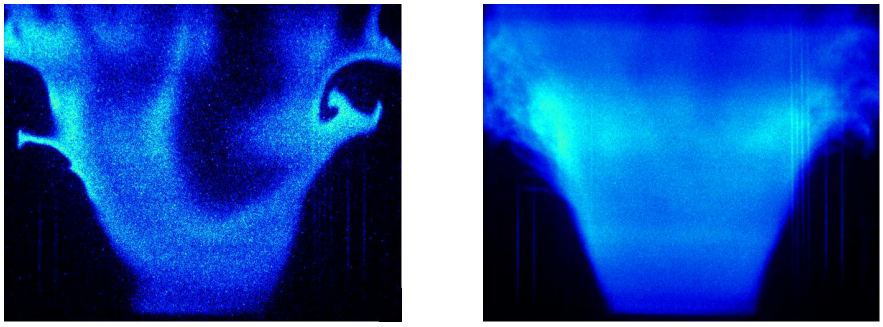

Figure 5.4: OH-PLIF images (a) instantaneous, (b) average over 200 images. U_{air} = 10 m/s, U_f = 5 m/s giving a global ϕ = 0.55. Image domain is 70×60 mm.

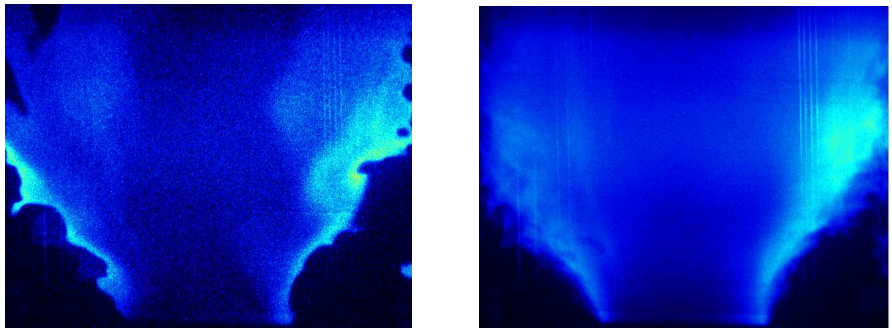

Figure 5.5: OH-PLIF images (a) instantaneous, (b) average over 200 images. U_{air} = 10 m/s, U_f = 5 m/s with swirl. Image domain is similar to Fig. 5.4.

in a stable condition, then the fuel flow rate was reduced gradually until the lean extinction observed. With the increase in air velocity, the stability region becomes wider due to the higher increase in the rich stability limit.

The lean and rich ignition limits have been also investigated in this experiment. By applying the strongest spark scenario used in the present work (3Hz sparks for 3 seconds) in different locations in the flow field and in particular the expected highest ignition probability locations, Section 5.2.7, the lean and rich ignition limits were identified. About 50 sparks were applied at each location of interest until the ignition was achieved. If so, the fuel flow rate was reduced gradually and the same procedure repeated. When ignition was not achieved at any location with such sparks, this velocity combination was decided to be the lean ignition limit. A similar method was used to determine the rich ignition limit. Fig. 5.6 shows that the ignitability region is much narrower than the stability region. A similar observation was found in the counterflow flame ignition, Section 4.2.4.

The main reason behind this observation could be related to the fact that the amount of heat flux away from the propagating edge flame front after the ignition is higher than that of an established continuous flame, as the flame front losses heat not only to its sides, but also to the flow ahead of it. This results in excessive reduction in the flame front temperature, which can lead to extinction. Another possible reason is that by reducing or increasing the fuel flow rate too much, the flame kernel after the ignition does not find a proper mixture to propagate through. Such case does not exist in the stable flame when the fuel flow rate reduces, as the stable flame always follows ξ_{st} iso-surface.

Figure 5.7 shows a similar graph of the swirl case. Both the stability limits and the ignition limits were determined as previously. The flame has the same three types with an increase in fuel velocity. It can be observed from Fig. 5.7

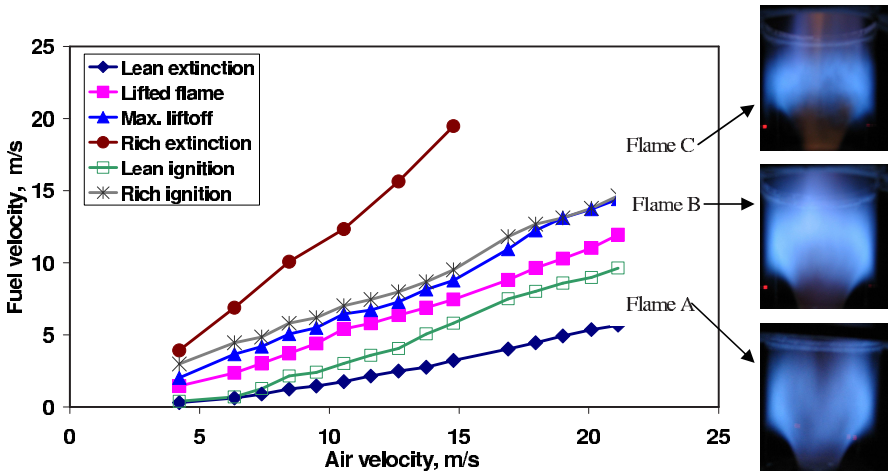

Figure 5.6: Stability limits, Ignition limits and different shapes of the bluff-body flame.

that both the stability and the ignition limits are much wider than the previous case. It should be mentioned here that the rich stability and ignition limits were not able to be measured above $U_{air} = 7$ m/s, as the flame does not extinguish even with the maximum fuel flow rate available in the mass flow controller used in this work. The other observation is that the ignitibility region is closer to the stability region than that of the previous case. This gives an indication that the enhancement of the mixing process with swirl, which was mentioned earlier, dominates in deciding whether the flame ignites or not.

5.2.4 Velocity and mixture fraction measurements

5.2.4.1 Velocity measurements

The axial and radial velocities in exactly the same burner have been measured recently by using the LDV technique (Dawson et al., 2007). The measurements were carried out on one flow condition only, $U_{air} = 10$ m/s ($Re = 1.67 \times 10^4$) without swirl and no fuel injection (i.e. $U_f = 0$), which is also the main condition

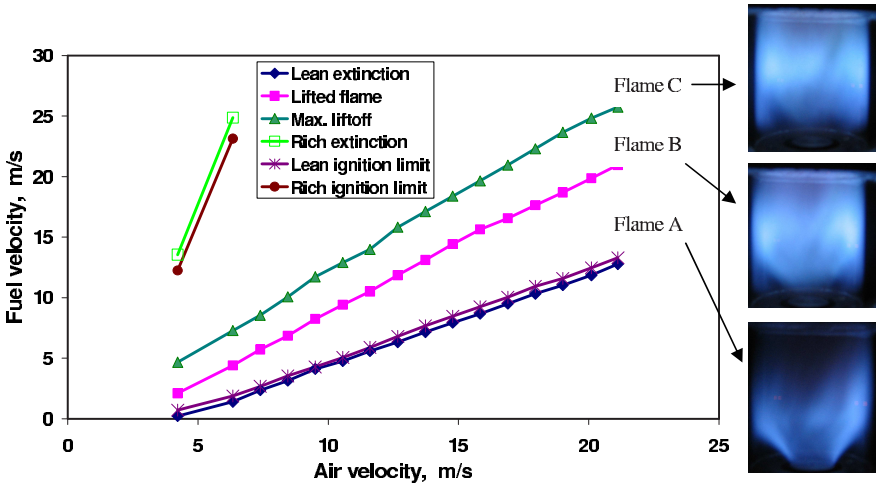

Figure 5.7: Stability limits, Ignition limits and different shapes of the swirl bluff-body flame.

in the present work. Five radial profiles were measured in which three of them were measured for both left-hand side (Lhs) and right-hand side (Rhs) of the burner to show the degree of symmetry of the flow.

These velocity measurements are reproduced here to assist later data interpretation. Figure 5.8 shows the radial profile of the mean axial velocity at five axial distances from the bluff-body. These measurements confirm the dimensions of the recirculation zone that have been collected from the smoke visualization of the recirculation zone (Section 5.1.2.1). It can be observed that the zero velocity iso-surface is located at about $r = \pm$ 10 mm up to $z =$ 15.5 mm, and then it shifts to $r = \pm$ 6 at about $z =$ 25 mm (1 D_b). This indicates that the width and the length of the recirculation zone are indeed about 1 and 1.5 D_b respectively. The reverse flow velocity reaches its maximum value of nearly 5 m/s at about z = 15.5 mm along the burner centerline. At $z =$ 50 mm, the flow up to $r =$ 10 mm has an almost a uniform velocity of about 8.5 m/s.

Figure 5.9 shows the r.m.s value of the axial velocity at the corresponding

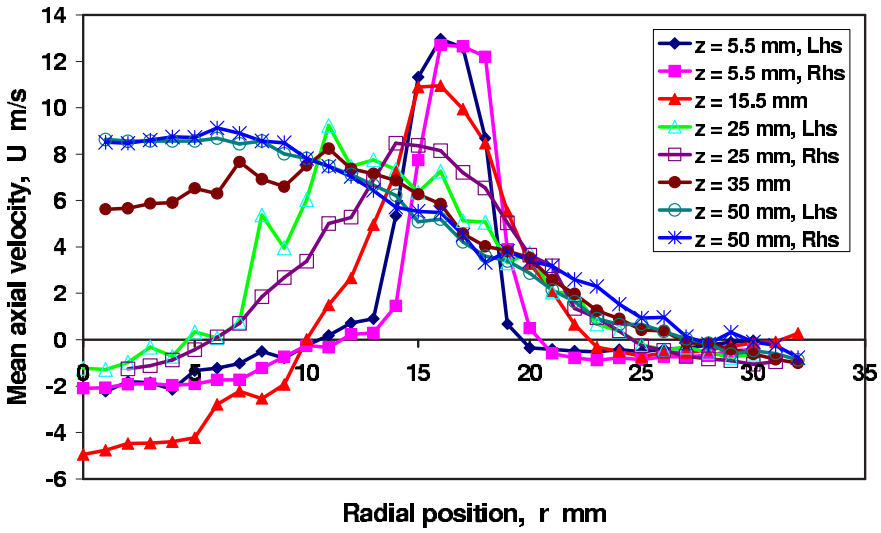

Figure 5.8: Radial distribution of the mean axial velocity, $U_{air} = 10$ m/s (Dawson et al., 2007).

locations. It can be observed that the turbulence in this flow peaks above the edge of the bluff-body, i.e. $r = \pm$ 12.5, and decays from both sides up to $z =$ 15.5 mm. This position corresponds to the maximum width of the recirculation zone. Above this location, the turbulence is relatively uniform, especially within the recirculation zone.

Figure 5.10 shows the radial profile of the mean radial velocity at the same axial location. The mean radial velocity has a maximum value of about 4 m/s at $z = 25$ mm above the edge of the bluff-body. All the other profiles are quite uniform within the recirculation zone with an average radial velocity of 1.5-2 m/s. The r.m.s value of the radial velocity increases as the axial distance above the bluff-body increases until a maximum value has been recorded at $z = 25$ mm along the centerline of the burner, Fig. 5.11. With further increase in the axial position, the r.m.s value decreases gradually. The r.m.s also peaks at the edge of the recirculation zone up to $z = 15.5$ mm. It should be mentioned that these axial

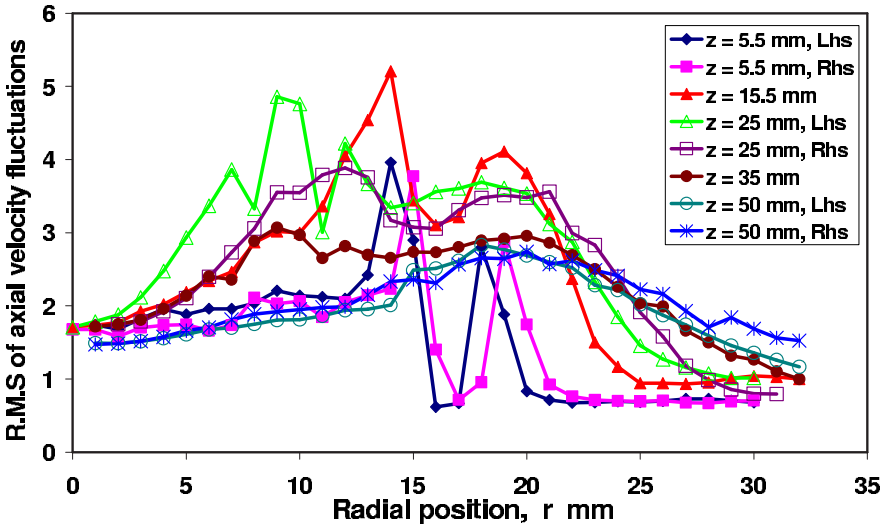

Figure 5.9: Radial distribution of the r.m.s. of the axial velocity, U_{air} = 10 m/s (Dawson et al., 2007).

and radial velocity measurements are in good agreement with the measurements of confined cone bluff-body flow of Taylor and Whitelaw (1984) and Pan et al. (1992a).

5.2.4.2 Mixture fraction distribution

The mixture fraction distribution has been measured by using PLIF of Acetone, section 2.4.1. A laser sheet of about 50 mm width passed through the quartz enclosure of the burner. Fuel was replaced by air in this experiments and the acetone was seeded in the "fuel" stream and carried by air. An area of 45×50 mm of the flow was covered by the ICCD camera to image the acetone distribution in this area of interest with an image size of 1079×1123 pixels giving a resolution of about 45 μm. The mixture fraction was measured through two stages of calculations. First, the bluff-body was raised a little to face the laser sheet in order to quantify the value of $\xi = 1$. Figure 5.12 shows an instantaneous and

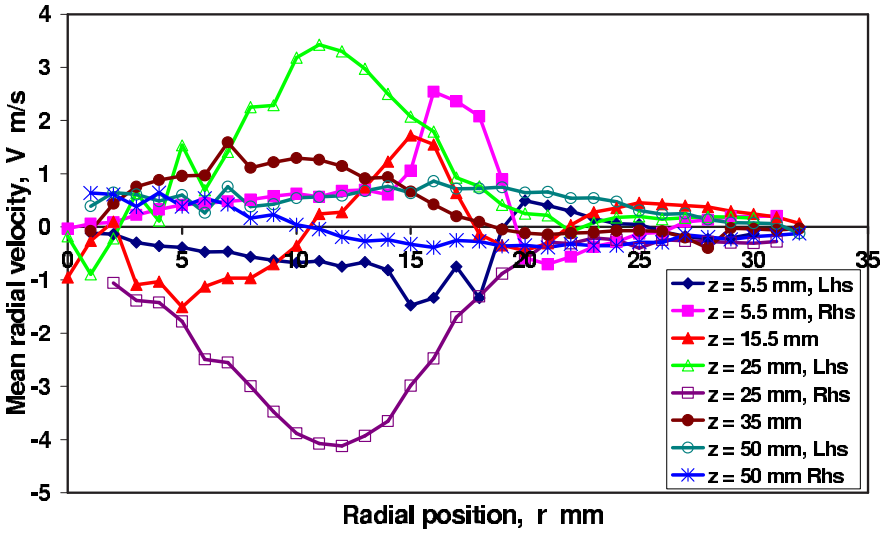

Figure 5.10: Radial distribution of the mean radial velocity, $U_{air} = 10$ m/s (Dawson et al., 2007).

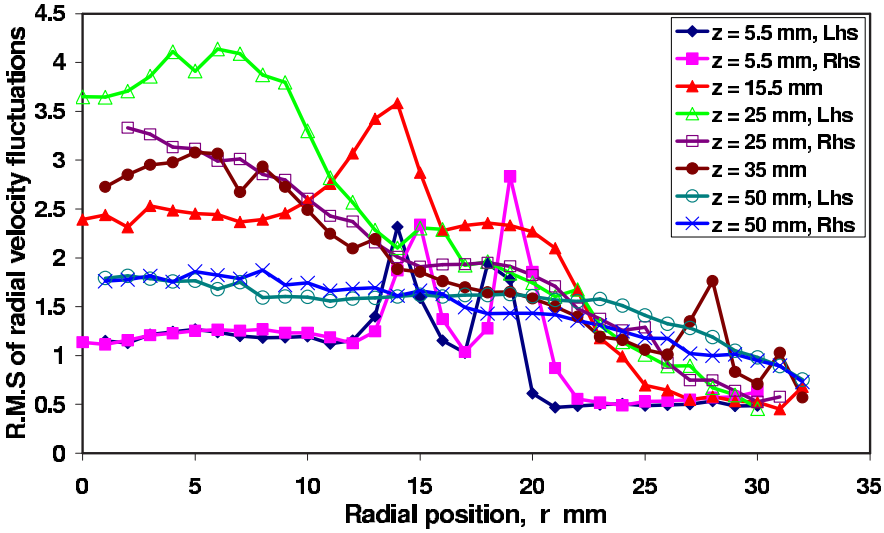

Figure 5.11: Radial distribution of the r.m.s. of the radial velocity, $U_{air} = 10$ m/s (Dawson et al., 2007).

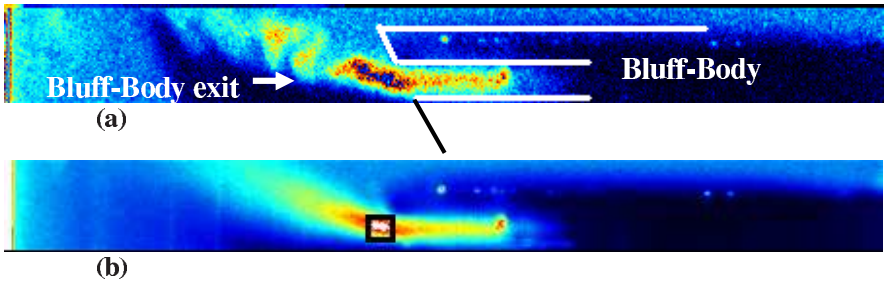

Figure 5.12: Raw acetone PLIF image of the fuel exit of the bluff-body; (a) instantaneous and (b) mean. $U_{acet} = 2.5$ m/s, $U_{air} = 0$.

the average acetone PLIF image of the fuel exit from the bluff-body after rising the bluff-body. The square in the image points to the area which was considered for calculating the value of 100% fuel. This area is about 0.7×0.7 mm, as 0.7 mm is equal to the slit width of the bluff-body. About 1000 images were taken with simultaneous measurement of the laser power variation with a Dye cell. The value of the fuel exit intensity was normalized by the intensity of the Dye cell shot by shot after doing all the necessary corrections, Section 2.4.1. The average of this normalized value was taken as a reference for the unity mixture fraction. It should be mentioned that the shot by shot variation of this normalized value does not exceeds 4%.

The second step was to normalize the intensity of the acetone PLIF in the main image with the Dye cell intensity after doing all the corrections. Then, all the normalized images were divided by the reference value of the unity mixture fraction to get the mixture fraction distribution. These two steps were repeated for the two conditions at which the mixture fraction have been measured, i.e. for the fuel velocities $U_f = 5$ and 8 m/s (simulated by $U_{acet} = 2.5$ m/s and 4 m/s when air replaced the fuel in the PLIF experiments) with $U_{air} = 10$ m/s. These two conditions were chosen, so that one is within the ignitability limits ($U_f = 5$

m/s) and the other one is above the rich ignition limit, Fig. 5.6.

It should be mentioned that the replacement of the fuel by air having equal mass flow rate in the fuel stream during the acetone PLIF experiments was done after comparing three options. They are as follows: the replacement of fuel by air having mass flow rate equal to the fuel mass flow rate, air having momentum equal to the fuel momentum $\rho_f U^2$ or air having velocity equal to the fuel velocity. ρ_f is the fuel density. Figure 5.13 shows the mean mixture fraction contour of these three options for the main case and it is evident that significant differences exist. However, the first option of using the "fuel" stream having the same mass flow rate as the fuel in the flame experiments was chosen to represent the actual fuel distribution because of the following reasons. First, to avoid the effect of the density difference between air and methane, which affects the intensity of the acetone in the fuel stream. Second, by comparing the ignition probability contour of this case shown in Fig. 5.29 with these three contours, it can be concluded that the values of the mixture fraction shown in Fig. 5.13a are quite reasonable and realistic. The other two contours have too rich mixture within the recirculation zone and also in areas, which have high probability of ignition. However, it should be cautioned that the first choice of air having mass flow rate similar to that of the fuel is still not 100% representative of the fuel distribution in the ignition experiments, as the effect of Re of the fuel jet on the mixing field is absent in this replacement because the air-acetone mixture has lower jet velocity (U_{acet} = 2.5 m/s).

Figure 5.14 shows an instantaneous, mean, and the r.m.s of the mixture fraction of the main case, i.e. $U_{acet} = 2.5$ m/s to simulate the case of $U_f = 5$ m/s. As mentioned in section 4.2, the lean, rich and stoichiometric mixture fraction limit of the methane are: $\xi_{lean} = 0.028$, $\xi_{rich} = 0.089$, and $\xi_{st} = 0.055$ respectively. The flammable range of the mixture fraction between ξ_{rich} and ξ_{lean} is shown with the

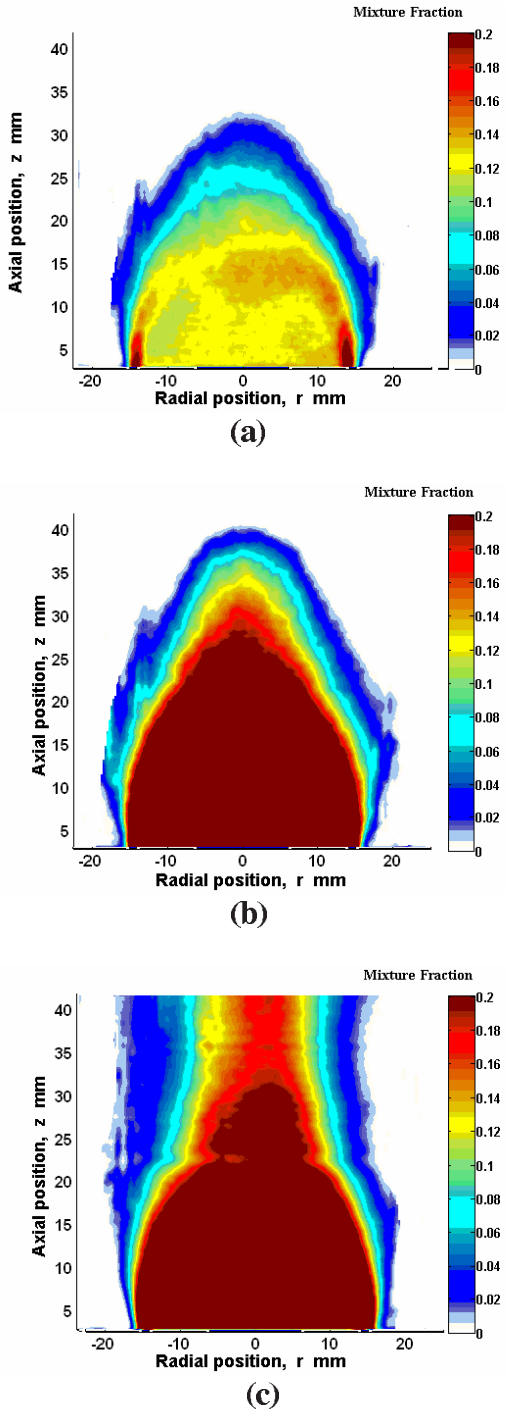

Figure 5.13: Mean mixture fraction with U_{air} = 10 m/s and U_{acet} = (a) 2.5 m/s, (b) 3.5 m/s and (c) 5 m/s, to simulate the case of U_f = 5 m/s.

arrow in Fig. 5.14b. It can be observed from the mean mixture fraction contour shown in Fig. 5.14 that the mean flammable region surrounds the recirculation zone with a thickness that varies between about 8 mm at the top of the recirculation zone along the centerline and 1 mm close to the exit of the burner. The fluctuations of the mixture fraction at this location are much higher than that at the top of the recirculation zone. This indicates that the ignitability area could be much wider than 1 mm close to the exit of the burner. Inside the recirculation zone, the mean mixture fraction is above ξ_{rich}, which indicates that the ignition may not be achieved inside the recirculation zone. In addition, it can be observed from Fig. 5.14c that the fluctuations in the mixture fraction are very low inside the recirculation zone. Finally, it can also be noted that the fluctuations of the mixture fraction are not zero above the recirculation zone.

Figure 5.15 shows mixture fraction distributions for the flow with $U_{acet} = 4$ m/s, i.e. to simulate the fuel injection at $U_f = 8$ m/s, with the air velocity kept constant at 10 m/s. The flammable region in this case shrinks dramatically around the recirculation zone and appears with reasonable thickness above $z = 1$ D_b. However, the area above the recirculation zone along the centerline still have mixture fraction values above the rich limit. This could be the reason behind the fact that this condition ($U_f = 8$ m/s) is above the rich ignition limit of this burner, Fig. 5.6. The r.m.s contour at this condition is nearly similar to the previous one with high fluctuations at the exit of the burner, and low and uniform fluctuations inside the recirculation zone.

It can be observed that a dramatic change happens in the mean mixture fraction values everywhere in the flow due to the increase in the fuel flow rate, even though the contribution of the fuel flow rate to the total flow rate at the exit of the burner is minor. This indicates that the distribution of the mixture fraction is very sensitive to any change in the fuel flow rate. The reason behind

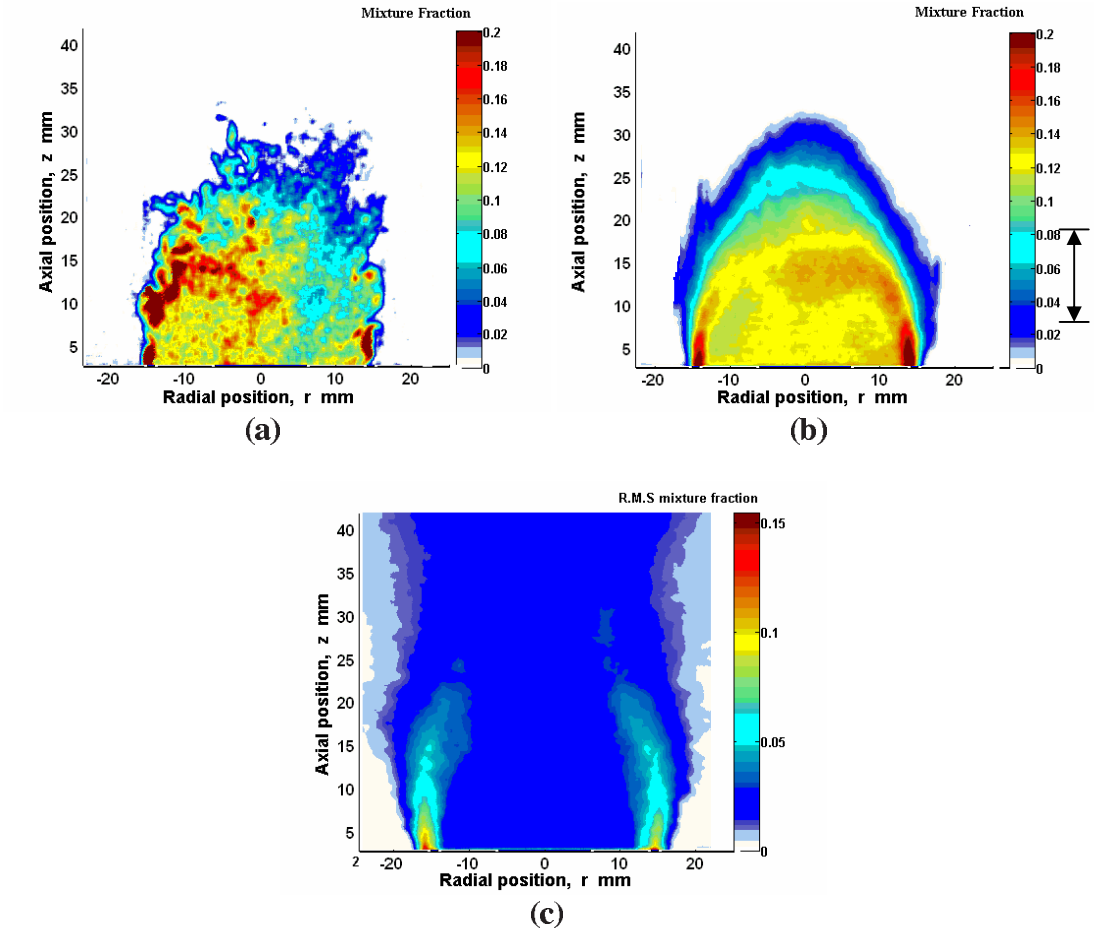

Figure 5.14: (a) Instantaneous, (b) mean and (c) r.m.s. mixture fraction measurements of the main case (U_{air} = 10 m/s, U_{acet} = 2.5 m/s).

this could be related to the fact that at the fuel exit the mixing between the fuel and the air streams may be thought of as a jet in cross-flow. In such a flow, the fuel stream bending mechanism in the air, which affects the mixing field later, depends significantly on the Reynolds number of the fuel stream (Yuan and Street, 1998).

The measured mixture fraction of the previous two cases has been used to calculate the flammability factor by integrating the pdf of the mixture fraction distribution between ξ_{rich} and ξ_{lean}, Eq. 3.3, which is used to interpret the ignition probability results in section 5.2.7. Fig. 5.16 shows the pdf of the mixture fraction distribution at three different locations, and the lean and the rich flammability limits.

Figure 5.17 shows an approximate mixture fraction distribution for the swirl case. Due to low signal to noise ratio, these measurements can not be trusted quantitatively. However, it is still clear from the mean mixture fraction, Fig. 5.17b, that the mixture fraction within the recirculation zone has lower values than those of the mixture outside the recirculation zone, i.e. in the area between $r = \pm 16$ and 25, $z = 5$ and 25. This behavior is opposite to the cases without swirl, in which the mixture inside the recirculation zone is richer than that out side the recirculation zone. Moreover, this distribution agrees with the observation that the flow impinged on the sidewall at around a distance of 1 D_b (Balachandran, 2005). This indicates that the mixture fraction distribution is altered significantly by the swirl.

5.2.5 Visualization of ignition and flame propagation

The ignition event from the moment of spark discharge to the stabilization of the flame has been visualized by using the high-speed camera at different flow conditions and different locations in the flow. In addition, different types of failed

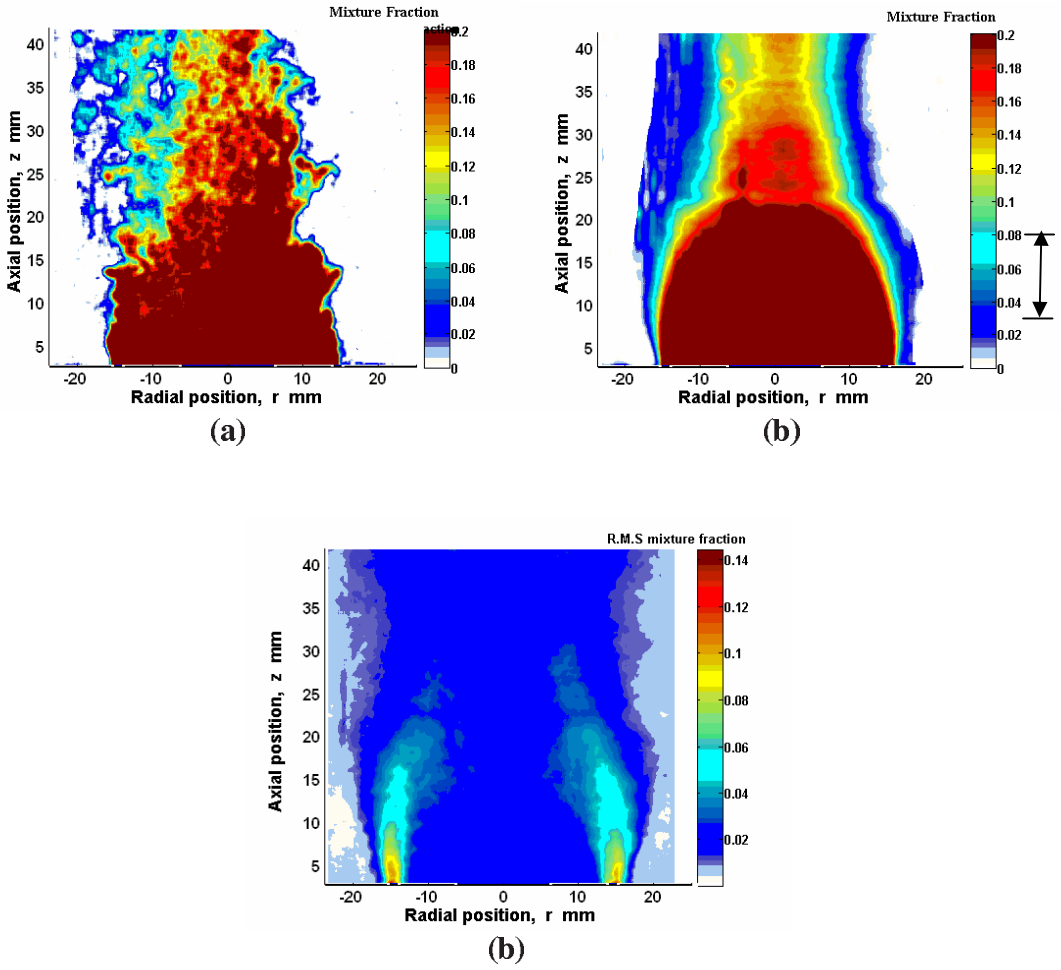

Figure 5.15: (a) Instantaneous, (b) mean and (c) r.m.s. mixture fraction measurements of the case of $U_f = 8$ m/s ($U_{air} = 10$ m/s, $U_{acet} = 4$ m/s).

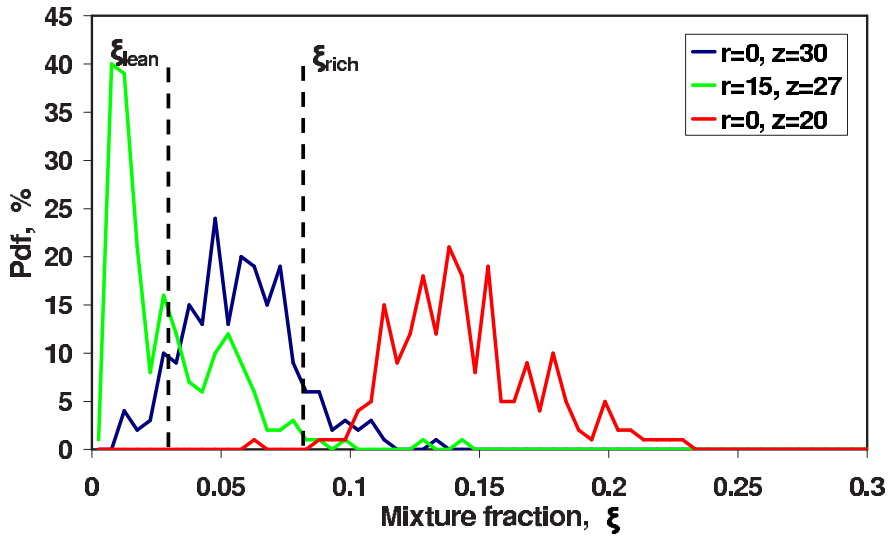

Figure 5.16: Probability density function (pdf) of the mixture fraction at different locations in the mixing field. U_{air} = 10 m/s, U_f = 5 m/s (U_{acet} = 2.5 m/s).

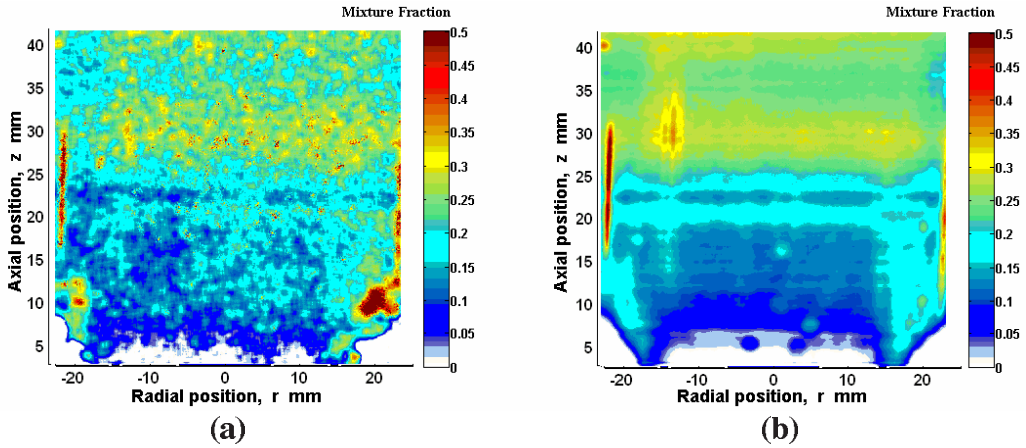

Figure 5.17: Approximate mixture fraction measurements of U_{air} = 10 m/s, U_{acet} = 2.5 m/s and 60° swirl ; (a) instantaneous and (b) mean.

ignition events have been visualized. The structure of the flame front during the propagation after the ignition has been studied by using OH-PLIF imaging at certain time delays from the spark. These results are presented in this section.

5.2.5.1 Direct visualization

The behavior of the flame propagation after the ignition in the bluff-body burner depends more on the ignition location relative to the recirculation zone, rather than on the flow condition. Figure 5.18 shows high-speed camera images of a successful ignition event at $z = 25$ mm, $r = 15$ mm in the main flow condition used in this work, $U_f = 5$ m/s. In this case the flame was ignited outside the recirculation zone, which results in axial flame propagation at the beginning to light up that side of the flow first, and then the flame propagates towards the other side in order to establish the flame, Fig. 5.18. It takes between 40 to 50 ms, on average, for the flame to stabilize from this ignition location. This flame propagation behavior can be understood from the mean velocity and mixture fraction measurements, Fig. 5.8 and Fig. 5.14 respectively. The axial velocity in the location of ignition is much higher than the radial velocity. Moreover, the mean flammable contour passes through the ignition location. Therefore, it is expected that the flame propagates in the axial direction first before it propagates radially and tangentially to the other side of the burner.

If the spark is located inside the recirculation zone, different flame propagation behavior can be observed after the ignition. Figure 5.19 shows an ignition event with similar flow conditions and camera settings like the previous case. The spark was applied at $z = 25$ mm, $r = 0$ mm. Unlike the previous case, the flame propagates towards the bluff-body first, and then starts propagating from the bluff-body downstream until the whole flame stabilizes. It can be observed that the flame front is not visible up to about 10 ms after the ignition, then

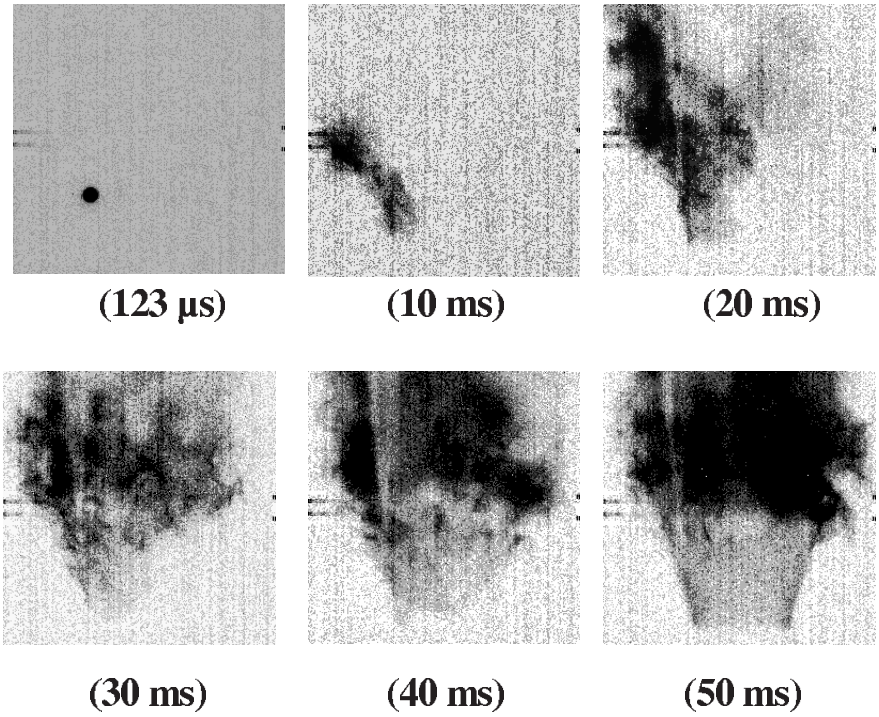

Figure 5.18: Instantaneous high-speed camera images of an ignition event with 8100 fps and exposure time 113 μs. $U_{air} = 10$ m/s, $U_f = 5$ m/s. Ignition at $z = 25$ mm, $r = 15$ mm. The images cover a region of 70×70 mm.

it appears after that at the bluff-body. This can be explained by the fact that the flame front starts propagating after the spark in presumably rich mixture in which the heat release during this period is very low to be detected by the camera. However, when the flame front reaches the bluff-body, it propagates close to the stoichiometric mixture in which the heat release becomes much higher and the flame becomes visible. Similar observation was detected before in the gas turbine ignition and this period was named as an "ignition delay" and lasts for about 13 ms (Naegeli and Dodge, 1991). In addition to the mixture fraction effect on the flame propagation, there is also another effect from the flow velocity, which has a negative value in the axial direction at the location of ignition. This pushes the flame kernel towards the bluff-body. It should be mentioned that the behavior of the flame propagation does not depend on the flow conditions within the ignitability limits, i.e. Figs. 5.18 and 5.19 are representative of all U_f and U_{air}.

If swirl is introduced to the flow, the flame propagates after the ignition as shown in Fig. 5.20. The flame is ignited at $z = 25$ mm, $r = 20$ mm. The flame front after the spark follows the flow rotation, apparently in the tangential direction. This rotation continues for about 30 ms until one side of the flow is lightened up and then the flame starts propagating from this side to the other side of the burner. The flame with swirl takes about 70 ms on average to stabilize, which is much longer than the case without the swirl. This longer flame establishment time can be related to the tangential rotation of the flame at the beginning, which does not exist in the previous two cases. It is also conceivable that the edge flame speed decreases due to the intense turbulence, as observed also for the jet (Fig. 3.33). Sparking at $z = 25$ mm, $r = 0$ with swirl does not result in a flame.

In case of failed ignition events, three types have been observed in this burner.

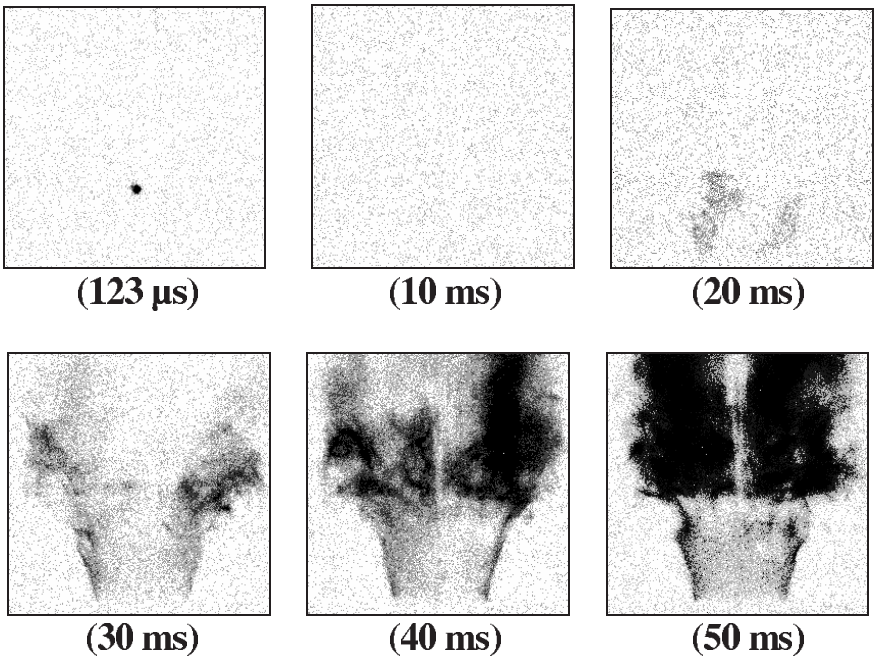

Figure 5.19: Instantaneous high-speed camera images of an ignition event with 8100 fps and exposure time 113 μs. $U_{air} = 10$ m/s, $U_f = 5$ m/s. Ignition at $z = 25$ mm, $r = 0$ mm. The images cover a region of 70×70 mm.

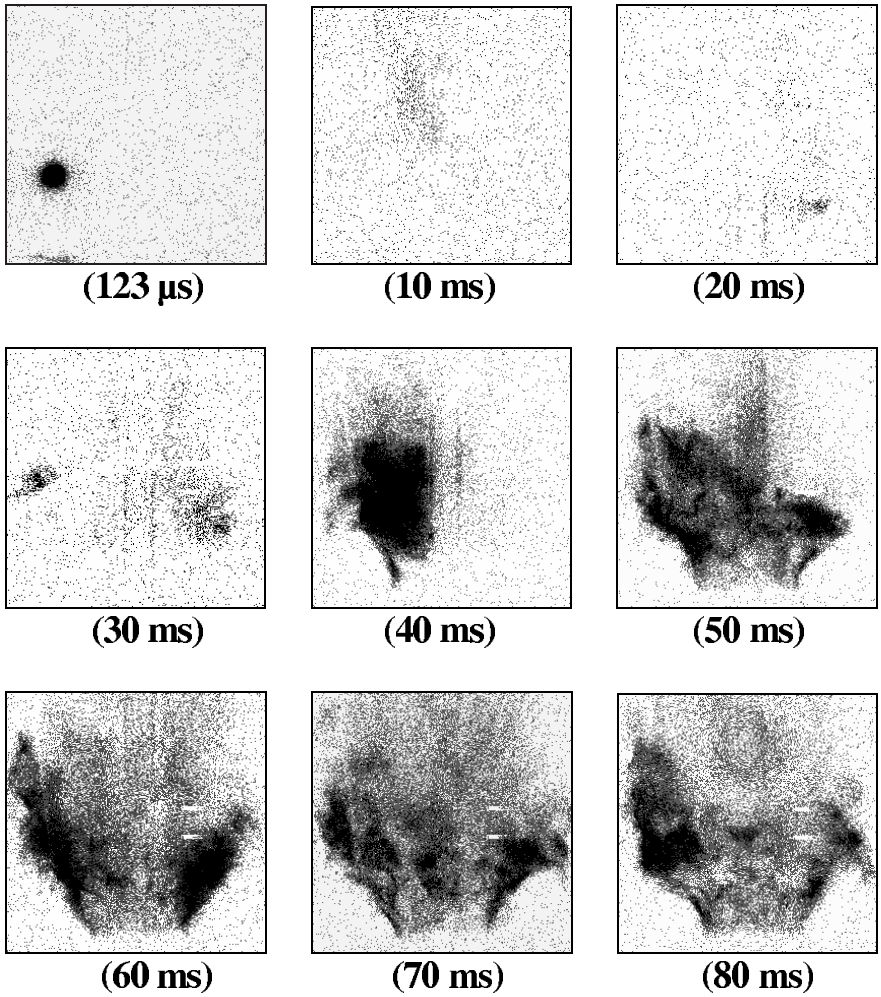

Figure 5.20: Instantaneous high-speed camera images of an ignition event with 8100 fps and exposure time 113 μs. U_{air} = 10 m/s, U_f = 5 m/s and 60° swirl. Ignition at z = 25 mm, r = 20 mm. The images cover a region of 70×70 mm.

First, a spark followed by no indication of any flame kernel initiation. Second, flame kernel initiation after the spark followed by flame propagation downstream of the burner that subsequently blows off. Third, flame propagation after the spark and stabilization of the flame for few milliseconds or less, followed by global flame extinction. The last type is very rare to happen; however, the first two types are common. Figure 5.21 shows the second type of the failed ignition events, in which the flame kernel propagates after the spark downstream and then blows off without establishing the flame. The flame front disappears from the image domain very quickly in less than 2 ms. However, in the third type of the failed ignition events, Fig. 5.22, the flame front propagated and the stable flame was almost achieved. However, for some reason which could be due to passing of a large eddy or the recirculation zone temperature was too low, the flame is broken from the middle and then extinguished.

5.2.5.2 OH-PLIF

To visualize the flame structure during evolution from the spark location to the stable flame, OH-PLIF imaging was performed using the technique mentioned in Section 2.4.2. The image domain covers an area of 70×50 mm of the flow. About 100 images of different successful ignition events at certain time delays from the spark were taken in order to compare the instantaneous flame front structures and then be in a position to calculate the average. It should be emphasized that images from successful ignition events only have been used. Figure 5.23 shows instantaneous OH-PLIF images of the flame front for the flow without swirl and the spark at $z = 25$ mm, $r = 0$ (i.e. inside the recirculation zone). It can be observed that there is no certain structure for the flame front (i.e. edge flame or triple flame) during the propagation. There seems to be a large variability of the flame shape in different ignition events. The general trend of the flame

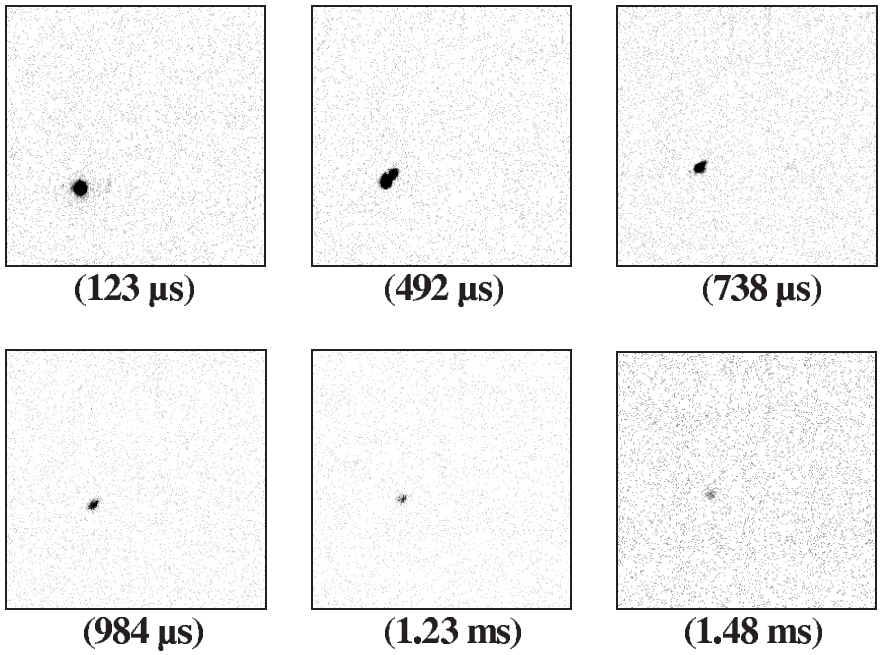

Figure 5.21: Instantaneous high-speed camera images of a failed ignition event with 8100 fps and exposure time 113 μs. $U_{air} = 10$ m/s, $U_f = 5$ m/s. Ignition at $z = 25$ mm, $r = 15$ mm. The images cover a region of 70×70 mm.

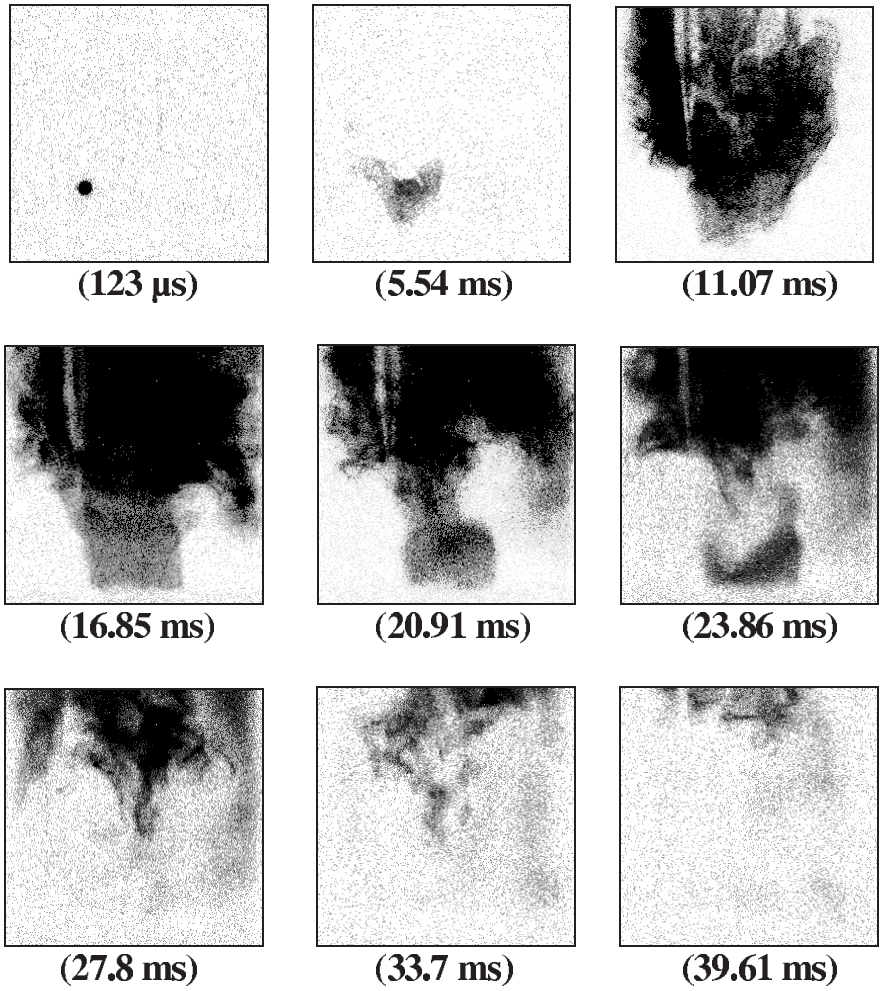

Figure 5.22: Instantaneous high-speed camera images of a failed ignition event with 8100 fps and exposure time 113 μs. $U_{air} = 10$ m/s, $U_f = 5$ m/s. Ignition at $z = 25$ mm, $r = 15$ mm. The images cover a region of 70×70 mm.

propagation direction agrees with the fast camera images shown in Fig. 5.19. On average, Fig. 5.24, the flame structure looks like a sphere, which expands toward the bluff-body, but at certain time, about 12 ms, it start propagating axially to form the stable flame structure. The OH radical is at high concentration around the stoichiometric iso-surface location, indicated by a comparison of Fig. 5.24 (30 ms) with Fig. 5.14b.

The instantaneous flame front structures during propagation in the flow with swirl are shown in Fig. 5.25. The spark was located at $z = 25$ mm, $r = 20$ mm. The flame becomes more irregular than the previous case due to the high turbulence created by the swirl. The flame propagates from one side to the other with a behavior similar to Fig. 5.20. The average OH-PLIF images of this case shown in Fig. 5.26 confirm the propagation behavior of this kind of flow without showing any certain structure of the flame front during the propagation. It should be mentioned that the images at 20 ms in Fig. 5.25 and 5.26 are not for the stable flame, as there was some technical difficulties in this experiment, which prevented continuing it for longer times. This data can be useful for validation of modeling methods that aim to capture flame propagation in inhomogeneous mixtures.

5.2.6 OH* chemiluminescence emission measurements

The OH* chemiluminescence emission during the spark and the subsequent flame propagation was recorded by a PMT, section 2.6. The PMT system was focused on the ignition plane about 500 mm from the spark location, which was at $z = 25$ and $r = 15$ mm. Figure 5.27 shows the raw signal of a typical OH* trace of a successful ignition event and the signal after a smoothing filter has been applied. It can be observed that the spark itself in the raw signal gives high intensity of OH*. This intensity, as mentioned before in Section 3.2.8, depends mainly at the mixture strength at the moment of the spark and it does not depend on the

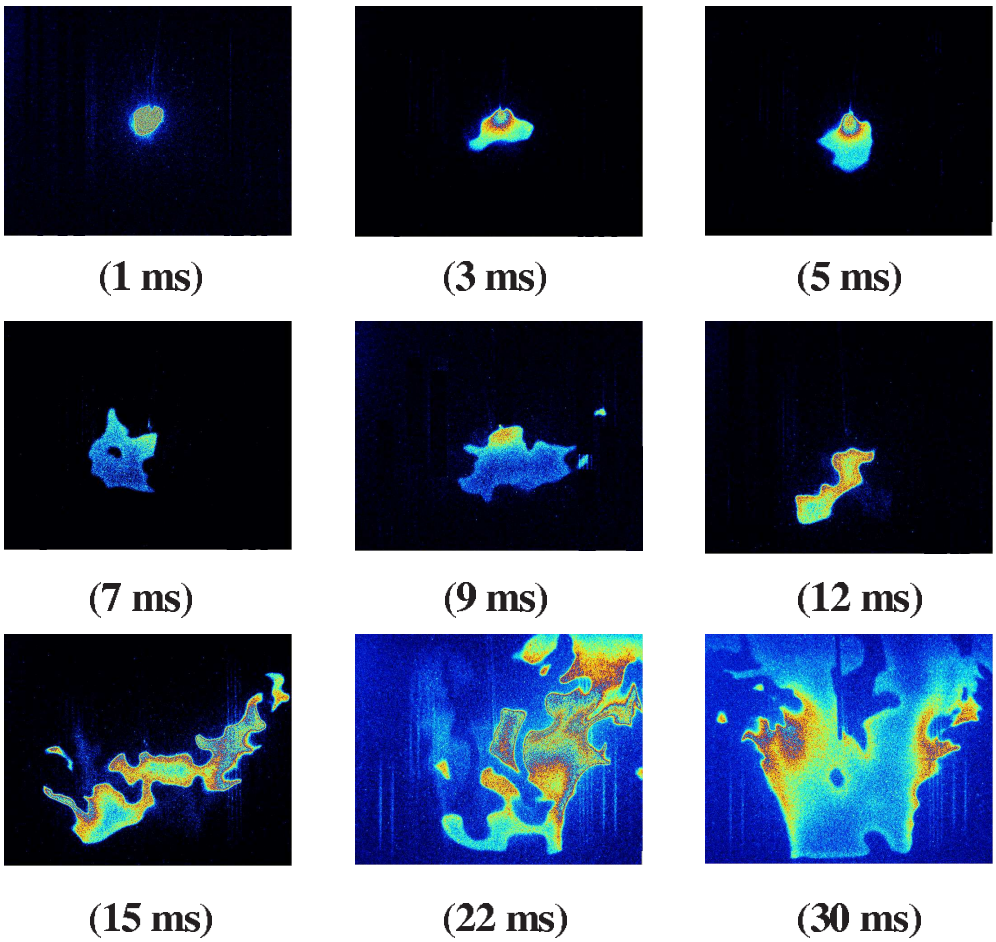

Figure 5.23: Instantaneous OH-PLIF images of different ignition events. U_{air} = 10 m/s, U_f = 5 m/s. Ignition at z = 25 mm, r = 0 mm. The images cover a region of 70×50 mm.

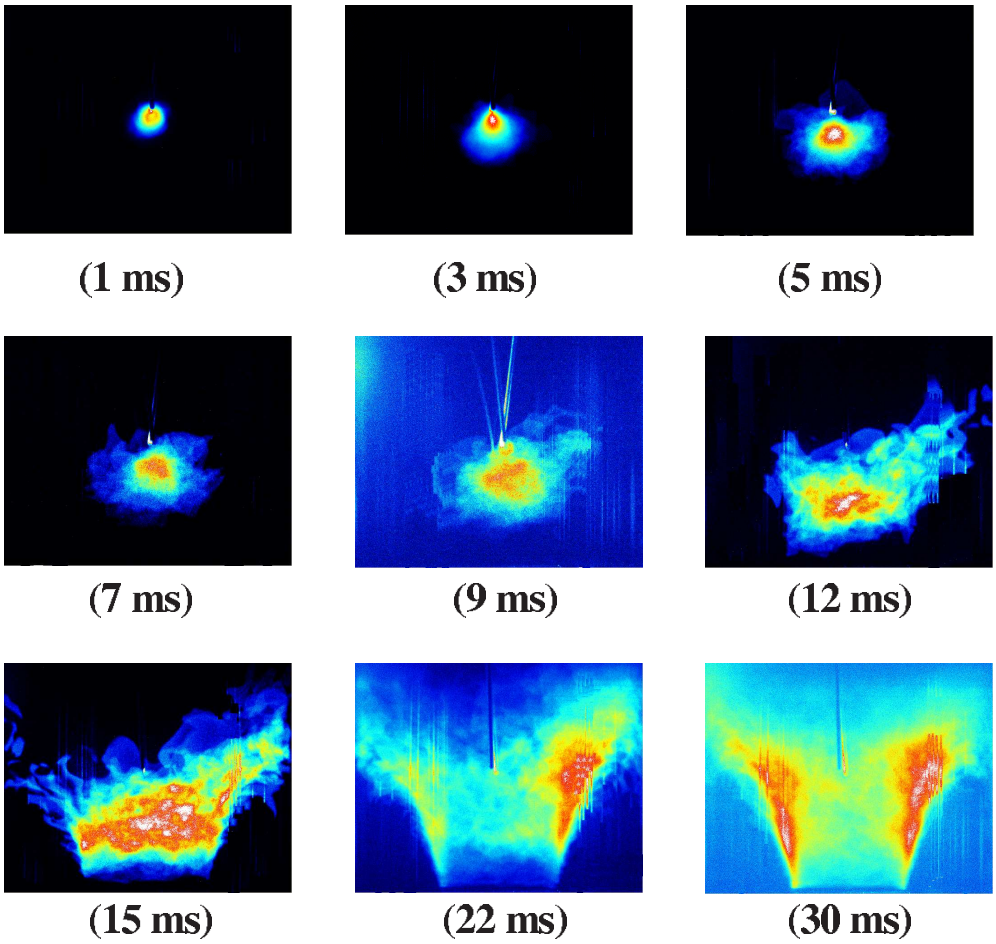

Figure 5.24: Average OH-PLIF images at different times from the spark. U_{air} = 10 m/s, U_f = 5 m/s. Ignition at z = 25 mm, r = 0 mm. The images cover a region of 70×50 mm.

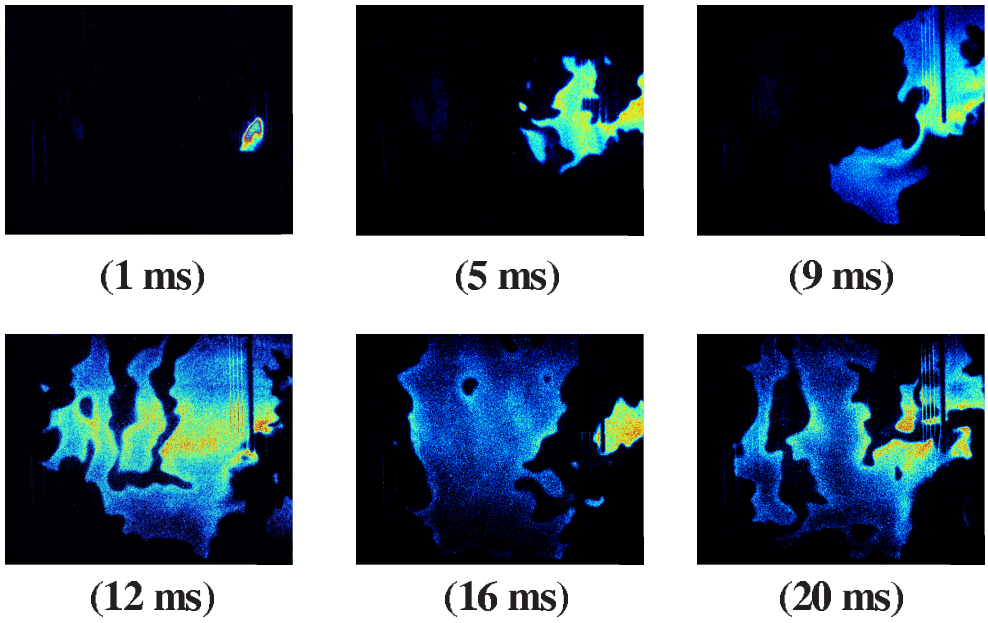

Figure 5.25: Instantaneous OH-PLIF images of different ignition events. U_{air} = 10 m/s, U_f = 5 m/s and 60° swirl. Ignition at z = 25 mm, r = 20 mm. The images cover a region of 70×50 mm.

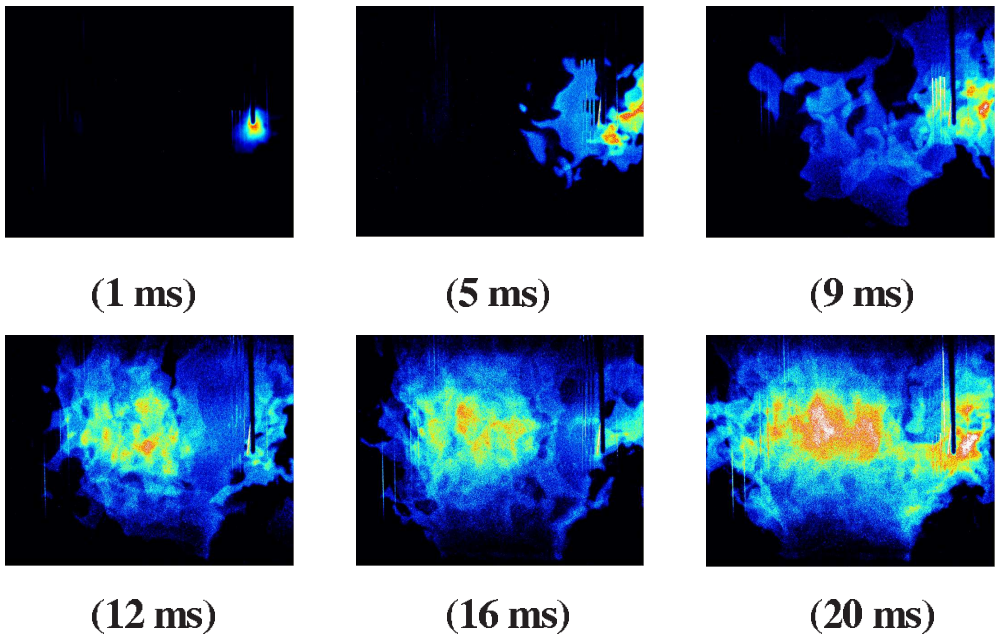

Figure 5.26: Average OH-PLIF images at different times from the spark. U_{air} = 10 m/s, U_f = 5 m/s and 60° swirl. Ignition at z = 25 mm, r = 20 mm. The images cover a region of 70×50 mm.

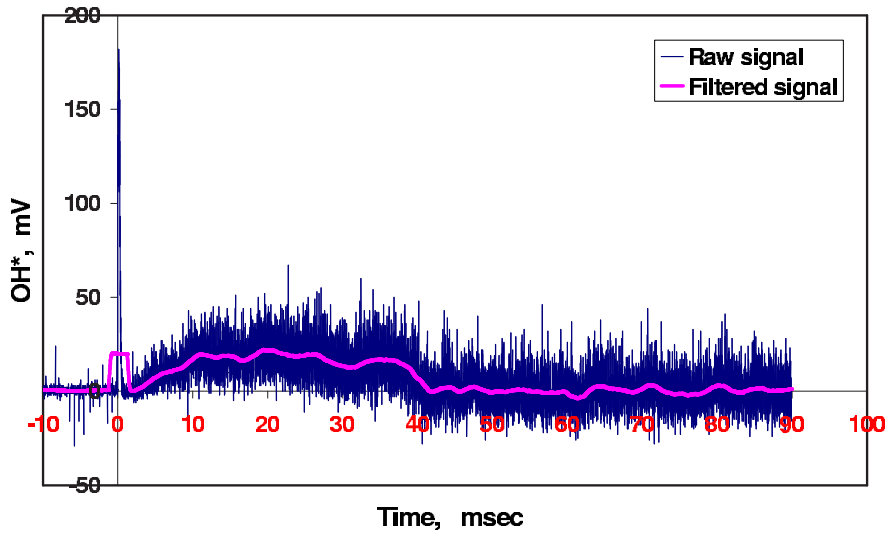

Figure 5.27: OH* emission of the spark and the flame development. Spark: 200 mJ and 500 μs. Conditions are similar to Fig. 5.22.

flow velocity. After this peak due to the spark, the OH* falls, but then starts increasing again with the flame propagation until it reaches a maximum value at about 20 ms after the spark, which corresponds to the complete lightening up of one side of the flame in Fig. 5.18. Then, the OH* decreases until it reaches a stable value when the stable flame is achieved.

Figure 5.28 shows the OH* emission of an instantaneous successful ignition and of two kinds of failed ignition events. As mentioned before, one of the failed ignition modes is when a spark appears without any flame kernel initiation. This kind is marked as 'A' in Fig. 5.28. It can be noted that after the peak of the spark in this kind of failed ignition, there is no indication of OH* intensity. However, in the curve marked 'B' which represents a failed ignition event after the flame propagation, it can be seen that the OH* emission is quite similar to the successful event, but with slightly lower values. About 100 events were recorded for both successful and failed ignition, and the average of both are shown in

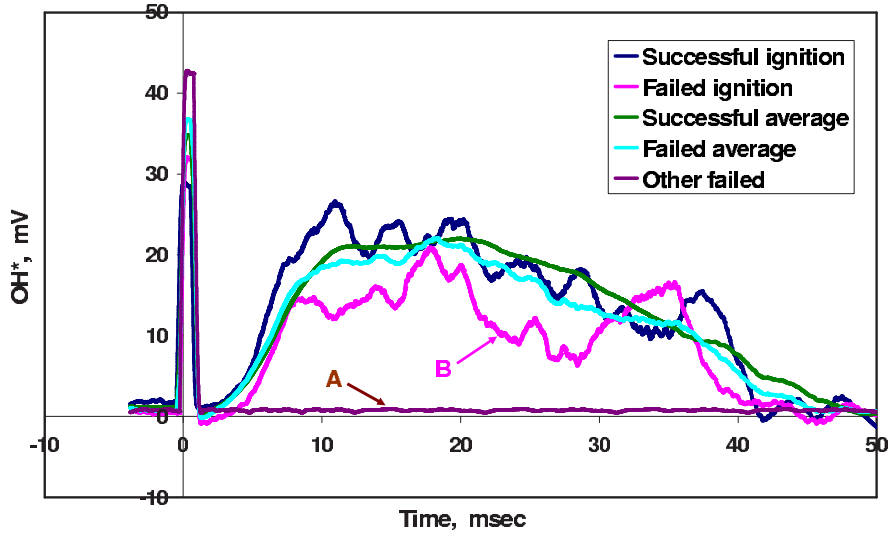

Figure 5.28: OH* hysteresis of successful and flailed ignition events. Spark: 200 mJ and 500 μs. Conditions are similar to Fig. 5.22.

Fig. 5.28. These two average traces are not too different, which indicates that differentiation between the failed and the successful ignition is hard if only PMT was used.

5.2.7 Ignition probability

The ignition probability was measured by applying 50 sparks at each location of interest. The number of successful events that result in a stable flame was divided by 50 to calculate the ignition probability. At all the conditions studied in this section, the spark has energy of 200 mJ and duration of 500 μs. The spark was created between two tungsten electrodes having 1 mm diameter each with sharp ends and the spark gap was 2 mm. Each of the ignition probability contours measured here was assembled from a matrix of 25×25 points across and along the burner, respectively. The ignition probability in this type of flow configuration was found to be very sensitive to the change in air and fuel velocities, which

Table 5.1: Ignition probability flow conditions.

Flame	U_f m/s	U_{air} m/s	60° vane swirl	Global ϕ	Remarks
$NB1$	5	10	NO	0.55	main case
$NB2$	8	10	NO	0.80	effect of fuel velocity
$NB3$	4	10	NO	0.37	effect of fuel velocity
$NB4$	7.5	15	NO	0.55	effect of air velocity
$SNB1$	5	10	YES	0.55	effect of swirl
$PB1$	-	10	NO	0.7	premixed flame

as shown in Fig. 5.13, change appreciably the mixture fraction distribution. In addition, introducing the swirl to the flow changes the ignitability region quite considerably. In the next sections, these parameters are investigated separately. Table 5.1 shows the flow conditions examined in this section.

5.2.7.1 Effect of fuel velocity

Three different fuel velocities are investigated in terms of the ignition probability at the same air velocity of $U_{air} = 10$ m/s. These fuel velocities are $U_f = 4$, 5 and 8 m/s and correspond to the three flames in Fig. 5.6. The case of $U_f = 5$ m/s ($NB1$) is the main case of investigation. Figure 5.29 shows the ignition probability contour for this case. By comparing the ignition probability contour with the flammability factor contour, calculated from the measured mixture fraction of this case, shown in Fig. 5.30, the following observations can be made. First, the highest ignition probability region is located between $r = \pm$ 10 to 20 mm and $z =$ 10 to 20 mm, which is close to the highest flammability factor region in Fig. 5.30. They do not match fully, as the ignition can be achieved in some areas that show zero flammability factor such as the area between $r = \pm$ 10 to 15 mm, and $z =$

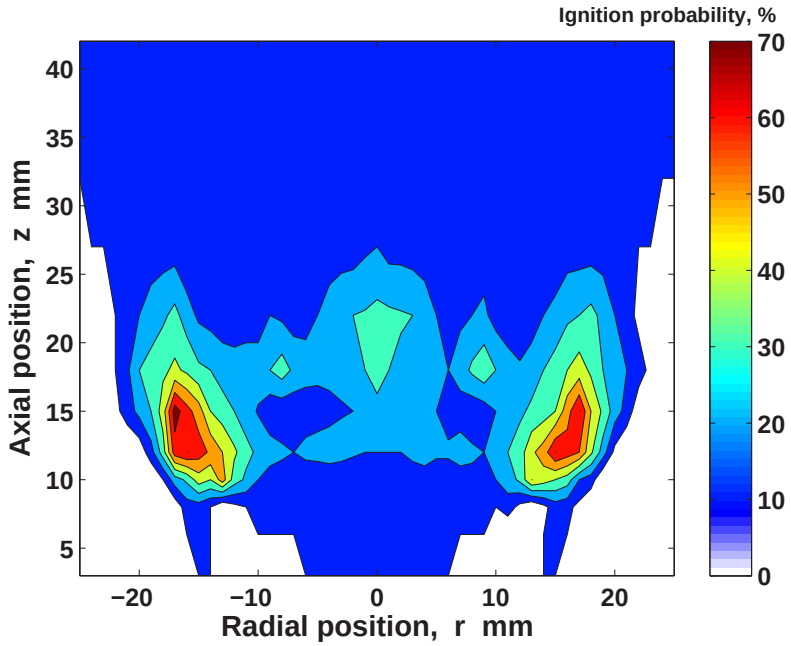

Figure 5.29: Ignition probability contour of U_{air} = 10 m/s and U_f = 5 m/s ($NB1$). Spark: 200 mJ and 500 μs.

10 to 15 mm. This can be explained by the fact that the average axial and radial velocity at this region have high values, 8 m/s and 2.5 m/s respectively. These high velocities can play a role in convecting the heat from the spark location to the flammable region and igniting the flame. A similar observation was found in the counter-flow ignition, section 4.2.4.

Second, the other high probability area is between z = 20 and 25 mm at the centerline. Again, part of this area lies within the flammable region, but the rest does not. Third, the recirculation zone is a non-flammable area with mixture fraction values above the ξ_{rich}, but still ignition with about 10% probability was observed, except the region close to the bluff-body exit in which the ignition probability is zero. This can be related to the effect of the high velocity close to the exit, which can result in blowing off the flame kernel and also to the rich

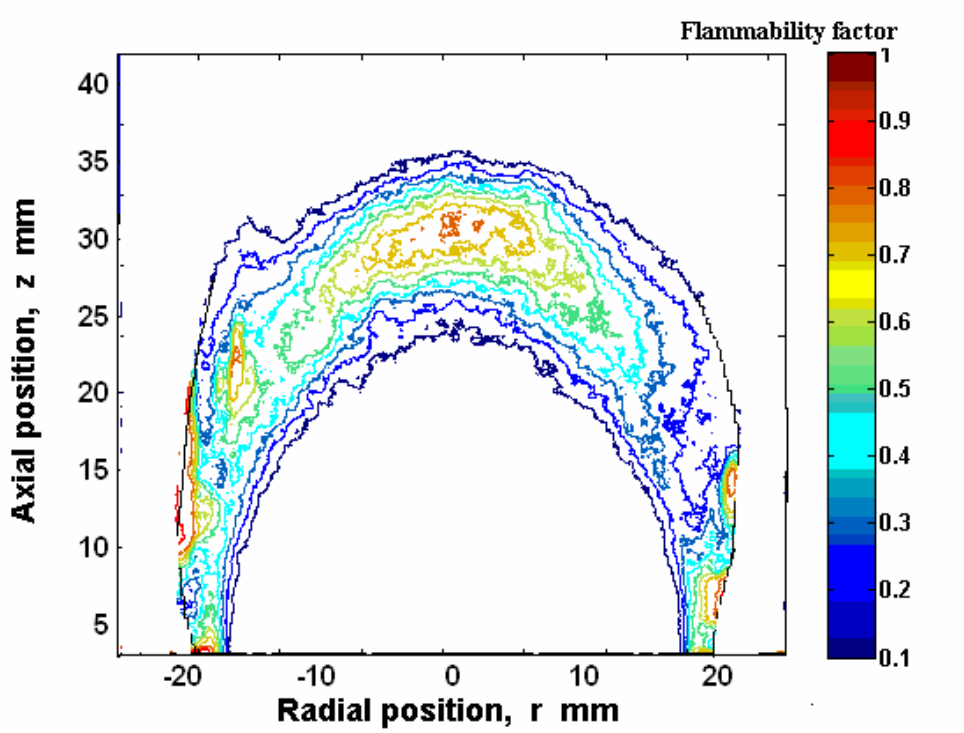

Figure 5.30: Calculated flammability factor contour from the measured mixture fraction of the flow condition of $U_{air} = 10$ m/s and $U_f = 5$ m/s ($U_{acet} = 2.5$ m/s).

mixture in this region. However, it can be expected that the radial velocity fluctuation, which is quite high inside the recirculation zone (Fig. 5.14), has a part in causing the ignition inside the recirculation zone by convecting the spark heat radially towards the flammable region. In addition, the spark duration (500 μs) is much longer than the average τ_k within the recirculation zone, which is about 80 μs. This can cause that many mixture fraction values pass through the spark gap and results in a time history effect, in which ignition can happen away from the spark location. These observations put more emphasis on the fact that a discrepancy between the ignitability and the local flammability factor exists, especially in such a complex flow field. Above $z = 30$ mm, the flow seems to have a premixed characteristic with global equivalence ratio close to 0.55. That is why the ignition probability above this location becomes uniform with about 10% probability.

It is important to mention here that the accuracy of the flammability factor contour shown in Fig. 5.30 is questionable for two main reasons. First, because of the normalization procedure mentioned in Section 5.2.4.2, as the mixture fraction distribution in the flow field has not been imaged simultaneously with the mixture fraction value at the fuel exit (i.e. $\xi = 1$). Second, due to the replacement of the fuel with air, in the fuel stream, having the same mass flow rate in the acetone PLIF experiments. These two reasons can cause error in representing the actual mixture fraction distribution. This can be considered an additional reason behind the discrepancy between the ignitability and the flammability regions.

Figure 5.31 shows the probability of only creating a flame kernel, rather than establishing a whole flame. This is classified earlier as the second type of failed ignition. This ignition probability contour includes also the successful ignition events that have been presented in Fig. 5.29. It can be observed that up to $z = 20$ mm, this probability is identical with the ignition probability of this case shown

in Fig. 5.29. That means that up to this location, any creation of flame kernel after the spark will result in a successful ignition. However, above this location, differences can be seen between the two probabilities. All the flammable region between $z = 20$ and 30 mm creates high probability of flame kernel initiation with about 25% more than the ignition probability in the same area. This can be attributed to the axial velocity, which increases in this region. Therefore, the flame kernel speed is less than the local velocity that results in convecting the flame kernel downstream without being able to propagate upstream towards the bluff-body and establishing the flame. It should be mentioned that the successful ignition events from sparks inside the recirculation zone may not be necessarily due to initiation of the flame kernel. As shown in the fast camera images in Fig. 5.19, after the spark, there is no indication of any flame kernel propagation inside the recirculation zone. However, the flame start propagating at the flammable region close to the burner exit. On the other hand, the OH-PLIF images in Fig. 5.23 show that there is OH radical inside the recirculation zone after the spark. This inconsistency could be attributed to that the high-speed camera could not detect such low OH intensity in this region. Further experiments are needed to clarify this point.

In case of increasing the fuel velocity to 8 m/s ($NB2$) and keeping the air velocity the same, no successful ignition can be achieved at any location in the flow field. As a result, this condition is above the ignition limit of this flame, Fig. 5.6. However, flame kernel initiation with downstream propagation was observed, especially in the region above $z = 25$. By looking at the flammability factor contour shown in Fig. 5.32, it can be noted that the non-flammable region extends above the recirculation zone to more than $z = 40$ with a dramatic change in the mixing field compared to the main case ($NB1$). This could give an explanation for not having any successful ignition at this flow condition, as the

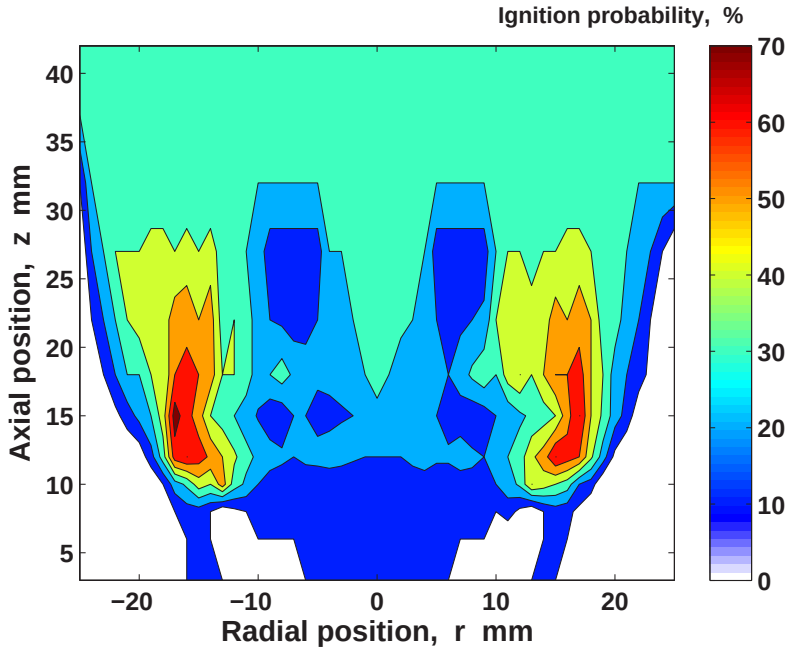

Figure 5.31: Probability contour of successful flame kernel initiation (rather than whole flame ignition). U_{air} = 10 m/s and U_f = 5 m/s. Spark: 200 mJ and 500 μs.

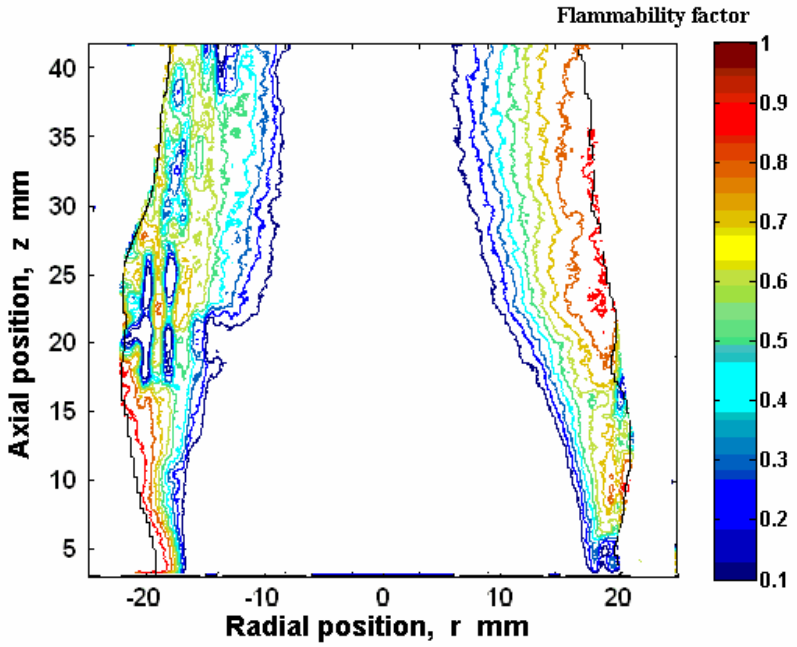

Figure 5.32: Calculated flammability factor contour from the measured mixture fraction of the flow condition of $U_{air} = 10$ m/s and $U_f = 8$ m/s ($U_{acet} = 4$ m/s).

flame front always faces a very rich mixture during propagation that quenches the flame. Furthermore, a comparison of Fig. 5.32 with Fig. 5.30 suggests that this mixing configuration is very sensitive to the change in the fuel velocity, as explained earlier in Section 5.2.4.2.

Figure 5.33 shows the ignition probability of $U_f = 4$ m/s ($NB3$) with the same air velocity. It should be mentioned that the global equivalence ratio of this case is about 0.37, which is below the lean premixed limit of the methane air flame ($\phi = 0.5$). The ignition probability contour shows that the ignition is only available within a thin mixing layer surrounding the recirculation zone. This is another indication for how sensitive the ignition is in respect to the change in fuel velocity. Unfortunately, the mixture fraction in this condition could not be measured due to the low value of the signal to noise ratio of the acetone-PLIF

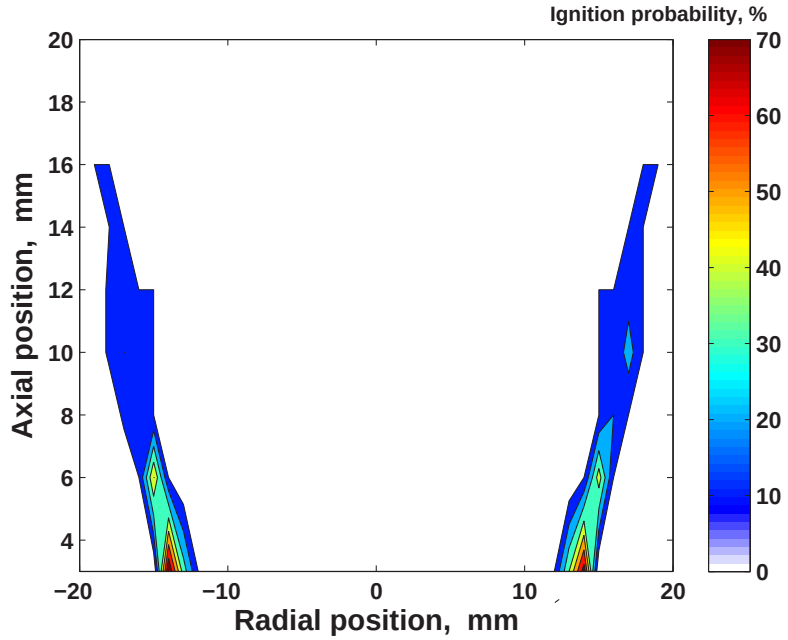

Figure 5.33: Ignition probability contour of U_{air} = 10 m/s and U_f = 4 m/s ($NB3$). Spark: 200 mJ and 500 μs.

images and more data are necessary to fully reveal the connection between the ignition probability and the flammability region.

If the fuel is premixed with air far upstream of the burner exit to create a mixture with $\phi = 0.7$, the ignition behavior is completely different from the non-premixed case. Figure 5.34 shows the ignition probability of this premixed case ($PB1$). The ignition probability is 100% everywhere in the flow within the enclosure length (80 mm above the bluff-body). This indicates that the available spark energy and duration are adequate to ignite the flame in such configuration and any failed ignition in the non-premixed cases is due to the local mixture and fluid mechanics conditions. Above the enclosure, air is entrained and hence the equivalence ratio decreases. Therefore, a consistent reduction in the ignition probability can be observed up to $z = 130$.

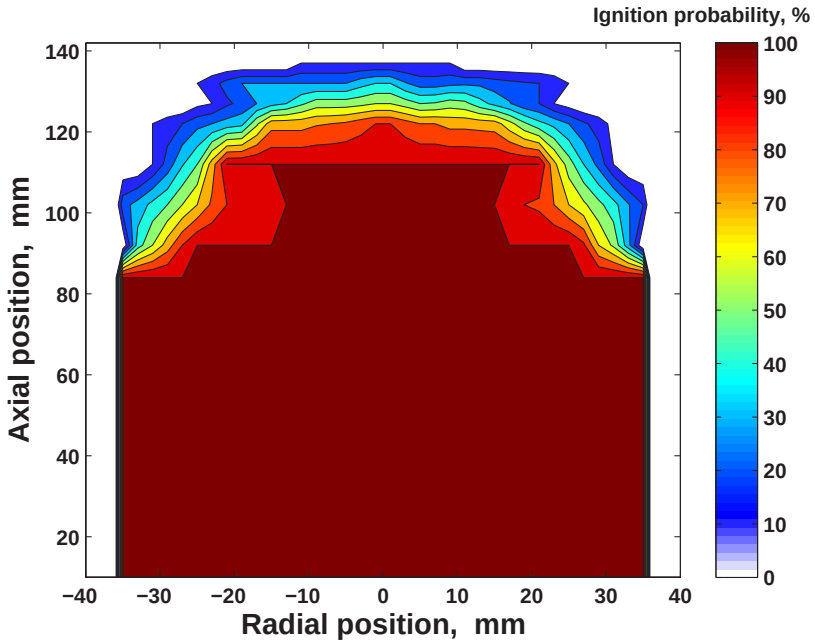

Figure 5.34: Ignition probability contour of premixed flame, U = 10 m/s and ϕ = 0.7 ($PB1$). Spark: 200 mJ and 500 μs.

5.2.7.2 Effect of air velocity

The effect of increasing the air velocity on the ignition probability has also been examined. The air velocity was increased to $U_{air} = 15$ m/s, and the global equivalence ratio was kept similar to the main case, $\phi = 0.55$, by increasing the fuel velocity proportionally to $U_f = 7.5$ m/s. The spark parameters were also kept similar to the main case. Figure 5.35 shows the ignition probability of this case ($NB4$). Although the air to fuel ratio is similar to the main case, a different ignition probability contour can be observed by comparing with Fig. 5.29. The ignition probability increases considerably within the recirculation zone. This indicates that the mixture fraction within the recirculation zone becomes more flammable due to the change of the recirculating fuel and air mass ratio as the flow velocity changes. Unfortunately, no mixture fraction data is available for this case. In addition to the increasing influence of the axial and radial velocities on the convection of the spark heat as these velocities have greater values within the recirculation zone. The ignition probability above $z = 20$ is similar to that in the main case. However, the values are slightly higher at about 20%.

5.2.7.3 Effect of swirl

By introducing a 60° vane swirl to the current flow configuration, the mixing process is expected to be enhanced significantly as Fig. 5.17 suggests. This is due to the higher turbulence. In this case, all the flow conditions and the spark parameters were kept similar to the main case. Figure 5.36 shows the effect of the swirl on the ignition probability contour ($SNB1$). It can be noted that the highest ignition probability region becomes closer to the burner exit, which can be considered as indication of the rapid mixing. In addition, no ignition was observed inside the recirculation zone and the ignitability region extends radially until it touches the enclosure. This ignitability behavior agrees well with the approximate

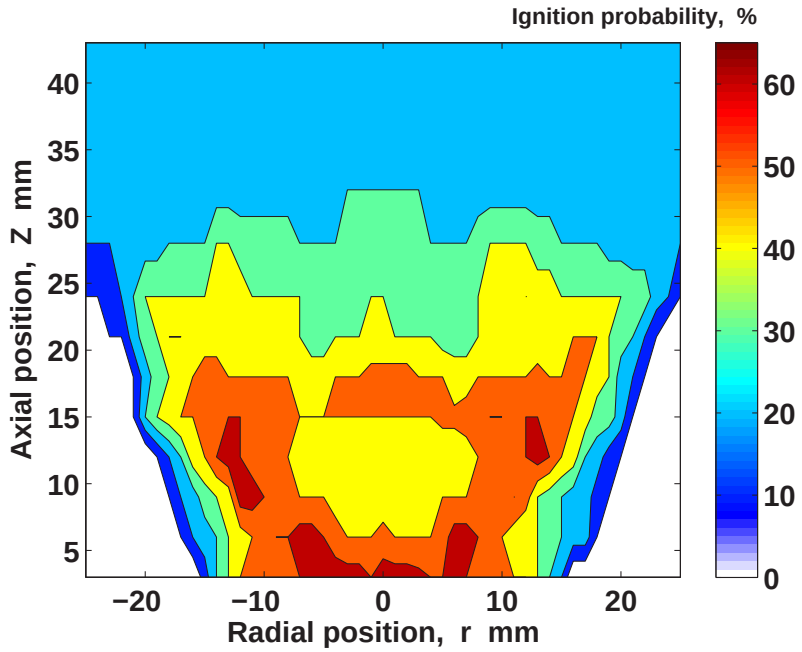

Figure 5.35: Ignition probability contour of U_{air} = 15 m/s and U_f = 7.5 m/s ($NB4$). Spark: 200 mJ and 500 μs.

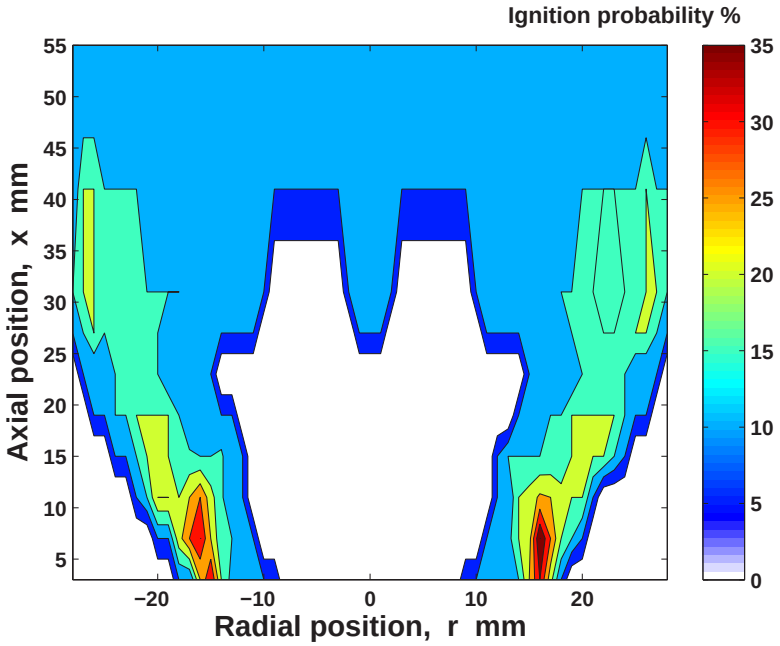

Figure 5.36: Ignition probability contour of U_{air} = 10 m/s, U_f = 5 m/s and 60° swirl ($SNB1$). Spark: 200 mJ and 500 μs.

mean mixture fraction measurements shown in Fig. 5.17b, as the mixture within the recirculation zone has quite lower values than those of the mixture outside the recirculation zone. As mentioned in the ignition visualization, section 5.2.5.1, the flame kernel after the spark close to the enclosure rotates tangentially. Therefore, the quenching of the flame kernel by the enclosure does not exist. The ignition probability becomes uniform with a value of 10%, which suggests that the mixture fraction above $z = 40$ becomes as in the previous case.

5.3 Conclusions

- A new turbulent non-premixed bluff-body burner with radial fuel injection was developed in order to study the spark ignition characteristics in a complex flow

configuration similar to the actual gas turbine combustor.

- The velocity measurements of the cold flow field follow the expected patterns in this flow and confirm the previous observations using smoke visualization. The width and the length of the recirculation zone are about 1 and 1.5 D_b respectively.

- The mixture fraction distribution was measured by using PLIF of acetone seeding in the fuel stream, and the mean and r.m.s of the mixture fraction were obtained. The mixture fraction values show high sensitivity to the fuel and air velocities. In addition, the average flammable region surrounds the recirculation zone.

- The direct visualization of the flame shows three different shapes, attached, lifted and maximum lift-off, depending on the air and fuel velocities. Similar shapes were found if swirl was introduced to the flow.

- The stability limits are much wider than the ignitability limits if the bluff-body was used without swirl. However, with the swirl, the stability limits expands considerably and the ignition limits become closer to the stability limits.

- The direct visualization of the ignition events shows that the direction that the flame propagates after the spark depends more on the ignition location than on the flow conditions. Ignition outside the recirculation zone results in axial propagation first at one side, followed by radial and tangential propagation to the other side. However, ignition inside the recirculation zone results in flame propagation towards the bluff-body edges to stabilize the flame.

- In case of using swirl, ignition is possible only if the spark is outside the recirculation zone. The flame kernel after the spark rotates tangentially with the flow until the whole flame lights up part by part.

- Three types of failed ignition have been observed in this flow configuration; a spark followed by no indication of flame kernel, a spark followed by flame kernel initiation and propagation downstream of the burner and extinction, and a spark

resulting in flame propagation and flame stabilization for few milliseconds only followed by blow off. The last one is rare.

- Instantaneously, the OH-PLIF images show no particular structure of the flame front during propagation. However, on average, the flame expands as a sphere up to certain point when it starts forming the shape of the stable flame.

- The OH* emission was recorded for successful and failed ignition events. The flame takes between 40 to 50 ms on average to stabilize after the ignition. However, differentiation between successful ignition, and the second or the third type of failed ignition event is not possible with this technique.

- The ignition probability contour of the main case studied here, $U_{air} = 10$ m/s, $U_f = 5$ m/s, shows that the highest ignitability regions are close to the highest flammability regions shown in the flammability factor contour. However, the ignition still can be achieved in locations that are outside the flammable region especially inside the recirculation zone. The discrepancy between the ignitability region and the flammability region was attributed to local and non-local fluid mechanics effects, and to the long spark duration used in this investigation.

- The present study suggests that simultaneous mixture fraction and velocity measurements at the moment of the spark are essential to fully correlate the ignition probability results. In addition, the distribution of the mixture fraction should be accurately quantified by using actual fuel in the acetone PLIF experiments.

- The probability of flame kernel initiation is wider than the probability of whole flame ignition.

- The mixture fraction distribution, and as a result the ignition probability, is very sensitive to the change of the fuel and air velocities. Different ignition probabilities were obtained with $U_{air} = 10$ m/s, $U_f = 5$ m/s, and with $U_{air} = 15$ m/s, $U_f = 7.5$ m/s, even though both have the same global equivalence ratio.

- The ignition probability of the swirl case shows that the highest ignition probability is at the exit of the burner, which is possible due to the quick mixing achieved when swirl is used. No ignition was observed inside the recirculation zone.

- In case of a premixed flow, 100% ignition probability was obtained within the enclosure limit, which shows that the spark parameters used in this flow configuration are adequate for ignition.

Chapter 6

Summary and Suggestions for Further Research

Spark ignition of various turbulent non-premixed flame configurations have been experimentally studied in order to have more understanding of this type of spark ignition. The present study provides details for the fundamental aspects of spark ignition in turbulent non-premixed flames, which aim to help in solving the high-altitude relight problem in the aviation gas turbine.

Turbulent non-premixed jet, counter-flow and bluff-body flames were investigated in terms of the ignition probability and the parameters affecting it. These parameters were found to be related to the spark igniter and to the global and local flow conditions. A custom-made ignition unit that allows separate control of spark duration and energy was specially designed and built to examine these parameters. In addition, different flow velocities and fuel dilutions were also examined in the flow configurations mentioned earlier. The successful ignition, defined as the spark follows by a flame propagation and establishment of the flame, was correlated with the local flow velocity and the measured mixture

fraction by using acetone PLIF. The early stage of the flame kernel growth and the flame propagation were studies and visualized by using high-speed imaging and OH PLIF.

In the next two sections, general conclusions of the present work are mentioned followed by suggestions for future research.

6.1 Summary and Conclusions

- The ignition probability nearly always decreased with increasing the flow velocity. However, in the bluff-body flames, the mixing field showed high sensitivity to the change in the fuel and air velocities and increasing the air velocity tended to increase the ignition probability, especially within the recirculation zone.

- Simultaneous measurements of local velocity in the turbulent jet at approximately the spark location and of ignition success showed that failed sparks were statistically associated with high local velocities.

- The ignition probability decreased with increasing air volume fraction in the fuel stream at the same flow velocity in the jet and counter-flow flames.

- A severely reduced ignition probability resulted when trying to ignite at conditions close to the extinction limit. Moreover, it is not possible to ignite the flame if the flow velocity exceeds 90% of the extinction velocity.

- The ignition probability contours of the cases studied here show that the highest ignitability regions are close to the highest flammability regions determined by the flammability factor contour. However, the ignition still can be achieved in locations that are outside the flammable region and that was attributed to local (strain rate) and non-local (heat convection) effects.

- The probability of ignition can be zero at locations well inside the flammable region. That was related to the flame kernel at these locations experiences large

adverse velocities and hence cannot propagate and establish the flame.

- The probability of flame kernel initiation is wider than the probability of whole flame ignition.

- The ignition probability improved with an increase in spark energy. Short spark duration is more effective in high velocity regions, while long duration gives the highest probability in low velocity locations.

- The effects of the other spark parameters (electrode diameter and spark gap) are in full agreement with the trends from ignition of premixed mixtures. The ignition probability increases with thinner electrodes and with wider gaps.

- In the case of a premixed flow, 100% ignition probability was obtained at the burner exit or within the enclosure limit, which shows that the spark parameters used in this flow configuration are adequate for ignition.

- The early flame kernel growth rate has been measured with different flow and spark parameters. The results show that higher growth rate correlated with higher ignition probability for all parameters studied, except for jet velocity. For high jet velocities, the initial kernel may grow quickly, but the ignition probability clearly decreases.

- Three types of failed ignition have been observed in these flow configurations; a spark followed by no indication of flame kernel, a spark followed by flame kernel initiation and propagation downstream and extinction, and a spark resulting in flame propagation and flame stabilization for few milliseconds then blowing off. The last one is rare and it has not been observed in the jet flame.

- The high-speed visualization of the ignition events shows a greater dependence of the way of the flame propagation after the spark on the ignition location and on the flow conditions.

- In bluff-body flames, ignition outside the recirculation zone results in axial propagation first at one side, followed by radial and tangential propagation to the

other side. However, ignition inside the recirculation zone results in downstream flame propagation at the bluff-body edges to stabilize the flame. In case of using swirl, ignition is possible only if the spark is outside the recirculation zone.

- The OH-PLIF study showed that, in the jet, the flame front following the ignition has a spherical shape initially, but quickly became an edge flame with a front that propagated upstream until it the flame stabilized at a certain liftoff height. In the counter-flow, the flame expands as an edge flame, with no evidence of triple flame structure. In the bluff-body, instantaneously, no particular structure of the flame front was found. However, on average, the flame expands as a sphere up to certain point when it starts forming the shape of the stable flame.

- The flame propagation speed in the jet was estimated to lie between 3 to 6 S_L, increasing with an increase in jet velocity. However, the relative edge flame speed in the counter-flow is higher than S_L for the premixed flame and is less than S_L for most of the radial travel of the non-premixed flame. These estimates should be treated with caution because of the error due to curve fitting and the estimate of the flow velocity at the flame position. Modeling efforts should more properly use the direct measurements of flame locations.

- The lift-off height after the ignition was always equal to the lift-off height of the decreasing velocity branch of the height-velocity hysteresis loop of the jet lifted flames.

- The stability limits are much wider the ignitability limits if the bluff-body was used without swirl. However, with the swirl, the stability limits expands considerably and the ignition limits become closer to the stability limits.

- The calibration of OH*/CH* ratio with the mixture fraction at the moment of the spark is non-monotonic over the whole range of interest of the mixture fraction.

- The data provides a useful validation set for unsteady turbulent combustion

models, for example those based on LES.

6.2 Suggestions for Further Research

- The present study suggests that simultaneous mixture fraction and velocity measurements at the moment of the spark are essential to fully correlate the ignition probability results.

- The distribution of the mean mixture fraction should be accurately quantified in the bluff-body configuration by using actual fuel in the acetone PLIF experiments.

- Simultaneous OH-PLIF and PIV measurements at the flame front position during propagation are useful to accurately measure the relative edge flame propagation speed.

- The calibration of CN* with the mixture fraction is recommended for the future research in order to have simultaneous correlation between the local mixture fraction and the successful of ignition.

Appendix A

Ignition Unit Characteristics

The ignition unit used in the present work consists of, as mentioned in Section 2.2, four main components; a transformer, variac, ignition coil and control unit. Before using this unit, the following safety instructions should be considered:

- Before connecting the mains, the four parts should be connected internally as follows: *Connect the variac to the transformer. *Connect the ignition coil to the variac. *Connect the control unit to the ignition coil through the red and black wires as shown in Fig. 2.10.

- Connect the transformer and the control unit to the mains.

- Before switching on the control unit, make sure that the variac indicator is at zero voltage. If the variac indicator is at a higher voltage value when the control unit is being switched on, an IMMEDIATE damage can occur to the system.

- Switch on the control unit and then choose an appropriate voltage value on the variac depending on the spark energy and duration required, following the calibration in Fig. A.1. However, under any circumstances, the chosen voltage value MUST NOT INCREASE OVER 230 volt.

- The spark duration can be controlled from the button on the control unit labeled as “width”.

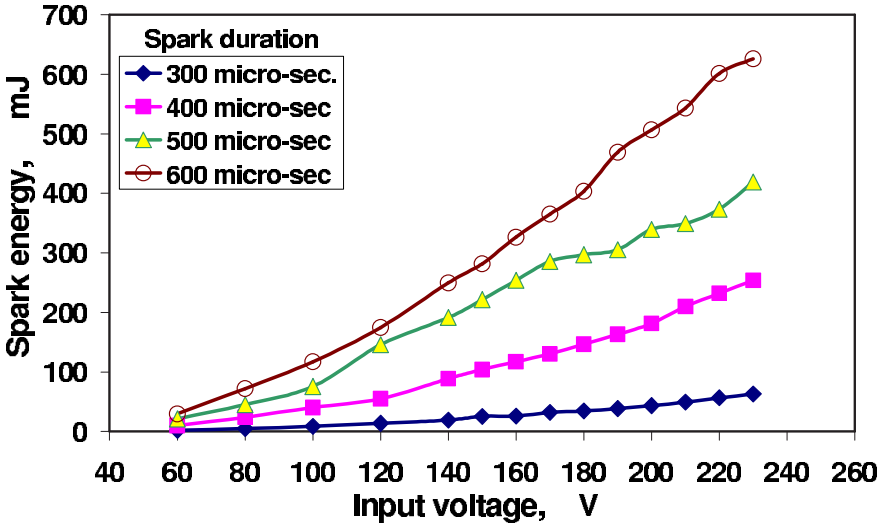

Figure A.1: Ignition unit characteristics.

- The secondary coil voltage (spark voltage) can be monitored from the ignition coil box, while the primary coil current can be monitored from the control unit.

The output voltage and current from the ignition coil should be connected to the igniter. The igniter design used in the present work is shown in Fig. A.2. It should be mentioned that tungsten is the best material for the electrodes due to its high temperature resistance. Ceramic and teflon are useful insulation materials that can be used with the present igniter as they can resist high temperatures and do not connect electricity.

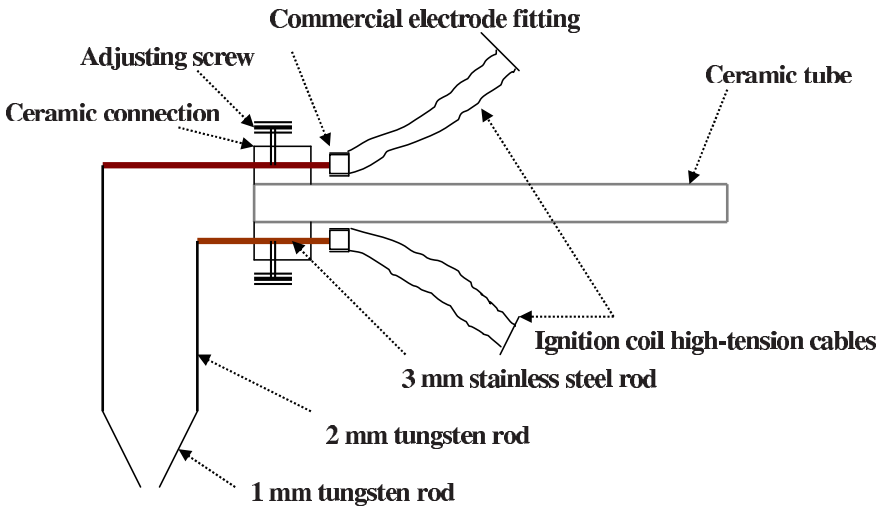

Figure A.2: Schematic diagram of the spark igniter design.

Appendix B

Image processing

The raw instantaneous image of the acetone PLIF underwent through different image correction processes before being used in the mixture fraction calculation. These processes can be summarized as follows:

- Before each measurement condition an average (from 20 images) background image was taken with the laser sheet in place, but without the acetone being injected to the flow in order to remove any reflections from the image domain. This results in signal-to-noise ratio between 20 and 25, in most of the experiments in the present work.

- The next step is to correct the raw image for the beam profile non-uniformity and the shot-to-shot variation in the laser power. This was done by using the instantaneous Dye cell images to correct the corresponding instantaneous raw images.

- The shot noise, mostly caused by the image intensifier, was then removed from the corrected raw image. Median smoothing is a non-linear operation that is generally accepted as being an efficient approach to remove this type of noise (Lim, 1990).

- All the corrected images were then normalized by the value of mixture frac-

tion $\xi = 1$, which is corresponds to the acetone PLIF of pure fuel, as explained in Section 4.2.2 and 5.2.4.2 for the counter-flow and bluff-body flames respectively. The instantaneous corrected images were transferred following this process to instantaneous mixture fraction images, which are about 1000 images for each case.

- The Wiener filter was then used to remove the high-frequency noise from the mixture fraction images. This filter is the optimal mean square error stationary linear filter for images degraded by additive noise and blurring and it is usually used for the current range of the signal-to-noise ratio (Portilla et al., 2003). In Matlap, this filter can be used with a function (wiener2).

- The instantaneous mixture fraction images were averaged over the number of images obtained to calculate the mean and the r.m.s of the mixture fraction.

Appendix C

List of Publications

Journal Publications

1. S.F. Ahmed, E. Mastorakos, Spark ignition of turbulent lifted jet flames, *Combustion and Flame* 146 (2006) 215-231.

2. S.F. Ahmed, R. Balachandran, E. Mastorakos, Measurements of the ignition probability in turbulent counter-flow flames, *Proceedings of the Combustion Institute* 31, (2006), In press.

Conference Publications

1. S.F. Ahmed, E. Mastorakos, Measurements of the probability of ignition and subsequent flame propagation speed in turbulent non-premixed jets, *20th International Curriculum in Dynamics of Explosion and Reactive Systems*, Montreal, Canada, August 2005.

2. S.F. Ahmed, R. Balachandran, Y.-Y. He, E. Mastorakos, Spark ignition of turbulent premixed and non-premixed opposed jet flames, 42^{nd} *AIAA/ASME/SAE/ASEE*

Joint Propulsion Conference and Exhibit, California, USA, July 2006.

3. S.F. Ahmed, T. Marchione, E. Mastorakos, Experimental investigation of ignition in turbulent non-premixed bluff-body flames, 43^{rd} *AIAA/ASME/SAE/ASEE Joint Propulsion Conference and Exhibit*, Cincinnati, USA, July 2007.

In Preparation

1. S.F. Ahmed, R. Balachandran, T. Marchione, E. Mastorakos, Spark ignition of turbulent non-premixed bluff-body flames, *Combustion and Flame*, 2007 [in preparation].

Bibliography

R.G. Abdel-Gayed, K.J. Al-Khishali, and D. Bradley. Turbulent burning velocity and flame strainig in explosions. *Proceedings of the Royal Society of London A*, 391:393–414, 1984a. 3.1.5.1

R.G. Abdel-Gayed, D. Bradley, M.N. Hamid, and M. Lawes. Lewis number effects on turbulent burning velocity. *Proceedings of the Combustion Institute*, 20:505–512, 1984b. 3.1.5.1

S.K. Aggarwal. A review of spray ignition phenomena: Present status and future research. *Progress in Energy and Combustion Science*, 24:565–600, 1998. 1.1

Y.M. Al-Abdeli and A.R. Masri. Recirculation and flowfield regimes of unconfined non-reacting swirling flows. *Experimental Thermal and Fluid Science*, 27:655–665, 2003. 5.1.2

P.G. Aleiferis, Y. Hardalupas, A.M.K.P. Taylor, K. Ishii, and Y. Urata. Flame chemiluminescence studies of cyclic combustion variations and air-to-fuel ratio of the reacting mixture in a lean-burn stratified-charge spark-ignition engine. *Combustion and Flame*, 136:72–90, 2004. 3.2.8, 3.2.8

R.F. Alvani and M. Fairweather. Ignition characteristics of turbulent jet flows. *Transaction Institution of Chemical Engineers*, 88:431–449, 2002. 3.1.3

G. Amantini, J.H. Frank, and A. Gomez. Experiments on standing and travelling edge flames around flame holes. *Proceedings of the Combustion Institute*, 30: 313–321, 2005. 4.1.4, 4.1.4

Anon. KLGignition equipment, igniters and glow plugs. Technical Report Smiths Aviation Division Maintenance Manual 74-20-102/01, 1961. 1.2, 1.2

A. Ata, J.s. Cowart, A. Vranos, and B.M. Cetegen. Effects of direct current electric field on the blowoff characteristics of bluff-body stabilized conical premixed flames. *Combustion Science and Technology*, 177:1291–1304, 2005. 5.1.3.2

R. Balachandran. *Experimental Investigation of the Response of Turbulent Premixed Flames to Acoustic Oscillations*. PhD thesis, University of Cambridge, 2005. (document), 2.1, 2.5, 2.4.2, 5.1.2.1, 5.1, 5.1.4, 5.2.4.2

D. R. Ballal and A. H. Lefebvre. The influence of flow parameters on minimum ignition energy and quenching distance. *Proceedings of the Combustion Institute*, 15:1473–1481, 1976. 3.1.2, 3.1.2

D. R. Ballal and A. H. Lefebvre. A general model of spark ignition for gaseous and liquid fuel-air mixtures. *Proceedings of the Combustion Institute*, 18:1737–1746, 1980. 3.1.2

D.R. Ballal and A.H. Lefebvre. The influence of spark discharge characteristics on minimum ignition energy in flowing gases. *Combustion and Flame*, 24:99–108, 1975a. 3.1.2, 3.1.2, 3.1.2, 3.2.5.3, 3.2.5.3

D.R. Ballal and A.H. Lefebvre. The structure and propagation of turbulent flames. *Proceedings of the Royal Society of London A*, 334:217–234, 1975b. 3.1.5.1

D.R. Ballal and A.H. Lefebvre. Ignition and flame quenching in flowing mixtures. *Proceedings of the Royal Society of London A*, 357:163–181, 1977. 3.1.2, 3.1.2

D.R. Ballal and A.H. Lefebvre. Ignition of liquid fuel sprays at subatmospheric pressures. *Combustion and Flame*, 31:115–126, 1978. 3.1.2, 3.1.2, 3.2.5.3

D.R. Ballal and A.H. Lefebvre. Ignition and flame quenching of flowing heterogeneous fuel-air mixtures. *Combustion and Flame*, 35:155–168, 1979. 3.1.2

J.M. Beer and N.A. Chigier. *Combustion Aerodynamics*. Applied Science, 1st edition, 1972. 5.1.2, 5.1.2.3, 5.1.2.3, 5.1.2.5

R.W. Bilger. The structure of turbulent nonpremixed flames. *Proceedings of the Combustion Institute*, 22:475–488, 1988. 1.3.2

R.W. Bilger, S.H. Starner, J.H. Frank, D.F. Marran, and M.B. Long. Mixture fraction imaging in a lifted methane jet flame. *Combustion and Flame*, 107: 307–313, 1996. 3.1.3

A.D. Birch, D.R. Brown, and M.G. Dodson. Ignition probabilities in turbulent mixing flows. *Proceedings of the Combustion Institute*, 18:1775–1780, 1981. 3.1.4, 3.2.5.1, 4.2.4.1

A.D. Birch, D.R. Brown, M.G. Dodson, and J.R. Thomas. Studies of flammability in turbulent flows using laser raman spectroscopy. *Proceedings of the Combustion Institute*, 17:307–314, 1978a. (document), 3.1.3, 3.1

A.D. Birch, D.R. Brown, M.G. Dodson, and J.R. Thomas. The turbulent concentration field of a methane jet. *Journal of Fluid Mechanics*, 88:431–449, 1978b. 3.1.3

N.K. Bourne. On the laser ignition and initiation of explosive. *Proccedings of Royal Society of London A*, 457:1401–1426, 2001. 1.2

D. Bradley, O.O. Akindele, P.W. Mak, and M. McMahon. Spark ignition of turbulent gases. *Combustion and Flame*, 47:129–155, 1982. 3.1.2

D. Bradley, M.Z. Haq, R.A. Hicks, T. Kitagawa, M. Lawes, C.G.W. Sheppard, and R. Woolley. Turbulent burning velocity, burned gas distribution, and associated flame surface definition. *Combustion and Flame*, 133:415–430, 2003. 3.1.5.1

D. Bradley, M. Lawes, and M.J. Scott. Afterburning in spherical premixed turbulent explosions. *Combustion and Flame*, 99:581–590, 1994. 3.1.5.1

D. Bradley and F.K-K. Lung. Spark ignition and the early stages of turbulent flame propagation. *Combustion and Flame*, 69:71–93, 1987. 3.1.2, 3.1.2, 3.1.2

K.N.C. Bray, M. Champion, and P.A. Libby. Premixed flames in stagnating turbulence: Part I. the general formation for counterflowing streams and gradient models for turbulent transport. *Combustion and Flame*, 84:391–410, 1991. 4.1.2

P.D. Brum and G.S. Samuelsen. Two-component laser anemometry measurements of non-reacting and reacting complex flows in a swirl-stabilized model combustor. *Experiments in Fluids*, 5:95–102, 1987. 5.1.2

J. Buckmaster. Egde-flames and their stability. *Combustion Science and Technology*, 115:41–68, 1996. 4.1.4, 4.1.4, 4.2.3.2, 4.2.4.3

J. Buckmaster and M. Matalon. Anomalous Lewis number effects in tribrachial flames. *Proceedings of the Combustion Institute*, 22:1527–1535, 1988. 3.2.7

W.F. Carnell-Jr and M.W. Renfro. Stable negative edge flame formation in a counterflow burner. *Combustion and Flame*, 141:350–359, 2005. 4.1.4

H.K. Chelliah, C.K. Law, T. Ueda, M.D. Smooke, and F.A. Williams. An experimental and theoretical investigation of the dilution, pressure and flow-field

effects on the extinction condition of methane-air-nitrogen diffusion flames. *Proceeding of the Combustion Institute*, 23:503–511, 1990. 4.1.3, 4.2.3.1

R.H. Chen and J.F. Driscoll. The role of the recirculation vortex in improving fuel-air mixing within swirling flames. *Proceedings of the Combustion Institute*, 22:536–540, 1989. 5.1.2.3, 5.1.2.3

R.H. Chen, J.F. Driscoll, J. Kelly, M. Namazian, and R.W. Schefer. A comparison of bluff-body and swirl-stabilized flames. *Combustion Science and Technology*, 71:197–217, 1990. 5.1.3.2

Y.C. Chen, C.C. Chang, K.L. Pan, and J.T. Yang. Flame lift-off and stabilization mechanisms of nonpremixed jet flames on a bluff-body burner. *Combustion and Flame*, 115:51–65, 1998. 5.1.3.2

T.S. Cheng, Y.C. Chao, D.C. Wu, T. Yuan, C.K. Cheng, and J.M. Chang. Effect of fuel-air mixing on flames structures and NO_x emissions in swirling methane jet flames. *Proceedings of the Combustion Institute*, 27:1229–1237, 1998. 5.1.3, 5.1.3.2, 5.2.3

J.S. Chin. The analysis of the effect of oxygen addition on minimum ignition energy. *AIAA Journal*, 82:1160, 1982. 1.2

P. Cho, C.K. Law, R.K. Cheng, and I.G. Shepherd. Velocity and scalar fields of turbulent premixed flames in stagnation flow. *Proceeding of the Combustion Institute*, 22:739–745, 1988. 4.1.2

Y.S. Cho, D.A. Santavicca, and R.M. Sconntag. The effect of the spark power on spark-ignited flame kernel growth. *SAE Technical Paper*, 922168:1–11, 1992. 3.1.4, 3.2.6

S.M. Correa and A. Gulati. Measurements and modeling of a bluff-body stabilized flame. *Combustion and Flame*, 89:195–213, 1992. 5.1.3.2

S.M. Correa and S.B. Pope. Comparison of a Monte Carlo PDF/finite-volume mean flow model with bluff-body Raman data. *Proceedings of the Combustion Institute*, 24:279–285, 1992. 5.1.2

D. Crosley. Collisional effects on laser-induced flourescence flame measuremnets. *Optical Engineering*, 20, 1993. 2.4

B.B. Dally, A.R. Masri, R.S. Barlow, and G.J. Fiechtner. Instantaneous and mean compositional structure of bluff-body stabilized nonpremixed flames. *Combustion and Flame*, 114:119–148, 1998. 5.1.3, 5.1.3.1

A.M. Danis, I. Namer, and N.P. Cernansky. Droplet size and equivalence ratio effects on spark ignition of monodisperse n-heptane and methanol sprays. *Combustion and Flame*, 74:285–294, 1988. 3.1.2

J. Dawson, R. Balachandran, and E. Mastorakos. Velocity measurements in acoustically forced recirculating flows. *In preparation*, 2007. (document), 5.2.1, 5.2.4.1, 5.8, 5.9, 5.10, 5.11

D.R. Dowling and P.E. Dimotakis. Similarity of the concentration field of gas-phase turbulent jets. *Journal of Fluid Mechanics*, 218:109–141, 1990. 3.1.3, 3.1.3, 3.2.2.2

A. Dreizler, S. Lindenmaier, U. Mass, M. Alden, and C.F. Kaminski. Characterization of a spark ignition system by planar laser-induced fluorescence of OH at high repetition rates and comparison with chemical kinetic calculations. *Applied Physics B*, 70:287–294, 2000. 3.1.2, 3.1.2

A. Dreizler, S. Lindenmaier, U. Mass, M. Thiele, J. Warnatz, A. Grant, and P. Ewart. Spark ignition hydrogen/air mixtures: Two dimensional detailed modeling and laser based diagnostics. *Combustion and Flame*, 128:74–87, 2002. 3.1.2

D. Dukic. Electronic Division - Department of Engineering - University of Cambridge. *Personal Communication*, 2003. 2.2

D.F.G. Durao and J.H. Whitelaw. Velocity characteristics of the flow in the near wake of a disk. *Journal of Fluid Mechanics*, 85:369–385, 1978. 5.1.2, 5.1.2.2, 5.1.2.5

D.A. Eichenberger and W.L. Roberts. Effect of unsteady stretch on spark-ignited flame kernel survival. *Combustion and Flame*, 118:469–478, 1999. 3.1.4

H. Eickhoff, B. Lenze, and W. Leuckel. Experimental investigation on the stabilization mechanism of jet diffusion flames. *Proceedings of the Combustion Institute*, 20:311–318, 1984. 3.1.6

I. Esquiva-Dano, H.T. Nguyen, and D. Escudie. Influence of a bluff-body's shape on the stabilization region of non-premixed flames. *Combustion and Flame*, 127:2167–2180, 2001. 5.1.2, 5.1.3.2

L. Fallot, M. Gonzalez, R. Elamraoui, and M. Obounou. Modelling finite-rate chemistry effects in nonpremixed turbulent combustion: Test on the bluff-body stabilized flame. *Combustion and Flame*, 110:298–318, 1997. 5.1.3

T.D. Fansler, B. Stojkovic, M.C. Drake, and M.E. Rosalik. Local fuel concentration measurements in internal combustion engines using spark-emission spectroscopy. *Applied Physics B*, 75:577–590, 2002. 3.2.8

V. Favier and L. Vervich. Edge flames and partially premixed combustion in diffusion flame quenching. *Combustion and Flame*, 125:788–803, 2001. 4.1.4

H.H. Foster. The effect of spark repetition rate on the ignition limits of a single tubular combustor. Technical Report NACA RM E51J18, 1951. 3.1.2, 3.1.2

C.E. Frouzakis, A.G. Tomboulides, J. Lee, and K. Boulouchos. From diffusion to premixed flames in an H_2/air opposed-jet burner: the role of edge flames. *Combustion and Flame*, 130:171–184, 2002. 4.1.4

D. Geyer, A. Kempf, A. Dreizler, and J. Janicka. Turbulent opposed-jet flames: A critical benchmark experiment for combustion LES. *Combustion and Flame*, 143:524–548, 2005. 4.1.1, 4.2.2, 4.2.2, 4.2.4.1

S.R. Gollahalli, O. Savas, R.F. Huang, and J.L. Azara. Structure of attached and lifted gas jet flames in hysteresis region. *Proceedings of the Combustion Institute*, 21:1463–1471, 1986. 3.1.6, 3.2.4

R.A. Granger. *Fluid Mechanics*. Holt, Rinehart and Winston, London, 1985. 2.1.1

A.K. Gupta, D.G. Lilley, and N. Syred. *Swirl Flows*. Abacus Press, 1st edition, 1984. 5.1.3.2

L.C. Haber. *An Investigation Into the Orgion, Measurements and Application of Chemiluminescence Light Emissions From Premixed Flames*. PhD thesis, Virginia Polytechnic Institute and State University, Blacksburg, Virginia, USA, 2000. 2.6

Y. Hardalupas and M. Orain. Local measurements of the time-dependent heat release rate and equivalence ratio using chemiluminescent emission from a flame. *Combustion and Flame*, 139:188–207, 2004. 3.2.8

J.P. Hornak. *Encyclopedia of Imaging Sceince and Technology*. John Wiley and Sons, New York, USA, 2002. 2.4.1

R.F. Huang and C.L. Lin. Visualized flow patterns of double concentric jets at low annulus velocities. *AIAA Journal*, 32:1868–1874, 1994. 5.1.2, 5.1.3.2

International Flame Research Foundation IFRF. Research at Ijmuiden during the triennial. Technical Report IFRF DOC No. K65/a/2, 1989. 5.1.2.4

T.A. Jarymowycz and A.M. Mellor. Effects of alternative fuels on ignition limits of the J85 annular combustor. *Journal of Propulsion and Power*, 3:283–288, 1987. 5.1.5

P.A.M. Kalt, Y.M. Al-Abdeli, A.R. Masri, and R.S. Barlow. Swirling turbulent non-premixed flames of methane: Flow field and compositional structure. *Proceedings of the Combustion Institute*, 29:1913–1919, 2002. 5.1.3, 5.1.3.1

C.F. Kaminski, X.S. Bai, J. Hult, A. Dreizler, S. Lindenmaier, and L. Fuchs. Flame growth and wrinkling in a turbulent flow. *Applied Physics B*, 71:711–716, 2000a. 3.1.4

C.F. Kaminski, J. Hult, M. Alden, S. Lindenmaier, A. Dreizler, U. Mass, and M. Baum. Spark ignition of turbulent methane air mixtures reveled by time-resolved planar laser-induced fluorescence and direct numerical simulations. *Proceedings of the Combustion Institute*, 28:399–405, 2000b. 3.1.2

J.B. Kelman and A.R. Masri. Quantitative technique for imaging mixture fraction, temperature, and the hydroxyl radical in turbulent diffusion flames. *Applied Optics*, 36:No.15, 1997. 3.1.3

I.S. Kim and E. Mastorakos. Simulation of turbulent non-premixed counter-

flow flames with first-order conditional moment closure. *Flow, Turbulence and Combustion*, 76:133–162, 2006. 4.1.3

A. Kitajima, H. Torikai, M. Takeuchi, and Masaaki Oya. Experimental study of extinction and its quantification in laminar and turbulent counterflow $CH_4 - N_2/O_2 - N_2$ nonpremixed flames. *Combustion and Flame*, 137:93–108, 2004. 4.1.3, 4.1.3

A. Kitajima, T. Ueda, A. Matsuo, and M. Mizomoto. Experimental investigation of the flame structure and extinction of turbulent counterflow non-premixed flames. *Proceedings of the Combustion Institute*, 26:137–143, 1996. 4.1.3

A. Kitajima, T. Ueda, A. Matsuo, and M. Mizomoto. A comparison examining of the structure and extinction of turbulent flames formed in a counterflow. *Combustion and Flame*, 121:301–311, 2000. 4.1.2

Y. Ko and R.W. Anderson. Electode heat transfer during spark ignition. *SAE Technical Paper*, 892083:2006–2014, 1989. 3.1.4, 3.2.5.3

Y.S. Ko and S.H. Chang. Propagation of unsteady tribrachial flames in laminar non-premixed jets. *Combustion and Flame*, 118:151–163, 1999. 3.1.5.2, 3.2.7

M. Kono, K. Hatori, and K. Iinuma. Investigation on ignition ability of composite sparks in flowing mixtures. *Proceedings of the Combustion Institute*, 20:133–140, 1984. 3.1.4, 4.2.4.1, 4.2.4.1

M. Kono, K. Niu, T. Tsukamoto, and Y. Ujiie. Mechanism of flame kernel formation produced by short duration sparks. *Proceedings of the Combustion Institute*, 22:1643–1649, 1988. 3.2.6

E. Korusoy and J.H. Whitelaw. Opposed jets with small separations and their

implications for the extinction of opposed flames. *Experiments in Fluids*, 31: 111–117, 2001. 4.1.2

L.W. Kostiuk, K.N. Bray, and R.K. Cheng. Experimental study of premixed turbulent combustion in opposed streams. part II-reacting flow field and extinction. *Combustion and Flame*, 92:396–409, 1993a. 4.1.3

L.W. Kostiuk, K.N. Bray, and R.K. Cheng. Experimental study of premixed turbulent combustion in opposed streams. partI-nonreacting flow field. *Combustion and Flame*, 92:377–395, 1993b. 4.1.2

L.W. Kostiuk, K.N. Bray, and T.C. Chew. Premixed turbulent combustion in counterflowing streams. *Combustion Science and Technology*, 64:233–241, 1989. 4.1.2

C.K. Law, D.L. Zhu, and G. Yu. Propagation and extinction of stretched premixed flames. *Proceeding of the Combustion Institute*, 21:1419–1426, 1986. 4.1.4

J. Lee, S.H. Won, S.H. Jin, S.H. Chung, O. Fujita, and K. Ito. Propagation speed of tribrachial (triple) flame of propane in laminar jets under normal and micro gravity conditions. *Combustion and Flame*, 134:411–420, 2003. 3.1.5.2

A.H. Lefebvre. *Gas Turbine Combustion*. Taylor and Francis, London, 2st edition, 1998. (document), 1.1, 1.1, 1.2, 1.2, 1.2, 1.2, 1.2, 2.1.1, 3.1.2, 3.1.2, 3.1.2, 3.2.5.1, 3.2.5.3, 4.2.4.3, 5.1.3.2

B. Lewis, M.V. Blanc, P.G. Guest, and G.V. Elbe. Ignition of explosive gas mixtures by electric sparks. *Proceedings of the Combustion Institute*, 3:363–367, 1954. 3.1.2

B. Lewis and G.V. Elbe. *Combustion, Flames and Explosions of Gases*. Harcourt Brace Jovanovich, Publishers, London, 1987. 2.2, 3.1.2, 3.1.5.1, 3.2.5.3, 3.2.5.3, 3.2.5.3

J.S. Lim. *Two-Dimentional Signal and Image Processing*. Prentice Hall, Englewood Cliffs, NJ, USA, 1990. B

M.T. Lim, R.W. Anderson, and V.S. Arpaci. Prediction of spark kernel development in constant volume combustion. *Combustion and Flame*, 69:303–316, 1987. 3.1.4

R.P. Lindstedt, D.S. Luff, and J.H. Whitelaw. Velocity and strain-rate characteristics of opposed isothermal flows. *Flow, Turbulence and Combustion*, 74: 169–194, 2005. (document), 4.1.2, 4.1

J.B. Liu and P.D. Ronney. Premixed edge-flames in spatially-varying straining flows. *Combustion Science and Technology*, 144:21–45, 1999. 4.1.4, 4.1.4

J.P. Longwell, E.E. Frost, and M.A. Weiss. Flame stability in bluff body recirculation zonees. *Industrial and Engineering Chemistry*, 45:1629–1633, 1953. 5.1.1

H.K. Ma and J.S. Harn. The jet mixing effect on reaction flow in a bluff-body burner. *International Journal of Heat and Mass Transfer*, 37:2957–2967, 1994. 5.1.2, 5.1.2.2, 5.1.2.3

R. Maly. Ignition model for spark discharges and the early phase of flame front growth. *Proceedings of the Combustion Institute*, 18:1747–1754, 1981. 3.1.4

R. Maly and M. Vogel. Initiation and propagation of flame fronts in lean CH_4-air mixture by the three modes of the ignition spark. *Proceedings of the Combustion Institute*, 17:821–831, 1978. 3.1.5.1

A.R. Masri and R.W. Bilger. Turbulent diffusion flames of hydrocarbon fuels stabilized on a bluff-body. *Proceedings of the Combustion Institute*, 20:319–326, 1984. 5.1.3.2

A.R. Masri, R.W. Bilger, and R.W. Dibble. Conditional probability density functions measured in turbulent nonpremixed flames of methane near extinction. *Combustion and Flame*, 74:267–284, 1988a. 3.1.3

A.R. Masri, R.W. Bilger, and R.W. Dibble. Turbulent nonpremixed flames of methane near extinction: Mean structure from Raman measurements. *Combustion and Flame*, 71:245–266, 1988b. 3.1.3

A.R. Masri, R.W. Bilger, and R.W. Dibble. Turbulent nonpremixed flames of methane near extinction: Probability density function. *Combustion and Flame*, 73:261–285, 1988c. 3.1.3

A.R. Masri, P.A.M. Kalt, and R.S. Barlow. The compositional structure of swirl-stabilised turbulent nonpremixed flames. *Combustion and Flame*, 137:1–37, 2004. 5.1.3.2

A.R. Masri, S.B. Pope, and B.B. Dally. Probability density function computations of a strongly swirling nonpremixed flame stabilized on a new burner. *Proceedings of the Combustion Institute*, 28:123–121, 2000. 5.1.3.2

E. Mastorakos. *Turbulent Combustion in Opposed Jet Flows*. PhD thesis, Imperial College, London, 1993. (document), 2.1, 2.3, 4.1.2, 4.1.5, 4.2.2, 4.2.2, 4.2.4.1, 4.2.5

E. Mastorakos, A.M.K.P. Taylor, and J.H. Whitelaw. Extinction and temperature characteristics of turbulent counterflow diffusion flames with partial premixing. *Combustion and Flame*, 91:40–54, 1992a. 4.1.3

E. Mastorakos, A.M.K.P. Taylor, and J.H. Whitelaw. Scalar dissipation rate at the extinction of turbulent counterflow nonpremixed flames. *Combustion and Flame*, 91:55–64, 1992b. 4.1.3, 4.1.3

W. Meier, O. Keck, B. Noll, O. Kunz, and W. Stricker. Investigations in the TECFLAM swirling diffusion flame: Laser Raman measurements and CFD calculations. *Applied Physics B*, 71:725–731, 2000. (document), 5.1.3, 5.1.3.1, 5.2

J. Mi, D.S. Nobes, and G.J. Nathan. Influence of jet exit conditions on the passive scalar field of an axisymmetric free jet. *Journal of Fluid Mechanics*, 432:91–125, 2001. 3.1.3, 3.2.2.2

R.C. Miake-Lye and J.A. Hammer. Lifted turbulent jet flames: a stability criterion based on the jet large-scale structure. *Proceedings of the Combustion Institute*, 22:817–824, 1988. 3.1.6, 3.2.4, 3.2.4

V.D. Milosavljevic, A.M.K.P. Taylor, and J.H. Whitelaw. The influence of burner geometry and flow rates on the stability and symmetry of swirl-stabilized non-premixed flames. *Combustion and Flame*, 80:196–208, 1990. 5.1.3, 5.1.3.1, 5.1.3.2

C.M. Muller, H. Breitbach, and N. Peters. Partially premixed turbulent flame propagation in jet flames. *Proceedings of the Combustion Institute*, 25:1099–1106, 1994. 3.2.7

D.W. Naegeli and L.G. Dodge. Ignition study in a gas turbine combustor. *Combustion Science and Technology*, 80:165–184, 1991. 5.1.5, 5.2.5.1

M. Namazian, J. Kelly, and R.W. Schefer. Concentration imaging measurements in turbulent concentric-jet flows. *AIAA Journal*, 30:384–394, 1992. 5.1.2

M. Namazian, J. Kelly, R.W. Schefer, S.C. Johnston, and M.B. Long. Non-premixed bluff-body burner flow and flame imaging study. *Experiments in Fluids*, 8:216–228, 1989. 5.1.3, 5.1.3.1

A. Olivani, G. Solero, F. Cozzi, and A. Coghe. Near field flow structure of isothermal swirling flows and reacting non-premixed swirling flames. In *Fourth Mediterranean Combustion Symposium*, Lisbon, 2005. Combustion Institute. 5.1.3, 5.1.3.1, 5.1.3.2

J.E. Orrin, I.M. Vince, and F.J. Weinberg. A study of plasma jet ignition mechanisms. *Proceedings of the Combustion Institute*, 18:1755–1765, 1981. (document), 1.2, 1.2

J.C. Pan, W.J. Schmoll, and D.R. Ballal. Turbulent combustion properties behind a confined conical stabilizer. *Journal of Engineering for Gas Turbines and Power*, 114:33–38, 1992a. 5.1.1, 5.1.2.2, 5.1.2.3, 5.1.2.5, 5.2.4.1

J.C. Pan, M.D. Vangsness, and D.R. Ballal. Aerodynamics of bluff-body stabilized confined turbulent premixed flames. *Journal of Engineering for Gas Turbines and Power*, 114:783–789, 1992b. 5.1.1

C. Pantano. Direct simulation of non-premixed flame extinction in a methane-air jet with reduced chemistry. *Journal of Fluid Mechanics*, 514:231–270, 2004. 4.2.3.1

N. Peters. Laminar flamelet concepts in turbulent combustion. *Proceedings of the Combustion Institute*, 21:1231–1250, 1986. 3.1.3

N. Peters. *Turbulent Combustion*. Cambridge University Press, 2000. 1.3, 3.1.6

N. Peters and F.A. Williams. Lift-off characteristics of turbulent jet diffusion flames. *AIAA Journal*, 21:423–429, 1983. 3.1.6

T.X. Phuoc, C.M. White, and D.H. Mcneill. Laser spark ignition of a jet diffusion flame. *Optics and Lasers Engineering*, 38:217–232, 2002. 3.1.4

S. Pischinger and J.B. Heywood. How heat losses to the spark plug electrodes affect flame kernel development in an SI-engine. *SAE Technical Paper*, 892083: 2006–2014, 1990. 3.1.4, 3.2.5.3, 3.2.6

S.B. Pope. *Turbulent Flows*. Cambridge University Press, Cambridge, 2000. 3.2.2.1

J. Portilla, V. Strela, M. Wainwright, and E.P. Simoncelli. Image denoising using scal mixtures of gaussians in the wavelet domain. *IEEE Transactions Image Processing*, 12:1338–1351, 2003. B

B. Prade and B. Lenze. Experimental investigation in extinction of turbulent non-premixed disk stabilized flames. *Proceedings of the Combustion Institute*, 24:369–375, 1992. 5.1.3, 5.1.3.2

I.K. Puri and K. Seshadri. Extinction of diffusion flames burning diluted methane and diluted propane in diluted air. *Combustion and Flame*, 65:137–150, 1986. 4.1.3

X. Qin, C.W. Choi, A. Mukhopadhyay, I.K. Puri, S.K. Aggarwal, and V.R. Katta. Triple flame propagation and stabilization in a laminar axisymmetric jet. *Combustion Theory and Modelling*, 8:293–314, 2004. (document), 3.1.5.2, 3.3, 3.2.7

K.V. Rao and A.H. Lefebvre. Minimum ignition energies in flowing kerosene-air mixtures. *Combustion and Flame*, 27:1–20, 1976. 3.1.2

S.A. Rashkovsky. Spark ignition of ill-mixed gases. In *First Mediterranean Combustion Symposium*, Antalya, Turkey, 1999. Combustion Institute. 4.1.1

C.D. Richards and W.M. Pitts. Global density effects on the self-preservation behaviour of turbulent free jets. *Journal of Fluid Mechanics*, 254:417–435, 1993. 3.1.3, 3.1.3, 3.1.3, 3.1.3, 3.2.2.2, 3.2.5.1

E. Richardson and E. Mastorakos. Numerical investigation of spark-ignition in a laminar methane-air counterflow. *Combustion Science and Technology, In Press*, 2007. 3.1.4, 4.1.1, 4.2.4.3

W.L. Roberts and D.A. Eichenberger. Effect of unsteady stretch on spark-ignited flame kernel survival. *Combustion and Flame*, 118:469–478, 1999. 3.1.2

J.C. Rolon, D. Veynante, and J.P. Martin. Counter jet stagnation flows. *Experiments in Fluids*, 11:313–324, 1991. 4.1.2

W.M. Roquemore, R.S. Tankin, H.H. Chiu, and S.A. Lottes. A study of a bluff-body combustor using laser sheet lighting. *Experiments in Fluids*, 4:205–213, 1986. 5.1.2

G.R. Ruetsch, L. Vervisch, and A. Liñán. Effects of heat release on triple flames. *Physics of fluids*, 7:293–314, 1995. 3.1.5.2, 3.2.7

V.S. Santoro and A. Liñán. Propagation of edge flames in counterflow mixing layers experiment and theory. *Proceedings of the Combustion Institute*, 28: 2039–2046, 2000. 4.1.4, 4.1.4, 4.2.3.2, 4.2.5

K. Sardi, A.M.K.P. Taylor, and J.H. Whitelaw. Conditional scalar dissipation statistics in a turbulent counterflow. *Journal of Fluid Mechanics*, 361:1–24, 1998. 4.1.2, 4.1.2

R.W. Schefer, M. Namazian, and J. Kelly. Velocity measurements in turbulent bluff-body stabilized flows. *AIAA Journal*, 32:1844–1851, 1994. 5.1.2

R.W. Schefer, M. Namazian, J. Kelly, and M. Perrin. Effect of confinement on bluff-body burner recirculation zone characteristics and flame stability. *Combustion Science and Technology*, 120:185–211, 1996. 5.1.2, 5.1.2.4

C. Schultz and V. Sick. Tracer-LIF diagnostic: quantitative measurement of fuel concentration, teperature and fuel-air ratio in practical combustion systems. *Progress in Energy and Combustion Science*, 31:75–121, 2005. 5.1.3.1

R. Seiser, J.H. Frank, S. Liu, J.H. Chen, R.J. Sigurdsson, and K. Seshadri. Ignition of hydrogen in unsteady nonpremixed flows. *Proceedings of the Combustion Institute*, 30:423–430, 2005. 4.1.4

R. Seiser, K. Seshadri, E. Piskernik, and A. Liñán. Ignition in the viscous layer between counterflowing streams: Asymptotic theory with comparison to experiments. *Combustion and Flame*, 122:339–349, 2000. 4.1.2

R. Seiser and K. Seshardi. The influence of water on extinction and ignition of hydrogen and methane flames. *Proceedings of the Combustion Institute*, 30: 407–414, 2005. 4.1.3

M.L. Shay and P.D. Ronney. Nonpremixed edge flames in spatially varying straining flows. *Combustion and Flame*, 112:171–180, 1998. 4.1.4, 4.1.4

J.O. Sinibaldi, J.F. Driscoll, C.J. Mueller, J.M. Donbar, and C.D. Carter. Propagation speeds and stretch rates measured along wrinkled flames to assess the theory of flame stretch. *Combustion and Flame*, 133:323–334, 2003. 3.1.5.1

M.T. Smith, A.D. Birch, D.R. Brown, and M. Fairweather. Studies of ignition and flame propagation in turbulent jets of natural gas, propane and a gas with a high hydrogen content. *Proceedings of the Combustion Institute*, 21: 1403–1408, 1986. (document), 2.2, 2.7, 3.1.4, 3.2, 3.1.4, 3.2.2.3, 3.2.5, 3.2.5.1, 3.2.5.2, 3.2.5.2, 4.2.4.1

M.D. Smooke, I.K. Puri, and K. Seshardi. A comparison between numerical calculations and experimental measurements of the structure of a counterflow diffusion flame burning diluted methane in diluted air. *Proceeding of the Combustion Institute*, 21:1783–1792, 1986. 4.1.2

G.G. Soete. Effects of geometrical and aerodynamic induced flame stretch on the propagation of spark fired premixed flames in early stages. *Proceedings of the Combustion Institute*, 20:161–168, 1984. 3.1.5.1

D.B. Spalding. Theoretical aspects of flame stabilization. *Aircraft Engineering*, 25:264–276, 1953. 5.1.1

G. Stan and A. Johnson. Experimental and numerical analysis of turbulent opposed impinging jets. *AIAA Journal*, 39:1901–1908, 2001. 4.1.1

S.H. Starner, R.W. Bilger, R.W. Dibble, and R.S. Barlow. Measurements of conserved scalars in turbulent diffusion flames. *Combustion science and Technology*, 86:223–236, 1992. 3.1.3

C.C. Swett. Spark ignition of flowing gases using long-duration discharges. *Proceedings of the Combustion Institute*, 6:523–532, 1957. 3.1.2, 3.1.2, 3.2.5.1

T. Takagi, I. Nakajima, and S. Kinoshita. Structure and propagation of strain-controlled $H_2/N_2/Air$ diffusion edge flames. *Proceedings of the Combustion Institute*, 29:1573–1579, 2002. 4.1.4

F. Takahashi, M. Mizomoto, S. Ikai, and N. Futaki. Lifting mechanism of free jet diffusion flames. *Proceedings of the Combustion Institute*, 20:295–302, 1984. 3.2.4

F. Takahashi and W.J. Schmoll. Lifting criteria of jet diffusion flames. *Proceedings of the Combustion Institute*, 23:677–683, 1990. 2.1.1

M.A. Tanoff, M.D. Smooke, R.J. Osborne, T.M. Brown, and R.W. Pitz. The sensitive structure of partially premixed methane-air vs. air counterflow flames. *Proceedings of the Combustion Institute*, 26:1121–1128, 1996. 4.1.2

A.M.K.P. Taylor and J.H. Whitelaw. Velocity characteristics in the turbulent near wakes of confined axisymmertic bluff bodies. *Journal of Fluid Mechanics*, 139:391–418, 1984. 5.1.2, 5.1.2.2, 5.2.4.1

R.E. Teets and J.A. Sell. Calorimetry of ignition sparks. *SAE Technical Paper*, 880204:6371–6383, 1988. 2.2, 3.1.2, 3.1.4, 3.2.5.3, 3.2.5.3

S.D. Terry and K.M. Lyons. Low Reynolds number turbulent lifted flames in high co-flow. *Combustion Science and Technology*, 177:2091–2112, 2005. 3.2.7

S.R. Tieszen, D.W. Stamps, and T.J. O'Hern. A heuristic model of turbulent mixing applied to blowout of turbulent jet diffusion flames. *Combustion and Flame*, 106:442–466, 1996. 3.2.2.1

A.A. Townsend. *The Structure of Turbulent Shear Flow.* Cambridge University Press, Cambridge, 1976. 3.2.2.1

H. Tsuji, A. Yoshida, and N. Endo. Effect of turbulence on extinction of counterflow diffusion flame. *Proceeding of the Combustion Institute*, 25:1191–1197, 1994. 4.1.3

S.R. Turns. *An Introduction to Combustion: Concepts and Applications.* McGraw Hill, London, 2000. 3.1.5.1, 4.2.4.3

L. Vanquickenborn and A. Van-Tiggelen. The stabilization mechanism of lifted diffusion flames. *Combustion and Flame*, 10:59–69, 1966. 3.1.6

T.G. Vedarajan, J. Buckmaster, and P. Ronney. Two-dimensional failure waves and ignition fronts in premixed combustion. *Proceedings of the Combustion Institute*, 27:537–544, 1998. 4.1.4

T.G. Vedrarajan and J. Buckmaster. Edge-flames in homogeneous mixture. *Combustion and Flame*, 114:267–273, 1998. 4.1.4

D. Verhoeven. Spark heat transfer measurements in flowing gases. *SAE Technical Paper*, 952450:1–9, 1995. 3.2.5.3

F.J. Weinberg. The first half-million years of combustion research and today's burning problems. *Progress in Energy and Combustion Science*, 1:17–31, 1975. 1.3.2

K. Wol, N.M. Kapp, and C. Gazley. The stability of open flames. *Proceedings of the Combustion Institute*, 3:3–21, 1949. 3.1.6

I. Wygnaski and H. Fiedler. Some measurements in self-preserving jet. *Journal of Fluid Mechanics*, 38:577–612, 1969. 3.1.3, 3.2.2.1, 3.2.2.1

B. Yip and M.B. Long. Instantaneous planar measurement of the complete three-dimensional scalar gradient in a turbulent jet. *Optics Letters*, 11:No.2, 1986. 3.1.3

M. Yoda, L. Hesselink, and M.G. Mungal. Instantaneous three-dimensional concentration measurements in the self-similar region of a round high-Schmidt-number jet. *Journal of Fluid Mechanics*, 279:313–350, 1994. 3.2.2.2, 3.2.5.1

L.L. Yuan and R.L. Street. Trajectory entrainment of a round jet in crossflow. *Physics of Fluids*, 10:2323–2335, 1998. 5.2.4.2

T. Zsak, C. Perlee, and N. Chigier. Hysteresis in the liftoff and reattachment of hydrocarbon flames. In *Fall Technical Meeting, Eastern Section*, Miami, 1984. Combustion Institute. 3.1.6, 3.2.4

E.A. De Zubay. Characteristics of disk-controlled flames. *Aero Digest*, 61:54–56, 1950. 5.1.1

E.E. Zukowski and F.E. Marble. The role of wake transition in the process of flame stabilization on bluff bodies. *AGARD Combustion Researches and Reviews*, pages 167–180, 1955. 5.1.1, 5.1.2.5